AN INVESTIGATION OF THE STRUCTURE AND PROPERTIES OF AGED ALUMINIUM BRONZES

BY

RICHARD LEONARD JONES

Ph.D. THESIS

THE UNIVERSITY OF ASTON IN BIRMINGHAM

NOVEMBER 1979

AN INVESTIGATION OF THE STRUCTURE AND PROPERTIES OF AGED ALUMINIUM BRONZES

BY

R L JONES

Ph.D Thesis 1979

Summary

The ageing response of wrought single phase aluminium bronze alloys containing additions of cobalt up to 1% is assessed for use as a bolting material by mechanical tests, microstructural examination, and constant strain rate stress corrosion trials. The dependence of mechanical properties on cobalt concentration, degree of ageing and level of cold work is established. The presence of a precipitation hardening mechanism is identified. The hardening phase in the final stages of the precipitation sequence is shown to be a compound based on CoAl having an orientation with respect to the matrix of $[\bar{1}01]_m \parallel [\bar{1}\bar{1}1]_{ppt}$, $(111)_m \parallel (1\bar{1}0)_{ppt}$. A susceptibility to stress corrosion cracking is established for the alloy system. Two basic mechanisms are identified 1) A strain-generated active path mechanism for solutions of pH≈12 and 2) a pre-existing active path mechanism for a sea water environment. The susceptibility to stress corrosion cracking in seawater is shown to depend on the metallurgical condition of the alloy.

KEY WORDS

ALUMINIUM BRONZE, PRECIPITATION, STRESS CORROSION

CONTENTS

LIST OF TABLES AND FIGURES

1. INTRODUCTION

1.1 Material Requirements for Fasteners in a Marine Environment

The particular material properties required for fasteners have been summarised [1] as adequate proof stress ($\simeq$ 400 N/mm^2) and ductility ($\simeq$ 15%), good general corrosion performance, galvanic compatibility with the materials to be joined and immunity to stress corrosion cracking.

Copper has been traditionally used for marine applications in the wrought form since the mid-eighteenth century when it was employed to sheath ships bottoms to reduce marine fouling [2] and the ravages of wood borers. However, with advances in marine engineering concepts there have been increased requirements for higher strength levels, which have invited the development of alloys having improved specific properties for particular design requirements. The tendency has been for these alloys to be based on copper because of the inherent advantages of bio-fouling deterrance and corrosion resistance. A summary of the mechanical properties and corrosion performance of some of the wrought alloys currently available for selection is given in Table 1. However, the mechanical properties tested are only useful as a guide, since these values for cold drawn products are influenced both by the degree of cold work and bar stock size. Also the corrosion data presented are an average for the generic type and not specifically related to the particular composition quoted.

Reference to Table 1 indicates that commercially pure copper although generally regarded as having good corrosion behaviour is restricted to applications involving slow water speed because

TABLE 1 - MECHANICAL PROPERTIES OF WROUGHT COPPER ALLOY

ALLOY	NOMINAL COMPOSITION	SPECIFICATION	UTS N/MM2	PROOF STRESS 0.1% N/MM2	ELONGATION %	CORROSION POTENTIAL mV SCE	SELF CORROSION MM/YEAR	CREVICE CORROSION MM/YEAR	IMPINGEMENT RESISTANCE M/SEC	STRESS CORROSION	SELECTIV PHASE CORROSIO
Phosphorus Deoxidised Copper	Cu 99.9, P0.02	BS2870, C106	238 339*	46 316*	58 15*	- 210	.038	0.025	1.8	NO	NO
Admiralty Brass	Cu 71, Sn 1, Zn Rem	BS2871, CZ111	370 585*	154 431*	60 10*	- 240	.050	0.05	3.1	YES	NO
HT Brass	Cu 66, Fe 1, Mn 1, Al 4.5, Zn Rem	BS2874, CZ116	724	462	15	- 280	.18	3.8	2.6	YES	YES
Phosphor Bronze	Sn 5, P0.03, Cu Rem	BS2870, PB102 BS2874, PB102	339 570*	123 508*	66 14*	- 200	.05	0.05	-	NO	NO
7% Aluminium Bronze	Cu 91, Al 7, Fe 2	BS2871, CA102	508	239	30	- 200	.05	0.05	4.3	NO	NO
9% Aluminium Bronze	Al 9.2, Fe 2, Cu Rem	BS2872, CA103 BS2874, CA103	554 655*	277 385	22 16	- 220	.06	0.08	4.6	YES	YES
Al Si Bronze	Al 6.5, Si 2, Fe 0.8, Cu Rem	ASTM B124 Alloy 11a	554 655*	231 370*	38 25*	- 190	.06	0.08	2.4	NO	NO
Complex Aluminium Bronze	Al 9.5, Ni 5, Fe 5, Mn 0.5, Cu Rem	BS2872, CA104	654 877*	402 450*	15 14*	- 190	.06	0.51	4.3	NO	NO
90/10 Cupro Nickel	Ni 10, Fe 1.5, Mn 0.8, Cu Rem	BS2871, CN102	323 416*	108 362*	45 16*	- 200	.04	0.04	3.7	NO	NO
70/30 Cupro Nickel	Ni 31, Mn 1, Fe 0.8, Cu Rem	BS2871, CN107	310 477*	131 424*	46 17*	- 180	0.025	0.025	4.6	NO	NO
Complex Cupro Nickel	Ni 13.5, Mn 3.5, Al 1.0, Fe 0.7, Cu Rem	Commercial Specification	726	430	22	- 190	0.025	0.025	3.2	YES	NO

*½ Hard or as Rolled

of low impingement resistance. Copper is also limited in use as an engineering material by inadequate mechanical properties even when cold drawn.

The brasses have improved tensile properties compared to copper and have been used as a fastener material. However, they are not now considered suitable for shipboard applications because of their poor corrosion performance. The single phase alloy (BS 2871, CZ111) is susceptible to dezincification,[3] and although additions of arsenic have been shown to be beneficial in this respect,[4,5] concentrations of this element in excess of 0.03 wt % increase the susceptibility of the alloy to stress corrosion. The high tensile brass (BS 2874 CZ116) with an $\alpha + \beta$ duplex structure gives a further order of improvement in mechanical properties and is more readily hot worked, but there is increased tendency for dezincification of the beta phase.[6]

The tin bronze alloys, an example being BS 2874, PB102, have good corrosion resistance and comparable mechanical properties in the cold worked state to high tensile brass. Their hot workability is, however, poor,[7] a particular disadvantage in the manufacture of bolts where hot-heading is often used in the production cycle to decrease the amount of machining required for larger bolts where cold heading is limited by press capacity. However, since the tin bronzes are mainly strengthened by cold work, hot-heading would not be desirable because of the accompanying reduction in mechanical properties.

Alloys based on the copper-nickel system encompass a wide range of mechanical properties dependent on composition. A critical iron addition, related to the nickel content, is made to the binary alloys to improve impingement resistance[8]. The general

corrosion resistance of these alloys (BS 2871, CN102 & CN107) is considered good, however, if the iron level exceeds the maximum specified and is precipitated from solid solution, then pitting corrosion can occur [9]. For higher strength applications, such as that required for fasteners, additional components are added to the basic binary system to give precipitation hardening or spinodal decomposition. Unfortunately the major strengthening additions have been shown to seriously affect hot ductility and thereby limit hot working operations. Also because of the higher strength levels these alloys have a lower tolerance to trace impurities [10].

Because of these limitations in the other alloys currently available, the aluminium bronzes best meet the needs for a fastener material in marine applications. This alloy type has currently replaced brass for naval use, having generally an improved corrosion resistance with the capacity for hot working.

The corrosion performance of the different alloys has been discussed in general terms, however, this is not a readily quantifiable parameter such as mechanical strength. In general the properties of sea water are relatively constant, but water velocity, stagnation, surface shielding, or alternating periods of wetting and drying can lead to localised changes in the environment. Therefore although materials may be listed according to their resistance to general corrosion by immersion in clean flowing sea water, these localised environmental effects can significantly alter a materials performance from that judged by such immersion trials. Therefore material selection should be dependent on the particular environmental conditions envisaged, which tend to be difficult to identify, to obviate

the unexpected deterioration of alloys under specific conditions. A further factor for consideration is galvanic coupling, which may have either an adverse or beneficial effect on the corrosion performance stated, a factor which should also be taken into account when materials selection is being undertaken.

Taking account of these observations relating to corrosion behaviour and the additional requirement for improved mechanical properties, this study concentrates on those factors which influence the stress corrosion cracking and strengthening of alloys within the Cu-Al alloy system.

1.2 Theoretical Considerations

1.2.1 Strengthening Mechanisms

One of the fundamental properties changed on alloying copper is the modulus of elasticity [11]. Nickel additions increase its value whilst Al, Zn, Mn, Si, Ge, In, Mg, As give rise to a reduction which increases in magnitude in the order of listing. However, although the modulus is a direct function of the atomic bond strength, [12] hardness and other strength properties are only improved at temperatures above 0.5 T_m [13]. At room temperature the order of strengthening additions is In, Mg, As, Mn, Si, Ge, Al, Ni, Zn and is determined by the type of the solid solution and the dislocation structure.

In general the effect of alloying on the dislocation structure may be considered in terms of stacking fault energy and thereby the equilibrium separation of partial dislocations. Additions of 7.5 atomic % aluminium to copper have been shown [14] to decrease the stacking fault energy from 700 joules/m^2 to 220 joules/m^2. Since the

stacking sequence between extended Shockley partials represents an intrinsic fault, and may be considered as a region of hexagonal close packing, the stacking fault energy would be expected to decrease in systems where alloying ultimately results in the formation of hexagonal electron compounds. A low value of stacking fault energy is associated with a high rate of work hardening since the equilibrium separation of dislocation partials is increased, which makes cross slip and the formation of jogs more difficult, and increases the size of barriers such as the sessile Lomar-Cotteral lock. The lowering of the stacking fault energy of copper by additions of aluminium has been shown to raise the transition from a low to a high temperature deformation mechanism from 0.45 T_m to 0.68 T_m. Also associated with the alloying is the increase by a factor of 3-4 times of the density of dislocations which corresponds to an increase in stress of 2-3 times to achieve an equivalent level of strain.

In addition to the change in dislocation structure, hardening may also result from alloying by interaction between solute atoms and dislocations. Two basic types can occur, 1) locking of stationary dislocations characterised by the presence of a pronounced yield point and 2) dislocation friction in which solute atoms interact with moving dislocations and effectively shift the stress/strain curve to higher values of stress. Some of the mechanisms proposed to give a pronounced yield point are:-

a. Chemical Locking [15]

Intrinsic stacking faults in face centred cubic crystals are considered as regions of hexagonal close packing in

which there may be a difference in solubility of the solute. If the solute segregates to the fault this may result in an increase in the width of the fault making dislocation interactions more difficult. The segregation also necessitates an additional force to unpin dislocations. This force is dependent on the solute concentration but independent of the temperature below that at which solute atom mobility is significant.

b. Elastic Locking [16]

Strengthening can also result from the localised elastic distortion associated with dislocations providing energetically favourable sites for solute atoms. This results from relief of the strain energy associated with defects such as dislocations, by suitable arrangements of solute atoms in the lattice, which is dependent on the relative size ratio of the solvent-solute atoms. The elastic interaction energy is greater for edge dislocations which have a hydrostatic component to their stress field associated with the dilation of the matrix. Since solute atoms do not interact strongly with screw dislocations cross slip may still be possible.

The stress required to free the dislocation from the atmosphere of solute atoms is dependent on the misfit parameter and independent of temperature except in the special instance where interstitial atoms condense along dislocation cores.

c. Stress Induced Order Locking [17]

The directionality of forces exerted by a dislocation may result in local ordering of the lattice.

Strengthening is therefore achieved since dislocation motion will necessarily disorder the lattice. The effect is related quadratically to concentration of solute, and is independent of temperature.

d. Electrostatic Locking [18]

It is also proposed that the dislocation core has an effective negative charge which can interact with solute atoms of valency differing from the solvent. However, the interaction energy associated with this mechanism is estimated as low and only approximately one fifth of that associated with elastic locking.

The mechanisms that are reported to give a shift in the stress-strain curve are:-

a. Mean Internal Stress Theory [19]

If solute atoms give rise to a misfit with the matrix a stress field will be generated around those atoms which will offer resistance to moving dislocations. The effect is, however, dependent on the concentration and associated degree of dispersion and when the distance between neighbouring stress centres is less than the minimum curvature of the dislocation, long range forces will cancel out and the degree of strengthening will be diminished.

It has been further suggested [20] that dislocation motion is not only retarded by a factor dependent on the misfit but that there is an additive force governed by the difference in elastic modulus between the solute and solvent. In such instances the frictional stress is

dependent on the square root of the concentration.

b. Local Order Friction [21]

A non-ideal solid solution may either favour short range ordering or clustering. In both instances the movement of dislocations will break these preferred bonds. This frictional stress is independent of temperature and shows a quadratic dependence on concentration for dilute alloys.

Strengthening can also be realised by annealing cold-worked substitutional solid solutions below the recrystallisation temperature. This effect termed anneal hardening has been observed in Cu/Zn [22] and Cu/Al [23] alloys. It has also been shown [24] that a greater strengthening effect is obtained for the yield stress than the 0.2% proof stress. Hardening by this mechanism has been reported as proceeding by two distinct stages both for isochronal and isothermal annealing [25]. The first stage occurring either at lower temperature or shorter annealing times was found to be unstable at room temperature [26]. The elastic modulus was also observed to increase following such a treatment indicating that processes other than dislocation recovery and recrystallisation contribute to the hardening process.
Differential thermal analysis of a primary Cu/Al solid solution [27] has identified four effects upon heating cold-rolled specimens 1) a weak exothermic peak below 100°C, 2) a large exothermic peak at 250°C, 3) an endothermic peak at 325°C and 4) an exothermic peak above 350°C. These results were respectively attributed to 1) ordering by vacancy diffusion, 2) local ordering

and recovery, 3) disordering and 4) recrystallisation.

Structural information on anneal hardening has been obtained from changes observed in the short range order parameter [28]. From this information it has been concluded that regions of high short range order are associated with lattice defects whereas the defect free lattice has a lower short range order. This ordering effect has been observed by transmission microscopy studies [29].

It is proposed [30] that the processes that could lead to clustering and short range ordering effects associated with defects and thereby hardening are:-

1) Vacancy annihilation, although the contribution of this process appears to be small.

2) Solute clustering at dislocations. This process can lead to large dislocation locking forces [31] and is therefore an important mechanism of anneal hardening. However the process is subject to reversion [32] which lessens its stability.

3) Local ordering at dislocations.

4) Local ordering in defect-free regions.

It is considered that the major strengthening on anneal hardening is obtained by local ordering at dislocations although ordering of the defect-free lattice will give a contributory superimposed effect.

More recently [33] it has been shown that hardening does not occur in single crystals and that therefore anneal hardening cannot be fully explained in terms of short

range ordering only. In fact it has been demonstrated that hardening occurs predominantly at a layer ≈ 100-150 μm in thickness from grain boundaries. In conclusion it is suggested that segregation of solute atoms to edge dislocations piled up at grain boundaries plays a major role in the mechanism of hardening.

Increased hardening from the solid solution can also be achieved by a precipitation mechanism.

The basic requirement for such a system is decreasing solid solubility with decreasing temperature, so that on quenching from the single phase field a super-saturated solid solution may be obtained. Subsequent ageing will result in precipitation of a second phase, the form of which is dictated by free energy terms. Metastable coherent precipitates or zones are usually formed initially because the critical size for stability of the equilibrium phase is improbably large. These phases are orientated with respect to the matrix to minimise the strain energy term dictated by the anisotropy of elastic modulus in each phase. Since the strain energy term increases with particle size, precipitation may go through stages of being partially coherent or incoherent before the equilibrium phase is formed.

The yield strength of an age-hardened alloy is governed by the interaction of dislocations with precipitates and is dependent on the size, shape and distribution of the precipitate as well as the degree of misfit or coherency. Although coherent precipitates give rise to an internal

stress field the degree of strengthening is dependent on the flexibility of the dislocation line [34]. An underaged alloy has small finely dispersed precipitates and the dislocation line will be unable to lie in the low-energy trough of the stress field. In this case the long range stress tends to cancel out. In contrast an over-aged alloy contains coarse, widely spaced precipitates and the dislocation line is able to bend and lie in the low-energy trough areas. Therefore in order for yielding to occur the dislocation must be moved from this low energy configuration across regions of high energy.

Although coherency strains make a contribution to the yield strength, the major effect arises from the direct interaction of dislocations with the second phase. It has been proposed that yielding can occur by a mechanism in which dislocations by-pass the second phase by bowing [35]. It has also been suggested that particles can be by-passed by cross slip [36], although calculations indicate that this mechanism can only occur when the inter-particle spacing is approximately ten times the particle diameter [37]. In contrast it is further suggested that the yield point is dependent on the stress required to shear the precipitates [38].

As an alloy ages a more stable and coarser precipitate is formed and the nature of the stress-strain curve changes. Alloys containing zones or coherent precipitates have a large critical resolved shear stress and a low rate of work hardening similar to that of the pure metal. Over-aged alloys show the opposite behaviour

i.e a low critical shear stress and a high rate of work hardening. It is assumed that in the initial ageing stages precipitates are sheared, giving rise to an increase in yield stress only, but as they grow, shearing becomes more difficult and a by-pass mechanism operates. The stress required to bow round over-aged particles is less than that to shear coherent precipitates, and therefore the yield stress is lower. However as plastic deformation progresses it is proposed that arrays of residual dislocation loops are formed about the precipitates which gives rise to a back stress and thus produces hardening [39].

The strength of a precipitation hardening system can be improved by employing a solution treatment, cold work, ageing routine since the presence of cold work and solute atoms have a synergestic effect on the yield point. Two basic mechanisms are observed, termed strain ageing and strain age hardening, and their effects can be demonstrated by tensile tests. If a specimen is loaded beyond its yield point, unloaded, then allowed to rest before retesting, a new yield point will be observed at a higher value of stress. However, apart from the new yield point, the remaining plastic portion of the curve is an extrapolation from the original stress-strain plot. This behaviour is termed strain ageing, and is related to the migration of solute atoms to unpinned dislocations, relocking them and giving an accompanying new yield point.

If, however, the tensile specimen is thermally aged prior to retesting, a new yield point is formed as previously

described together with displacement of the stress-strain curve to higher values of stress. This behaviour is termed strain age hardening and is associated with the growth of precipitation on dislocations [40]. In this instance the unpinned dislocations are more severely locked by the precipitates and new dislocations have to be generated. Such an action will result in a new yield point and increased strengthening.

1.2.2 Stress Corrosion Mechanism

A characteristic feature of stress corrosion cracking is failure with little attendant macroscopic plastic deformation. This factor is highlighted by alloys normally regarded as ductile, which may fail in an apparently brittle manner when subjected to specific environments. The propensity of a material to brittle failure is determined by the fracture mechanics concept of a critical stress intensity factor K_{IC}. Because of the effective embrittlement associated with stress corrosion cracking, unified equations containing mechanical and electrochemical parameters have been developed [41] [42]. In general the susceptibility to stress corrosion cracking is enhanced by increasing the anodic overpotential. This effectively raises the energy of the metal lattice adjacent to the crack resulting in an energy release as metal ions pass into solution. Factors which lower the plastic work term such as an increase in yield stress and work hardening rate or those which give embrittlement due to the environment will also increase the susceptibility to stress corrosion cracking.

It has been proposed [43] that a spectrum of stress corrosion processes exists in which the emphasis shifts from stress being the important factor with corrosion playing a minor role, to one in which corrosion plays a major role and stress is of lower significance. For convenience this spectrum has been divided into three types of mechanisms:- these being:-

a) pre-existing active paths

b) strain generated active paths

c) adsorption of specific elements at sub-critically stressed sites.

In those instances where corrosion plays a predominant part in the stress corrosion mechanism, the localisation of corrosion, necessary to achieve a narrow crack front, has been proposed as being related to the presence of a pre-existing active path [44].

It is suggested that precipitation or segregation which may form preferentially at grain boundary sites may cause preferential attack of either the segregated phase or adjacent matrix. Such forms of stress corrosion are normally encountered in materials which show selective attack in the unstressed condition. A schematic representation of this form of stress corrosion and a higher magnification micrograph showing intergranular attack are illustrated in Figs 1 and 2.

Alloys which have no pre-existing active paths may by disruption of a protective surface film, show a further mode of stress corrosion cracking termed strain-generated active path [45]. A schematic representation of two such

mechanisms is given in Fig 3, namely film rupture and slip step dissolution. It is claimed that the rate of cracking from such mechanisms is dependent upon the rate of film growth [46]. Transgranular cracking is favoured by planar slip and will only occur if the slip step exceeds the film thickness. This is facilitated in f.c.c metals by a low stacking fault energy, making cross slip difficult and thereby facilitating the formation of planar arrays of dislocations. The dependence of transgranular stress corrosion on stacking fault energy has been demonstrated for copper alloys and austenitic stainless steel [47]. Materials having a low fracture toughness may show a faster rate of stress corrosion crack propagation, if the crack formed in the protective film propagates into the underlying metal to some degree before being arrested by plastic deformation. The strain-generated active path does not always lead to transgranular failure. Situations which result in dislocation networks hindering planar slip, such as extensive deformation, result in a concentration of plastic strain at grain boundaries giving film rupture which can result in intergranular failure [48].

As indicated previously, factors which decrease the plastic work term such as localised embrittlement or reduction in surface energy, increase the susceptibility to stress corrosion cracking. Diagramatic representations of some of these mechanisms are given in Fig 4, where it is postulated that hydrogen may diffuse in advance of the crack to form a brittle hydride or to give decohesion or nucleation of cracks. In these instances the environment is not usually considered specific as long as it is a source of

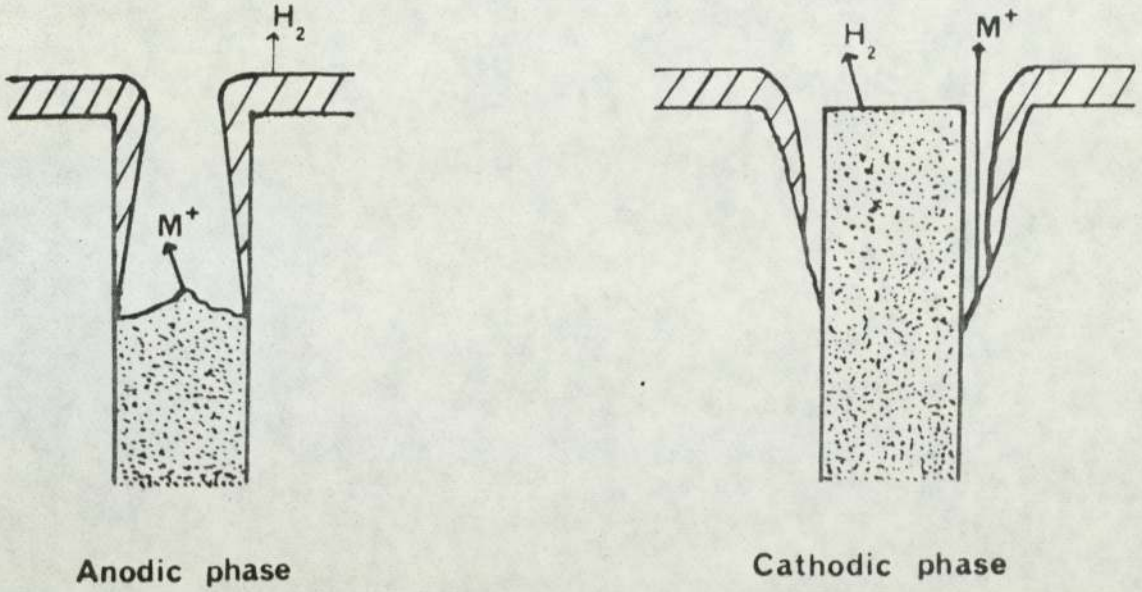

FIG 1 Schematic representation of pre–existing active path attack

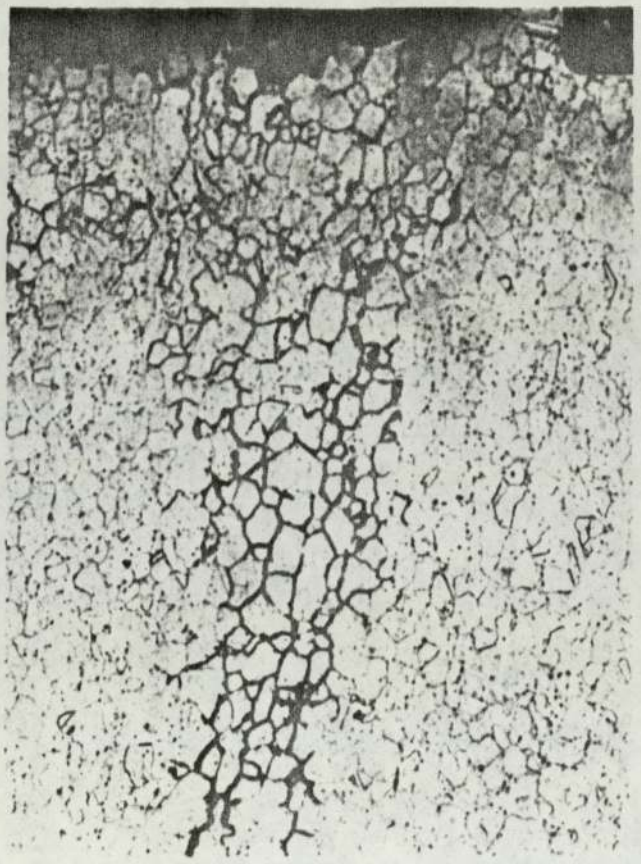

FIG 2 Intergranular stress corrosion in 9% Al, 2% Fe Aluminium Bronze to BS 2874, CA 103. ×400

hydrogen. However, the presence of such ions as arsenic in solution which have a low exchange current density for the hydrogen evolution reaction, 'poisons' the formation of bubbles on the metal surface and therefore facilitates adsorption. Hydrogen embrittlement may be considered as a separate form of stress corrosion cracking since cathodic polarisation will increase its susceptibility whereas such a treatment results in a decrease in susceptibility in other modes of stress corrosion.

The lowering of surface energy has been proposed [49] as the important factor in all forms of stress corrosion cracking, however, this model does not adequately account for the cracking observed in ductile metals where the critical stress intensity factor is more dependent on the local plastic work than surface energy.

The electrochemistry within the crack is also of importance in determining stress corrosion behaviour. It has been shown [50] that geometries such as cracks which restrict the access of the electrolyte result in a lowering of the pH value in these regions in comparison to the bulk solution. The acidification can be considered to be due to hydrolysis of the anodically formed metallic ions by a reaction such as:-

$$Fe^{2+} + 2Fe^{3+} + 4H_2O = Fe_3O_4 + 8H^+$$

Concomitant with this reaction if the bulk solution contains oxygen, (a situation which is often necessary for passivation of the bulk sample), the cathode reaction may result in an increase in pH by the reaction:-

$$O_2(\text{dissolved}) + 2H_2O + 4_e - = 4OH^-$$

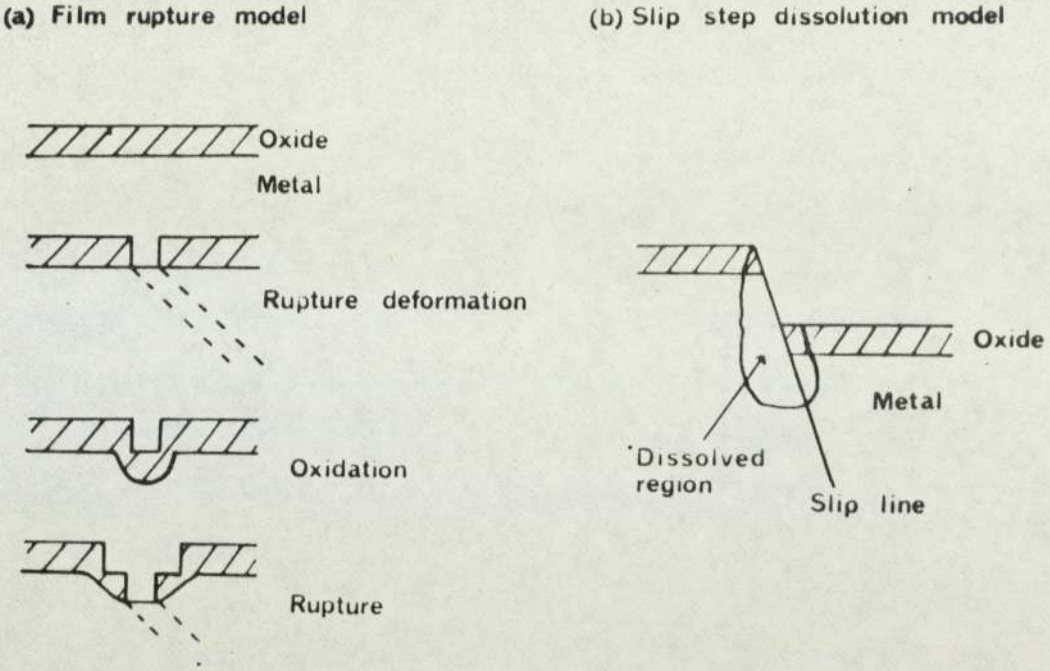

FIG 3 Schematic representation of strain-generated active path stress corrosion.

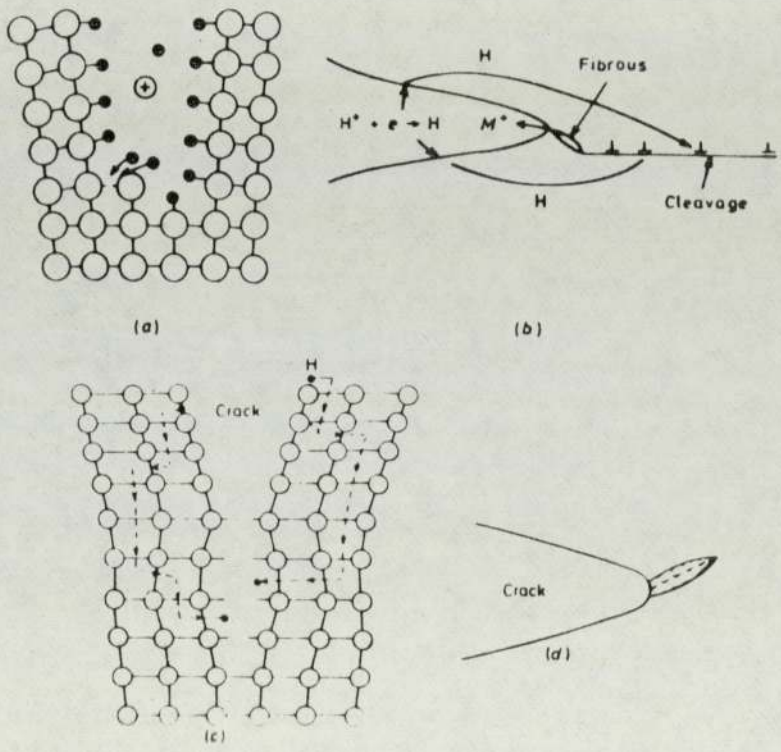

FIG 4 Schematic representation of (a) crack tip adsorption, (b) hydrogen adsorption, (c) hydrogen decohesion, (d) brittle hydride formation.

To maintain electroneutrality, the spacial separation of the anode from the cathode results in transfer of anions, which can result in the formation of hydrochloric acid within the crack in neutral electrolytes containing chloride anions. The effect of decreasing oxygen content, pH and increasing chloride content on the formation of a crack is illustrated in Fig 5 and 6. Curve 1 in Fig 5 represents the anodic polarisation plot of the surface of a passive alloy. The conditions pertaining to the formation of a pit are represented by curves 2 and 3, showing partial passivation associated with increasing chloride ion concentration, decreasing oxygen content and falling pH. Curve 4 relates to dissolution at an emergent slip step. The intersection of these curves with the cathodic polarisation plot determines the current density at each location. For cracking to occur the difference in current density between curve 3 and 4 must be large otherwise broad general fissuring will result.

The rate of crack propagation and the anodic current density are related by [51] :-

$$i_a = \frac{V.ZF_e}{M}$$

where i_a = anodic current density

V = rate crack propagation

2F = charge to oxidise one Mole

e = density

M = atomic weight.

If experimentally measured figures for anodic dissolution of $10A/cm^2$ and $100\ A/cm^2$ for aluminium [52] and iron [53] respectively are substituted, then the maximum rate of crack

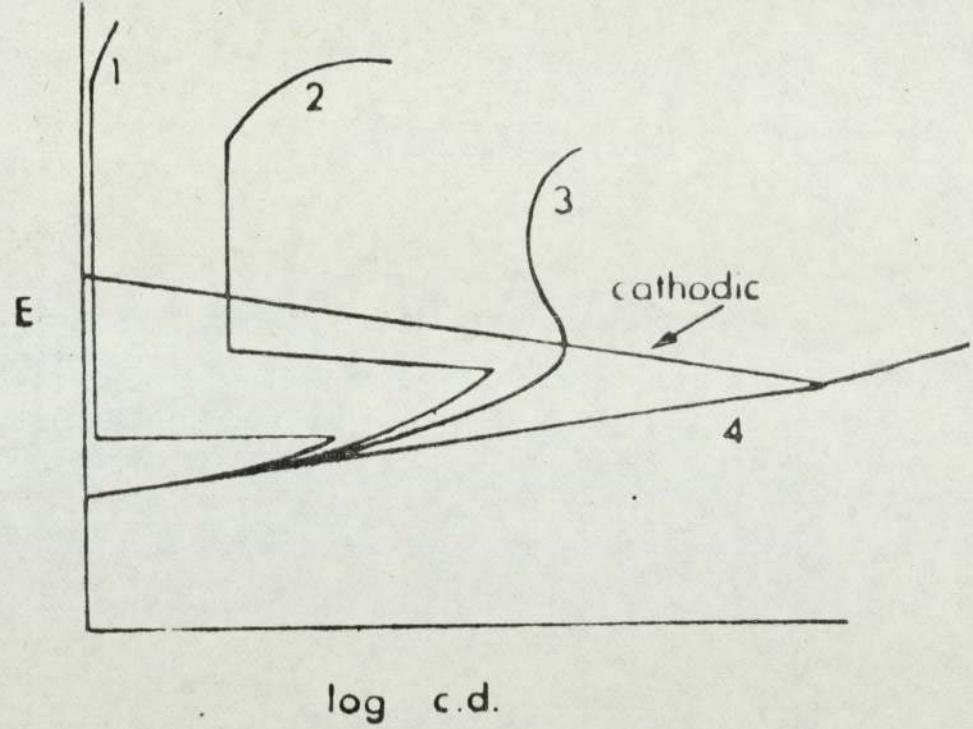

FIG 5 Showing effect on anodic polarisation plot with decreasing oxygen content, pH, and increasing chloride content.

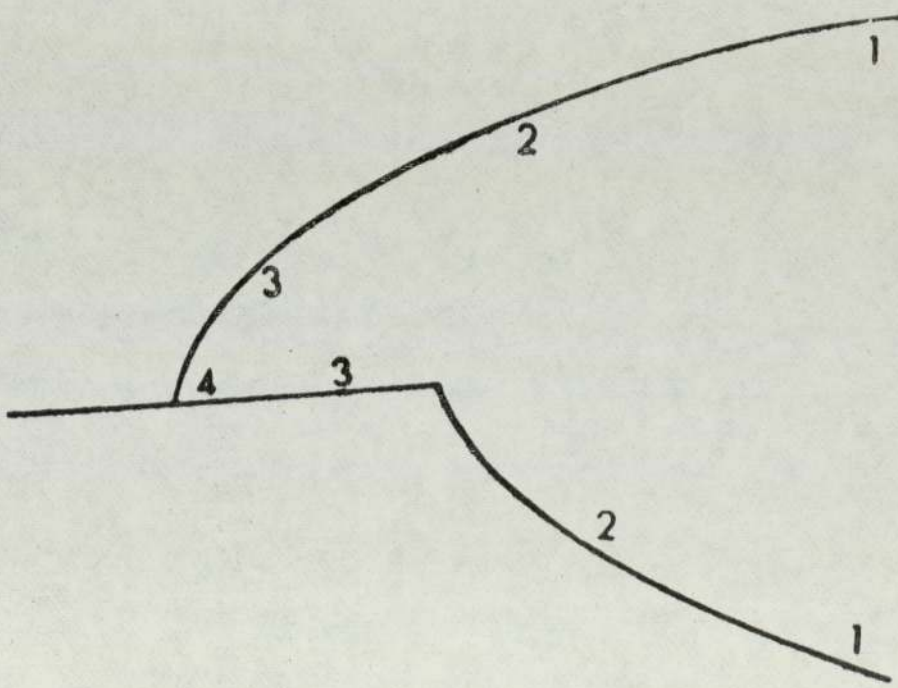

FIG 6 Schematic representation of crack formation relating to conditions identified in Fig 5.

propagation determined by such electrochemical means will be of the order of 10^{-3} cm/s. Since the alloys normally associated with stress corrosion cracking have good general corrosion resistance and associated low anodic current density, crack propagation by electrochemical means must be associated with change in electrochemical behaviour between the low corrosion associated with the bulk sample and the crack tip. The rate of anodic dissolution and associated current density of an alloy can be changed across a potential/pH range by the formation of surface films. The thermodynamic stability of phases in equilibrium as a function of pH and potential are illustrated in Pourbaix diagrams, as shown in Fig 7 and 8, for the system Cu-H_2O [54] and Cu-sea water [55] respectively. Figure 7 shows that at pH 8 metallic copper is stable in the presence of hydrogen. More positive potentials give rise to the stability of Cu_2O, CuO and finally Cu_2O_3 hydrate. The presence of chloride ions in sea water gives a modification to the basic diagram as shown in Fig 8. Four variations to this diagram have been obtained by considering the different solid phases that may be present. In essence, however, it is concluded that at pH 8 the precipitation of a protective film of cupric compounds requires a very low ($\simeq 10^{-6}$ g.ion/l) total concentration of Cu^{II} in solution while the concentration of Cu^{I} in solution required for the formation of the protective Cu_2O is greater than 10^{-4} g.ion/l.

Thermodynamics determine the probability of a metal being immune, corroding or being passivated by film formation. The potential of the reaction $M \rightleftharpoons M^{n+}+ne$ is referred to a standard electrode such as the standard Hydrogen Electrode (SHE), at which the reaction is $H_2 \rightleftharpoons 2H^{+}+2e$. Such Standard

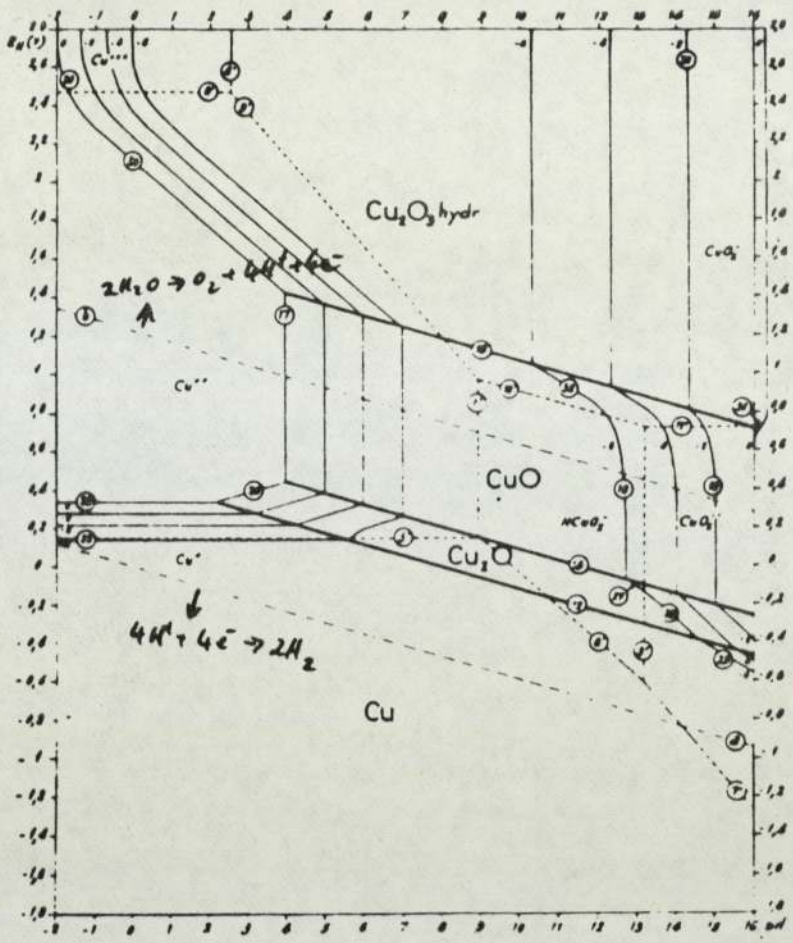

FIG 7 Equilibrium potential / pH diagram for the Cu - H_2O system.

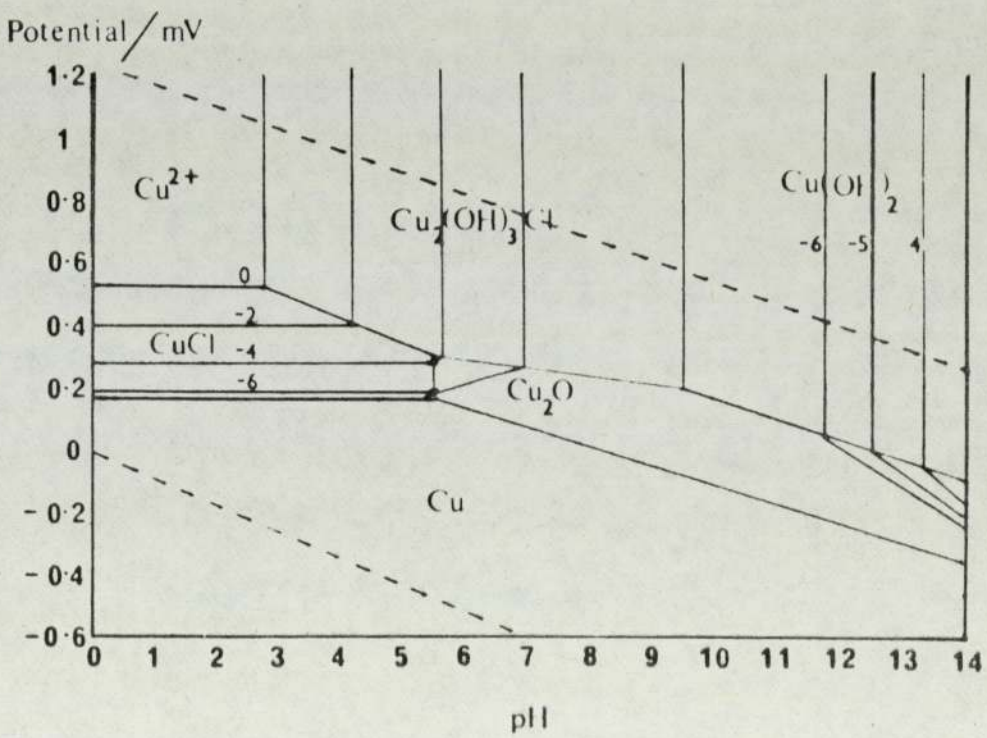

FIG 8 Equilibrium potential / pH diagram for the Cu - Sea Water system.

Electrode Potentials are defined for unit concentration of products and reactants, where this does not apply the modified potential can be calculated from the Nernst Equation:- (56)

$$E = E^{O} + \frac{RT}{ZF} \ln \frac{(ox)}{(red)}$$

where E^{O} = Standard Electrode Potential

R = Gas Constant

F = Faraday Constant

T = Absolute Temperature

Z = no electrons in reaction

(ox) = concentration of oxidised species

(red) = concentration of reduced species.

The electrode potential of the system is given by the algebraic difference in the cathode and anode half cell reactions. For a reaction to proceed spontaneously the free energy change must be given by $-\Delta G = ZFE$. The boundaries of the Pourbaix diagram are determined by an arbitrary figure of 10^{-6} g . ion/l, such that corrosion is said to be occurring when there is in excess of 10^{-6} g.ion/l of M^{+} in solution.

Although potential/pH diagrams form a useful base for understanding film formation, the thermodynamic data needed for their construction is limited for alloys in complex electrolytes. Further, the kinetics of reactions are not considered, whereas differing insoluble phases formed will influence the electrochemical reaction. The electronic or ionic conduction and the adherence of the film are important considerations which will influence the rate of reaction.

The influence of kinetics can be considered by the mixed potential theory [57] which assumes that the kinetics of the various partial reactions can be treated separately and that no net current flows from an electrode which is in equilibrium. Equilibrium for a reversible cell is regarded as a dynamic situation in which reactants and products jump back and forth but give no net accumulation. This equilibrium exchange is termed the exchange current density.

The simplest class of corrosion reactions are those in which the partial processes involve ionization and may be described as being under activation control. In contrast to the reversible system there is a net chemical reaction at the corrosion potential although there is no net current flow. Figure 9 shows a system whereby the electrons generated during oxidation of the metal reduce hydrogen ions. Each component of corrosion has its own reversible potential and polarisation parameters. The corrosion potential of the reaction is determined by the point at which the total rate of oxidation equals the total rate of reduction. The observed applied-current potential curve (solid line) shows a departure from the semi-logarithmic form near the corrosion potential which illustrates that the applied current is the difference between the anodic and cathodic rates of reaction.

Charge transfer at a finite rate involves an activation overpotential ηa, given by $\eta a = E_A - E_{corr}$ where E_A = applied potential, E_{corr} = corrosion potential. This overpotential is related to the rate of charge transfer by the Tafel equation:-

$$\eta a = A + B \log i$$

FIG. 9 E vs. LOG i CURVES FOR THE CORROSION OF A METAL IN A REDUCING ACID

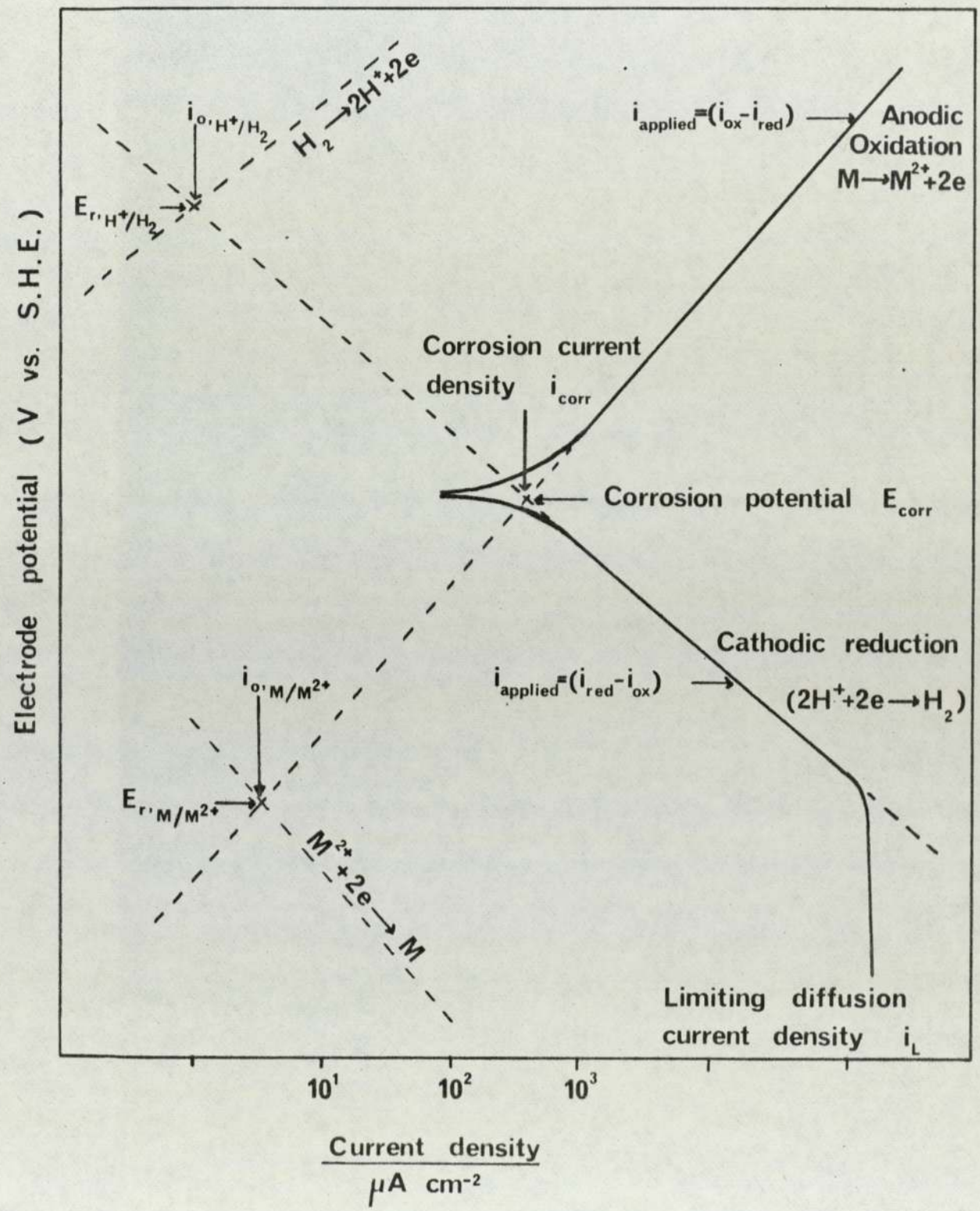

where a and b are the Tafel constants and i the current density. The Tafel constants are dependent on the equilibrium exchange current density (i_o) such that the smaller the magnitude of i_o, the greater is η_a and the lower is the rate of the process for any given potential. From these considerations it can be seen that the corrosion potential is not determined by the difference between the reversible partial reactions but by the kinetic parameter of the exchange current density.

Since the reaction forms products, concentration gradients will tend to form which can result in a transport or diffusion overpotential (ηT). More important, however, in terms of stress corrosion is the resistance overpotential (η_R). In addition to the term dependent on the conductivity of the solution, any insulating film deposited on the anode site will increase η_R and lead to passivation. The formation of insoluble products as indicated by Pourbaix diagrams can result in a modification of the anodic polarisation curve as shown schematically in Fig 10, which dependent on the intersection with the cathodic polarisation curve can result in passivation as depicted in Fig 11. As shown, the position of the point of intersection of the anodic polarisation curve of the metal (solid line) and the cathodic polarisation curve of the environment/dashed line) determines the corrosion potential and corrosion current density, and indicates whether the system will actively corrode or be in a stable or metastable passive state [58]. Incomplete passivation will result, however, in rapid corrosion of local active areas. In such situations grain boundaries and sites of emergent dislocations are often

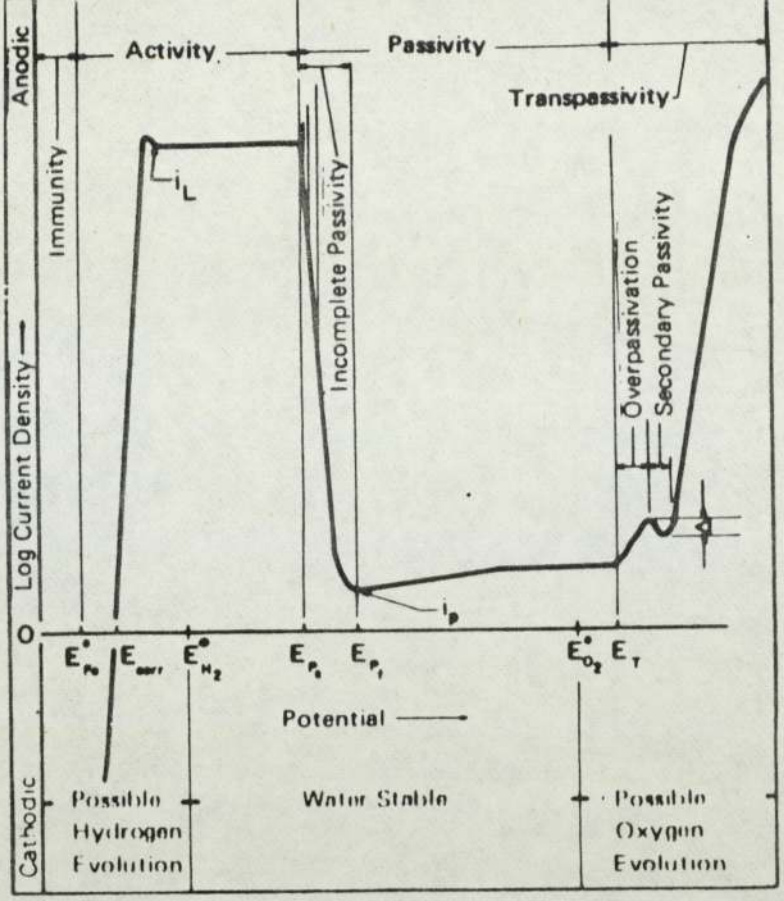

FIG 10 Schematic Potentiostatic Polarisation Curve.

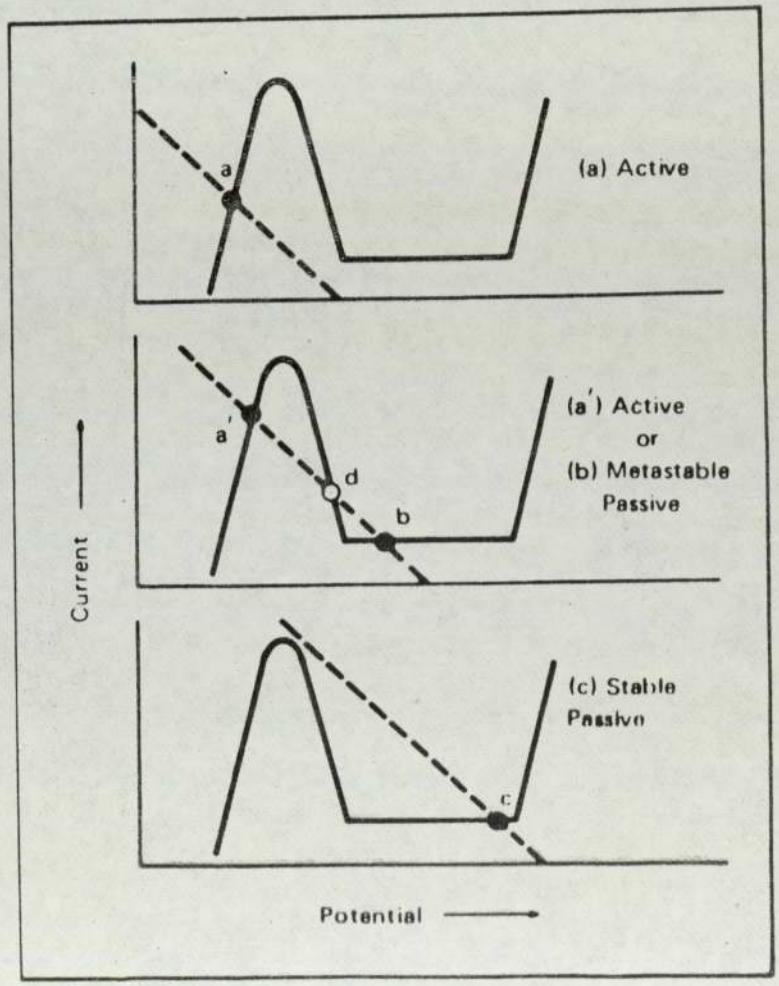

FIG 11 Schematic polarisation curves showing active, metastable and passive behaviour dependent on the intersection of the anodic and cathodic curve

preferential sites and pitting or stress corrosion may result [59].

The majority of the research into the mechanism of stress corrosion of copper alloys has been undertaken on brass. It has been demonstrated that solutions of aqueous ammonia containing $Cu(NH_3)_n^{2+}$ gives rise to cracking in these alloys [60]. It has been reported [61] that a certain level of copper tetramine in solution is necessary for stress corrosion cracking in that it promotes the formation of copper oxide preferentially in fissures, where the solution is most readily deprived of ammonia. Depending on the composition of this complex copper ammonia solution, tarnishing of the metal surface may or may not occur giving intergranular or transgranular crack modes respectively [62]. The susceptibility to failure in both types of solution is increased with increasing concentration of the complex copper ion [63] and increased solute content of the alloy [64].

The mechanism of stress corrosion in tarnishing environments has been reported [65] [66] as repeated rupture of this film which has been shown to be Cu_2O. The basic feature of this mechanism is oxidation of the metal at the crack tip followed by fracture of this film when it has reached a critical thickness [67]. This model predicts that the fracture surface should be covered by the tarnish film. However, instances have been reported to the contrary [68] [69] where this surface remains the normal metallic yellow colour of the alloy. Although it has been demonstrated by electron diffraction that this surface is still covered with a Cu_2O film the hypothesis of rupture of a relatively thick tarnish does not apply. As a result of this evidence it

has been proposed [69] [70] that dezincification at the crack tip, causing structural weakening plays a major part in the mechanism of stress corrosion.

It has been shown [71] that for non-tarnishing solutions the dislocation structure determines the mode of cracking in both Cu/Zn and Cu/Al alloys. Planar dislocation arrays lend themselves to transgranular failure whilst cellular configurations are associated with intergranular failure. It has been proposed that embrittlement in the brass alloys can result from pinning of dislocations by vacancies introduced into the lattice during dezincification [72]. Unalloyed copper is not regarded as susceptible to stress corrosion cracking and it is of note that cold work results in a cellular dislocation network. However, additions of zinc, aluminium, germanium or silicon lower the stacking fault energy [73] resulting in a planar distribution of dislocations on working. Further, it has been shown that in general [74] [75], transgranular stress corrosion of primary solid solutions of copper is associated with such dislocation networks. Electropolishing of low stacking fault energy alloys gives preferential attack in the regions of the slip planes. This phenomenon has been tentatively associated with the segregation of solute atoms to stacking faults [76]. However, it is recognised that this should lead to a larger number of preferred sites than that observed. It has been found that there is a rapid increase in short range order on ageing disordered Cu/Al alloys at room temperature [77]. Based on this fact it is suggested [47] that the formation and destruction of chemically active sites by respective

slip and reordering is a dynamic process, and that short range order must be destroyed by several dislocations moving on the same slip planes in order to produce chemically active sites. Such a proposal explains the lack of transgranular cracking in unstressed alloys and pure metals.

1.3 Aluminium Bronzes

1.3.1 Alloy Systems

The aluminium bronzes are a group of copper alloys containing aluminium as the principle alloying addition, the properties of which depend on both composition and microstructure.

Reference to the binary phase diagram [78] depicted in Fig 12, shows that under equilibrium conditions up to 9% aluminium can be accommodated in the terminal alpha solid solution. The commercial single phase alloy (BS2871, CA102), however, also contains up to 3% iron to give grain refinement. Under equilibrium conditions, the solubility of iron in this type of alloy below 550°C is less than 1%, but the precipitation reaction of δ iron begins when the temperature drops below 1000°C [79].

It has been shown [80] that the addition of 1-2% cobalt to the 93/7 aluminium bronze also confers precipitation hardening characteristics. Ageing the solution-treated material at 400°C, gives an incubation period of 10 hours, during which there is no change in hardness, followed by an abrupt increase to a maximum value. The incubation period is decreased by prior cold work and higher ageing temperatures. Optical microscopy showed that precipitates were present along grain boundaries at peak ageing times

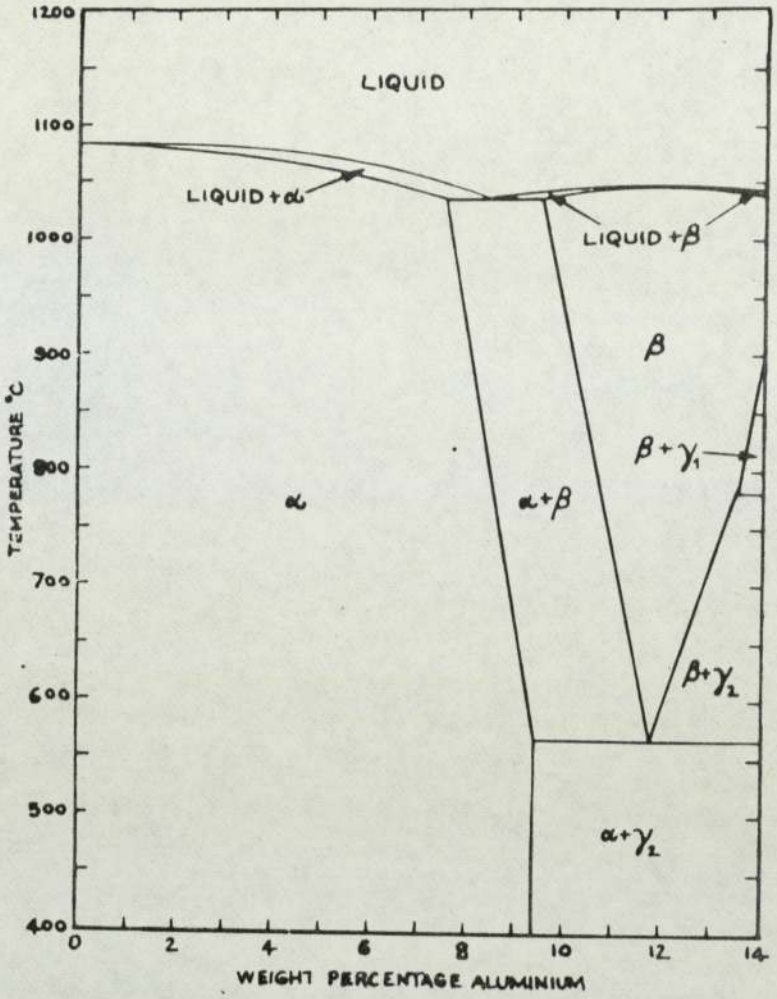

FIG 12 Copper - Aluminium phase diagram

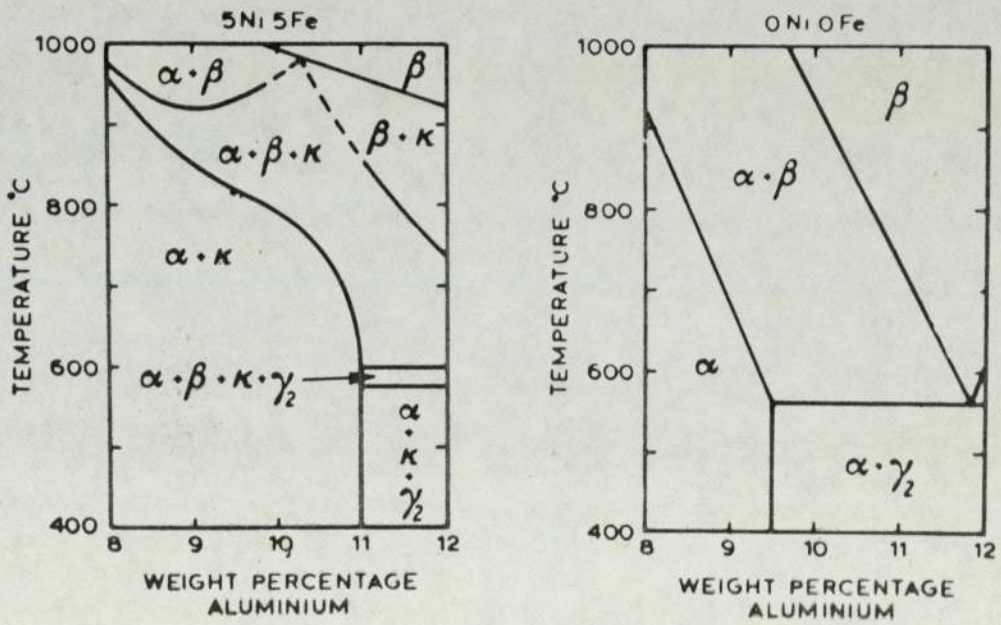

FIG 13 Showing effect of 5% Ni and 5% Fe addition on Cu - Al phase diagram.

and on preferred lattice planes following over-ageing. The maximum solubility limit of cobalt in this alloy following solution treatment was found to be 2%.

Concurrent investigations [81] have confirmed the age hardening of alpha-based Cu-Al alloys containing 0.5% Ni by 1-2% Co. A further addition of trace quantities of silicon or phosphorus (<0.1%) was shown to give the ageing response in a shorter time period and increase the maximum hardness obtained, without changing the precipitation mechanism.

Further investigations [82] of a similar alloy system (Cu, 7% Al, 1.5% Co, 0.01% P) have shown an activation energy of 153.7 kJ/mole for isothermal ageing to peak hardness at temperatures above 350°C. This is similar to the activation energy for the diffusion of aluminium in copper. X-ray diffraction studies showed an initial increase in lattice parameter during the primary stages of hardening followed by a reduction during rapid hardening and over-aging. These results are attributed to an initial decrease in cobalt concentration of the matrix during the primary stages, followed by a decline in the aluminium content coincident with rapid hardening. Extraction replica techniques gave no evidence of precipitation on prolonged ageing at 450°C, but samples aged at 800°C contained rectangular precipitates with a cubic Fm3m symmetry and a lattice parameter of 5.77Å. It is concluded that hardening of this alloy is due to the initial formation of GP zones rich in cobalt and aluminium. These coarsen during the terminal stage of hardening into a metastable precipitate before finally losing coherency and reverting to a stable phase.

The effects of cold work on the alloy have also been investigated [83], showing that cold rolling of solution treated material (up to 50% deformation) results in an almost linear increase in hardness. It is also demonstrated that by increasing the degree of reduction, the incubation period on subsequent isothermal ageing is decreased, and the rate of hardening and maximum hardness obtained increased.

Differential thermal analysis of cold-rolled solution-treated material revealed two exothermic peaks, one at 200-350°C, the second at 470-550°C which correlated well with hardness peaks observed from isochronal ageing plots. In comparison, DTA of cold-rolled over-aged samples only showed one exothermic peak at 150-350°C. A correlation was found between the degree of reduction and size of exothermic peak, showing that the greater the degree of reduction the larger the exothermic peak observed. Over-aged samples with zero reduction show no change in hardness on isochronal ageing to 600°C, with higher temperatures resulting in softening. However, the cold-rolled, over-aged material shows initial softening at 150°C, followed by hardening to a maximum at 350°C, and finally softening at higher temperatures. It is suggested that a reduction in short range order and an increase in stacking fault density occurs as a result of the cold work and that during annealing there is recovery of short range order and a migration of solute atoms to areas of stacking fault. Precipitation hardening, which occurs at higher ageing temperatures, is reported as being independent of the strain ageing, although cold work does promote precipitation. It is suggested that atmospheres of solute atoms formed during

strain ageing may act as nucleation sites for the formation of GP zones and the precipitation of a metastable phase.

Investigations [84] on a system containing Cu, 2% Co, 3.6% Al, have shown that ageing between 400-600°C proceeds in two stages. The first stage is the formation of a coherent precipitate. Although no diffraction evidence for this was observed, magnetic susceptibility studies indicated the formation of a variant of cobalt having a face-centered cubic lattic similar to the copper based matrix. The second stage of hardening is attributed to solution of the coherent phase with simultaneous precipitation of a stable incoherent Co/Al intermetallic with cubic Pm3m symmetry. However, alloys containing 7% Al, 2% Co were shown both by electron microscopy and magnetic susceptibility to age in one stage by the formation of incoherent CoAl precipitates.

Binary alloys containing more than about 8% aluminium are no longer single phase and in general exhibit a duplex alpha-beta structure. However, as shown in Fig 12 the body-centred cubic beta phase is metastable and will decompose eutectoidally during slow cooling or annealing below 565°C to form α and γ_2. The γ_2 phase is an intermetallic compound of approximate composition Cu_9Al_4 and has a $D8_3$ crystal structure [85].

Silicon additions to these alloys stabilise the beta phase and decrease the aluminium content of the terminal alpha solid solution [86]. At moderate rates of cooling a CuSi A3 type phase is precipitated, but because the $\alpha + \gamma_2$ eutectoid transition is depressed to approximately 400°C

this reaction does not usually take place in alloys cooled at normal rates, and the α/β structure persists to room temperature.

A further important group of alloys is the complex aluminium bronzes, containing additions of nickel, iron and manganese. Manganese has equivalent effects to aluminium in that it stabilises the beta phase [87]. Nickel is rarely added to binary alloys to the exclusion of other elements, but it has been shown [88] that at addition levels below 2% this element remains essentially in solid solution, further additions promoting the formation of a NiAl precipitate.

A pseudoquaternary phase diagram [89] of a complex aluminium bronze (BS2872, CA104) is shown in Fig 13. This indicates that the alloy has an equilibrium alpha-kappa structure. It is considered that the kappa phase is a non-stoichiometric (Ni,Fe)Al compound related to the NiAl precipitate formed in the ternary Cu-Al-Ni alloy. The δ phase observed at higher aluminium levels is isostructural with the binary γ_2 phase. However, the phase diagram relates to equilibrium conditions which may not be readily obtained. It has been suggested [90] [91] that in practical situations the alloy completes solidification as a single phase beta alloy, and as it cools there is growth of alpha at the beta grain boundaries and along specific crystallographic planes, to form a Widmanstatten structure. Further cooling results in precipitation of various phases designated kappa. Initially a phase of rounded or rosette form, rich in iron, is precipitated from the beta, followed at lower temperatures by a lamellar form of kappa produced by a eutectoid reaction. Finally there is precipitation of a fine kappa phase within

the primary alpha. The different morphologies of kappa have been numerically designated K_I, K_{II}, K_{III} and K_{IV} [92]. The identification and microprobe analysis of three of these phases is as follows:- [93]

K_I a large rosette phase, formed from the melt, of composition 6% Al, 8% Ni, 6-% Fe, 13% Cu.

K_{III} a transformation structure of $\beta \rightarrow \alpha + \kappa$ having either the lamellar or globular form of composition 18-20% Al, 23-34% Ni, 26-43% Fe, 13-20% Cu.

K_{IV} a fine inter alpha precipitate not quantitatively analysed but considered iron rich.

More recent work [94] has shown the following phase transformation to occur at a cooling rate of 0.13°C/s.

$\beta \rightarrow \alpha + \beta$ 925°C

$\beta \rightarrow \alpha + \kappa_I$ 820-830°C

$\beta \rightarrow \alpha + \kappa_{II} + \kappa_{III}$ 775-750°C

$\alpha \rightarrow \alpha + \kappa_{IV}$ 700-675°C

Analysis of the phases by SEM and STEM techniques indicated that the globular K_{II} and K_{IV} were of similar composition and related to Fe_3Al. However, although the K_{II} and K_{III} phases were precipitated from the matrix at the same temperature there was a significant difference in the Ni-Fe ratio. The average composition obtained was:

	Al	Mn	Fe	Ni	Cu
K_I	18±4	1.6±0.3	34±5	24±5	23±4
K_{III}	22±4	1.6±0.4	22±5	28±5	26±4

Fast cooling can result in the retention of the beta phase at room temperature, giving a complex martensitic structure.

This phase is reported [95] as being distorted hexagonal close packed and more recently [96] as a mixture of face centred cubic and hexagonal close packed.

The K_I phase has been shown by neutron diffraction studies [97] to have a body centred cubic (b_2) type of structure with a lattice parameter of 2.97Å. The crystal structure of the remaining kappa phases have not been determined.

1.3.2 Corrosion Performance

The single phase alloy is considered to have good general corrosion resistance (ref Table 1), and although stress corrosion failures have been reported, [98] additions of 0.5% tin or silver have been shown to be beneficial in conferring immunity to intergranular failure. It is suggested that this mode of cracking is related to segregation of atoms at grain boundaries, and to a lesser extent within the crystal lattice. Such concentrations allow selective corrosion to occur. It is considered that aluminium segregates in this manner in the alpha aluminium bronze alloy, but that the additions of tin or silver, because of their atomic diameter, accumulate preferentially in these sites, and by their more noble nature inhibit intergranular corrosion.

The duplex alpha-beta aluminium bronze is considered to have better corrosion resistance than high tensile brass. However, corrosion trials [99] (twelve months immersion in Langstone Harbour) have shown that the γ_2 phase which may form in this alloy is susceptible to selective attack. The anodic nature of this phase has been confirmed by open circuit equilibrium potential measurements in seawater [100].

Potentials of -240 mV (SCE) were obtained for the alpha and beta phases and -500 mV (SCE) for the γ_2 phase. A more significant indication of the corrosion performance was obtained from polarisation studies. These showed a significantly higher current density on polarising the γ_2 phase to the alpha phase compared with that obtained on polarising the beta phase to the alpha phase. These results are in agreement with the preferential corrosion rates of 0.05 mm/year and 4 mm/year for the beta and γ_2 phase respectively. As shown in Fig 14 [101], a continuous network of γ_2 can lead to an effective disintegration of the structure, with concomitant loss of mechanical strength, for little observable weight loss.

Although iron additions, present in the commercial alloy (BS2874, CA103) as a grain refining agent, modify the binary equilibrium diagram [102], additions up to 3% have no effect on the susceptibility to selective phase corrosion. However, it has been demonstrated that an improvement in corrosion performance of the basic 90% Cu - 10% Al alloy can be achieved by control of composition [103]. In particular, restriction of the aluminium content to 9.0% produces the γ_2 in an isolated form on slow cooling. This will prevent the continuous selective network of corrosion, although pitting attack may still occur. Additions of manganese to inhibit the eutectoid reaction, however, result in increased rates of corrosion of retained beta phase compared with the manganese-free alloy. This is particularly so under deaerated crevice conditions when fairly rapid beta corrosion can occur [104].

x 500

Fig.14. Showing selective corrosion of γ_2 phase in duplex aluminium bronze (BS CA103).

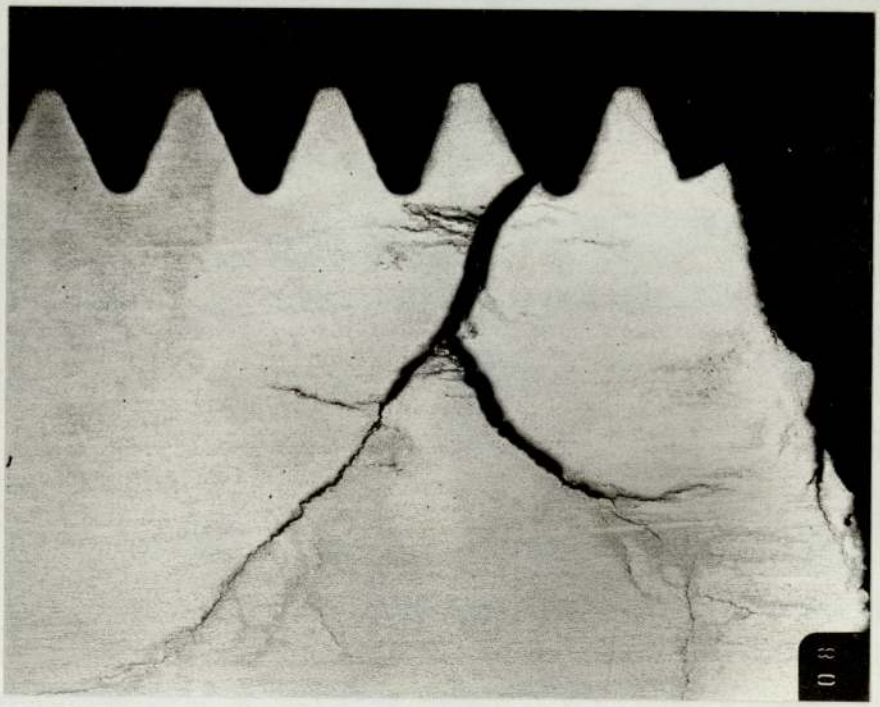

x 12

Fig.15. Showing stress corrosion cracking in a duplex aluminium bronze bolt (BS2874, CA103).

Additions of silicon to the binary alloy also retard the $\beta \rightarrow \alpha + \gamma_2$ transformation, and the beta and CuSi precipitate formed have good resistance to selective attack. However, commercial alloys usually contain approximately 1% Fe (ASTM-B124, 11a) and the beta phase can decompose to give iron-silicon compounds. The morphology and type of compound formed is dependent on cooling rate, but air cooling from 850°C can give stringers of $Fe Si_3$ and an associated risk of selective path corrosion [104].

As an alternative method of stabilising the beta phase, fast cooling may be adopted to prevent the eutectoid reaction in small section components such as fasteners. Such a procedure unfortunately has the disadvantage of increasing the internal stress which may decrease the resistance of the alloy to stress corrosion. An example of such a failure in a bolt is shown in Fig 15 [105].

In contrast with the γ_2 phase formed in the duplex alloy from decomposition of the beta, the lamellar kappa (K_{III}) in the complex alloy (BS2872 CA104) is considered to be cathodic to the alpha phase within the eutectoid. A micro-section, from a corrosion coupon, subjected to a six month immersion in Langstone Harbour, confirming this effect in the cast version of the alloy is shown in Fig 16 [106]. However, following certain heat treatments, such as that obtained in the HAZ of weldments, sensitisation of the kappa III phase to sea water corrosion can occur. [107] It has been shown that kappa III exists as a non-stoichiometric compound. Therefore it is suggested that heat treatments such as rapid cooling from the alpha plus beta region, give kappa transformation products of composition and corrosion

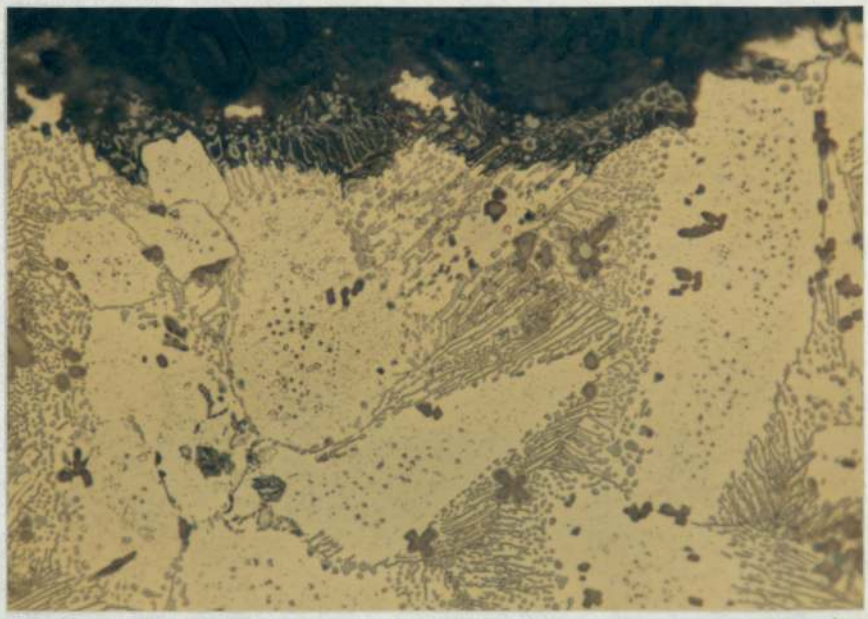

Fig.16.

Showing cathodic nature of K phase in complex aluminium bronze BS1400,AB2

x 500

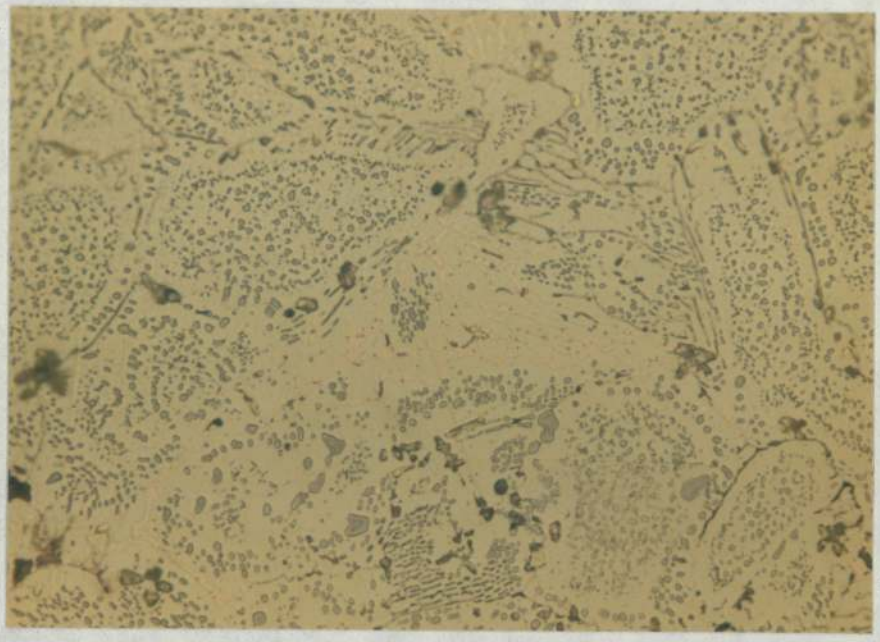

Fig.17.

Showing sensitisation and selective attack of K phase in complex aluminium bronze.

x 500

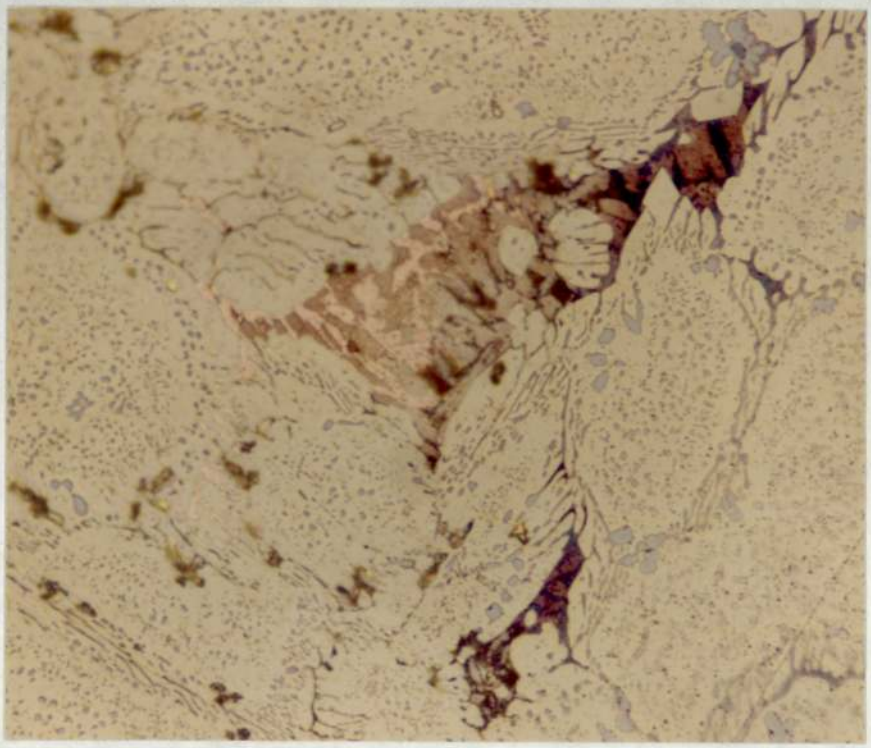

Fig.18.

Showing selective attack of K phase and partial transfer-mation of β.

X 600

performance differing to those in the parent material. This selective form of attack can be eliminated by heat treating above 675°C to homogenise the alpha-kappa microstructure, but the cooling rate must be controlled, since it has been shown that rapid air cooling of small specimens, from above 800°C, can also sensitise the microstructure (Fig 17 and 18) [107].

The wrought complex alloy is generally accepted to be free from stress corrosion cracking in sea water, [108] [109] however, two separate instances have been recorded where fasteners have failed in this mode. [110] It was noted that in both cases the fracture surfaces were covered with a blue-black adherent deposit which was tentatively identified by X-ray diffraction as a modified form of Cu_2O. Sections of the failed samples showing classic branched transgranular cracking are given in Figs 19 and 20. It is of interest that the general microstructure differs, reflecting a variation in chemical composition, although both comply with the British Standard specification. It is therefore considered that the failures may be attributed to environmental rather than metallurgical conditions. The sensitivity of this alloy to stress corrosion cracking in sea water has also been demonstrated by laboratory trials [111], using a constant strain rate test (10^{-6}/s) within the potential range -75 to -200 mV (SCE).

1.3.3 Mechanical Properties

The factors determining the mechanical properties of the binary aluminium bronze alloys have been summarised as [112]:-

1. the tensile strength is proportional to the aluminium content, whilst the elongation reaches a maximum of 75%

x 500

Fig.19. Showing stress corrosion crack in complex aluminium bronze bolt to BS2872, CA104.

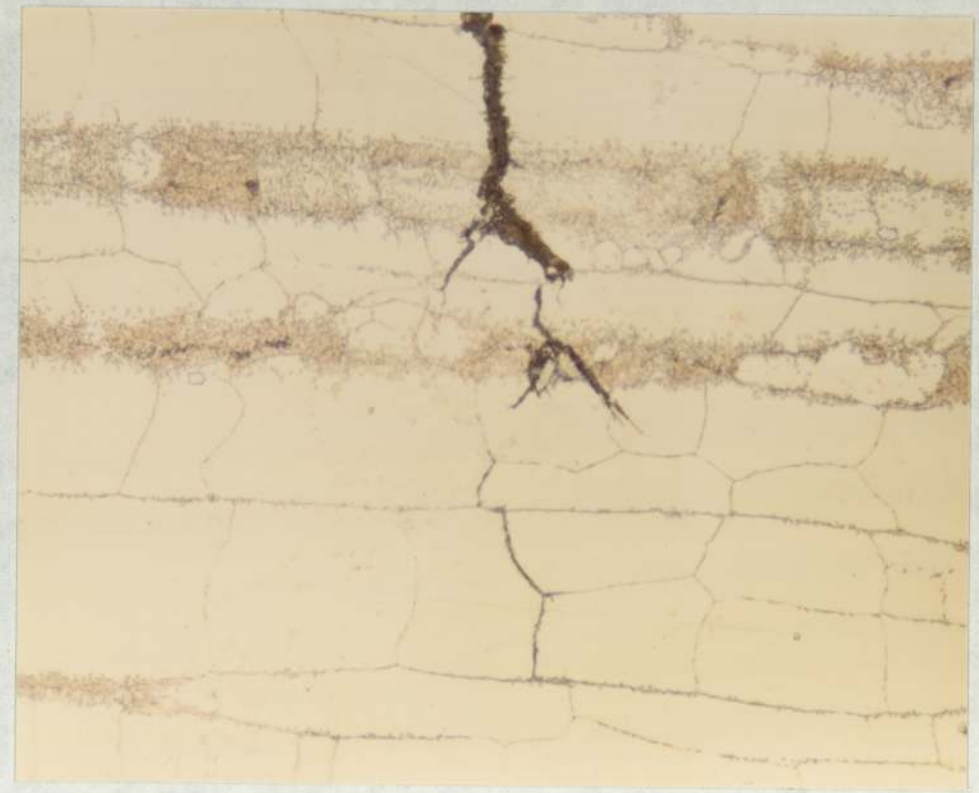

x 500

Fig.20. Showing stress corrosion crack in complex aluminium bronze bolt to BS2872, CA104.

at 7% aluminium prior to decreasing at higher levels.

2. increasing tensile strength and lower ductility is associated with the formation of the beta phase.

3. breakdown of the metastable beta to the $\alpha + \gamma_2$ eutectoid lowers both the elongation and tensile strength.

Although the iron addition to the single phase alloy does confer dispersion hardening, the ageing response is limited [113] and is offset by a reduction in the dislocation density [114]. Therefore these alloys which have lower intrinsic strength than the duplex aluminium bronzes, are normally further strengthened by cold work.

Although the iron addition has a use in the cast alloy as a grain refining agent, its inclusion has been queried [115] in the wrought version, where grain size control may be achieved by hot and cold working. Further, it has been shown necessary for the iron to be held in solution for good corrosion resistance. This leads to a loss in ductility and restricts the amount of cold work that may be applied. In fact it has been shown that higher strength levels combined with greater ductility can be attained by cold working the iron-free alloy. The range of properties that can be achieved, depending on the degree of deformation are illustrated in Fig 21 [115]. The alpha alloy can be softened from the cold drawn condition on annealing above 400°C as shown in Fig 22 [112]. The heat treatment cooling rate is not critical for alloys containing less than 7% aluminium, though some beta may be retained, on fast cooling of the richer alloys.

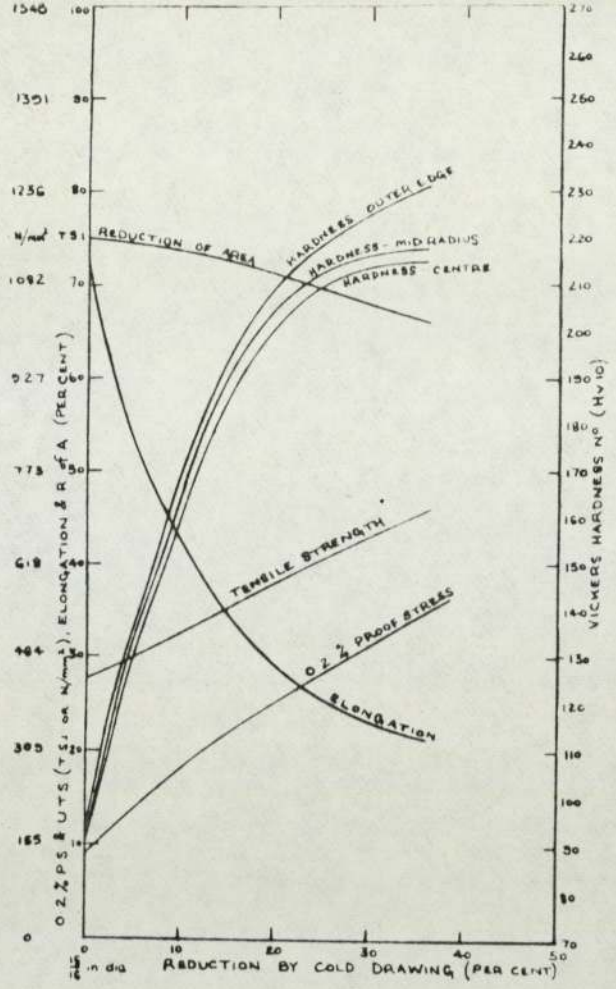

FIG 21 Showing mechanical properties of 93/7 Cu/Al alloy as a function of cold work.

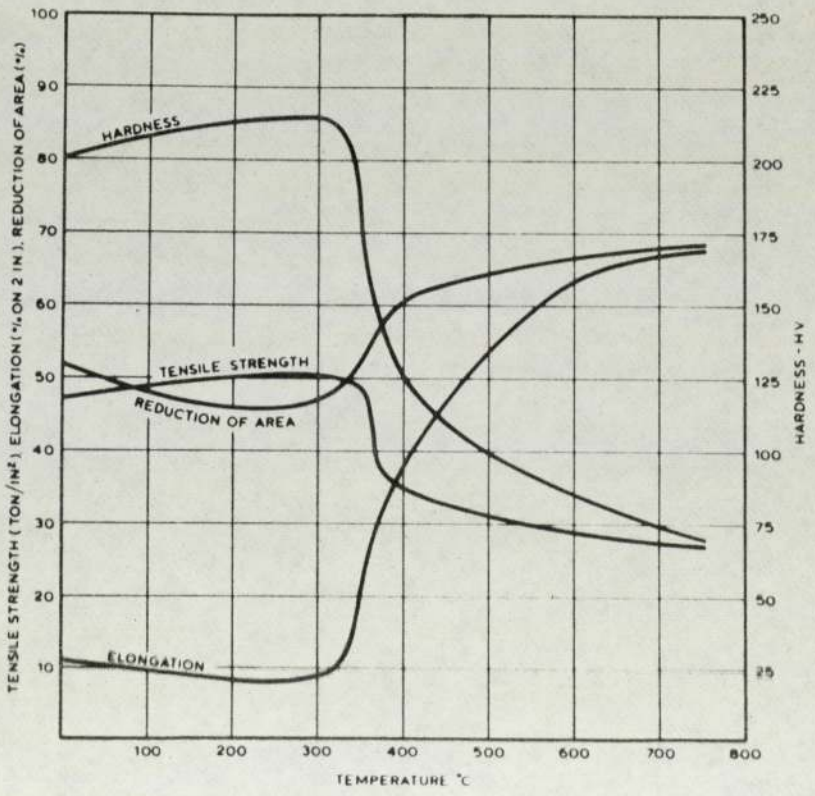

FIG 22 Showing effect of annealing temperature on mechanical properties of cold drawn (50%) 93/7 Cu/Al alloy.

The mechanical properties of the duplex alloys have a greater dependence on heat treatment conditions, and in particular the BS 2872 CA103 type alloy must be fast cooled from above 565°C to prevent the formation of the brittle and corrosion susceptible γ_2 phase. In contrast, a heat treatment of 675 ± 15°C for six hours followed by air cooling may be used to prevent the sensitisation of the complex alloy (BS 2872, CA104) to selective attack [116]. However, since this treatment results in precipitation of finely dispersed kappa IV within the alpha matrix, and a concomitant reduction in ductility, the composition must be controlled within closer tolerances than permitted in the BS specification if an elongation value of 15% is to be attained in the cast alloy. This heat treatment is not, however, universally applied. In particular it has been suggested [117] that hot headed bolts manufactured from the complex alloy should be heat treated for 2 hours at 800°C followed by air cooling. This proposal has been based on a series of tests which show that bolts in the 'as manufactured' condition fail a wedge test complying to BS 3692 and that the 800°C heat treatment optimises the mechanical properties.

Increased tensile strength may be achieved in the complex alloy by quenching from 950°C followed by tempering at 650°C for 4 hours.[118] However, it has been shown [119] that such a treatment gives low values of impact energy and a reduction of the iron and nickel content to 3% and 4% respectively is required to maintain ductility.

1.4 Summary

From this appraisal of the copper based alloys currently available for the manufacture of bolts and fittings, it may be seen that

none completely meet the requirements for high strength applications in a sea water environment.

Brass had been used as a fastener material but is not now considered suitable for naval applications because of its poor corrosion resistance, and has been replaced by aluminium bronze. However, the binary alloy BS2872 CA103, is also limited in its use by a susceptibility to selective phase attack and stress corrosion cracking. The complex aluminium bronze, BS2872 CA104, is generally considered to most nearly meet the criteria for mechanical properties and corrosion performance but a lack of ductility, as measured by a wedge test, in bolts made from this alloy is a detrimental feature of behaviour. To optimise the mechanical properties of fasteners an 800^{o}C air cool heat treatment has been proposed. However, it has been demonstrated that the microstructure can be sensitised to selective attack following such a treatment. Furthermore the alloy can no longer be regarded as immune to stress corrosion cracking since instances of failure by this mode have been observed.

Alpha single phase aluminium bronze alloys can be regarded as having improved general corrosion resistance when compared to the duplex and complex alloys, and although the single phase alloys are generally regarded as having a greater sensitivity to stress corrosion cracking, it has been proposed that minor additions of tin or silver confer immunity. The major disadvantage associated with the use of these alloys for fasteners is reduced strength in the annealed condition compared with the complex alloy. This can be rectified by the use of cold work to achieve a comparable strength level but has the attendant disadvantages of 1) increasing susceptibility to stress corrosion cracking and 2) precluding the use of hot forming due to the

associated softening and reversal of the strengthening achieved by cold work.

To overcome these limitations a proprietary single phase alloy having a nominal 93/7 Cu/Al composition, with additions of 0.5% Co, 0.25% Sn is to be considered as an alternative for Naval use. The alloy is reported as being strengthened by ageing from the cold-worked, solution-treated condition and therefore the limitations applying to the non-hardenable single phase alloy no longer apply. Since grain refinement is achieved during rolling or forging it is claimed by the manufacturers that the need for an iron addition as a grain refining agent is superfluous, resulting in improved ductility. General corrosion resistance of this alloy is expected to be good, being essentially single phase. It has been proposed that the tin addition to the alloy will give immunity to stress corrosion cracking. However, the addition primarily reduces the susceptibility to intergranular failure, but because aluminium additions to copper promote the formation of planar dislocation arrays transgranular failure can also occur.

It has been reported that terminal single-phase aluminium bronze alloys containing additions of 1-2% cobalt show age hardening characteristics, and it has been shown that the prolonged incubation period may be reduced by prior cold work and higher ageing temperatures. The strengthening mechanism has not, however, been fully identified, the over-aged precipitate being reported as having either a Fm3m or Pm3m symmetry with respective lattice parameters of 5.77Å and 2.85Å.

The object of this investigation therefore has been to study the strengthening mechanism of nominal 93/7 Cu/Al alloys containing 0, 0.5, 0.7, and 1.0% cobalt. By ageing from the solution-treated

and solution-treated, cold-drawn conditions a determination of the effect of strain ageing has been made. Since it is not considered that the volume fraction of precipitate produced in the proprietary alloy is sufficient to account for the reputed degree of strengthening, the contribution of anneal hardening has also been considered. Finally the effect of ageing on mechanical properties and stress corrosion resistance has been investigated with the objective of establishing the potential of this class of alloy for use as high strength marine fasteners.

2. EXPERIMENTAL

2.1 Material

In order to determine the inter-relationship between composition, degree of cold work and ageing treatment on the properties of the alloy, material in the conditions listed below with their designated codes were ordered in rod form (approximately 19 mm diameter) from N C Ashton Ltd.

Nominal Composition	Condition	Code
93 Cu/7Al + 0.5% Co + 0.25% Sn	Solution treated	5A
93 Cu/7Al + 0.5% Co + 0.25% Sn	Solution treated followed by 12% cold work	5B
93 Cu/7Al + 0.5% Co + 0.25% Sn	Solution treated followed by 25% cold work	5C
93 Cu/7Al + 0.75% Co+ 0.25% Sn	Solution treated	7A
"	Solution treated followed by 12% cold work	7B
"	Solution treated followed by 25% cold work	7C
93 Cu/7Al + 1.0% Co + 0.25% Sn	Solution treated	1A
"	Solution treated followed by 12% cold work	1B
"	Solution treated followed by 25% cold work	1C
93 Cu/7Al	Solution treated	OA
"	Solution treated followed by 12% cold work	OB

Chemical analysis undertaken by AMTE(HH) on the four nominal compositions gave the following results:-

Composition %	Nominal 93 Cu/7Al	Nominal 93Cu/7Al+0.5% Co+0.25%Sn	Nominal 93Cu/7Al+0.75 %Co+0.25%Sn	Nominal 93Cu/7Al +1.0%Co+ 0.25%Sn
Aluminium	7.59	7.10	7.18	6.94
Iron	<0.05	0.13	<0.05	<0.05
Tin	0.01	0.20	0.20	0.21
Cobalt	-	0.53	0.79	1.01
Total Impurities	<0.1	<0.1	<0.1	<0.10
Copper	Remainder	Remainder	Remainder	Remainder

2.2 Heat Treatment

In order to evaluate the response to heat treatment 120 mm lengths were aged for a range of temperatures and times in a muffle furnace followed by water quenching. The samples were contained within a wire mesh basket and a Pt-Pt/13% Rh thermocouple, spot welded to a standard specimen was used to monitor the temperature. The time of heat treatment was taken from the moment the temperature reached T-10°. The matrix of temperatures and times chosen for the heat treatment exercise and the designated codes are listed below.

		Time (Seconds)				
		10^2	10^3	10^4	10^5	10^6
Temperature (°C)	400	42	43	44	45	46
	500	52	53	54	55	56
	600	62	63	64	65	66
	700	72	73	74	75	

An example of the code system used is 5B43, which refers to the nominal 0.5% Co alloy, solution treated followed by 12% cold reduction then heat treated at 400°C for 10^3 seconds.

2.3 Mechanical Properties

Standard circular test pieces (25 mm^2) to BS18 part 1 were machined from the rod lengths for tensile property evaluation. Testing was undertaken using a Mayes servo hydraulic system in strain control to yield and position control to fracture, at a

strain rate of 1×10^{-3}/min and 9×10^{-2}/min respectively.

In addition to the properties of 0.2% proof stress, ultimate tensile stress and percentage elongation to failure, a work hardening index was calculated to give an indication of the form of the stress-strain curve. The index was obtained by assuming a power law of the form $\sigma - \sigma_o = K (E_p^n)$ where σ = true stress, σ_o = elastic limit, K = constant, E_p = true plastic strain and n the work hardening index.

The tensile properties were supplemented by Vickers Hardness tests. Values being obtained from longitudinal sections having been metallurgically polished to a 1 μm finish. The hardness values were obtained, using a diamond indenter at a load of 30 kg, from the mid-longitudinal axis of the specimen. The standard error of the mean was calculated from a minimum of ten results.

2.4 Microscopy

Optical microscopic examination was undertaken on longitudinal sections. These were mounted in Bakelite and prepared for metallographic examination to a 1 μm diamond finish then etched in acid alcoholic ferric chloride. The examination was undertaken using a Zeiss Ultraphot optical microscope.

Thin foils were prepared for transmission electron microscopy from 3 mm diameter discs spark machined from longitudinal sections. The blanks were initially hand ground on flooded silicon carbide paper to a thickness less than 75 μm. Final thinning to perforation was undertaken using the jet technique employing a 5% perchloric acid in 2 butoxyethanol electrolyte at 120 V, 40 mA. Transmission electron microscopy and electron diffraction studies were undertaken using a Jeol 100B transmission electron microscope.

2.5 Stress Corrosion

2.5.1 Test Methods

The different methods of stress corrosion testing have been reviewed [120] and classified under the headings:-

a) Constant strain

b) Constant load

c) Constant strain rate

Constant strain tests are most commonly employed since this type of test only requires simple restraining jigs. Difficulties, however, exist in measuring and obtaining reproducible stress levels, and care must also be taken to ensure that the restraining frame has sufficient stiffness in comparison with the specimen to be tested.

The constant strain test is characterised by load relaxation, resulting from crack propagation increasing the elastic stress to the yield point and thereby converting a proportion of the elastic strain to plastic strain [121]. The degree of relaxation is dependant on the number of cracks formed. Marked relaxation being related to the development of many cracks. The degree of relaxation will in turn affect the time to failure, since if only a single crack is formed this will propagate at a smaller stress, because the applied load in this situation will be greater than a specimen containing many cracks in which there has been a higher level of load relaxation. Because of this inherent factor the use of this test as a comparative measure of the susceptibility to stress corrosion cracking may lead to erroneous results if conclusions are drawn from the time to failure at fixed loads. Although a better

approach is to compare failure time as a function of respective yield stress, the only completely satisfactory approach involves the determination of a threshold stress. This unfortunately requires the undertaking of a large series of tests to produce the necessary stress versus failure time curve.

The major advantage of direct loading associated with the constant load test is the more accurate control over the applied stress level. This test is more likely to lead to early failure compared with the constant strain test since crack propagation will not lead to load relaxation, in fact as the crack grows the stress level will increase. The test frame again needs to be of adequate stiffness in comparison with the specimen size. In order to satisfy this requirement and still allow the use of smaller testing frames, there has been a tendency to reduce the cross section of the specimen, however, this practice can lead to erroneous results if pitting of the specimen occurs during the test, giving an attendant increase in the effective applied stress.

If crack propagation occurs by dissolution at an active crack tip, with the crack sides rendered in-active by filming, the maintenance of film-free conditions may be dependent not only upon the electrochemical conditions but also upon the rate at which metal is exposed at the crack tip by plastic strain. Therefore it may not be stress but the resultant strain rate that is a deciding factor. Clearly in such a situation the boundary conditions will be 1) when the strain rate produces ductile fracture

faster than the electrochemical reactions can cause filming and 2) when the rate at which new surfaces are created by straining does not exceed the rate at which the surface is rendered inactive. It could therefore be considered that for the constant strain and load type of test, cracks will only propagate if their rate of advancement is sufficient to maintain the crack tip strain rate above the minimum strain rate for cracking. It would therefore be expected that cracks will stop propagating if relaxation or work hardening causes a sufficient decrease in the strain rate.[73]

From such considerations it has been proposed that the constant strain rate test is not completely divorced from the service conditions pertaining to failure. The test has been successfully employed for mild steel in hydroxide solutions[122] and basically entails the application of a uniaxial load to a tensile specimen at a constant strain, or more correctly deflection rate, whilst the specimen is contained within a given environment. Testing is usually undertaken within a range of deflection of 10^{-4} - 10^{-6} mm/s, the particular value chosen being dependent on how readily the alloy films.

The susceptibility to stress corrosion cracking may be evaluated by this test from the maximum load, the elongation to failure or from metallographic examination.

2.5.2 Experimental Procedure

In order to allow an evaluation of variables such as alloy composition, metallurgical state and environment on the susceptibility to stress corrosion cracking it was

decided that the constant strain rate test was best suited. The design of the test rig was based on previously published information [123] using a standard Hounsfield Tensometer geared to give a strain rate range of 10^{-3}/s to 10^{-6}/s on a 28 mm gauge length specimen. However, for this work a modified Hounsfield Tensometer was used which allowed the automatic plot of load versus displacement. The environmental cell (Fig 24) was machined from a cylindrical block of Perspex and contained an integral platinum mesh electrode and facilities for a calomel reference electrode and an entrance and exit to allow the continuous circulation of the environment media.

Since pitting is often a necessary prerequisite for stress corrosion the test specimens were designed to incorporate a 0.13 mm radius notch situated at the centre of the gauge length.

Prior to undertaking stress corrosion testing a series of potential versus log. current diagrams were potentiostatically plotted in order to ascertain the influence of environmental conditions on the corrosion performance. The potential range to be examined was automatically scanned using a stepping potentiometer in conjunction with a Wenking Potentiostat, and the values of current and potential plotted using an X-Y log -lin recorder. The area of the specimen was chosen as 1 cm^2 which resulted in the current being directly plotted as log current density. The dimensions of the working and platinum counter electrodes were chosen to give an area ratio of 1:10 to ensure that the electrochemical process on the working electrode was controlling. The working electrode specimens

were mounted in a thermosetting polymer and prepared by hand grinding to a 600 grade emery paper finish. Electrical contact was made by drilling and tapping a thread through the mounting enabling a brass rod to be screwed into the specimen. The rod was protected from the electrolyte by a Perspex sleeve and a rubber 'O' ring seal. Electrical contact between the environment and calomel reference electrode was made by use of a salt bridge. This was constructed from glass tubing which had been drawn to a point and filled with a gel of agar-agar and KCl. The narrow end of the salt bridge enabled it to be positioned adjacent to the working electrode.

The technique applied in the production of the potential/log current diagrams involved holding the specimen at -2000 mV (with reference to a standard saturated calomel electrode) for ten minutes prior to beginning the scan. The ensuing evolution of hydrogen ensured that any atmospheric films were removed to produce a 'clean' surface. Initial broad range potential assessments were carried out at scan rates between 50-100 mV/min followed by detailed plots over narrower potential ranges at 2-25 mV/min.

For future reference to service conditions potential regions pertaining to film formation were identified from the potential/log current diagrams produced. Working electrode specimens were then reground and potentiostatically stepped from -2000 mV to the appropriate potential identified and held at this value for film growth. On removing the specimen from the electrolyte the film if sufficiently thick

was scraped off the surface using a nickel spatula, then analysed by the powder X-ray diffraction technique. A Debye Sherrer camera was used with copper Kα radiation. Exposure times varied from eight to eighteen hours depending on the density of the diffraction lines formed. A Philips diffractometer was used for the remaining specimens where the film was too thin and tenacious to be removed from the surface of the specimen.

The potential/log current graphs were also examined to determine conditions of unstable film formation which would indicate a possible susceptibility to stress corrosion. However, those formed with current densities in excess of 0.10 mA/cm^2 were excluded since it is considered that the high general rate of corrosion associated with such values would not favour stress corrosion.

Prior to undertaking the stress corrosion tests it was considered necessary to determine the influence of strain rate in air on the tensile failure mode. Practical observations on brass have shown stress corrosion crack propagation rates to be within the range 10^{-5} - 10^{-3} mm/s [124] giving a strain rate range on a 28 mm gauge length of 3.6×10^{-8} - 3.6×10^{-5}/s. For this work the range of 1×10^{-6}/s - 1×10^{-7}/s was chosen since it was considered that this was sufficiently fast to maintain the crack tip strain rate above the minimum for cracking yet slow enough to allow electrochemical reactions sufficient time to influence the mode of failure.

To maintain standard pH conditions during testing two ten litre reservoirs were used in conjunction with the test

cell. This enabled continuous circulation of the environment solution, diluting the anodic/cathodic products and by aerating the infill reservoir replenishment of dissolved carbon dioxide to maintain the buffering action of the carbonate-bicarbonate reaction [125] which occurs in sea water. However, alkaline solutions other than sea water were found to decline in pH during testing, due to an increase in the dissolved carbon dioxide content and therefore aeration was not undertaken for these environments. Additionally, since circulation also aerates the solution, to maintain a constant pH it was found necessary to include carbon dioxide filters to the air inlets of the reservoir.

3. RESULTS

3.1 Microscopy and Mechanical Properties

3.1.1. As Received Material

Metallographic examination of the eleven 'as received' materials in the ground, polished and etched condition (Figs 23-33) showed in all instances a twinned microstructure typical of a wrought single phase alloy. A variation in grain size was observed between the eleven specimens, which did not appear to show a dependence on either degree of cold work or chemical composition. However, the level of cold work within a composition group was discernible from the density of slip lines present within the grains, and it was possible to relate alloy composition with the slip line density. The presence of globular precipitates along grain boundaries and within the grains was noted, but there was no significant variation in precipitate volume between solution-treated and cold drawn samples.

The results of the tensile tests on the 'as received' material are shown in Figs 34-37. As a generalisation it was found that the ultimate tensile strength, 0.2% proof stress and elongation varied with cobalt content and level of cold work. The influence of cobalt content on these properties was found to be greater in the solution treated condition and to diminish with increasing levels of cold work. Cold work had the more significant effect.

A more complex relationship was observed for the work hardening exponent 'n'. The highest values were recorded for the solution treated material, however, unexpectedly the 25% cold drawn samples had higher values than those

obtained from the 12% cold drawn material. In general there was not a large variation with cobalt apart from a significant reduction for the 0.7% Co containing alloy for all three material conditions.

Vickers hardness values (HV 30kg) on longitudinal sections of as received material are given in Fig 38 which plots the best line through the standard error of the mean (95% probability). In general the hardness values were similar to the results of UTS and 0.2% proof stress. It was again noted that the level of cold work had the more significant effect.

3.1.2 Aged Material

Contour maps of the 0.2% proof stress, ultimate tensile stress, % elongation, strain hardening exponent n, and Vickers hardness plotted as a function of ageing temperature verses ageing time are shown in Figs 39-58. From these graphs the effect of cobalt content and degree of prior cold work on the ageing response is discernable.

The effect of ageing 'as received' material on its 0.2% proof stress is shown in Figs 39-42. Following the 400^{o}C heat treatment it was found that the cobalt containing alloys increased in strength as a function of ageing time and level of cold work. The effect could not, however, be directly related to cobalt content although in general higher values were recorded with increasing cobalt content. In comparison the solution treated control, OA, showed virtually constant properties on ageing at this temperature while the cold worked control, OB, indicated a tendency for softening on prolonged heat treatment.

Ageing the cobalt-containing alloys at higher temperatures was shown to decrease the incubation period although the maximum hardening achieved was reduced. Over-ageing was also achieved, which occurred at a time-temperature combination related to the degree of prior cold work. Ageing the solution treated control, OA, at higher temperatures, however, showed invariant properties, although the cold worked control, OB, was shown to soften at shorter times for higher temperatures.

It may be seen that a maximum value of proof stress of 600 N/mm^2 may be achieved on ageing the 25% cold worked cobalt containing alloys for 10^6 seconds at 400°C. Ageing the solution treated alloys for similar time/temperatures also gives peak strengthening, however, the values achieved are approximately halved. The contour maps also show that the solution treated alloys 7A and 1A, exhibit a minor ageing peak prior to major strengthening. In general, similarities in the form of the contour maps were observed for a given cobalt content between the solution treated, 12% and 25% cold worked conditions.

The result of ageing on the ultimate tensile stress is shown in Fig 43-46. The same trends, as observed for the 0.2% proof stress were found, namely strengthening of the cobalt-containing alloys prior to softening, dependent on a time-temperature relationship. The cobalt-free control alloy OA again showed an invariant response and the cold worked control OB softened with increasing time at temperature. The changes observed in ultimate tensile stress were not, however, as great as those recorded for the 0.2% proof stress, either in absolute terms or expressed as a percentage.

Examination of the ultimate tensile strength contour maps shows that a maximum value of 735 N/mm^2 is achieved on ageing alloy 1C for 10^6 seconds at 400°C. Peak hardening in general, was observed to occur at similar time/ temperature combinations observed for the plots of proof stress. Lower figures again being obtained from ageing solution treated material in comparison to cold drawn material. It was noted, however, that there appeared to be a closer relationship of cobalt content with ultimate tensile stress than with proof stress.

A generalised observation may be made relating to both ultimate tensile strength and 0.2% proof stress namely that increasing strength is related to increasing cobalt content in the 'as received' condition, and that on ageing, the 0.5, 0.7 and 1.0% cobalt containing alloys strengthen by approximately the same degree.

The ageing response of percentage elongation to failure is shown in Fig 47-50, where it may be seen that there is a broadly inverse relationship to both ultimate tensile stress and 0.2% proof stress.

It was observed that maximum strengthening following ageing of the 25% cold worked, 12% cold worked and solution treated alloys resulted in respective % elongations of 16-20, 32-44, and 45-52. The scatter recorded is a function of the cobalt content the lower figure for each condition being related to 1% cobalt and the higher figure to 0.5% cobalt. The form of the percentage elongation contour map was not, however, similar in detail to those obtained from the strength properties which indicated that

the ductility of the alloy was not inversely proportional to strength.

The work hardening exponent n showed broadly inverse ageing characteristics to the proof stress and UTS, but different in detail. The strain hardening exponent n was calculated for tensile samples selected from pre-peak, peak and overaged states, identified from the results of the 0.2% proof stress. The results of the calculations to obtain n are plotted graphically in Fig 51-54. Within the scatter of the technique it was observed that the exponent decreased with cobalt content and level of cold work, and reached a minimum in the peak aged condition. The largest changes occurred in the samples cold worked 25%. At all times the value of n was found to be less than that reported for annealed copper (0.54) and annealed 70-30 brass (0.49). Values of approximately 0.4 were recorded for the solution-treated state although higher values (0.45) were achieved following prolonged ageing at 700°C. The lowest value obtained was 0.1 which corresponded to a peak ageing treatment for material which had been cold worked by 25%.

Vickers hardness values (HV 30 kg) as a function of ageing time and temperature plotted as the best line through the standard error of the mean (95% probability) are shown in Figs 55-58. In general terms the response was similar to that observed for ultimate tensile strength and 0.2% proof stress.

The metallography of the ageing process was studied using 500°C aged samples of alloys OB, 7A, 7B and 7C. These

alloys encompass to some degree the changes on ageing found in all the other combinations of composition and heat-treatment and thus may be considered to be representative of the whole series of alloys and conditions.

It was observed that the OB alloy had an approximately invariant grain size on ageing for 10^2 - 10^6 seconds when compared to the as-received state (Figs 59-64). The only apparent change observed was a reduction in the density of the internal strain lines with increasing time at temperature. For times in excess of 10^4 seconds the strain lines were no longer visible.

In comparison similar ageing treatments on the cobalt containing alloy 7A (Figs 65-70) showed grain growth on prolonged heat treatment. More significant, however, was the observed increase in precipitate density which appeared to reach a maximum after 10^4 seconds prior to decreasing at longer ageing times. Ageing the 12% cold drawn version of the alloy (7B, Fig 71-76) did not show the same level of grain growth, although it was noted that the 'as received' grain size was larger. In contrast, recrystallisation was observed in the higher cold worked alloy, 7C, on ageing for periods in excess of 10^5 seconds. (Fig 77-82).

Scanning electron microscope examination at higher magnification confirmed the precipitation of a second phase in the cobalt-containing alloys. Although precipitates were observed in the solution treated (as-received) state (Fig 83) they were generally large and randomly distributed throughout the structure while

ageing (500°C for 10^6 seconds) resulted in a high density of fine precipitation throughout the structure (Fig 84). The form of this second phase was found to depend on its location. Coarse, globular precipitates were observed along the grain boundaries, with smaller but still globular precipitates along twin boundaries. However, within the grains the precipitate showed a needle-like morphology. Adjacent to both grain and twin boundaries was a precipitate-free zone.

Similar grain boundary precipitation was also observed in the cold worked alloy (7C) in the 'as received' state. Examination of this alloy following ageing for 10^6 seconds at 500°C confirmed the optical observation of recrystallisation, and it was noted that resolution of precipitates had occurred.

The precipitate size precluded quantitative analysis by electron probe microanalysis. However, a quantitative spot analysis of a precipitate is shown in Fig 85 which illustrates an X-ray trace from which the matrix contribution has been electronically stripped. The analysis indicates that the precipitate phase is basically an aluminium-cobalt compound.

The presence of another precipitate phase was also established by the scanning microprobe analysis. This phase was found to be sulphur rich, mainly globular in nature (5-10 μm) and to be randomly distributed throughout the matrix. By reducing the accelerating voltage to 10 kV it was possible to reduce the beam penetration to a degree that allowed quantitative analysis to be undertaken. A

series of spot analyses across the diameter of a precipitate gave similar results which confirmed that there was no contribution from the matrix due to beam overlap. The analysis, corrected for atomic number, fluorescence and absorption effects [126] indicated that the composition of this phase by weight was, Cu 25%, Al 15%, S 60%. By converting these figures to atomic percentages it was shown that the compound is $Al_{0.6}$ $Cu_{0.4}$ S_2 and could be most nearly represented by the formula (Al Cu)S_2.

3.2 Electron Microscopy

Transmission electron microscopy of the 0.7% cobalt containing alloy in the solution treated condition (7A) showed fine parallel features representing either planar networks of extended dislocations or fine twins. A speckled background contrast suggested that a fine matrix precipitate might also be present (Fig 86). Bend contours (Fig 87) highlighted the precipitate by tilting the foil into favourable contrast conditions. The horizontal features in Fig 87 displace the bend contours and probably represent twins running through the thickness of the foil parallel to the beam.

In comparison, Fig 88 illustrates the structure of the 25% cold worked version of this alloy (7C) and shows broad twins with a heavily dislocated substructure. A selected area diffraction pattern of the twinned region is shown in Fig 90 and a centred-dark field from the $(\bar{1}11)$ diffraction spot in Fig 89. A stereographic projection of a cubic crystal twinned on the (111) plane is shown in Fig 91. On this is marked the planes corresponding to the twinned diffraction pattern of Fig 90. The sharp contrast change between the broad twin bands shows that the twins alternate in crystal orientation across the twin planes. The

extended dislocations are clearly shown by this dark field technique. The twin bands are running almost parallel to the electron beam and the twin plane must therefore be represented by one of the diffraction spots in Fig 90. Compensating for image rotation between the dark field image and the diffraction pattern puts the trace normal close to the $(1\bar{1}1)$ reciprocal lattice vector, indicating that this is the twin plane. However the diffraction pattern indexing requires the twin plane to be the (111) which lies about 20° from the zone axis. It is concluded that twinning must occur on at least two different twin planes to explain these results.

The effect of tilting the foil on precipitate and stacking fault contrast is shown in Figs 92, 93 and 96 which show a different area of the foil. These micrographs show large precipitates $\simeq$200 nm diameter and some very small ones. There are large numbers of dislocations, many in extended form giving stacking fault contrasts between the separated partials. The stacking faults lie on two principle crystallographic planes. Correcting for rotation, the projected normal of one stacking fault plane lies close to the $(\bar{3}31)$. The tilt angle of the stacking fault plane was calculated to be $\simeq 22^{\circ}$, assuming the foil thickness to be 40 nm. Since the $(\bar{1}11)$ plane lies 22° from the $(\bar{3}31)$ plane towards the zone axis, it is considered that this is the fault plane. The second set of stacking faults are orientated 85° from the first and about 50 nm wide in projection, indicating a tilt angle of about 40°. The (111) plane lies 40° from the plane of the diffraction pattern towards the zone axis, and is the probable fault plane. A centred dark field photograph from the $(\bar{1}11)$ twin plane with the corresponding diffraction pattern is shown in Figs 95 and 94). The indexed diffraction

pattern is plotted on the (111) twin stereographic projection in Fig 91. The centred dark field photograph also highlights the precipitates, which indicates that the (111) planes of the matrix are coincident in direction and interplanar spacing with some precipitate planes. Large spheroidal precipitates (≃ 200 nm diameter) were found throughout the foils examined for all material conditions. These in general were too thick to give diffraction patterns. However, Figs 97 and 99 show a bright field photograph with a corresponding selected area diffraction pattern from such a precipitate which had been sufficiently thinned. The precipitate reflections were indexed as simple cubic with a lattice parameter of 3.08Å. The orientation of the precipitate with respect to the matrix was analysed as $(2\bar{2}0)_m$ // $(\bar{1}\bar{1}2)_{ppt}$, $[113]_m$ // $[1\bar{1}0]_{ppt}$. A dark field from the $(10\bar{1})$ precipitate plane is shown in Fig 98. This confirms that the diffraction pattern is indeed from the precipitate.

Examination of the aged solution treated alloy (7A55) to pre-peak hardness showed groups of precipitates approximately 50 nm in diameter located in broad bands. The parallelism of these bands and the thickness fringes within them are reminiscent of twin boundaries. No strain fields were associated with these precipitates. In addition to these globular precipitates a rod-like phase was also observed which was found with various orientations within the foil. Examples of these precipitates with a selected area diffraction pattern and respective dark fields from a $(01\bar{1})$ precipitate plane are shown in Figs 100-104. From the diffraction pattern the smaller globular precipitate was found to be simple cubic with a lattice parameter identical to that of the large globular precipitate. A series of matrix zones were identified in the diffraction pattern which are

related by an approximate 30° total tilt. The dislocation structure of the aged alloy 7A55 is shown in Fig 105 where a planar array of partial dislocations with associated small stacking faults are observed. Evidence that the larger globular precipitates could obstruct dislocation movement is shown in Fig 106 where a line of dissociated dislocations is shown piled up against such a precipitate.

Ageing the solution treated alloy (7A56) to peak hardness eliminates stacking faults within the foil, in their place narrow single dislocations were observed. A typical example is shown in Fig 107. A selected area diffraction pattern from this region is shown in Fig 109, in which a simple cubic precipitate phase having a lattice parameter of 3.08Å is identified. The precipitate was found to have an orientation relationship with the matrix of $(111)_m \,//\, (110)_{ppt}, \left[\bar{1}01\right]_m \,//\, \left[\bar{1}11\right]_{ppt}$ which conforms to the Kurdjamov-Sachs relationship. A centred dark field photograph from the $(00\bar{1})$ precipitate reflection is shown in Fig 108. This shows strong diffraction from a small rounded precipitate and also some diffracted intensity from two rod-like precipitates. A very fine background precipitate is also revealed in this dark-field photograph. A stereographic projection representing the Kurdjamov-Sachs orientation relationship between body and face-centred cubic crystals showing the indexed diffraction pattern and the tilt axis of the foil is shown in Fig 110. A diffraction pattern from the same area of the foil but tilted by approximately 17° is shown in Fig 111. The precipitate and matrix zones from this pattern are also plotted in Fig 110 with respect to the foil tilt axis. It may be seen that there is again an agreement with the Kurdjamov-Sachs orientation relationship. A diffraction pattern from a different region of the foil giving matrix and

precipitate reflections is shown in Fig 112. The lattice parameter of the precipitate phase was similar to that previously identified, however, the $[211]_m$ // $[310]_{ppt}$ zones did not fit the Kurdjamov-Sachs relationship and did not put matrix and precipitate major planes in coincident positions.

Ageing the solution treated/cold drawn alloy to peak hardness (7C53) appeared to decrease the stacking fault density. A photomicrograph showing this effect is given in Fig 113 and a corresponding selected area diffraction pattern showing a $\langle 310 \rangle$ zone with weak additional reflections in Fig 114. A further bright field micrograph from this material condition is given in Fig 115 which shows the presence of precipitates associated with stacking faults. A selected area diffraction pattern of this region is given in Fig 117, which shows a similar $\langle 310 \rangle$ zone with extra reflections. In addition, however, a line of (00L) precipitate spots were present. A dark field from a precipitate reflection produced the photograph of Fig 116.

A further decrease in the planar dislocation density coincided with the appearance of a rod like background precipitate in the overaged state of the cold drawn alloy (7C55) (Figs 118, 119). A selected area diffraction pattern (Fig 120) showed the precipitate to be simple cubic (a = 3.08Å) with an apparent orientation relationship with the matrix of $[\bar{3}43]_m$ // $[\bar{1}11]_{ppt}$, $(101)_m$ // $(211)_{ppt}$.

3.3 Stress Corrosion

3.3.1 Polarisation Studies

It was considered from examination of the equilibrium potential - pH diagram of copper in seawater that three pH conditions would encompass the changes resulting from this

variable. It is shown that at pH three copper passes from the immune state to a state where free Cu^{2+} forms with increasing positive potentials. On increasing the pH towards that of natural seawater (8.1) more positive potentials give rise to the formation of Cu_2O then CuO and finally $Cu_2(OH)_3Cl$. A further change is observed at pH values in excess of twelve when $Cu(OH)_2$ is formed in preference to the complex chloride-hydroxide.

A potentiostatic plot of alloy OB in hydrochloric acid at pH 3.1 is shown in Fig 121. It was found that on polarising in the anodic direction from -2000mV the current density showed a minimum of 0.035 mA/cm^2 on the cathodic side of the corrosion potential (-175 mV) at -280 mV. A continuous increase in current was observed on further polarisation in the anodic direction.

In comparison Fig 122 shows a similar plot obtained from sodium hydroxide at pH 8.1. Although a minimum is again observed on the cathodic side of the corrosion potential it was located at -175mV. However, it was noted that the corrosion potential has also changed position and that the potential difference between E_{corr} and E_{min} remain relatively constant. Polarising away from the corrosion potential again showed an increase in current density, although it was not continuous and there were two minor troughs at +400mV and +650mV. A potentiostatic plot obtained from sodium hydroxide at the higher pH level (12.35) is given in Fig 123. This increase in pH was shown to modify the form of the potentiostatic curves previously identified. In this instance no significant minimum was observed on the cathodic side of the corrosion potential,

however, a passivation trough having a current density of $0.05mA/cm^2$ was observed over the potential range +200-+550mV. In contrast to the two previous results which showed that by increasing the pH from 3.1 to 8.1 the corrosion potential shifted to more noble potentials, a further increase in pH to 12.25 has resulted in a move in the reverse direction to a more base potential. It is also apparent from Fig 123 that at this higher pH level, fluctuations exist in the current density on both the anodic slope of the corrosion potential and within the anodic passivation trough.

It has been reported that the presence of copper ions is necessary for the promotion of stress corrosion of copper alloys in complex ammonia solutions. As a prelude to investigating the possibility of a similar influence in aqueous sodium hydroxide, a potentiostatic plot was obtained from a solution of sodium hydroxide at pH 12.25 with the addition of fifteen parts per million of Cu^+ ions. (Fig 124). It is shown that the addition of the copper ions altered the corrosion potential to -350mV. It was also apparent that a plateau in current density of $0.05mA/cm^2$ between -600mV and the corrosion potential had formed as a result of the addition. Furthermore no anodic current density peak was observed and instead a continuous passivation trough was observed to extend from the corrosion potential to +400mV.

In order to determine the effect of specific ions as opposed to pH it was decided to obtain a polarisation curve from sodium carbonate solution. However, a direct comparison cannot be made with sodium hydroxide solution

since it was not possible to increase the pH value of a sodium carbonate solution above the value of 11.5 for the saturated state. Examination of the plot obtained (Fig 125) shows the corrosion potential to be now -400mV. In general the plot was more similar to the Cu^{+} ion containing than the Cu^{+} free sodium hydroxide solution. However, the anodic passivation region had been extended to +700mV.

The effect of an addition of fifteen parts per million of Cu^{+} ions to the sodium carbonate solution is shown in Fig 126. Although the corrosion potential has remained unaltered and the general form of the curve is the same, the presence of a current density peak at -150mV is apparent. In addition a minor passivation trough was observed on the anodic slope of the corrosion potential which was not present in the copper-free solution.

A factor which was common to all of the higher -pH solution potentiostatic curves was that they all showed, to various degrees, fluctuations in their current density.

A potentiostatic plot of the alloy in aerated seawater (pH 8.1) is shown in Fig 127. This illustrates that the alloy has a more base corrosion potential in this environment than in sodium hydroxide at a similar pH. In addition a small anodic passivation trough was observed in seawater at -320mV prior to the current density rising to a plateau value of approximately $7mA/cm^{2}$ at 40mV.

In comparison an anodic polarisation curve from the free corrosion potential in seawater, is shown in Fig 128. The

free corrosion potential was measured as -250mV which may be compared with -500mV and -300mV for the respective corrosion and passivation potentials observed on polarising from -2000mV as shown from the previous graph. However, this apart, the form of the anodic plot was similar to the anodic section of Fig 127.

A polarisation curve in seawater from the solution-treated version of the OB alloy (OA) is shown in Fig 129. This shows that although the corrosion potential and anodic passivation potential have shifted to -400mV and -200mV respectively, the overall form of the plot is the same as that from the cold worked version of the alloy.

In comparison the effect of a one per cent addition of cobalt, with the level of cold work remaining constant (IB), on the seawater polarisation behaviour is shown in Fig 130. In contrast to the effect of cold work/solution treatment, this shows that the change in alloy composition has not affected the corrosion potential. However, there is now no longer any evidence of an anodic passivation trough, although a similar current density plateau was observed between the potential range 0 + 800mV.

The potentiostatic curve of the solution treated version of this alloy (IA) is shown in Fig 131, which illustrates that the behaviour was similar to that of the IB alloy. From the graphs it may be seen that for the cobalt containing alloy the solution treated version has a corrosion potential 100mV more base than the cold worked version whilst for the cobalt free alloy the solution treated corrosion potential is 100mV more noble than the cold worked version.

3.2.2 Analysis of Corrosion Films

To ascertain the nature of the corrosion films present on OB in seawater, the corrosion products formed at various potentials were analysed by X-ray diffraction. Although the analysis indicated that the products were multiphase, three principle compounds were identified as being present dependent on the degree of anodic polarisation. At -320mV, corresponding to the first anodic trough a thin white coating was formed. The main constituent of this coating was either Ag(Cl,Br) or NaCl, since within the accuracy of the work it was not possible to distinguish between the two. This compound was also identified as the major phase at the more positive potential of -100mV. On increasing the potential to +60mV i.e to a value sufficient to reach the plateau in current density recorded in Fig 127 a copious flossy green product was formed. The previous compound and the compound $Cu_7Cl_4(OH)_{10}H_2O$ were identified at this potential. At an increased anodic polarisation potential of +340mV the corrosion product observed was still copious, green, and had poor adherence qualities. However, in this instance the products were identified as being mainly CuCl.

X-ray diffraction studies on the seawater corrosion products from the one per cent cobalt containing alloy showed that similar compounds were formed. However, the potentials at which the compounds were different as suggested by the relevant polarisation diagrams.

In order to determine the effect of pH on the composition of the corrosion products, films were grown on OB in seawater modified to a pH of 12.5 by the addition of

NaOH. At a potential of OmV corresponding to the anodic slope of the corrosion potential, a thin, tenacious black film was observed. Since this film could not be readily removed from the surface a back reflection technique was employed. The limited information generated indicated that the corrosion product was Cu_2O. The corrosion product formed in this environment at +400mV, i.e within the passivation trough was more abundant, and found to be mainly Cu(OH)Cl. The results obtained for the various corrosion products are listed in Table 2, which may be compared with the interplanar spacings 'd' of standard compounds given in Table 3.

3.2.3 Constant Strain Rate Tests

In order to ascertain the susceptibility of the alloys to stress corrosion cracking the series of tests shown in Table 4 were undertaken. The effect of strain rate in air is demonstrated on OB where it may be seen that there is a significant reduction in the percentage elongation to failure on reducing the strain rate from $1x10^{-3}$/s to $1x10^{-6}$/s. A slight additional reduction in elongation was also observed on further reducing the strain rate to $1x10^{-7}$/s. The fracture surfaces of these specimens are shown in Figs 132-137. At the strain rate of $1x10^{-3}$/s ductile dimples were observed covering the entire fracture surface. However, at the two slower strain rates although ductile dimpling was still predominant, areas were also observed which showed secondary grain boundary cracking and flat facets. There also appeared to be a tendency for intergranular failure at the slower strain rates.

In comparison to the tests undertaken in air, the elongations to failure of OB in seawater (pH = 8.3) at both $\dot{\varepsilon}$ = 1.10^{-6}/s and $1x10^{-7}$/s were more than doubled.

Fractography of these samples again indicated (Figs 138-141) that ductile dimpling had occurred, but in addition the fracture surfaces were also covered with corrosion products. However these corrosion films were not continuous, and areas of crazing were observed.

Anodic polarisation of OB in seawater to -200mV at $\dot{\varepsilon}$ = $1x10^{-7}$/s suggested that in comparison to the previous test undertaken at the rest potential these conditions increased the susceptibility to stress corrosion cracking. In conjunction with this decrease in elongation secondary cracking of the underlying material was observed on the fracture surface and there was also evidence of selective corrosion (Figs 142-143).

A repeat of this test at the more anodic potential of -100mV gave an increase in the elongation to failure, but it was also noted that extensive general corrosion of the specimen occurred during the test period. Details of the fracture surface relating to this test are shown in Fig 144-145, where significant intergranular corrosion is apparent.

An addition of 10 ppm of L.cystine to seawater was shown to have no significant effect on the susceptibility of OB to stress corrosion cracking at the rest potential. General corrosion products were again observed on the fracture surface which covered the underlying structure of coarse ductile dimples. Secondary cracking of the surface was also observed (Fig 146-147).

A susceptibility of OB to stress corrosion cracking (2.3% elongation to failure) was observed, however, in NaOH (pH 12.3) at the rest potential for the strain rate of $1x10^{-6}$/s. The fracture surface in this instance showed two distinct modes of failure. Whilst the majority of the surface was indicative of cleavage there was also a smaller area adjacent to part of the circumference where intergranular failure had occurred, as illustrated in Fig 148-149.

Anodic polarising OB in this solution to a potential (+500mV) corresponding to the passivation trough shown in Fig 123 gave a higher elongation to failure indicating a lessening of sensitivity to stress corrosion cracking. This was supported by the fractographic evidence which indicated a transition mode between ductile dimples and cleavage. (Figs 150-151).

The effect of an addition of 15 ppm of Cu^{+} ions on the stress corrosion resistance of OB at its rest potential in NaOH (pH 12.3) was also determined. Although the elongation to failure suggested that this addition had not increased the susceptibility, the fracture surface was more indicative of cleavage than from the copper-free solution (Fig 152-153).

Similar tests were also undertaken in saturated $NaCO_3$ solution (pH 11.5) with an addition of 15 ppm of Cu^{+} ions to determine the influence of specific ions for a given pH value. The elongation to failure in this solution was identical to the test in NaOH solution and the fracture surface similarly showed areas of both intergranular and cleavage/ductile cracking. (Fig 154-155).

The effect of the cobalt addition on the stress corrosion resistance of the basic 93/7 Cu/Al alloy was determined by testing IB in seawater. The test was undertaken at the

rest potential at a strain rate of $1x10^{-6}$/s.

Similarly to the test on OB, corrosion products were observed on the fracture surface covering an underlying dimpled structure. Fig 156-157. It was noted, however, that the elongation to failure was higher (14%) for the cobalt containing alloy.

To ascertain the influence of strain rate, tests were also undertaken on this alloy in air. A reduction in the elongation value to failure was again observed on decreasing the strain rate, however, in contrast to the cobalt free OB alloy the reduction was not as significant. Values of 3.1% and 11.3% were respectively obtained at $\dot{\varepsilon} = 1x10^{-6}$/s for OB and IB, whilst at $\dot{\varepsilon} = 1x10^{-1}$/s the respective values were 46% and 31%. Illustrations of the fractography of IB in air at $\dot{\varepsilon} = 1x10^{-6}$/s are given in Figs 158-159 which mainly show ductile dimpling although regions exhibiting a flat fracture form were also observed.

Anodic polarising IB in seawater to -200mV was not found to increase the susceptibility of the alloy to stress corrosion cracking. Corrosion products overlaying a dimpled network as in the case of the rest potential test were observed and are shown in Fig 160-161. However, there was also an indication of selective corrosion of the fracture surface.

Seawater stress corrosion tests were also undertaken on the aged version of this alloy (IB54 and IB56).Commensurate with the ageing response a change was observed in the stress corrosion resistance of the alloys. In the partially aged condition (IB54) preferential pitting of the fracture surface along twin boundaries and dislocations was observed (Fig 162-163). Whilst in the fully aged condition (IB56) cleavage cracking was predominant. (Fig 164-165).

Stress corrosion tests on the solution treated version of the cobalt containing alloy IA in seawater gave higher elongation to failure values than the cold drawn IB material. General corrosion of the dimpled fracture surface was again observed as shown in Fig 166-167. Similar tests undertaken on the alloys IA54 and IA56 showed that ageing the solution treated alloy also increased the susceptibility to stress corrosion, although the degree of sensitisation was not as significant as that shown for the cold worked version. The fracture surfaces from both ageing treatments showed preferential corrosion at dislocations but it was noted that the effect was greater for the longer ageing treatment (Fig 168-171). Commensurate with this effect the elongation to failure was found to decrease with increased ageing.

Tests undertaken on the 25% cold drawn cobalt alloy IC further confirmed the influence of ageing on the susceptibility to stress corrosion in seawater. However, it was shown that prolonged ageing which resulted in recrystallisation and softening removed this sensitivity. Fractographs from IC, IC54 and IC56 are shown in Figs 172-177. It may be seen that ductile dimples are present on IC and IC56 whilst IC54 shows cleavage with selective corrosion at dislocations.

Stress corrosion tests were also undertaken on the IB alloy in the as-received and aged conditions in sodium hydroxide (pH 12.3) of the free corrosion potential. Fractographs from these specimens indicating cleavage cracking are shown in Figs 178-181.

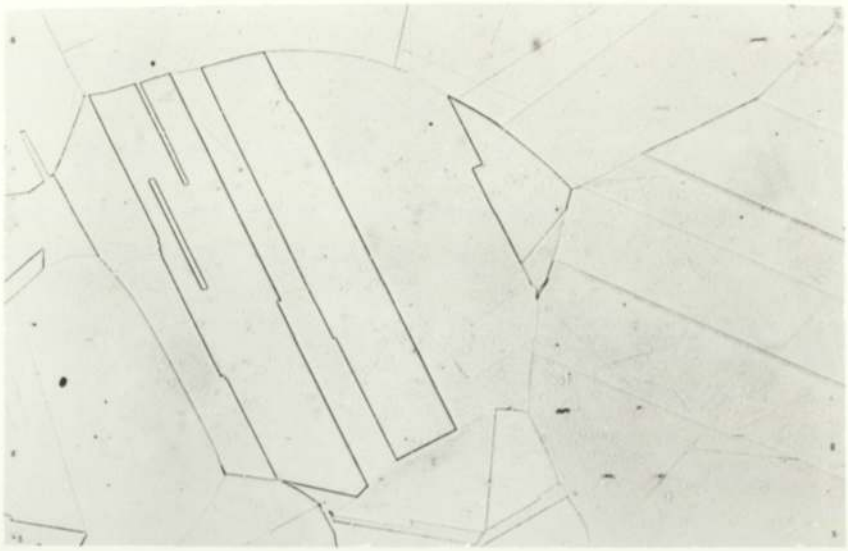

FIG 23 0A 0% Co Solution Treated x304

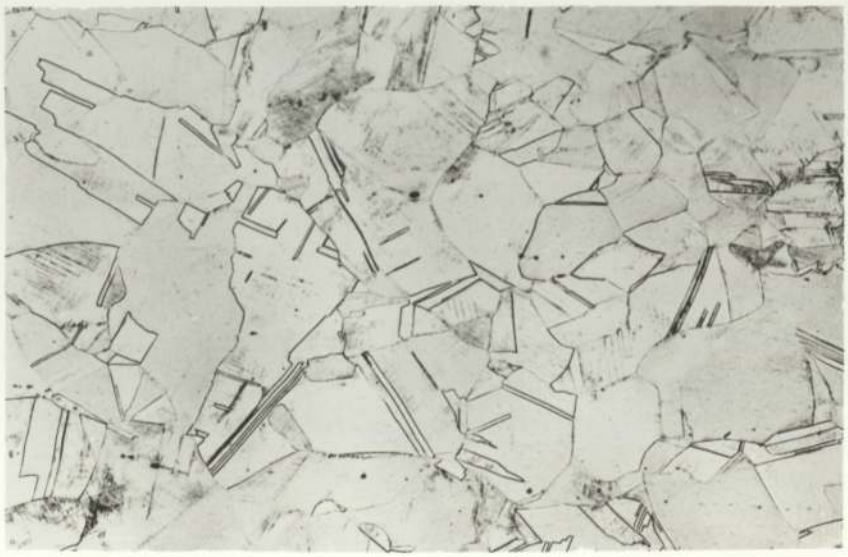

FIG 24 0B 0% Co Solution Treated + 12% Cold Work x304

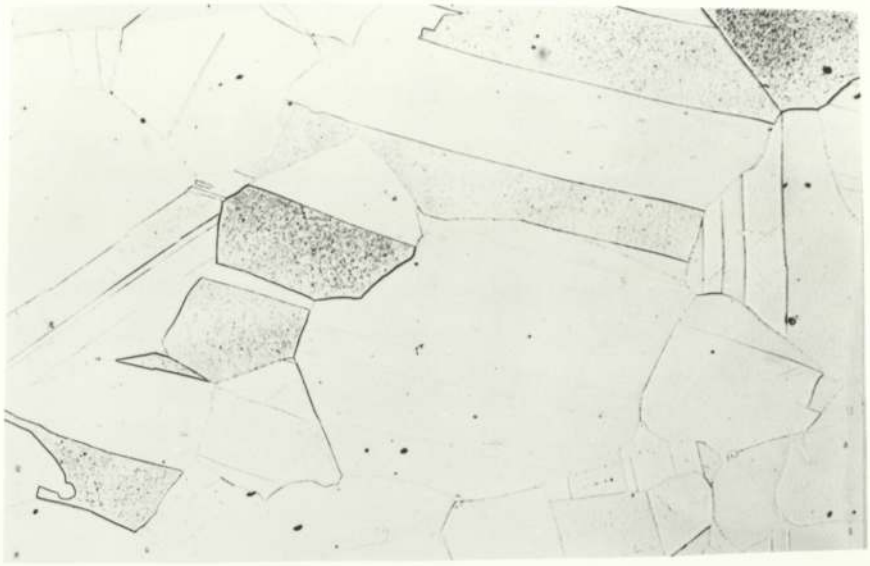

FIG 25 5A 0.5% Co Solution Treated x304

FIG 26 5B 0.5% Co Solution Treated + 12% Cold Work x304

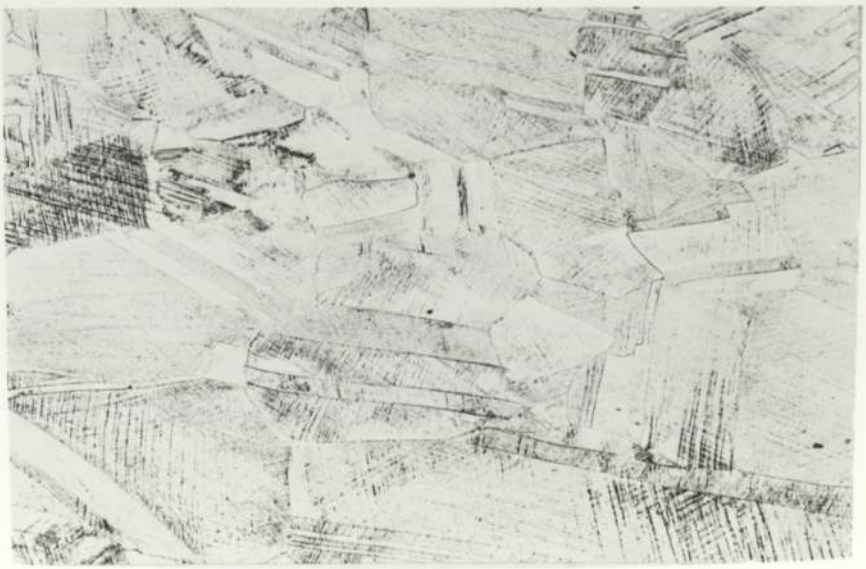

FIG 27 5C 0.5% Co Solution Treated + 25% Cold Work x304

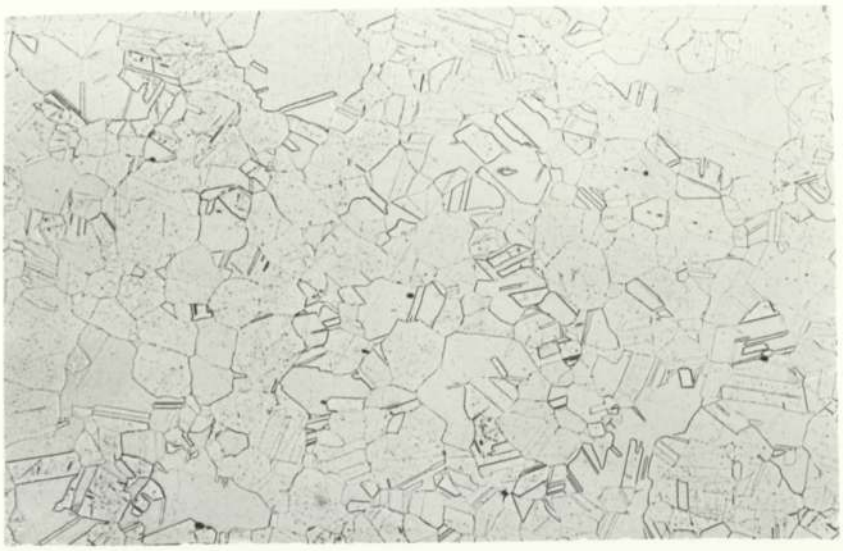

FIG 28 7A 0.7% Co Solution Treated x304

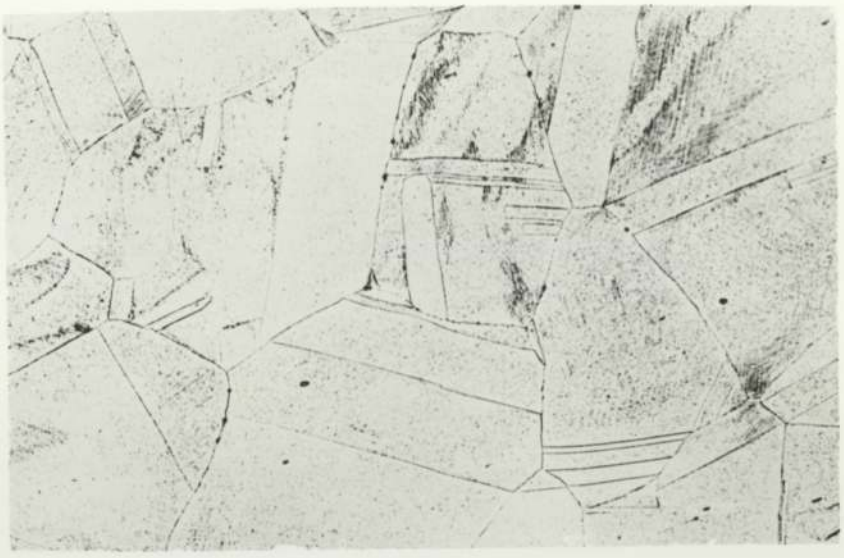

FIG 29 7B 0.7% Co Solution Treated + 12% Cold Work x304

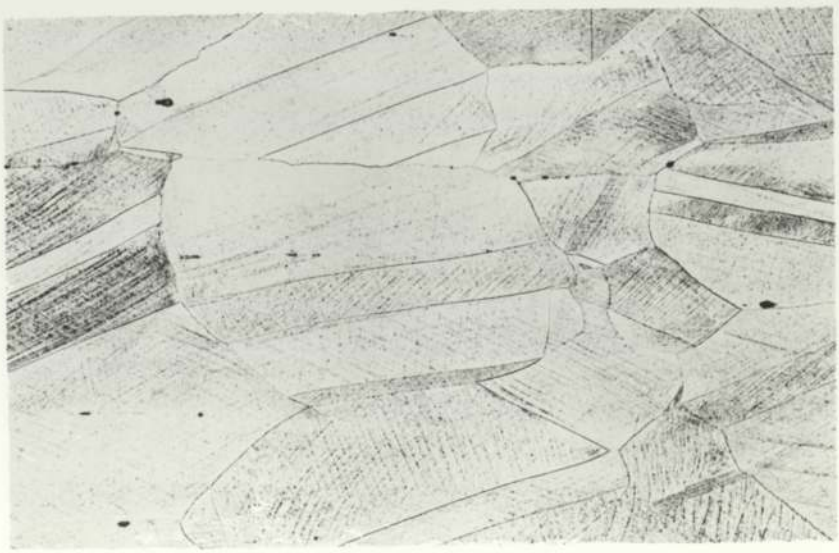

FIG 30 7C 0.7% Co Solution Treated + 25% Cold Work x304

FIG 31 1A 1% Co Solution Treated x304

FIG 32 1B 1% Co Solution Treated + 12% Cold Work x304

FIG 33 1C 1% Co Solution Treated + 25% Cold Work x304

FIG 34

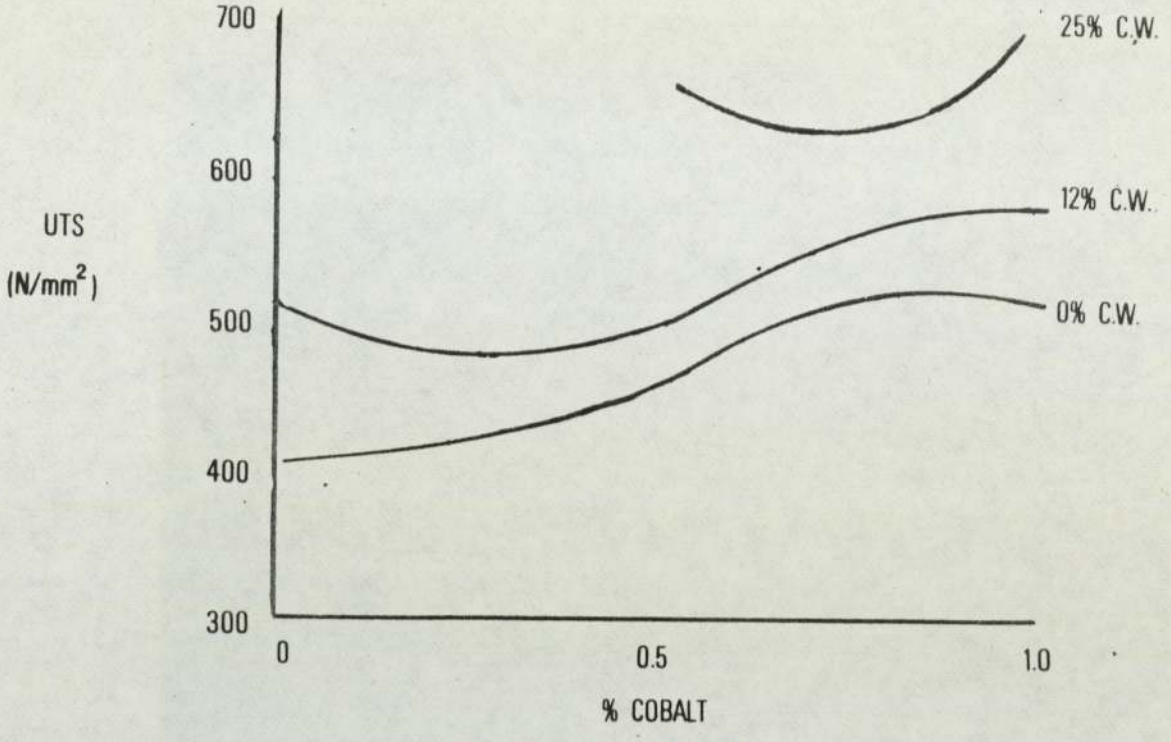
700
600
500
400
300
UTS
(N/mm²)
25% C.W.
12% C.W.
0% C.W.
0
0.5
1.0
% COBALT

FIG 35

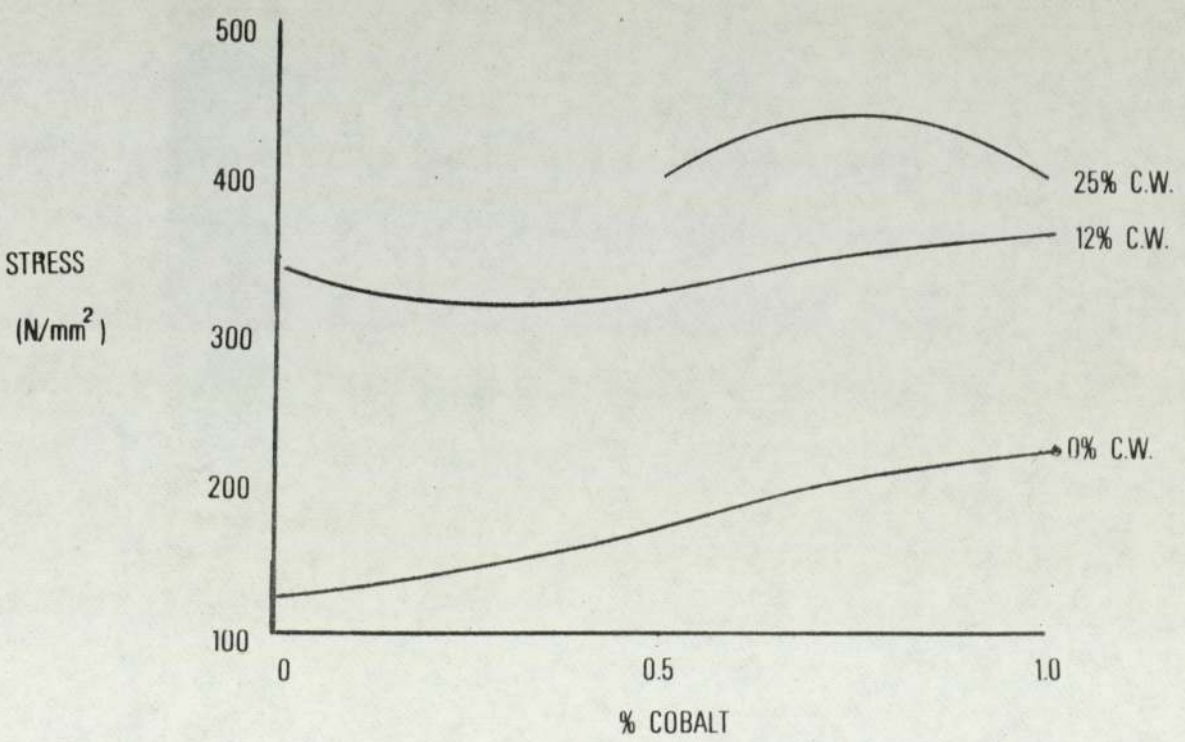
500
400
300
200
100
STRESS
(N/mm²)
25% C.W.
12% C.W.
0% C.W.
0
0.5
1.0
% COBALT

FIG. 36

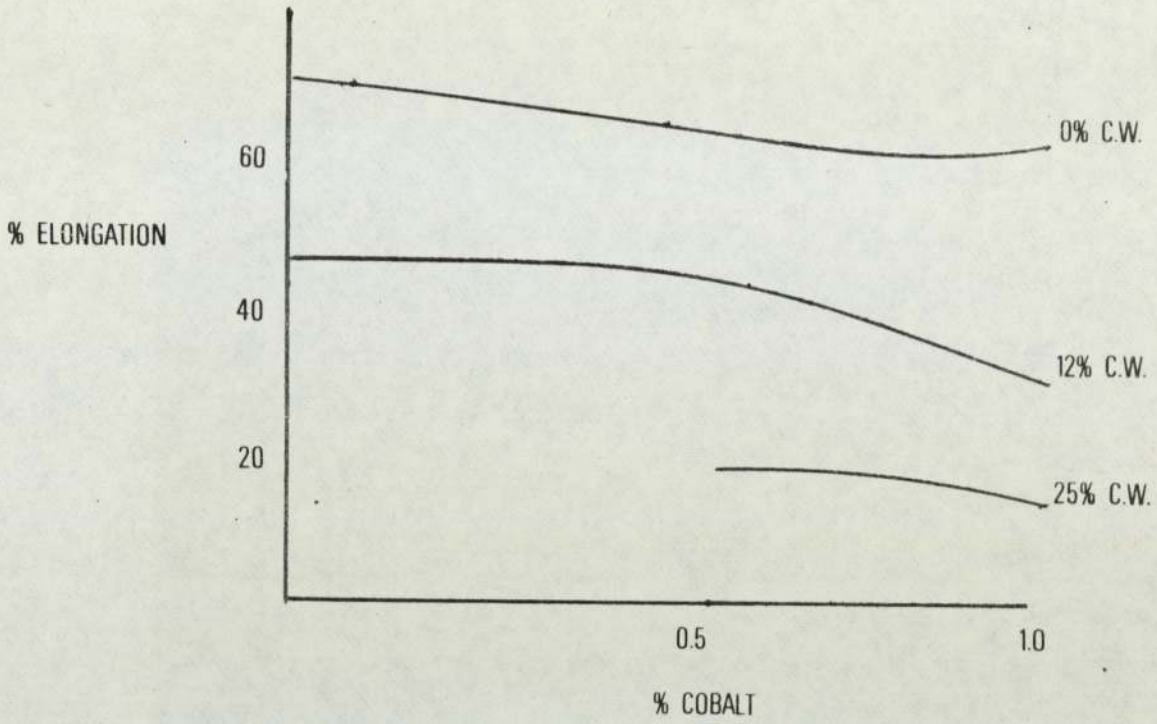
% ELONGATION
60
40
20
0% C.W.
12% C.W.
25% C.W.
0.5
1.0
% COBALT

FIG. 37

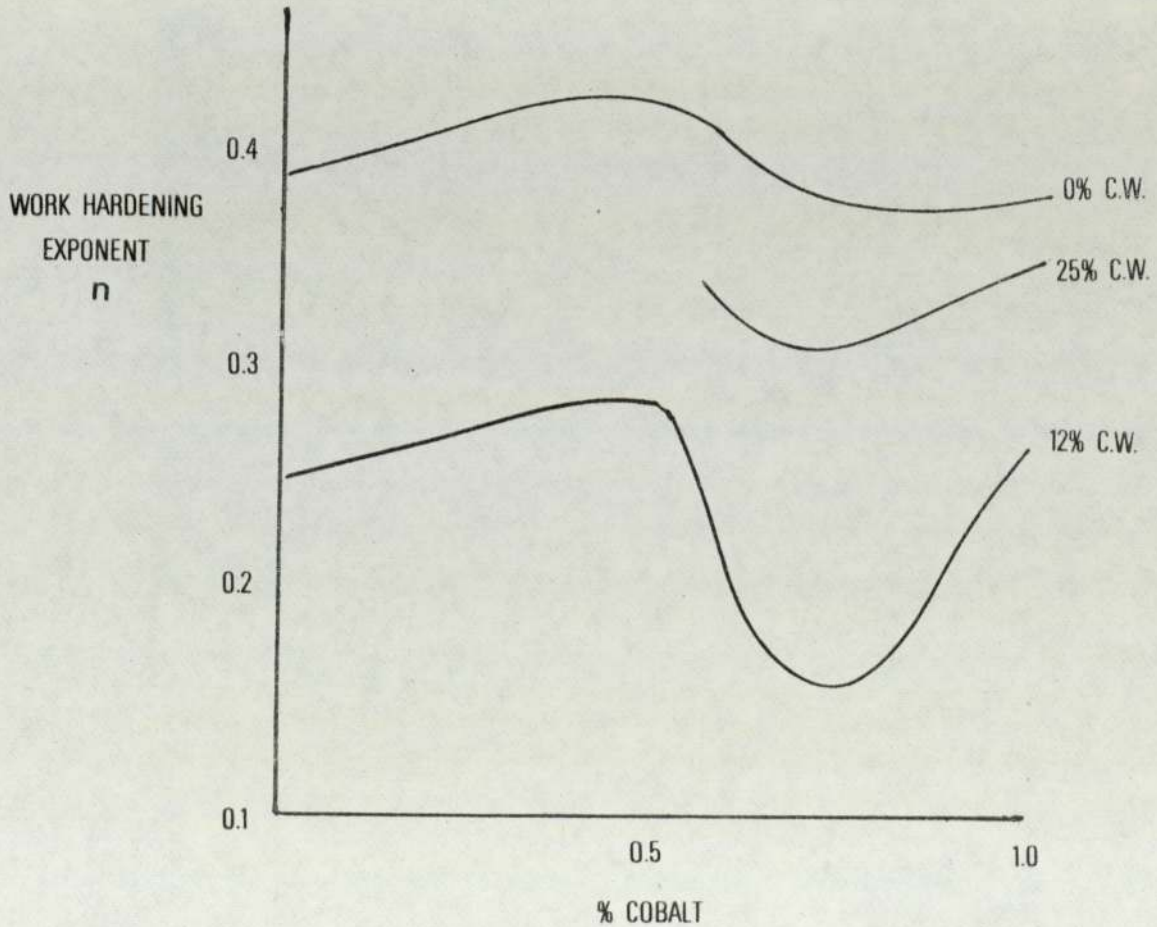
WORK HARDENING
EXPONENT
n
0.4
0.3
0.2
0.1
0% C.W.
25% C.W.
12% C.W.
0.5
1.0
% COBALT

FIG. 38

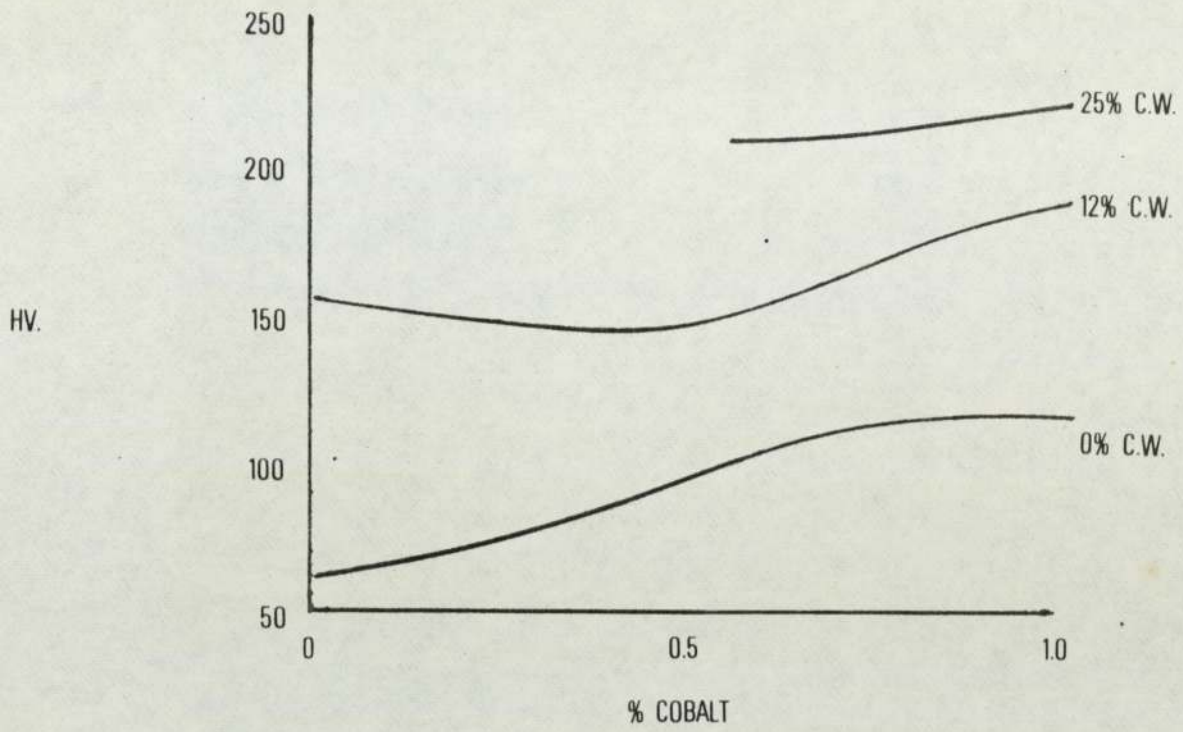

FIG 39. 0.2% PROOF STRESS AS A FUNCTION OF AGEING TIME AND TEMPERATURE

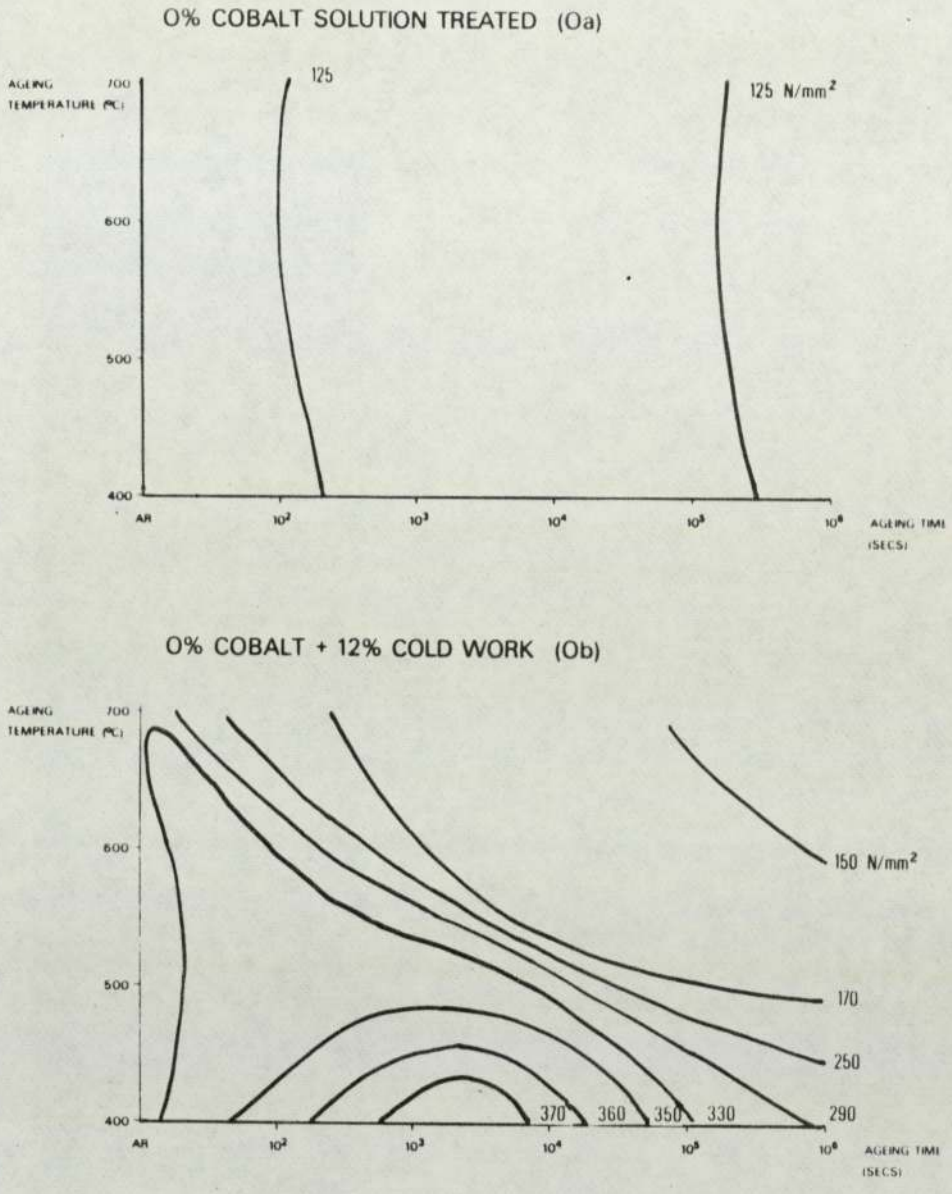

FIG 40. 0.2% PROOF STRESS AS A FUNCTION OF AGEING TIME AND TEMPERATURE

0.5% COBALT SOLUTION TREATED (5a)

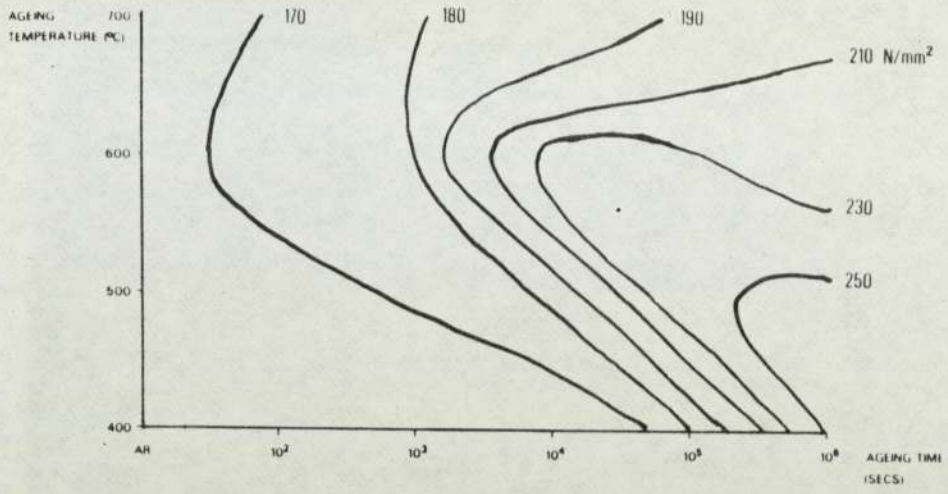

0.5% COBALT + 12% COLD WORK (5b)

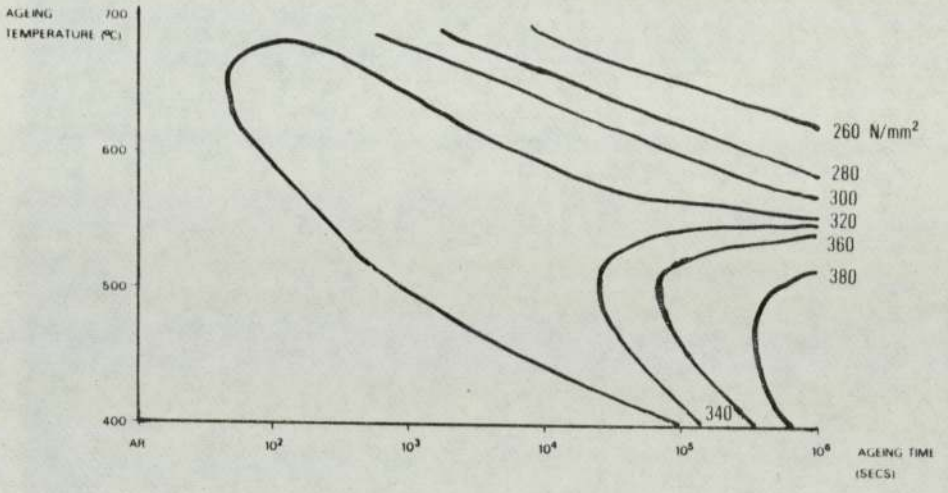

0.5% COBALT + 25% COLD WORK (5c)

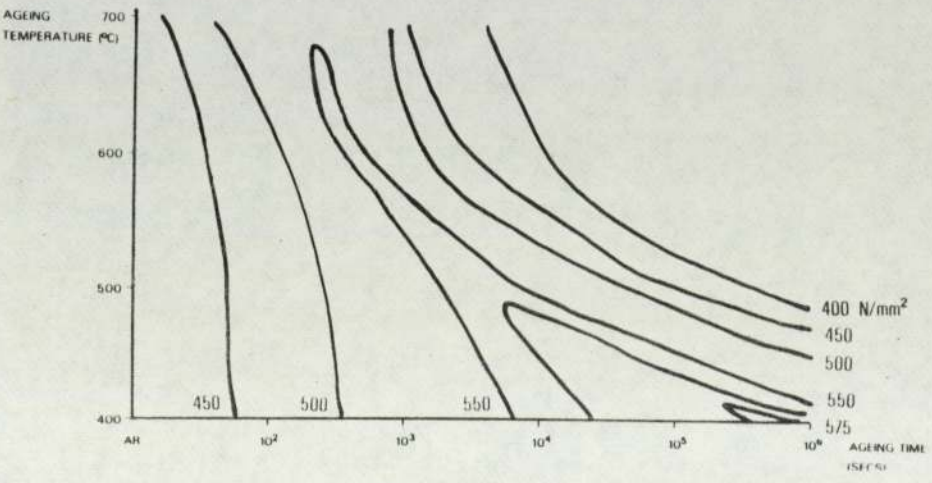

FIG 41. O.2% PROOF STRESS AS A FUNCTION OF AGEING TIME AND TEMPERATURE

O.7% COBALT SOLUTION TREATED (7a)

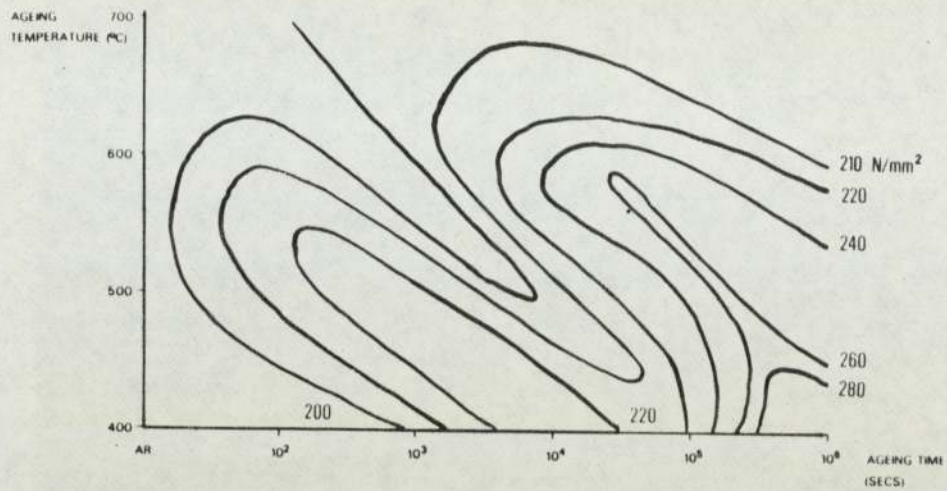

O.7% COBALT + 12% COLD WORK (7b)

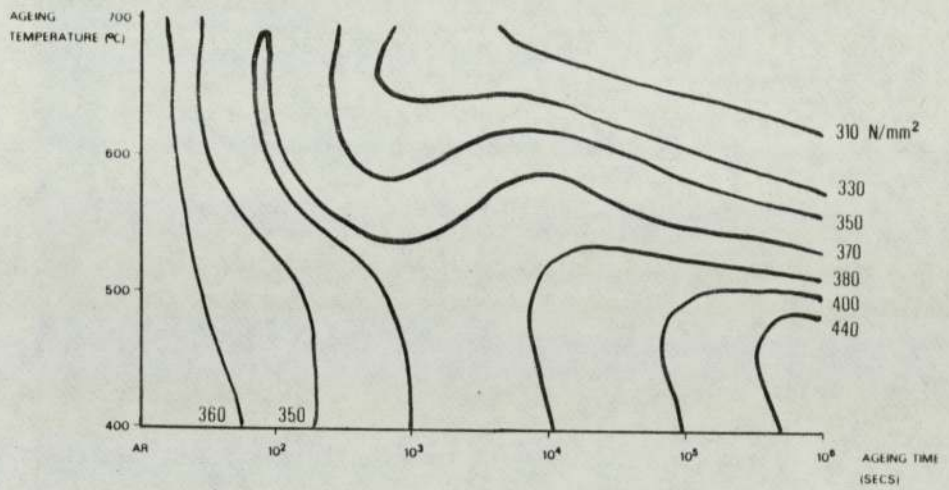

O.7% COBALT + 25% COLD WORK (7c)

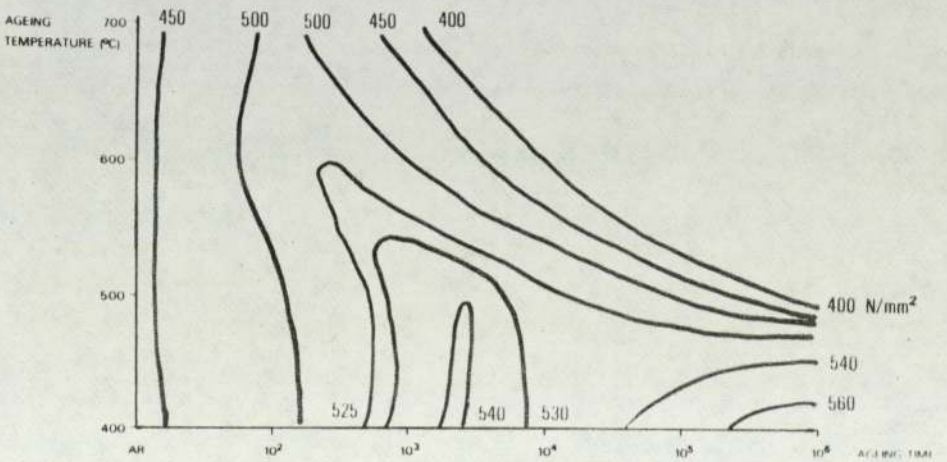

FIG 42 0.2% PROOF STRESS AS A FUNCTION OF AGEING TIME AND TEMPERATURE

1% COBALT SOLUTION TREATED (1a)

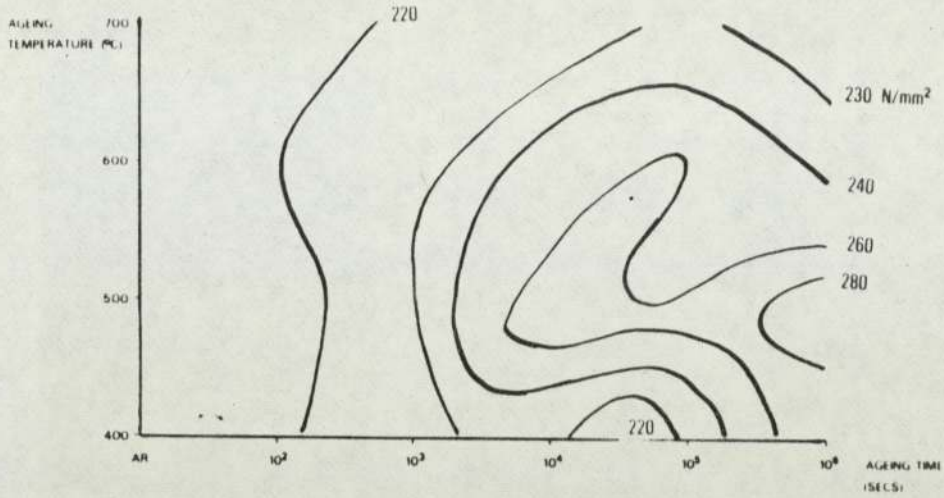

1% COBALT + 12% COLD WORK (1b)

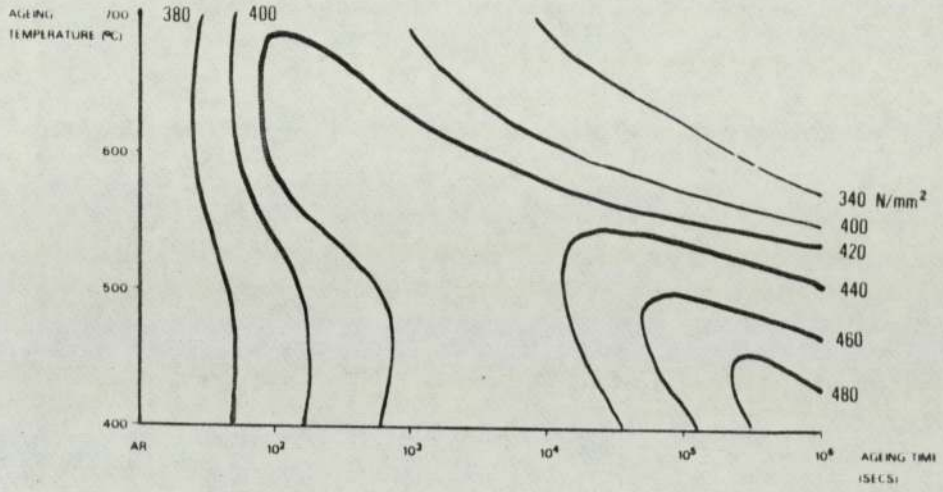

1% COBALT + 25% COLD WORK (1c)

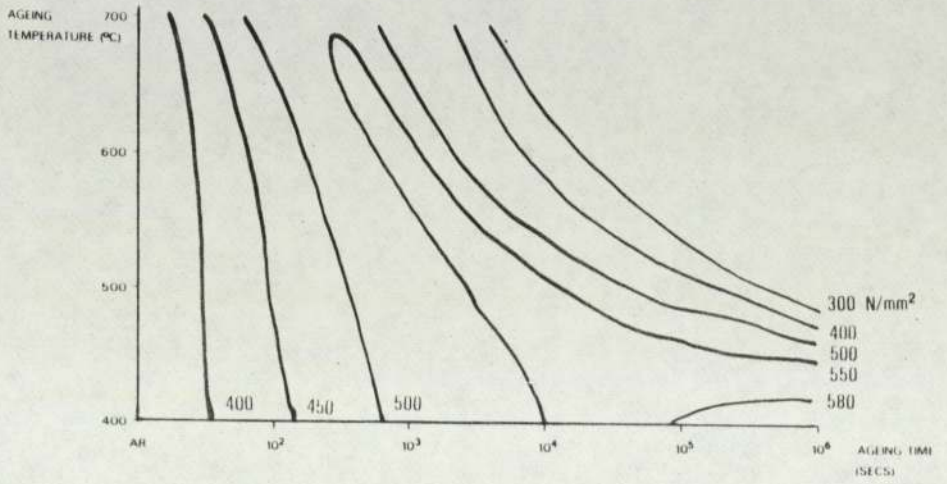

FIG 43. U.T.S. AS A FUNCTION OF AGEING TIME AND TEMPERATURE

0% COBALT SOLUTION TREATED (Oa)

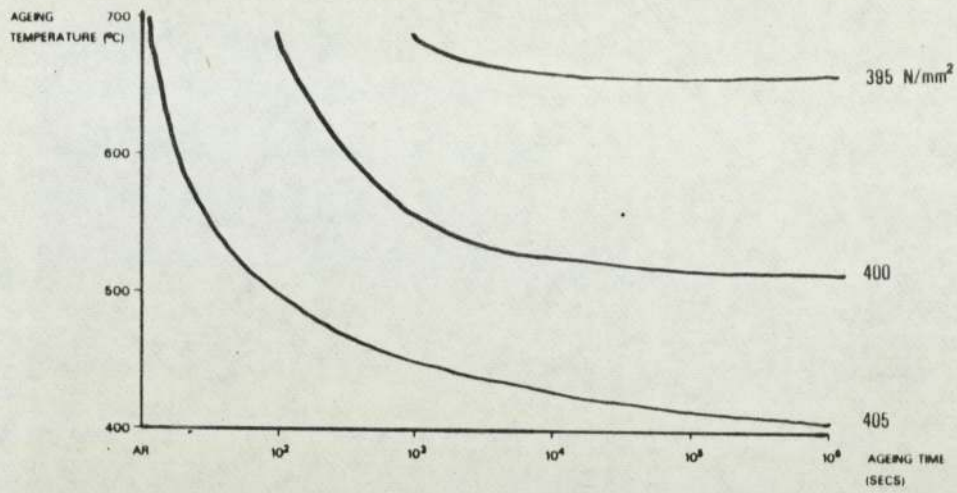

0% COBALT + 12% COLD WORK (Ob)

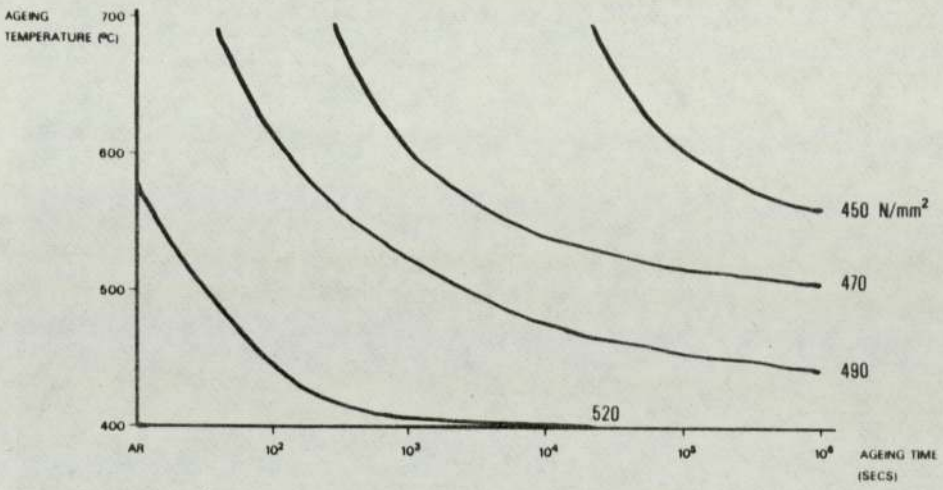

FIG 44. U.T.S. AS A FUNCTION OF AGEING TIME AND TEMPERATURE

0.5% COBALT SOLUTION TREATED (5a)

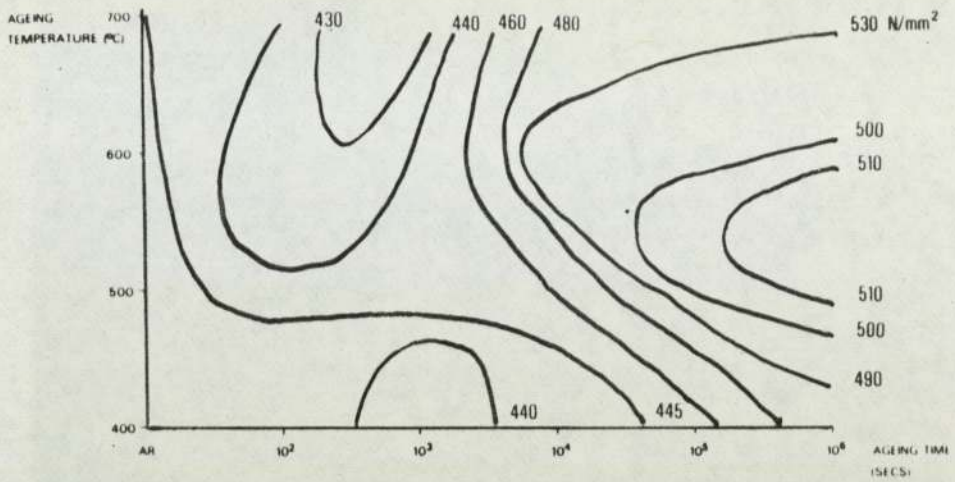

0.5% COBALT + 12% COLD WORK (5b)

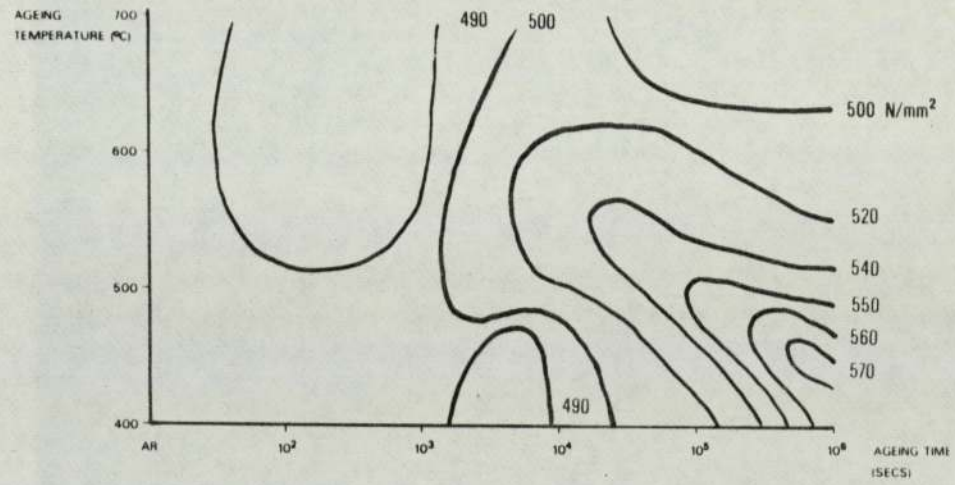

0.5% COBALT + 25% COLD WORK (5c)

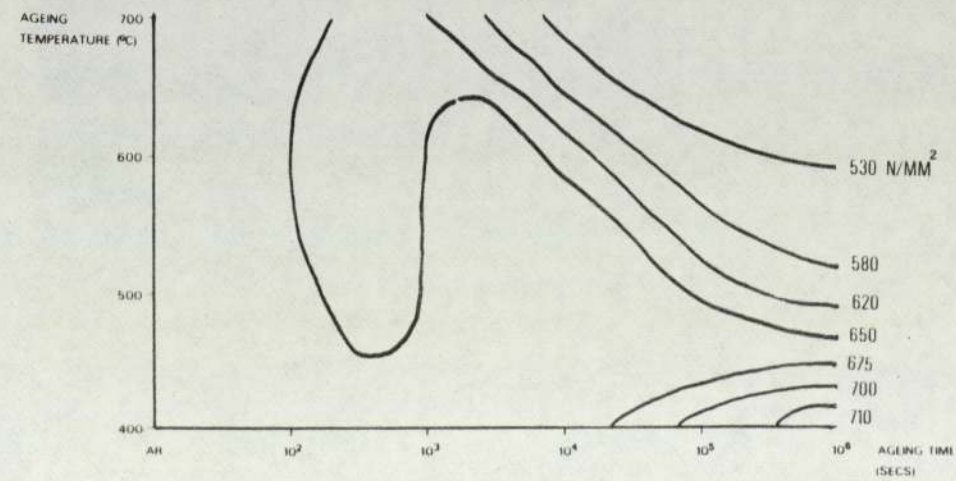

FIG 45. U.T.S. AS A FUNCTION OF AGEING TIME AND TEMPERATURE

0.7% COBALT SOLUTION TREATED (7a)

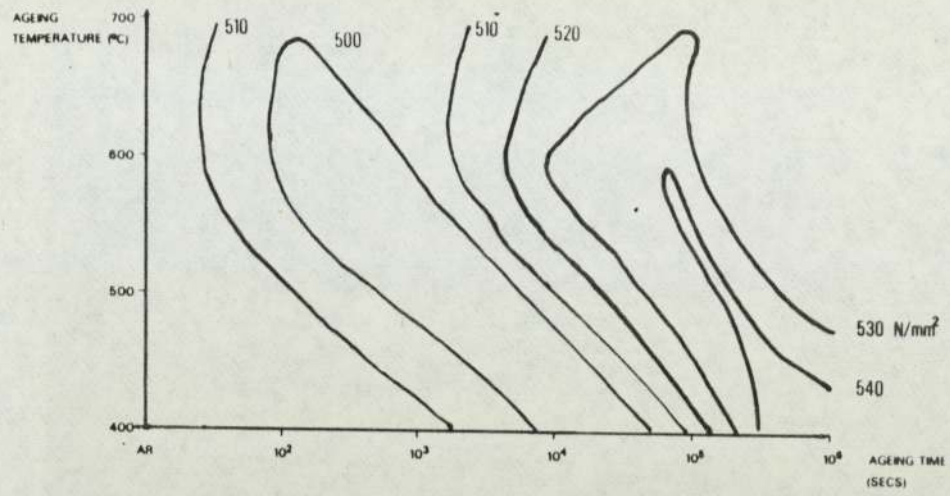

0.7% COBALT + 12% COLD WORK (7b)

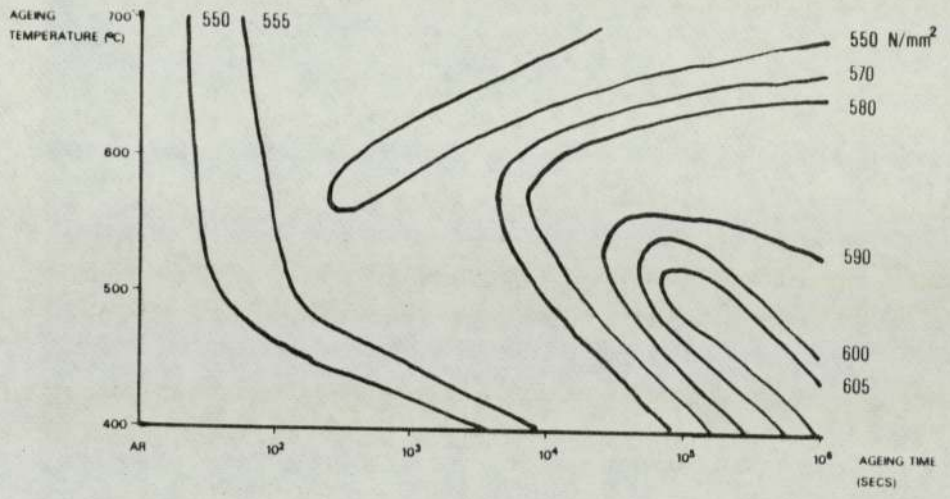

0.7% COBALT + 25% COLD WORK (7c)

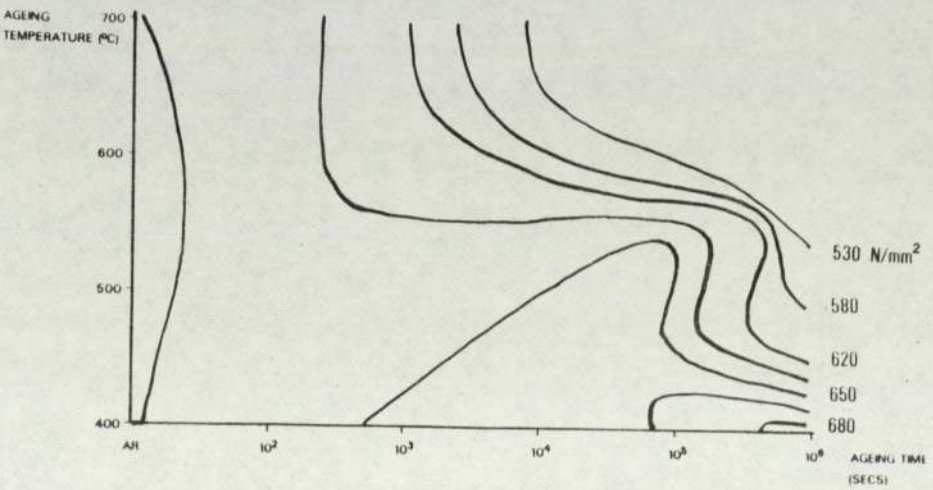

FIG 46. U.T.S. AS A FUNCTION OF AGEING TIME AND TEMPERATURE

1% COBALT SOLUTION TREATED (1a)

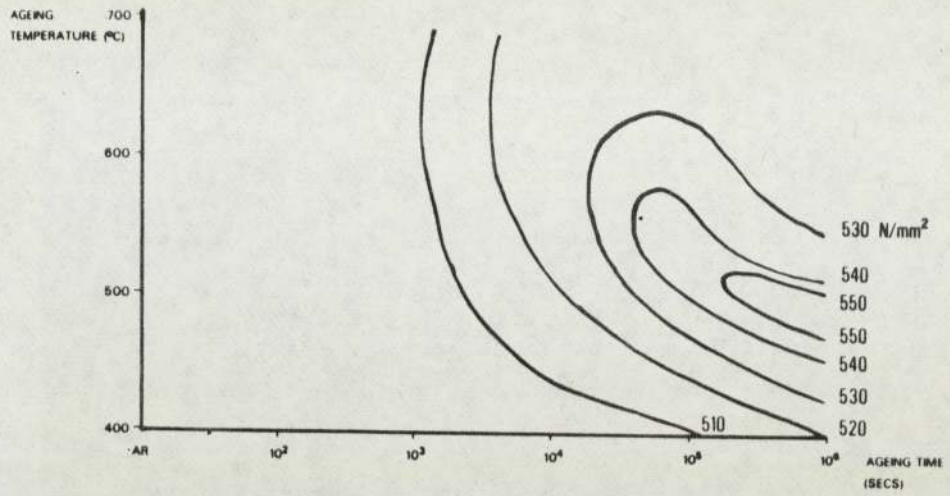

1% COBALT + 12% COLD WORK (1b)

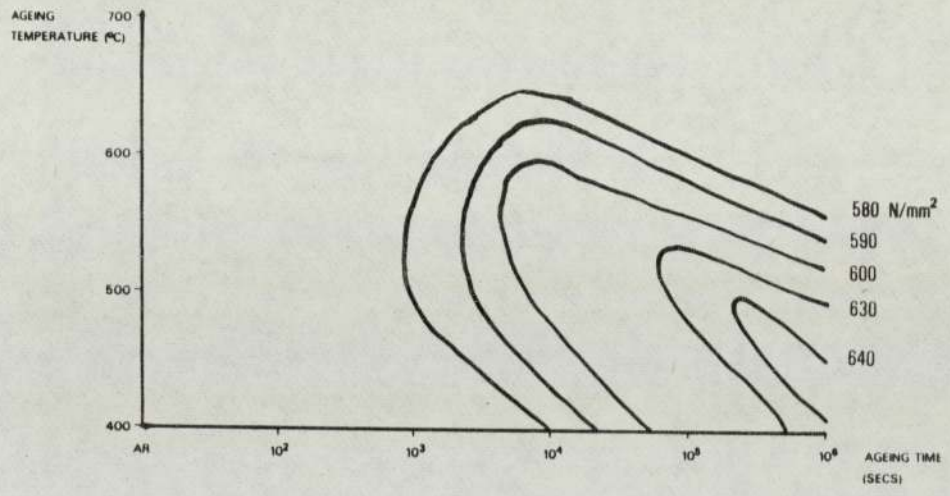

1% COBALT + 25% COLD WORK (1c)

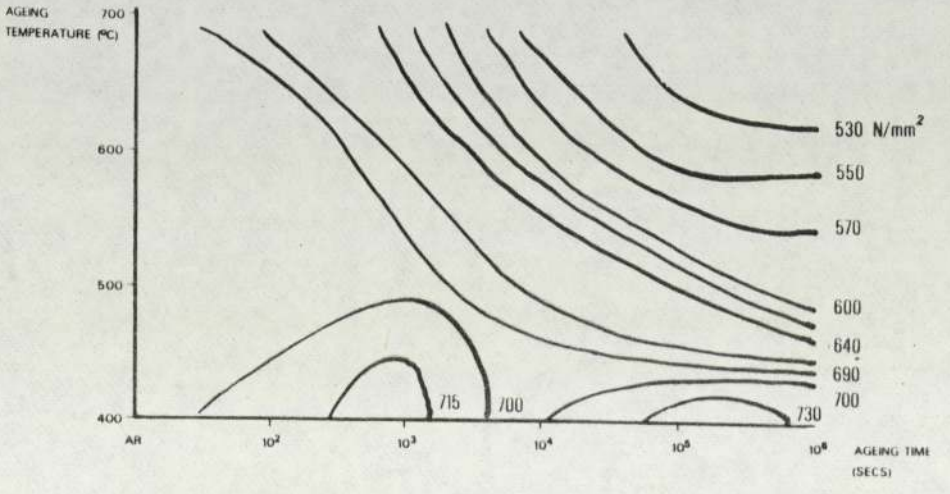

FIG 47. % ELONGATION AS A FUNCTION OF AGEING TIME AND TEMPERATURE

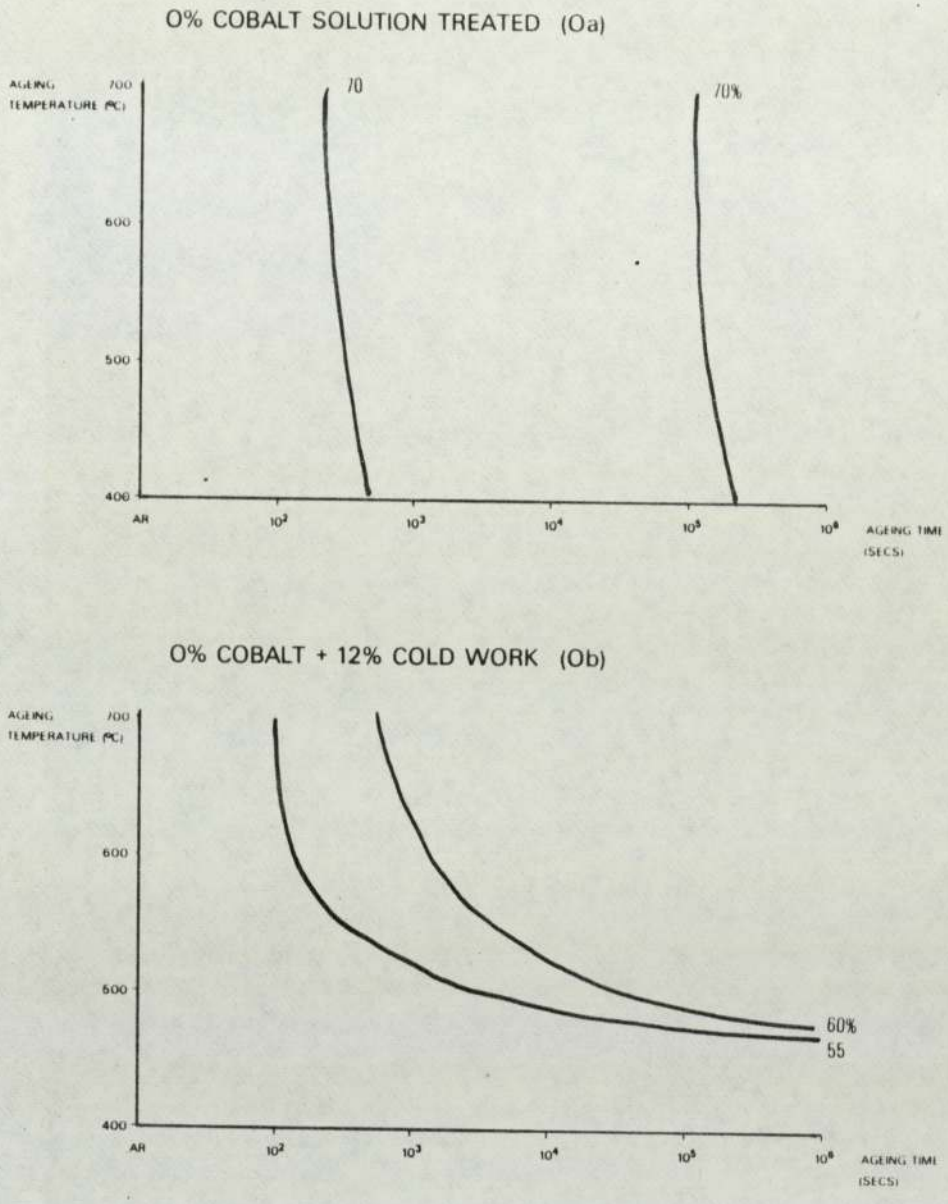

FIG 48. % ELONGATION AS A FUNCTION OF AGEING TIME AND TEMPERATURE

0.5% COBALT SOLUTION TREATED (5a)

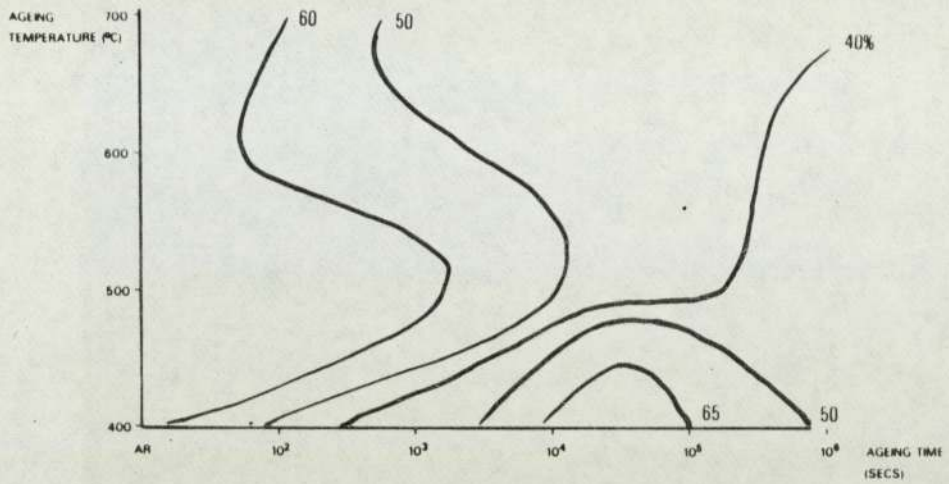

0.5% COBALT + 12% COLD WORK (5b)

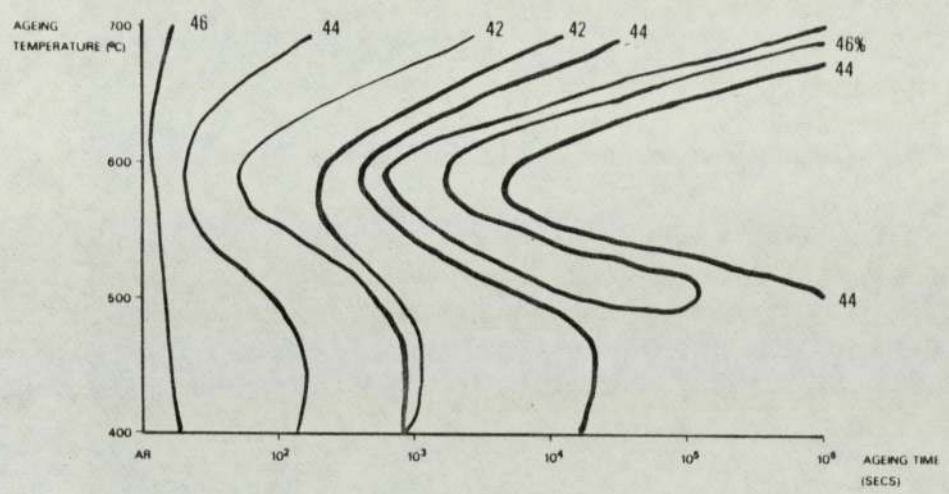

0.5% COBALT + 25% COLD WORK (5c)

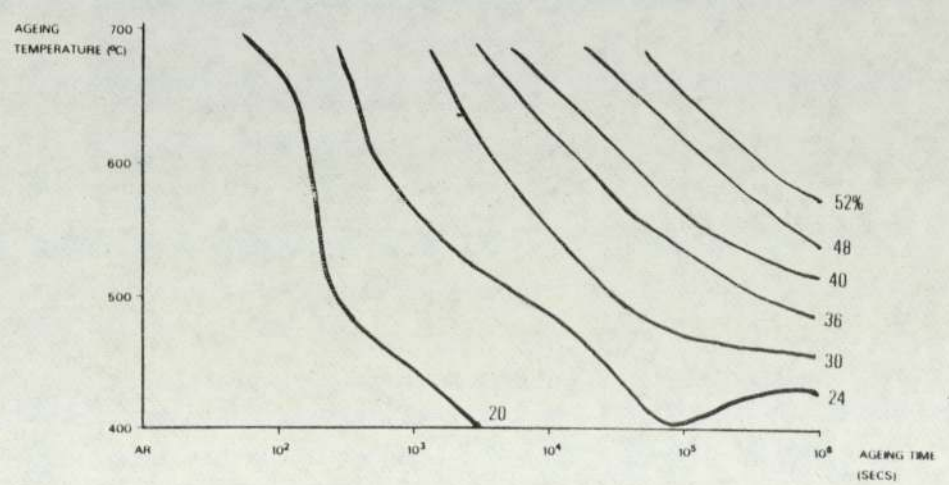

FIG 49. % ELONGATION AS A FUNCTION OF AGEING TIME AND TEMPERATURE

0.7% COBALT SOLUTION TREATED (7a)

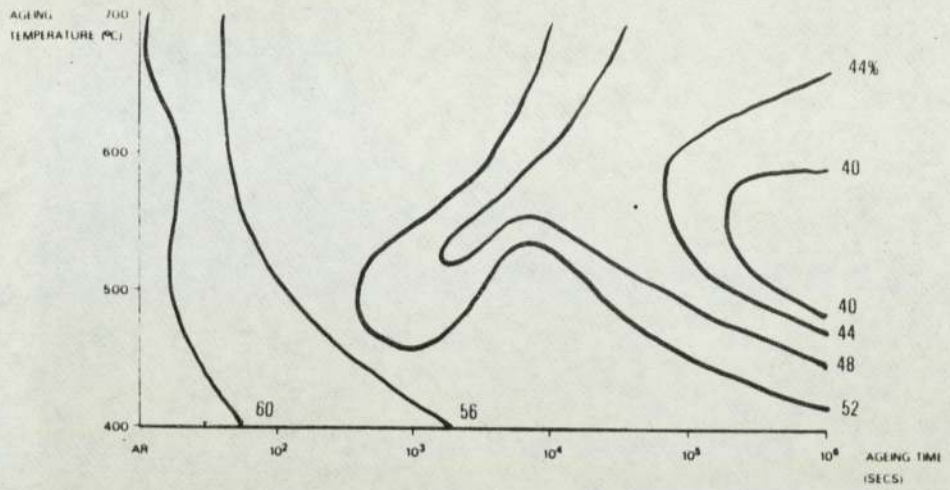

0.7% COBALT + 12% COLD WORK (7b)

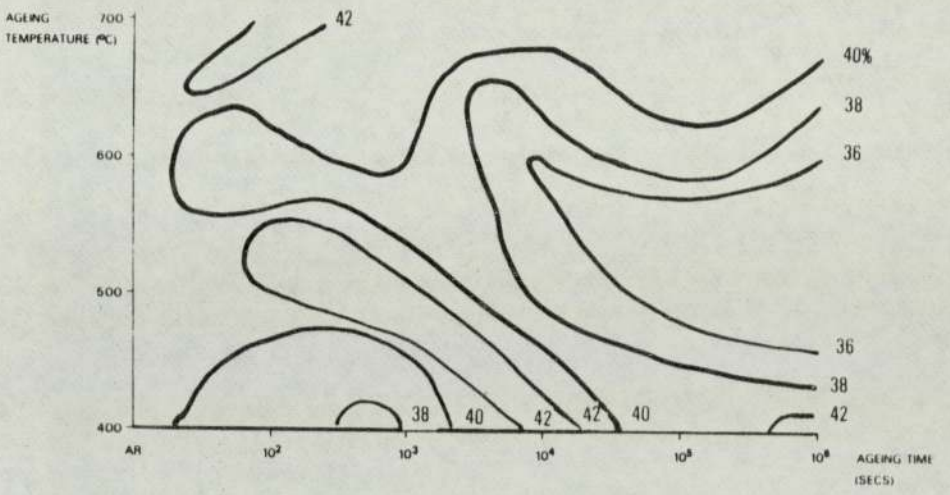

0.7% COBALT + 25% COLD WORK (7c)

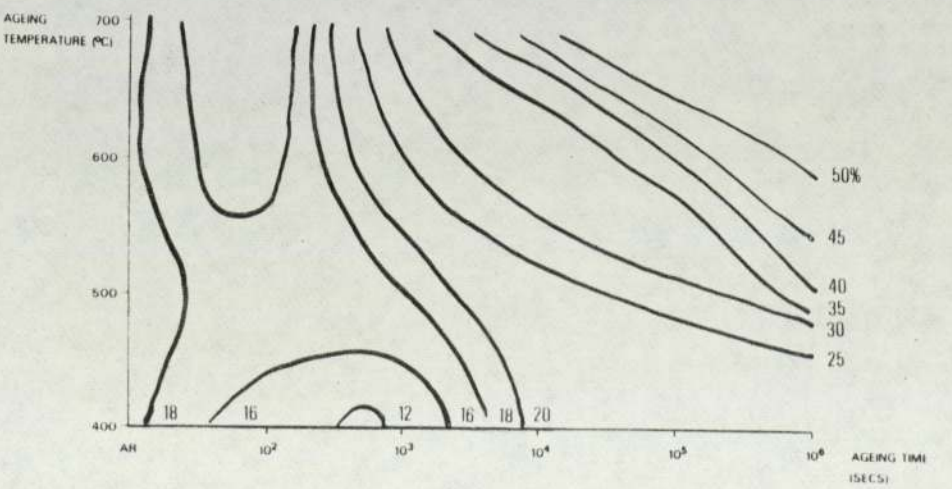

FIG 50. % ELONGATION AS A FUNCTION OF AGEING TIME AND TEMPERATURE

1% COBALT SOLUTION TREATED (1a)

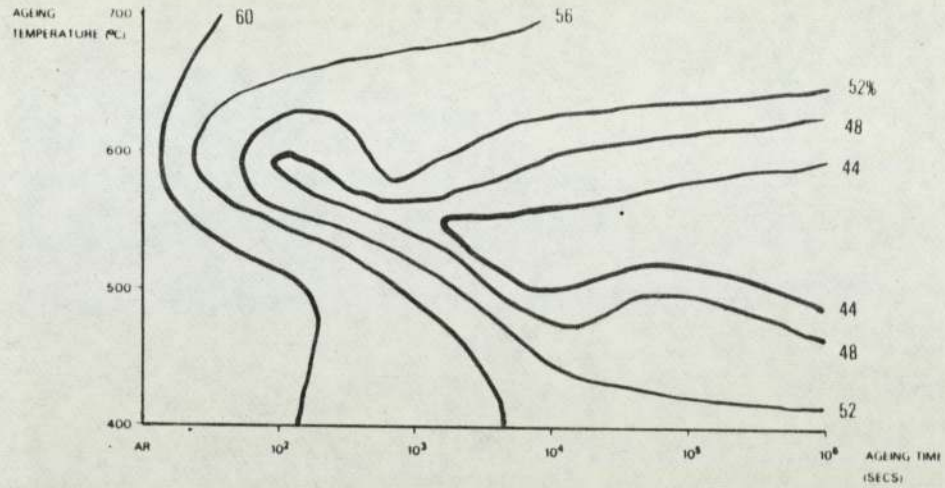

1% COBALT + 12% COLD WORK (1b)

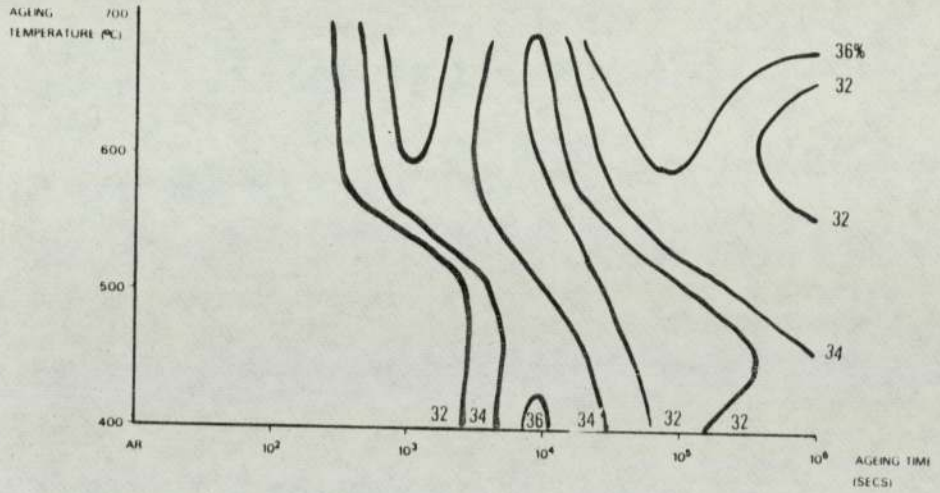

1% COBALT + 25% COLD WORK (1c)

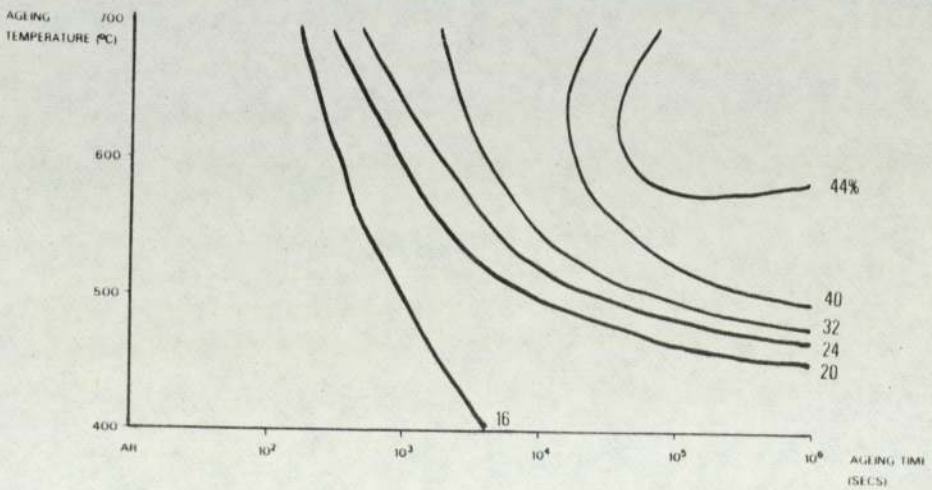

FIG 51. WORK HARDENING EXPONENT n AS A FUNCTION OF AGEING TIME AND TEMPERATURE

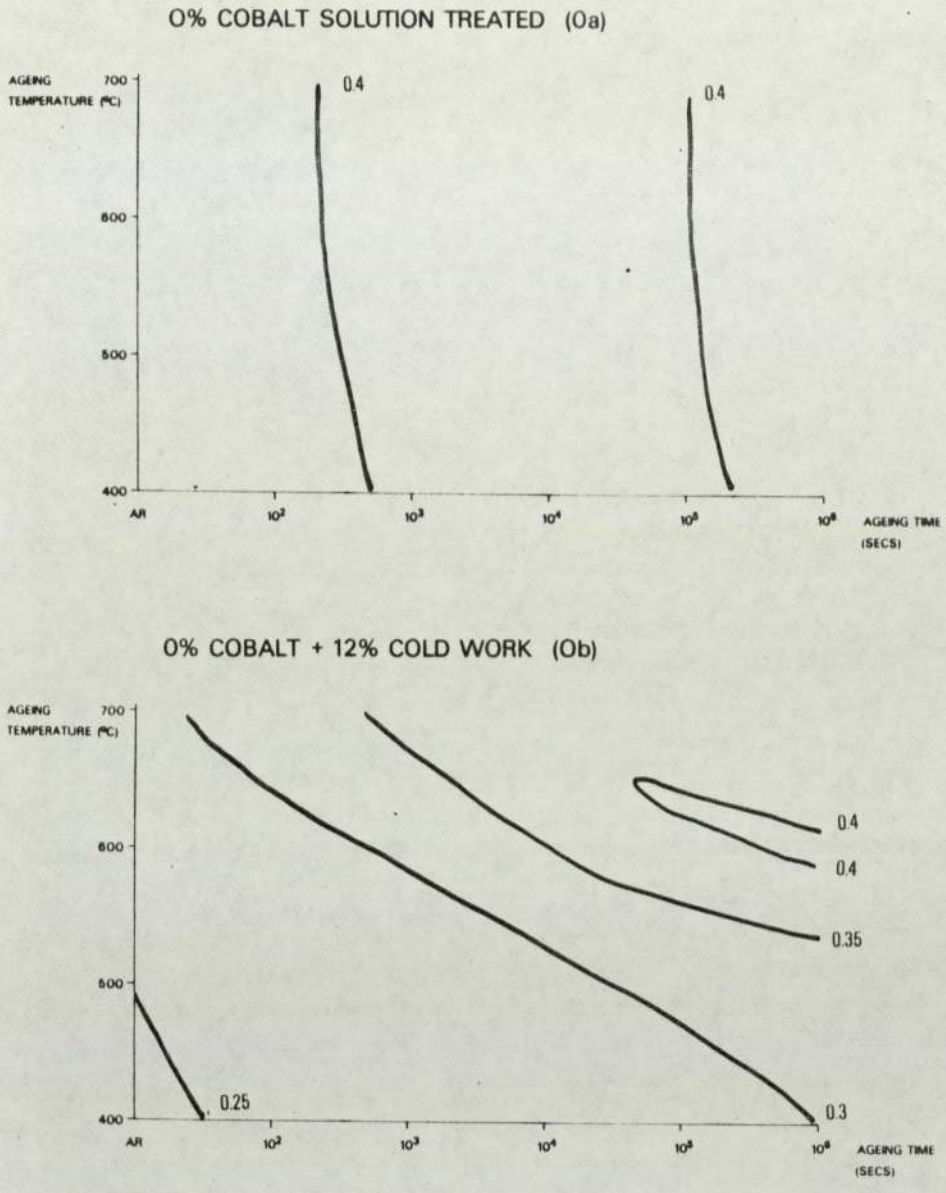

FIG 52. WORK HARDENING EXPONENT n AS A FUNCTION OF AGEING TIME AND TEMPERATURE

0.5% COBALT SOLUTION TREATED (5a)

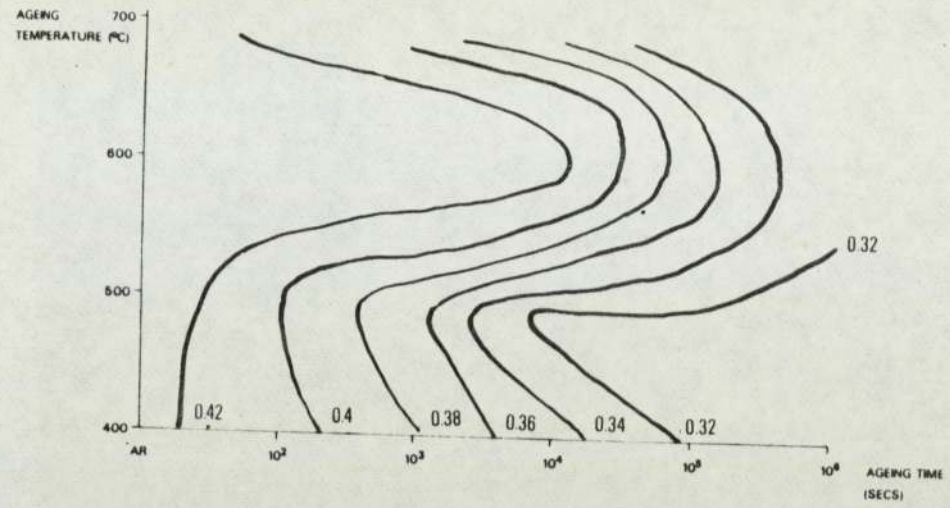

0.5% COBALT + 12% COLD WORK (5b)

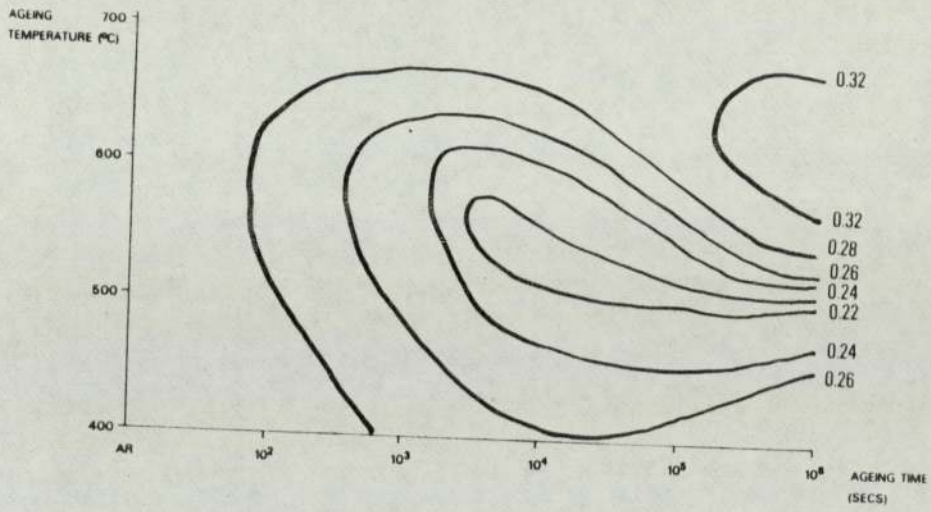

0.5% COBALT + 25% COLD WORK (5c)

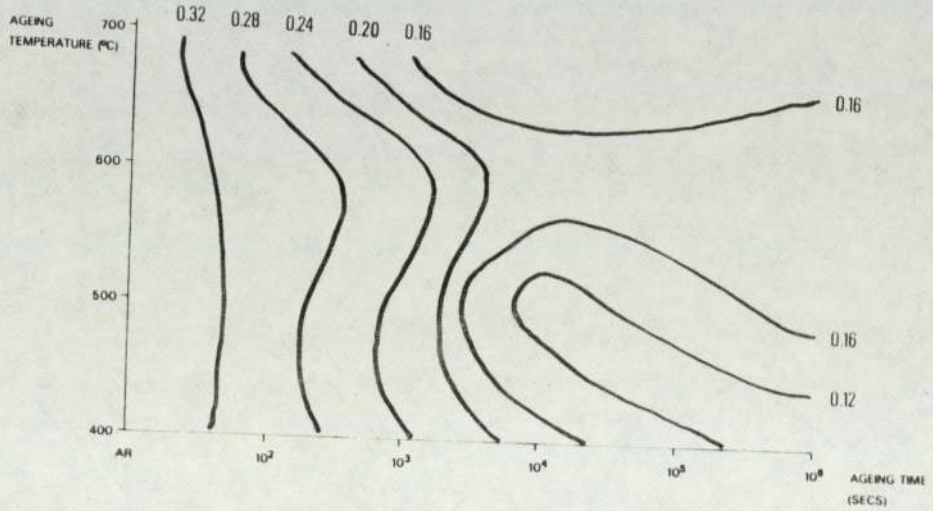

FIG 53. WORK HARDENING EXPONENT n AS A FUNCTION OF AGEING TIME AND TEMPERATURE

0.7% COBALT SOLUTION TREATED (7a)

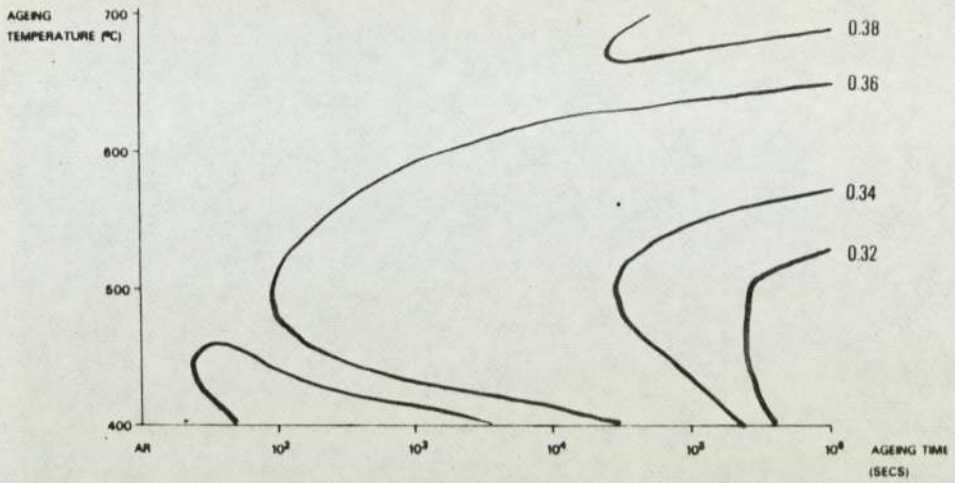

0.7% COBALT + 12% COLD WORK (7b)

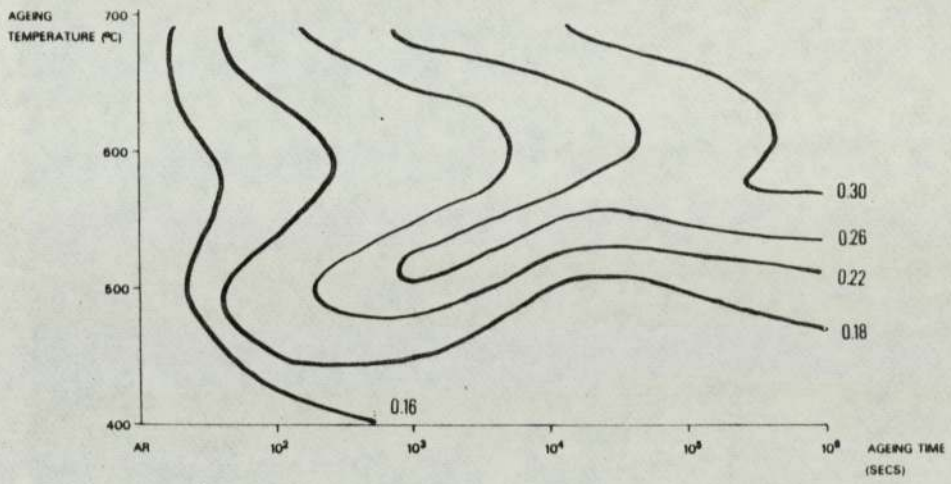

0.7% COBALT + 25% COLD WORK (7c)

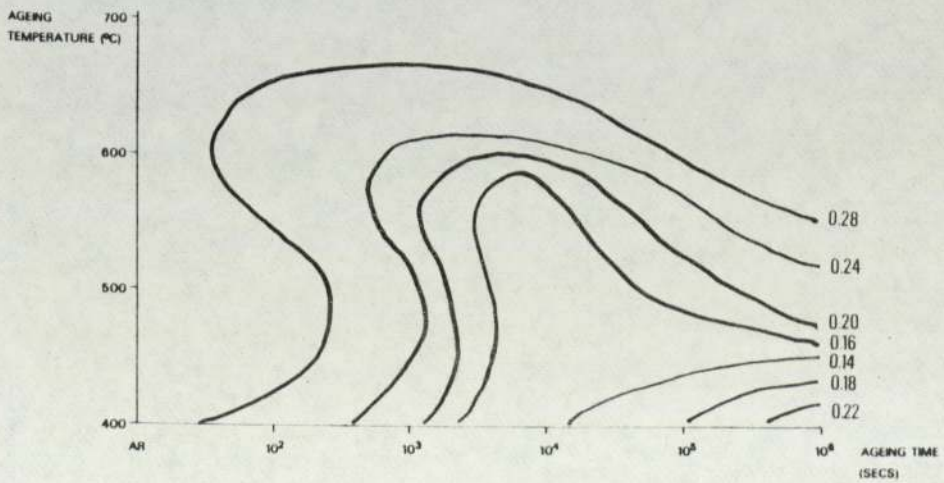

FIG 54. WORK HARDENING EXPONENT n AS A FUNCTION OF AGEING TIME AND TEMPERATURE

1% COBALT SOLUTION TREATED (1a)

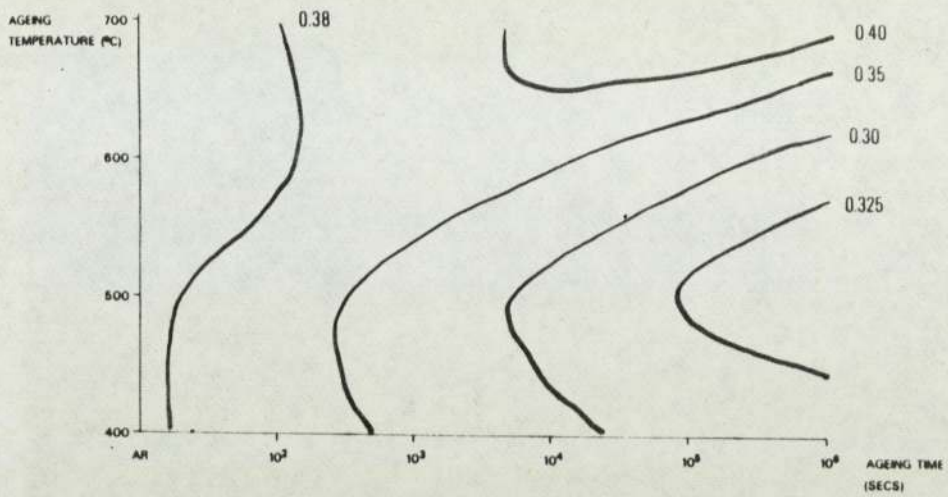

1% COBALT + 12% COLD WORK (1b)

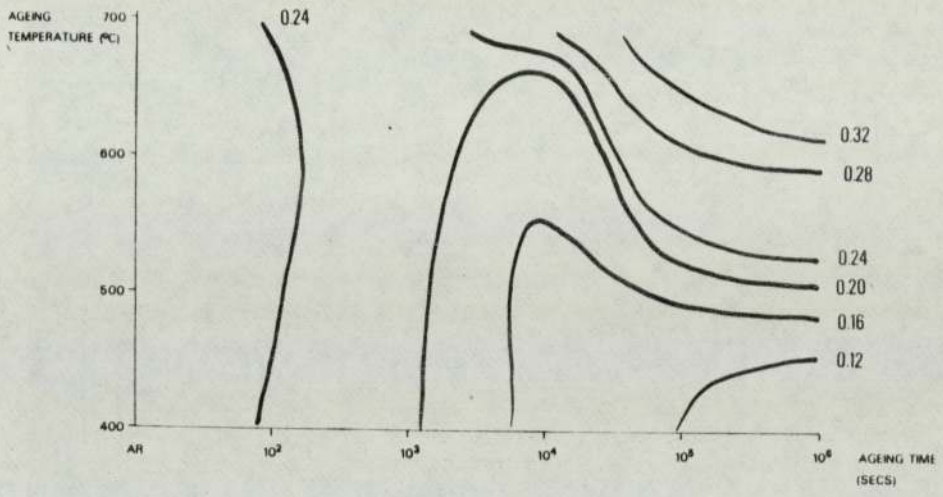

1% COBALT + 25% COLD WORK (1c)

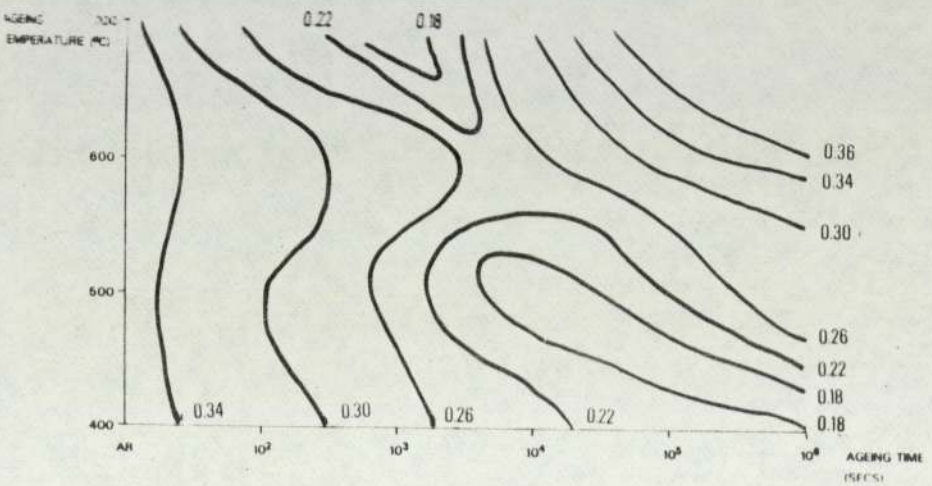

FIG 55. VICKERS HARDNESS AS A FUNCTION OF AGEING TIME AND TEMPERATURE

0% COBALT SOLUTION TREATED (Oa)

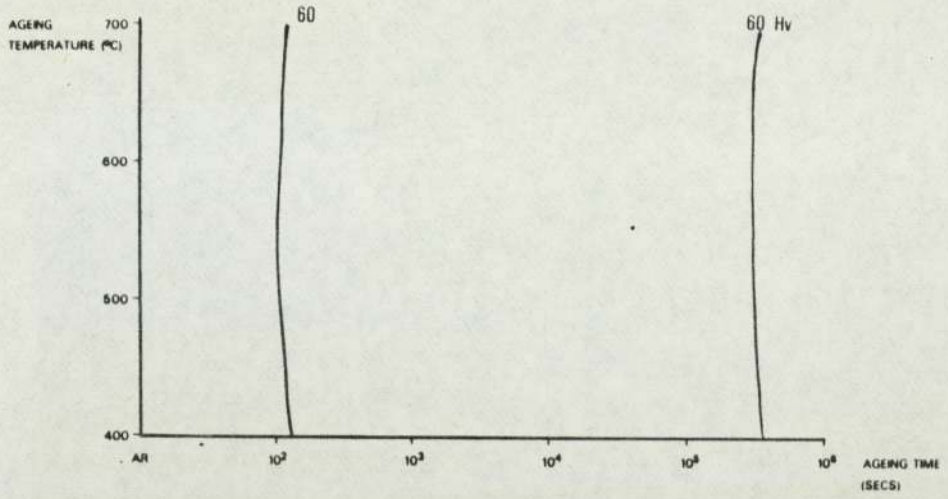

0% COBALT + 12% COLD WORK (Ob)

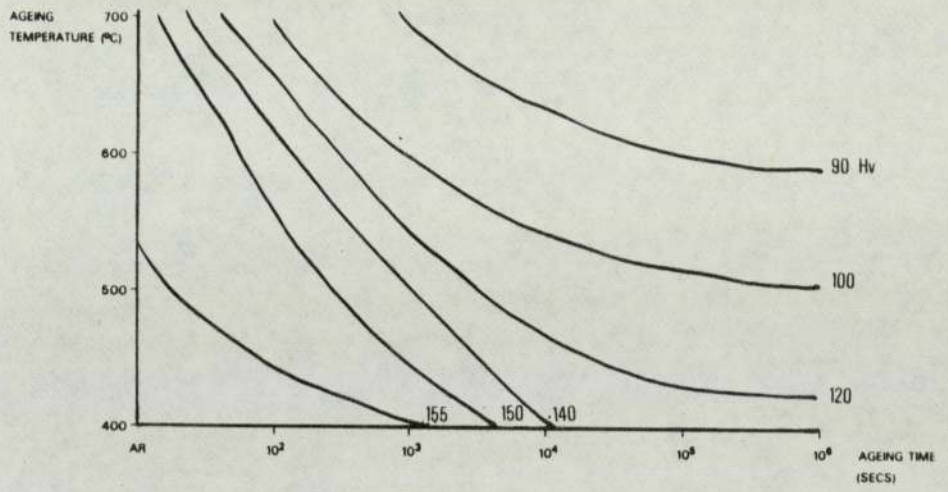

FIG 56. VICKERS HARDNESS AS A FUNCTION OF AGEING TIME AND TEMPERATURE

0.5% COBALT SOLUTION TREATED (5a)

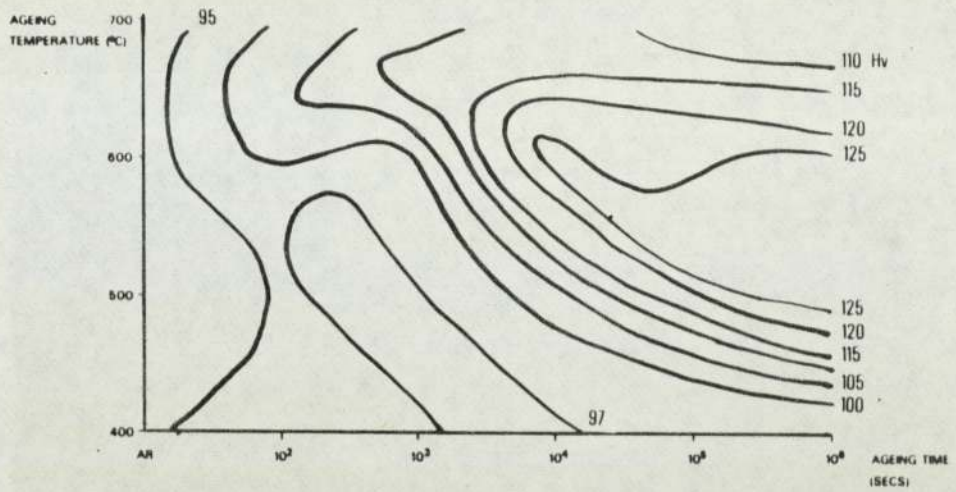

0.5% COBALT + 12% COLD WORK (5b)

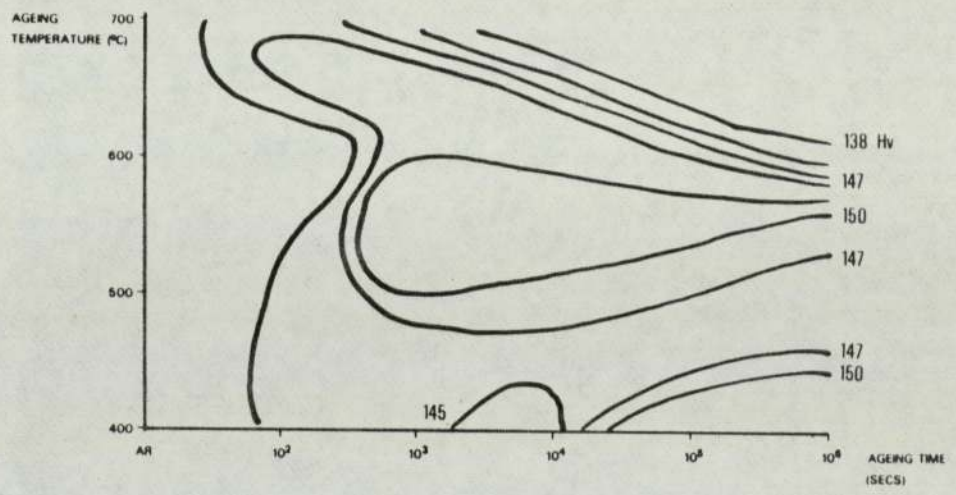

0.5% COBALT + 25% COLD WORK (5c)

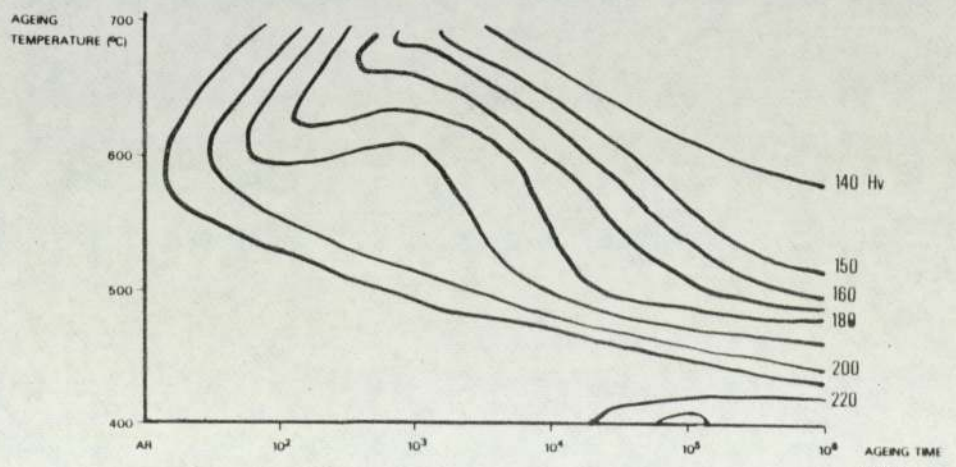

FIG 57. VICKERS HARDNESS AS A FUNCTION OF AGEING TIME AND TEMPERATURE

0.7% COBALT SOLUTION TREATED (7a)

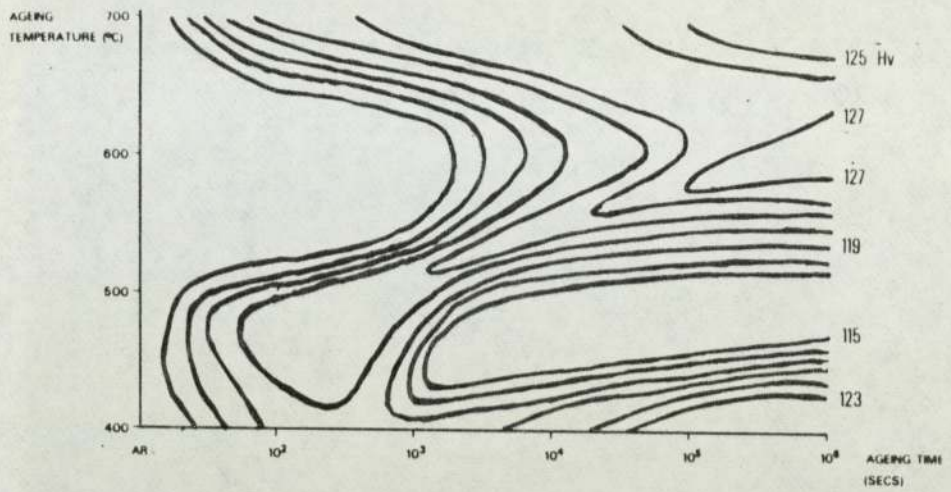

0.7% COBALT + 12% COLD WORK (7b)

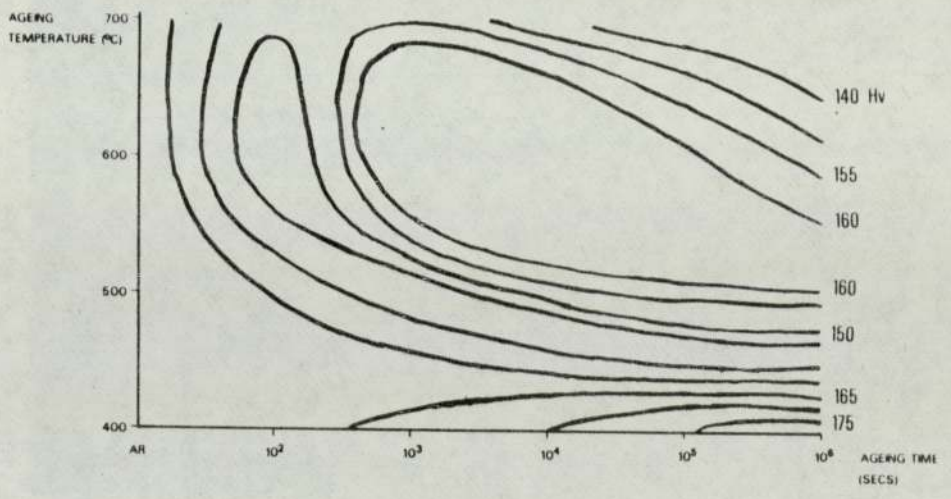

0.7% COBALT + 25% COLD WORK (7c)

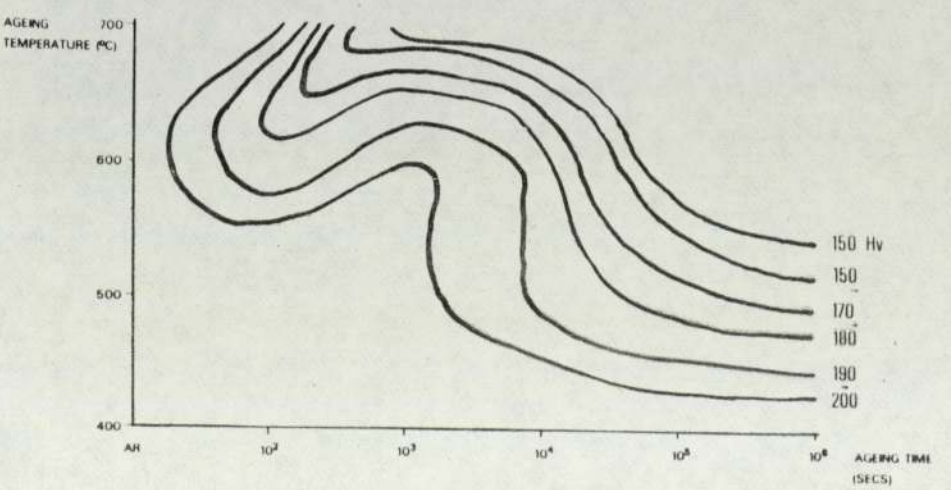

FIG 58. VICKERS HARDNESS AS A FUNCTION OF AGEING TIME AND TEMPERATURE

1% COBALT SOLUTION TREATED (1a)

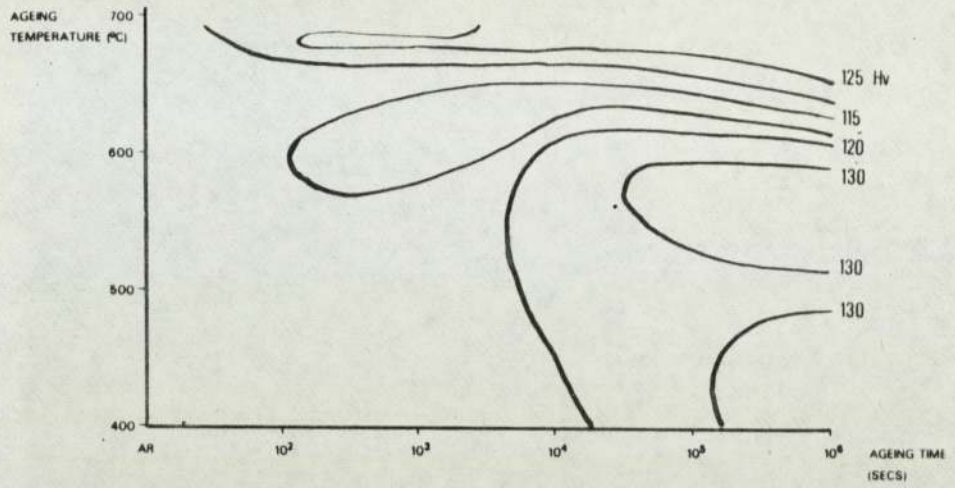

1% COBALT + 12% COLD WORK (1b)

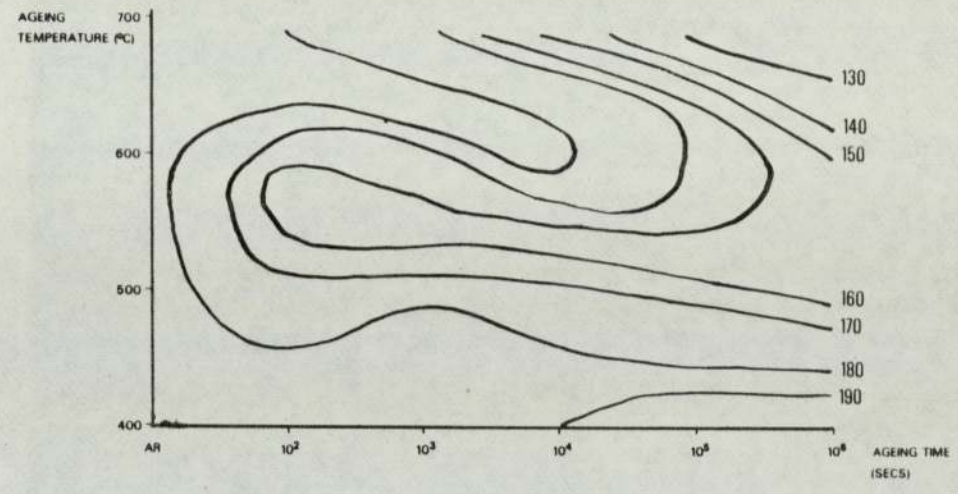

1% COBALT + 25% COLD WORK (1c)

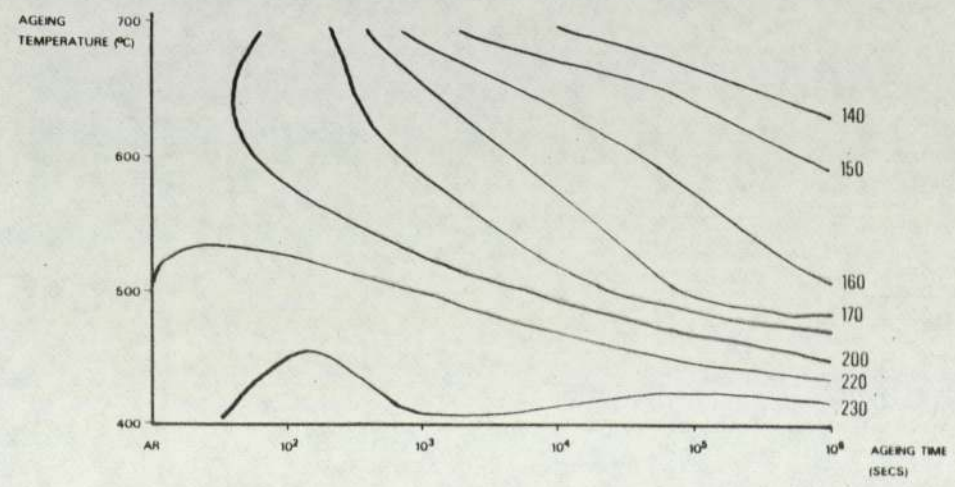

FIG 59 OB 0% Co Solution Treated + 12% Cold Work x304

FIG 60 OB52 Aged 500°C for 10^2 s x304

FIG 61 OB53 Aged 500°C for 10^3 s x304

FIG 62 OB54 Aged 500°C for 10^4 s x304

FIG 63 OB55 Aged 500°C for 10^5 s x304

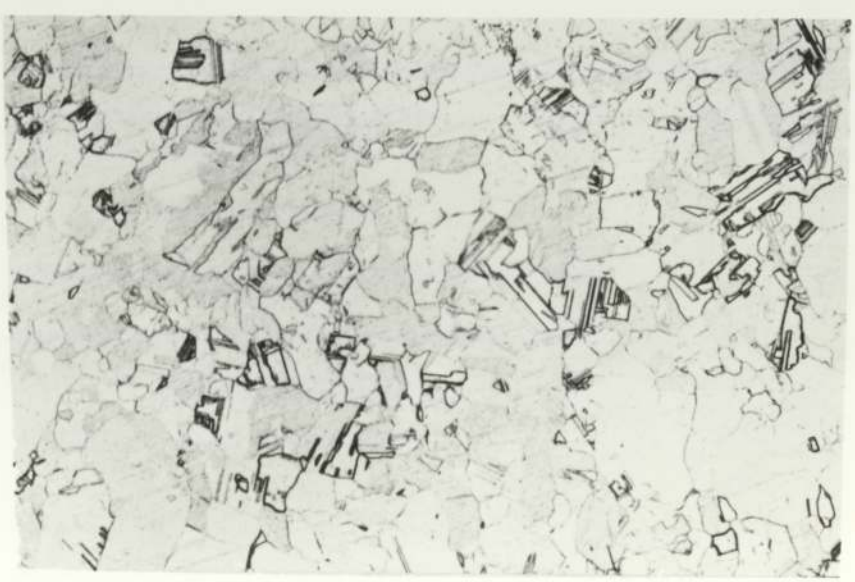

FIG 64 OB56 Aged 500°C for 10^6 s x304

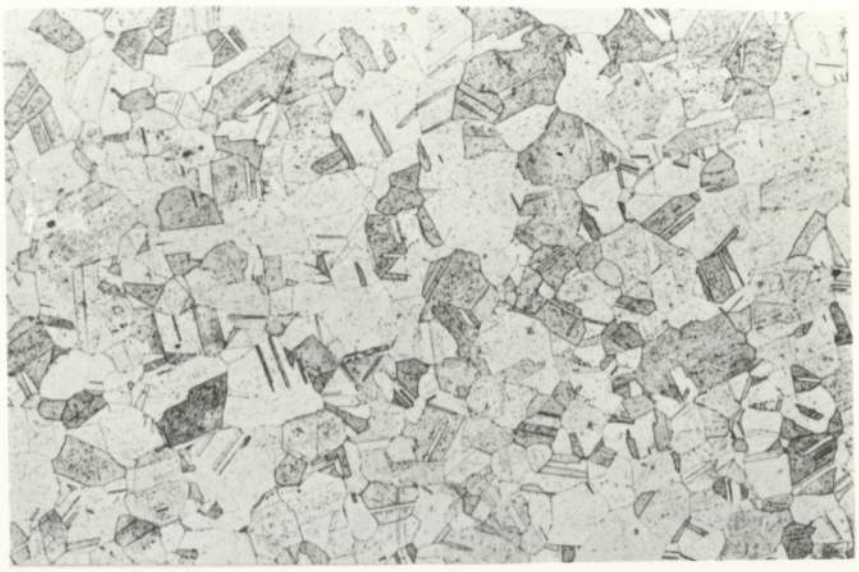

FIG 65 7A 0.7% Co Solution Treated ×304

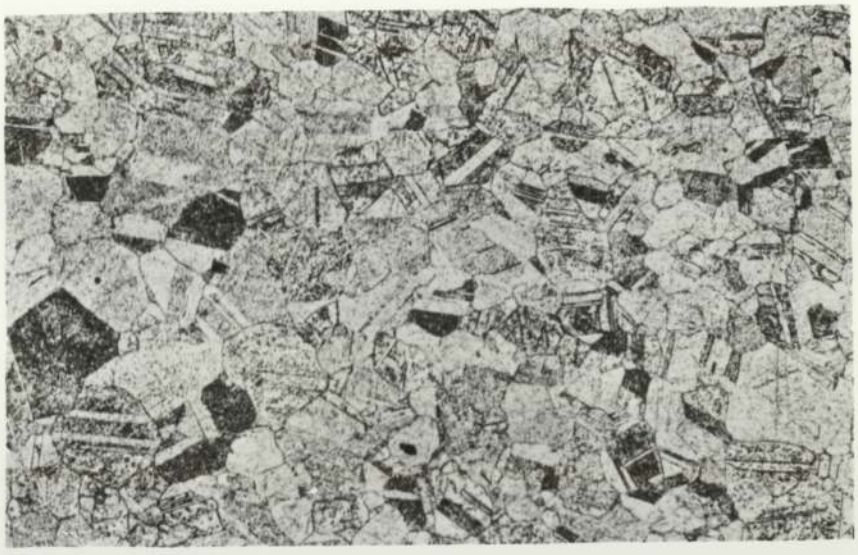

FIG 66 7A52 Aged 500°C for 10^2 s x304

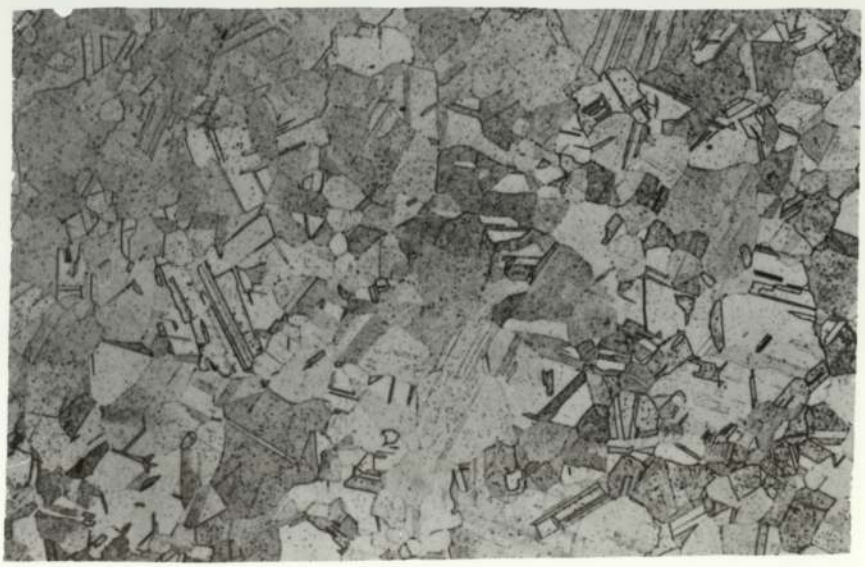

FIG 67 7A53 Aged 500°C for 10^3 s ×304

FIG 68 7A54 Aged 500°C for 10^4 s x304

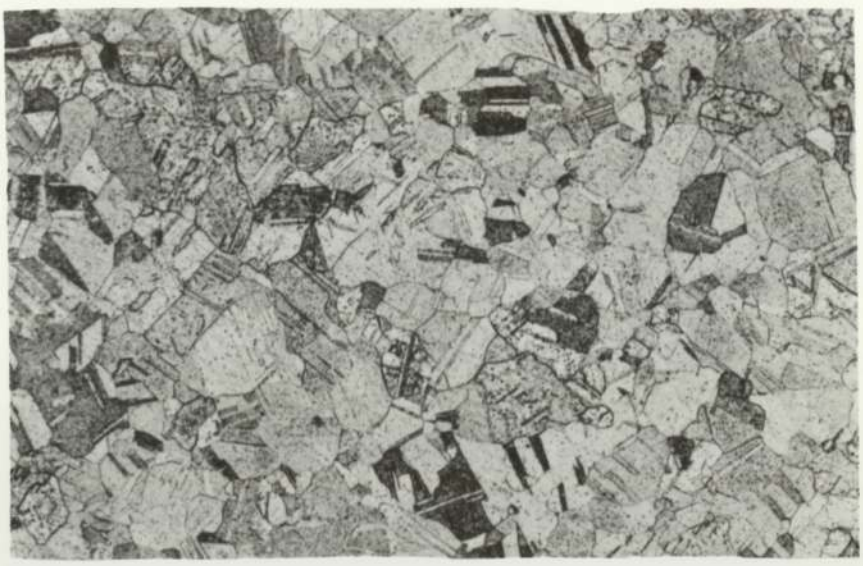

FIG 69 7A55 Aged 500°C for 10^5 s x304

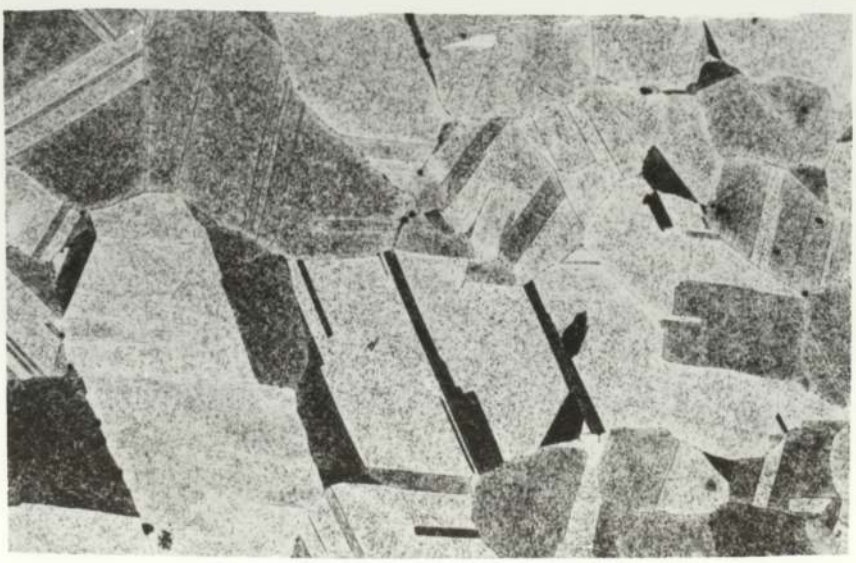

FIG 70 7A56 Aged 500°C for 10^6 s x304

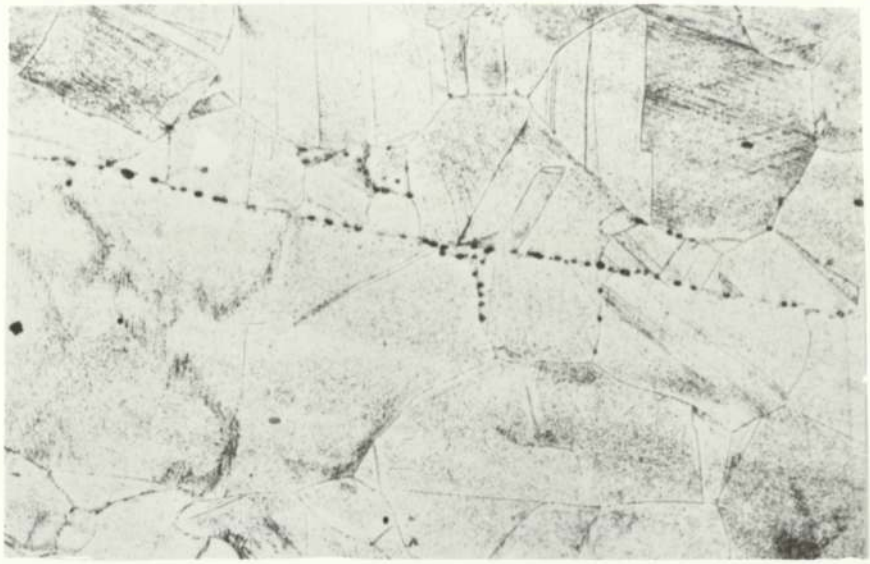

FIG 71 7B 0.7% Co Solution Treated x304

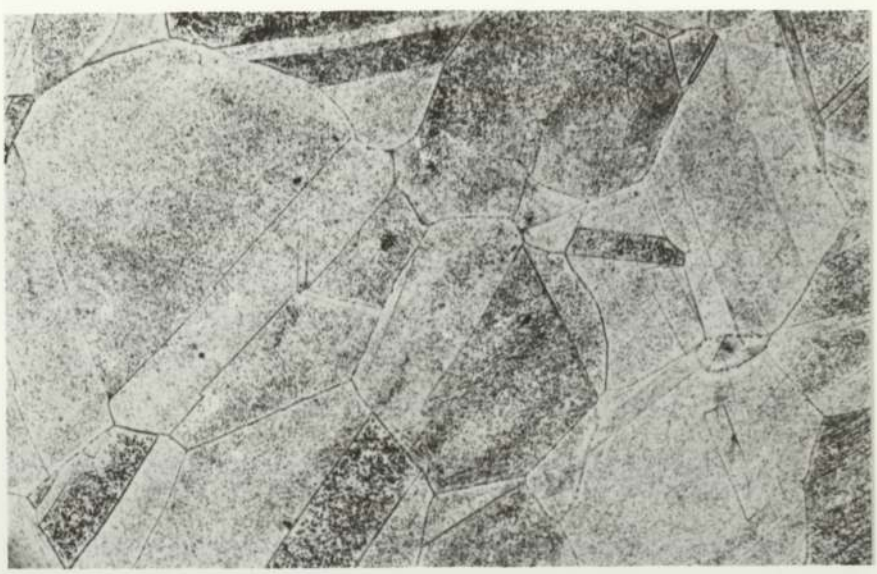

FIG 72 7B52 Aged 500°C for 10^2 s x304

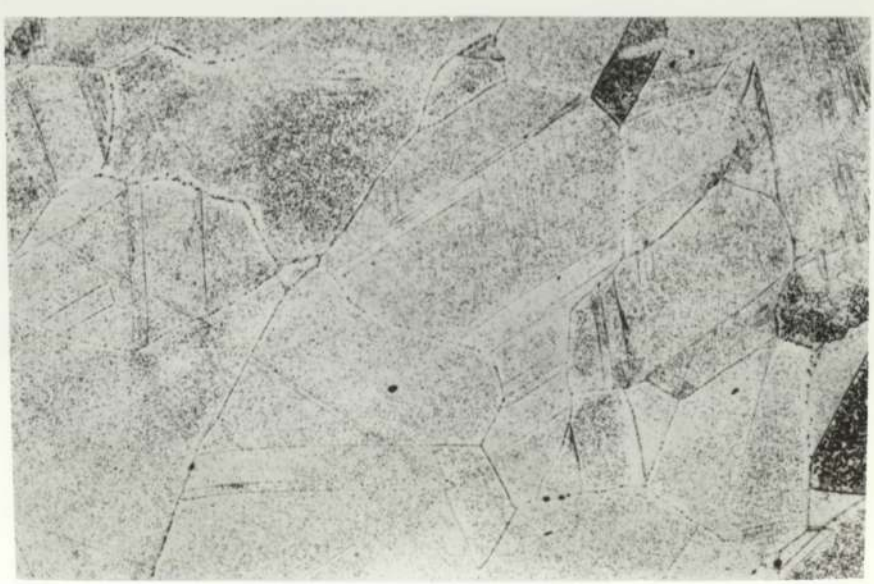

FIG 73 7B53 Aged 500°C for 10^3 s x304

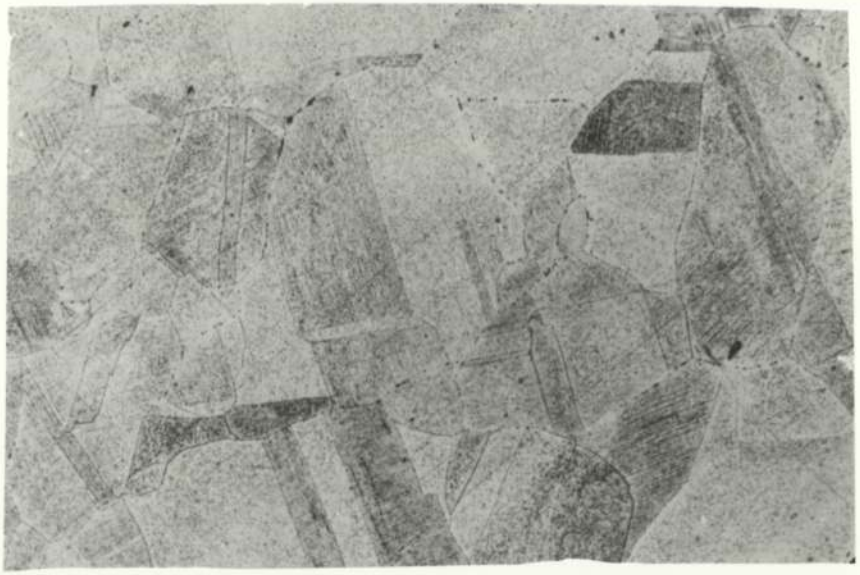

FIG 74 7B54 Aged 500°C for 10^4 s x304

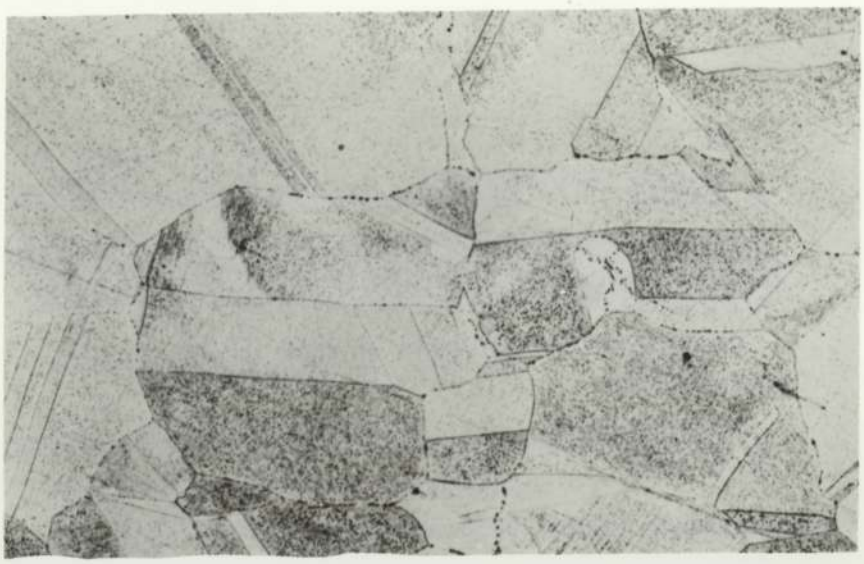

FIG 75 7B55 Aged 500°C for 10^5 s x304

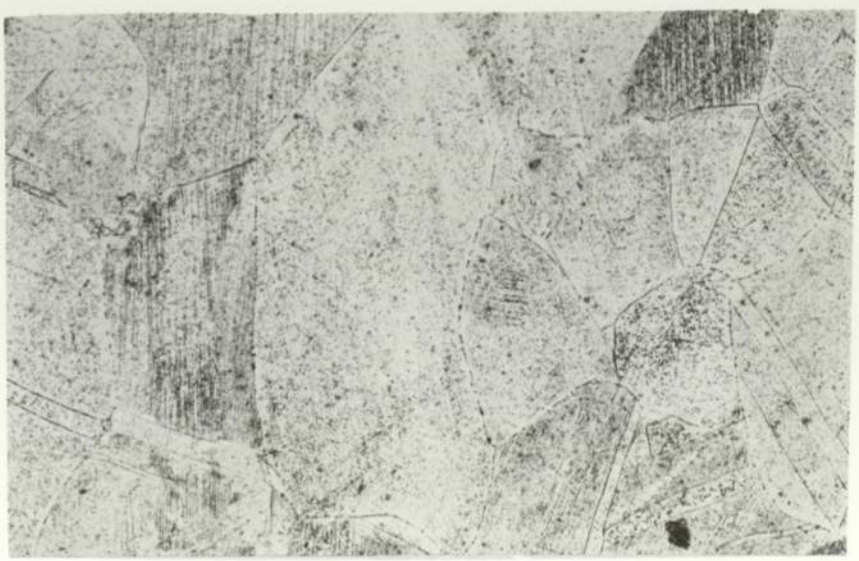

FIG 76 7B56 Aged 500°C for 10^6 s x304

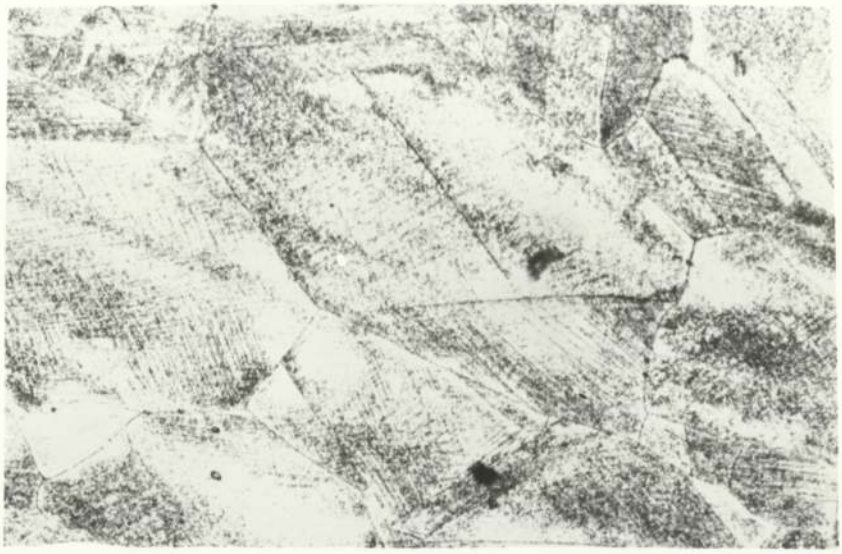

FIG 77 7C 0.7% Co Solution Treated + 25% Cold Work x304

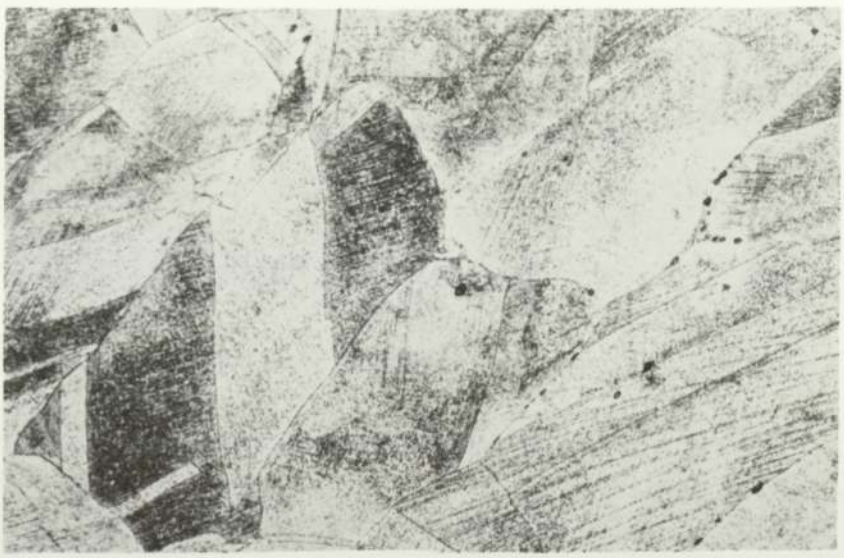

FIG 78 7C52 Aged 500°C for 10^2 s x304

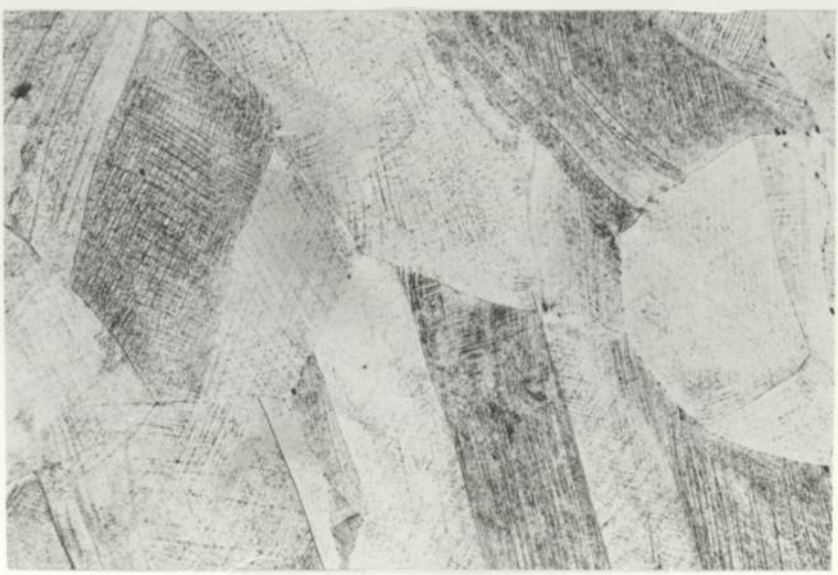

FIG 79 7C53 Aged 500°C for 10^3 s x304

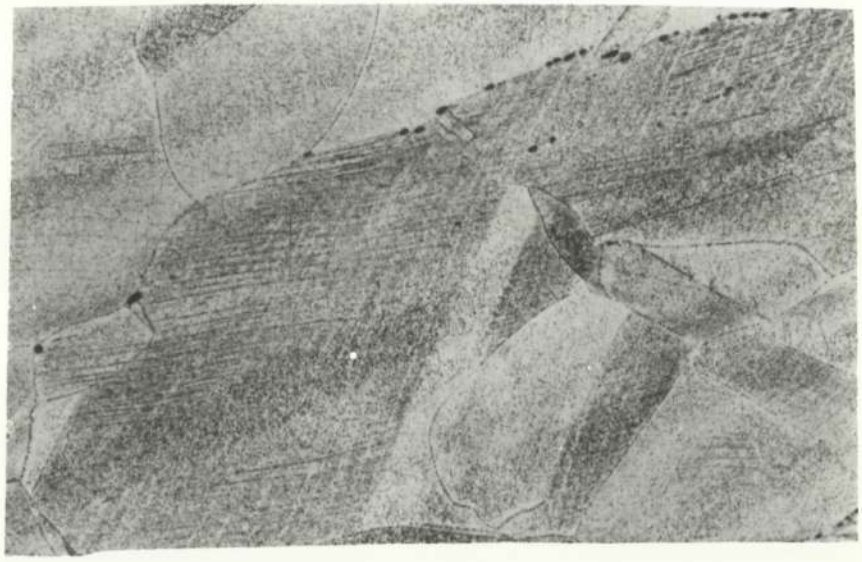

FIG 80 7C54 Aged 500°C for 10^4 s x304

FIG 81 7C55 Aged 500°C for 10^5 s x304

FIG 82 7C56 Aged 500°C for 10^6 s x304

FIG 83 7A 0.7% Co Solution Treated x2200

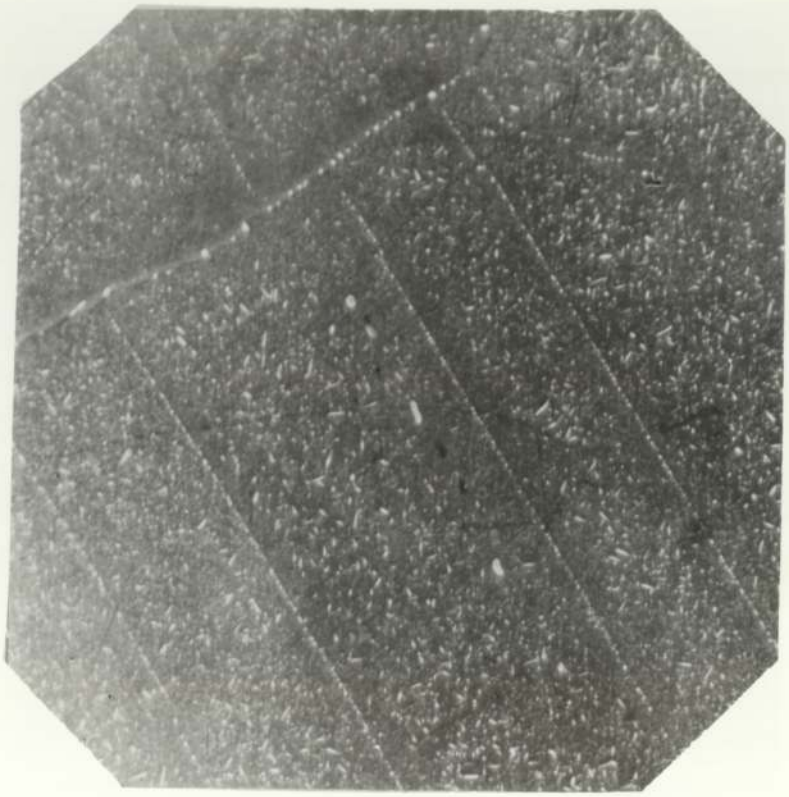

FIG 84 7A56 0.7% Co Solution Treated + Aged 500°C for 10^6 s x1500

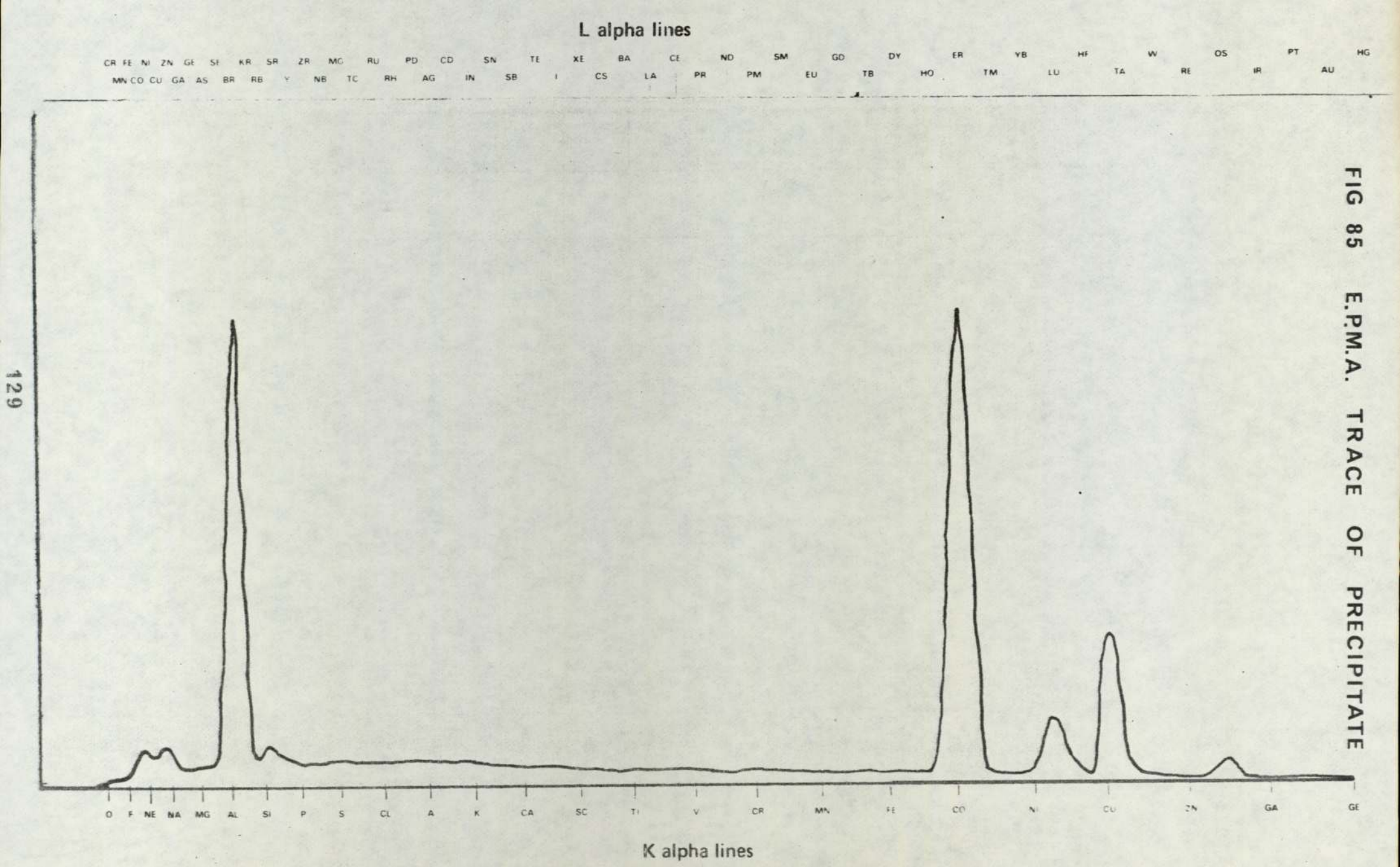

FIG 85 E.P.M.A. TRACE OF PRECIPITATE

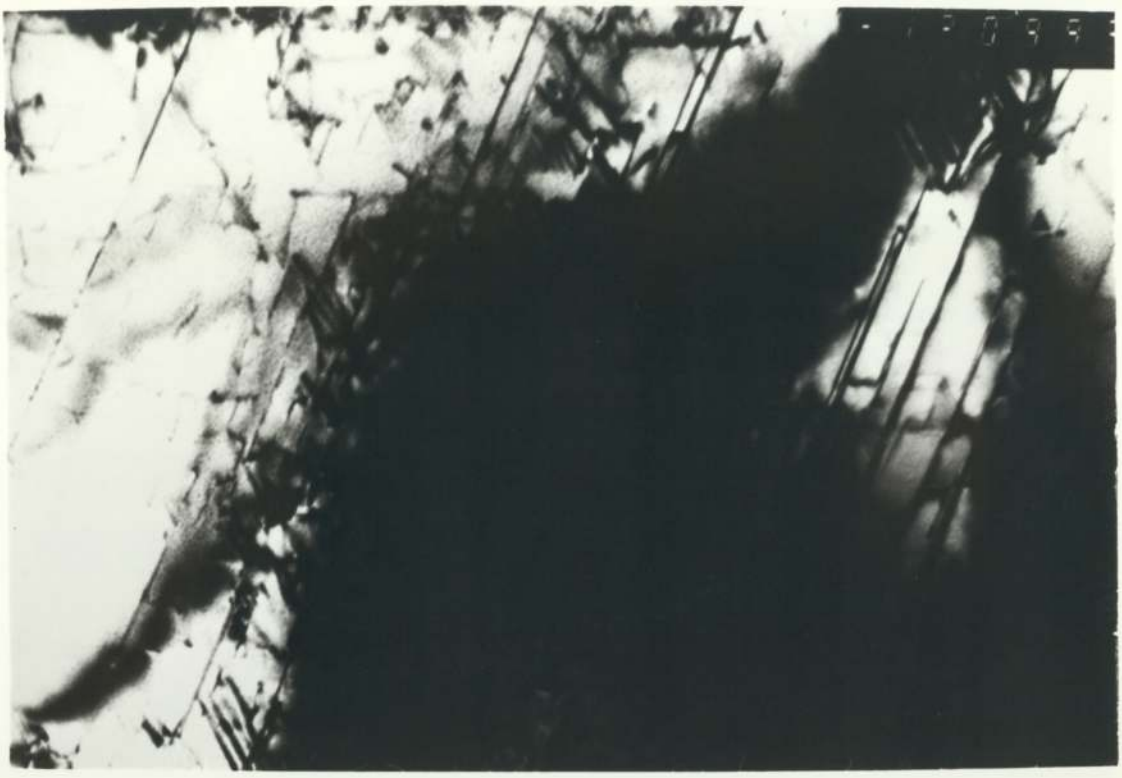

FIG 86 7A Bright Field x80k

FIG 87 7A Bright Field x120k

FIG 88 7C Bright Field x60k

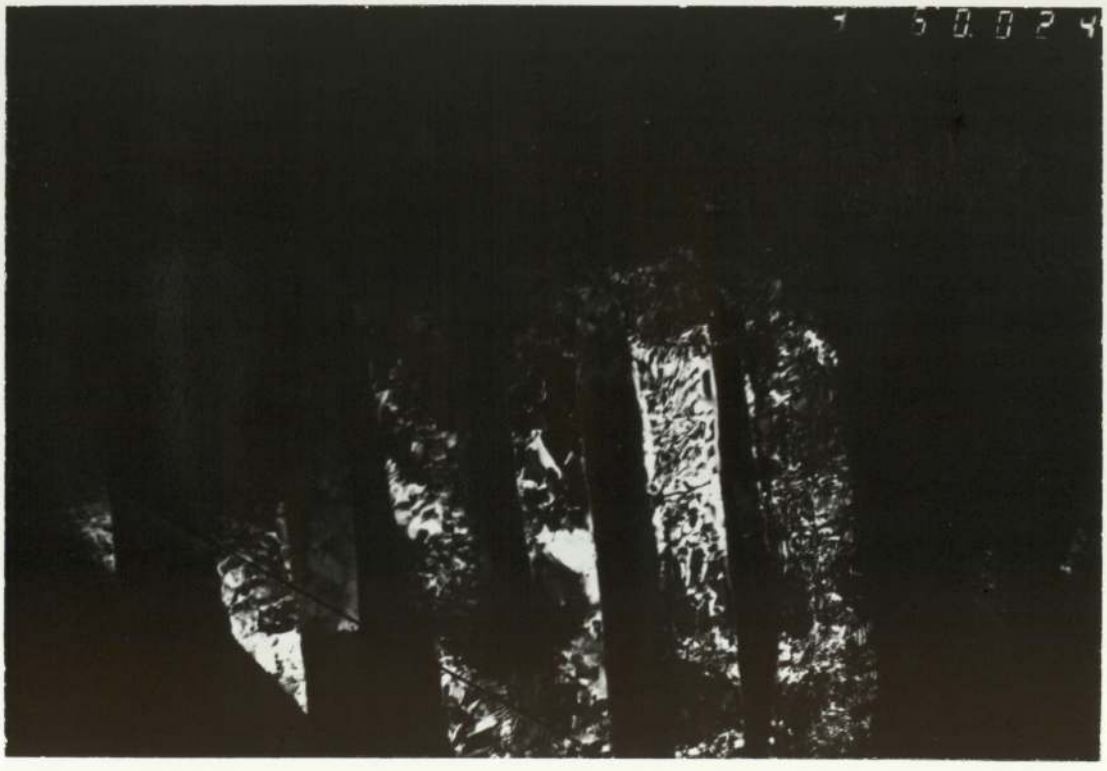

FIG 89 7C Centered Dark Field of Fig 88 (from (T11) M) x60k

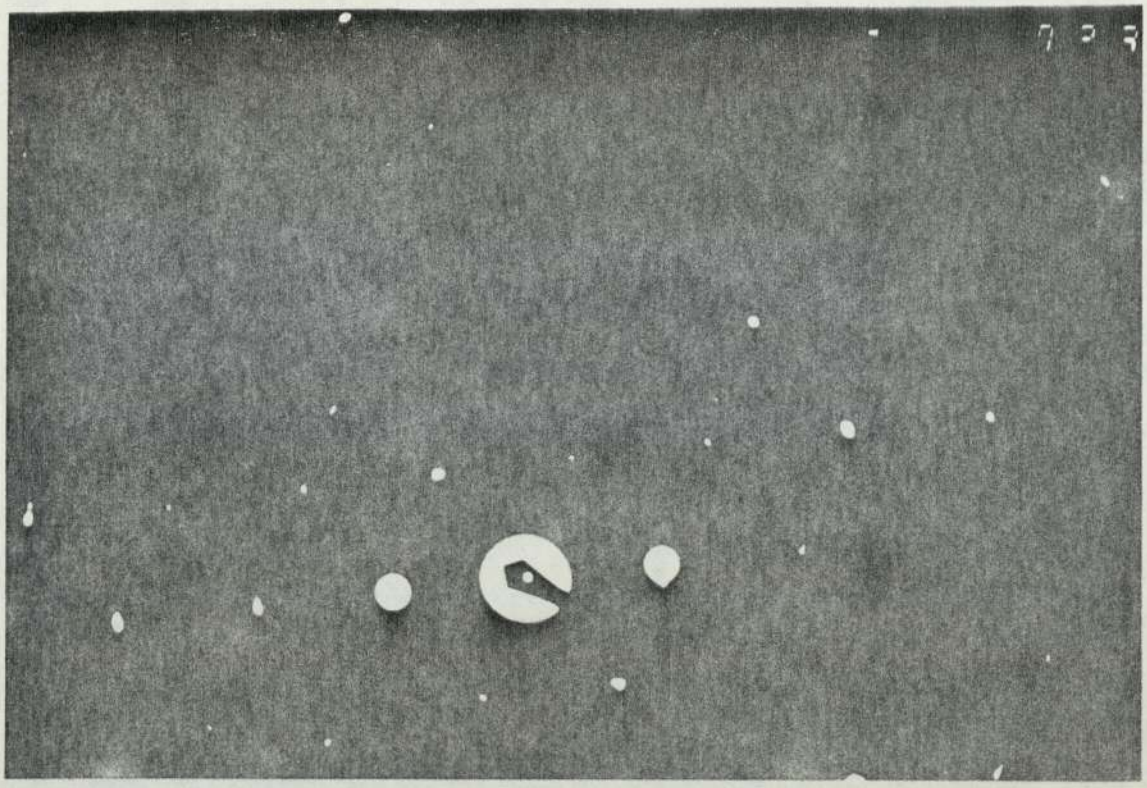

FIG 90 7C Selected Area Diffraction of Fig 88

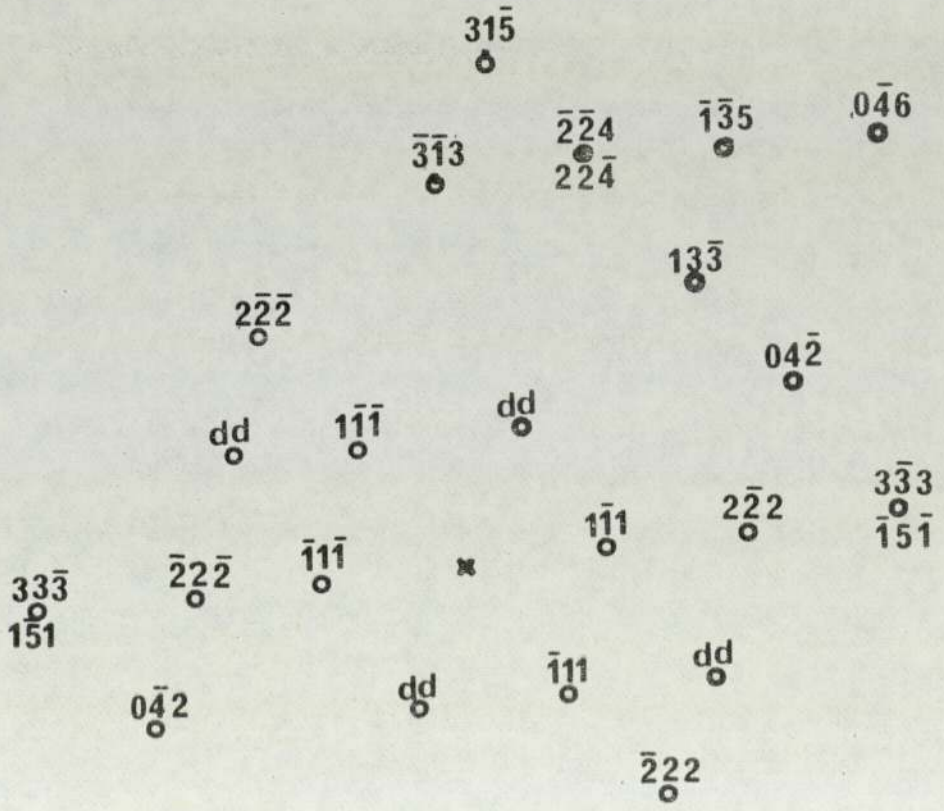

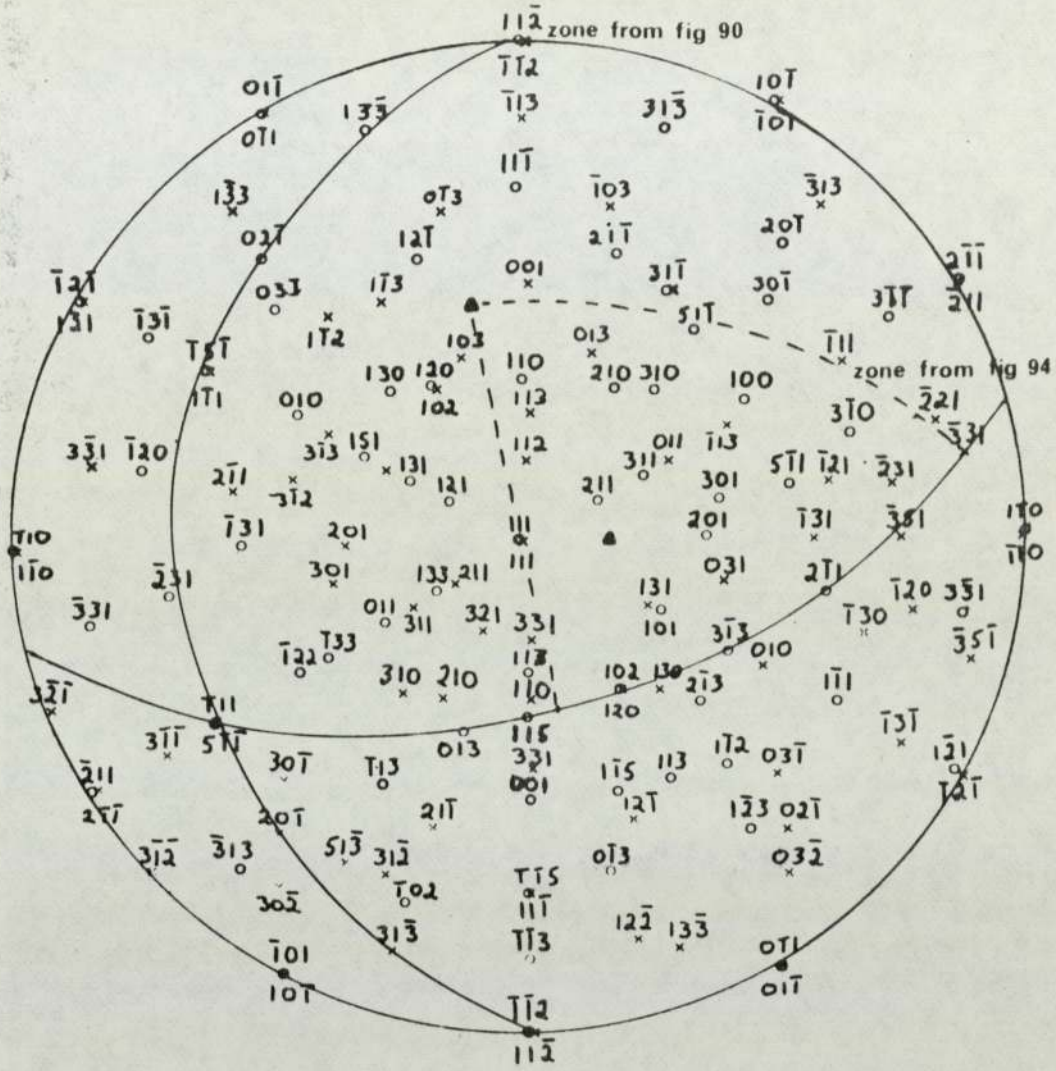

FIG 91 Stereographic Projection of (111) Twin Plane

FIG 92 7C Bright Field +20° Tilt x25k

FIG 93 7C Bright Field +30° Tilt x25k

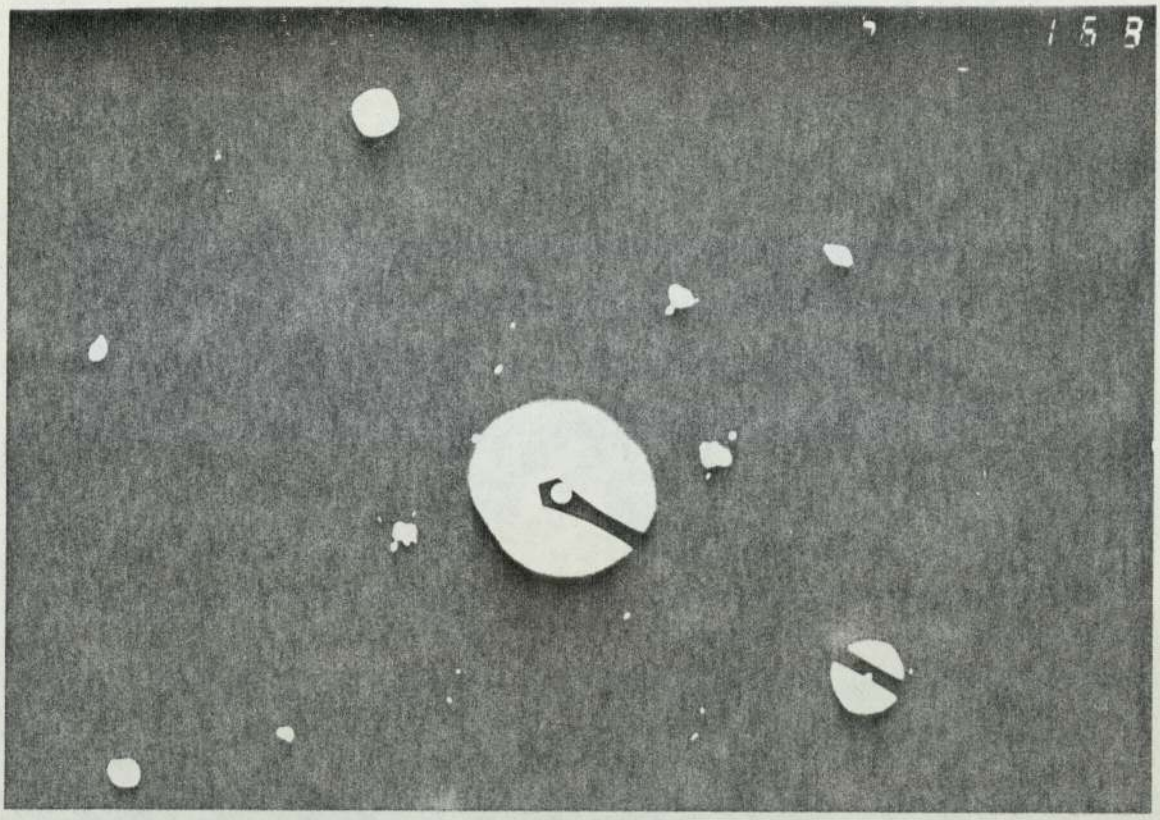

FIG 94 7C Selected Area Diffraction Pattern of Fig 93

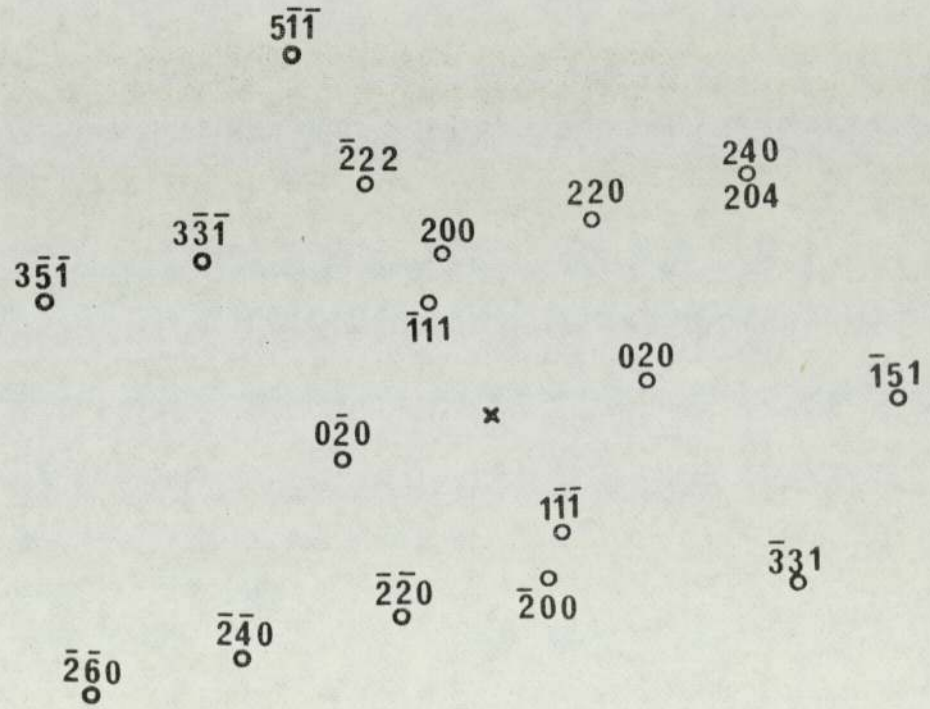

FIG 95 7C Centered Dark Field of Fig 93

FIG 96 7C Bright Field –5° Tilt x25k

FIG 97 7A55 Bright Field x120k

FIG 98 7A55 Centered Dark Field of Fig 97 x120k

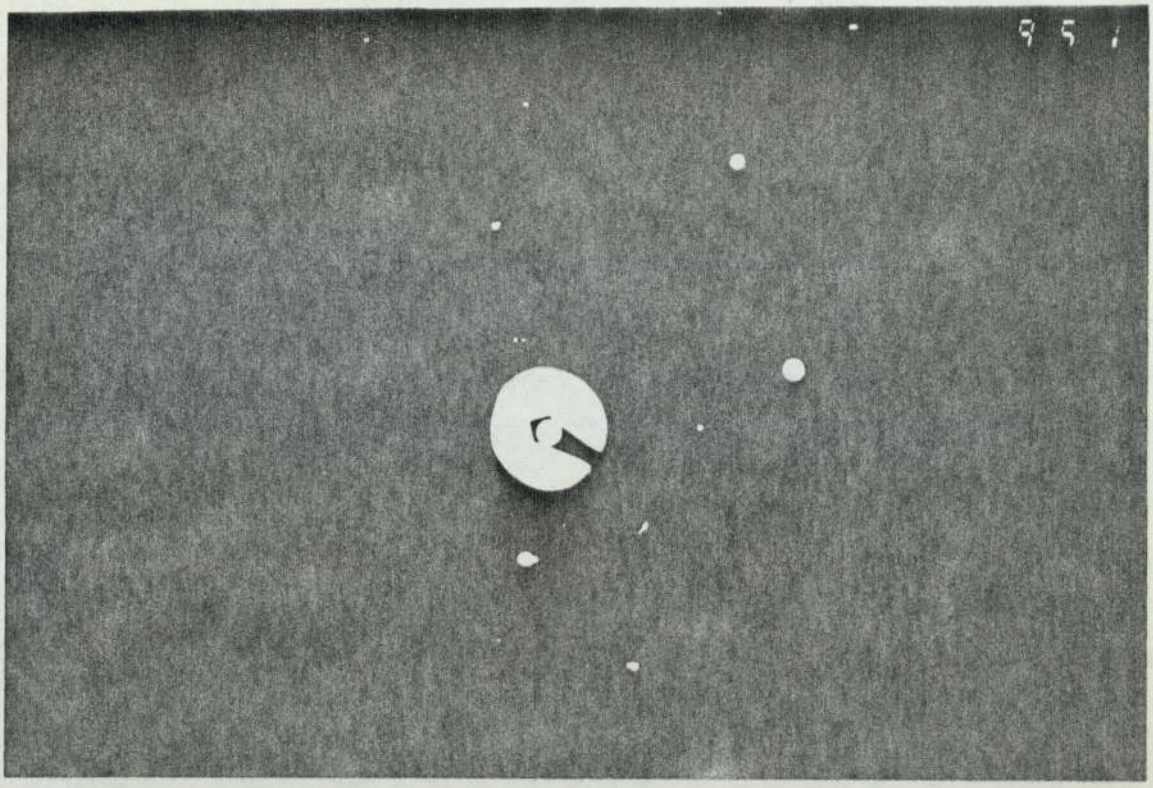

FIG 99 7A55 Selected Area Diffraction Pattern of Fig 98

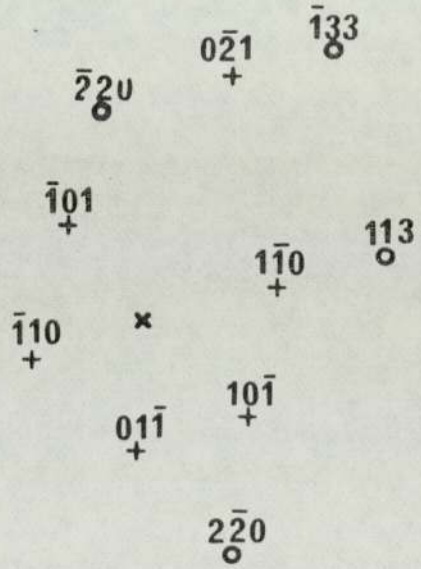

+ ppt

o matrix

FIG 100 7A55 Bright Field x45k

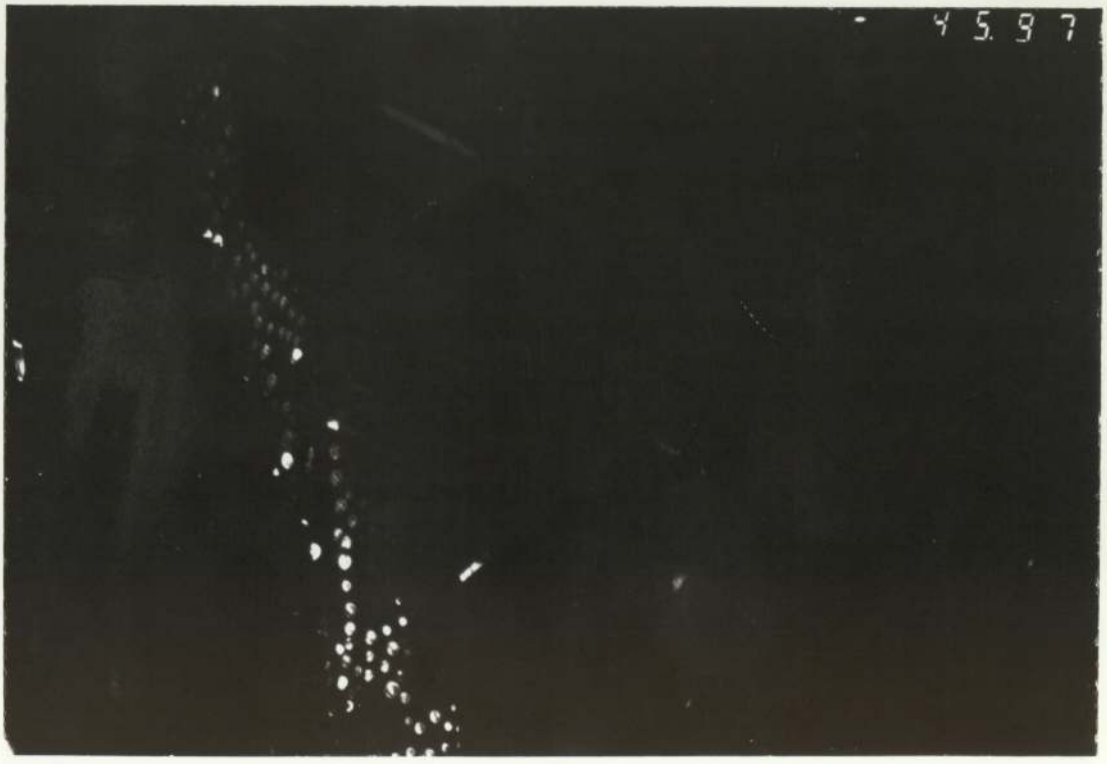

FIG 101 7A55 Centered Dark Field of Fig 100 x45k

FIG 102 7A55 Bright Field x80k

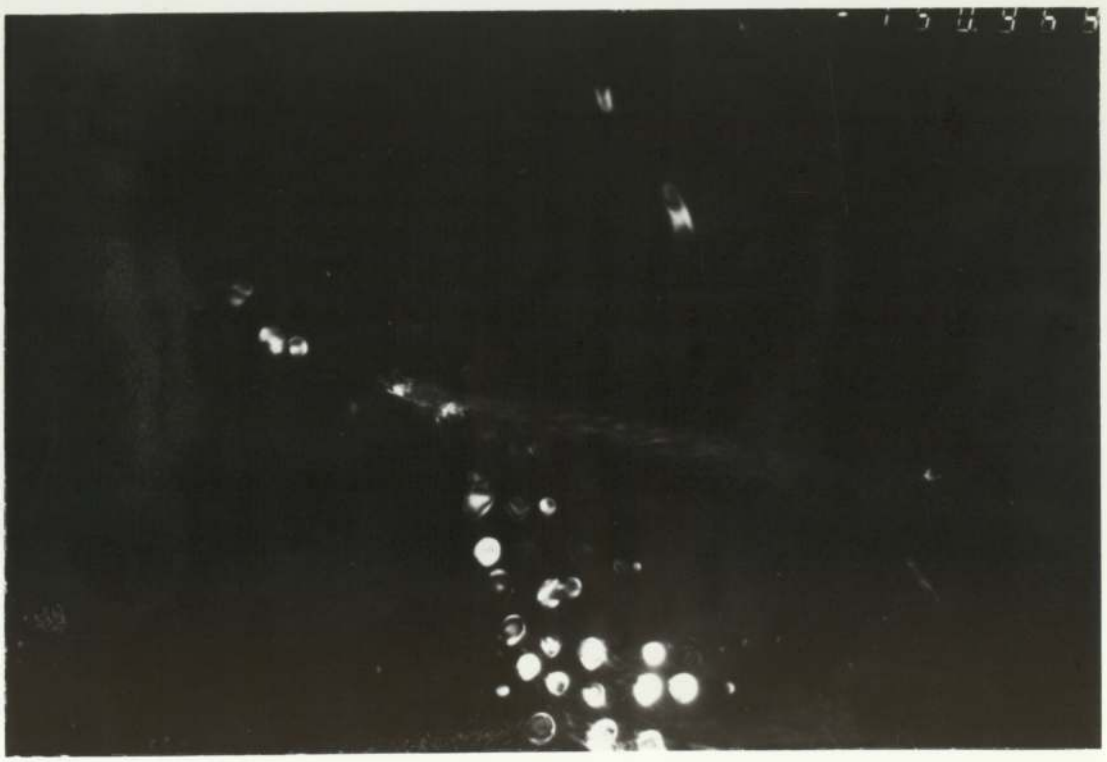

FIG 103 7A55 Centered Dark Field from $(01\bar{1})$ ppt x80k

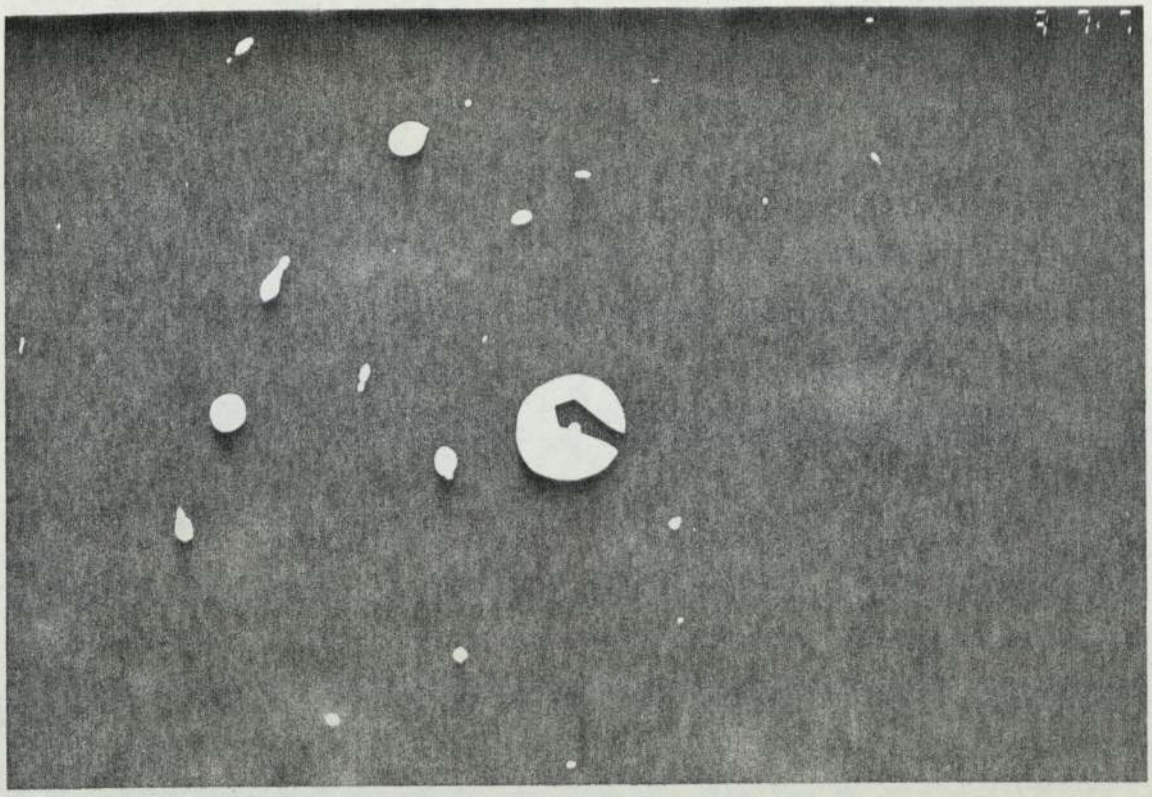

FIG 104 7A55 Selected Area Diffraction Pattern of Fig 102

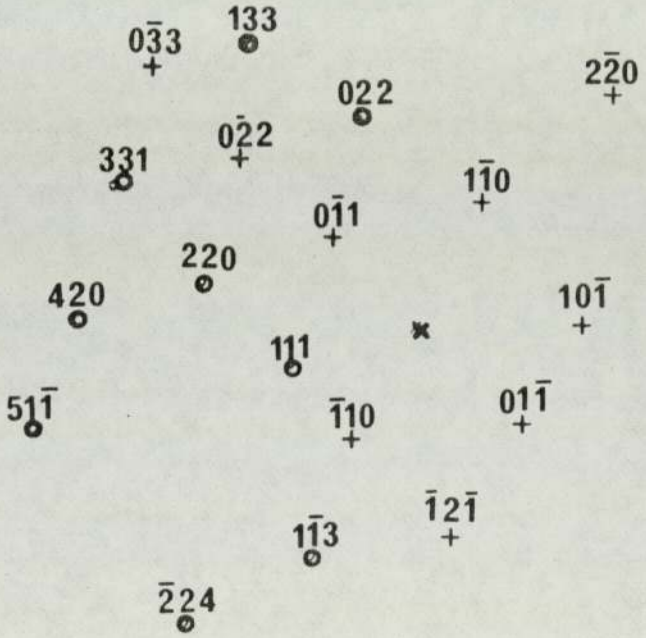

o matrix

+ ppt

FIG 105 7A55 Bright Field x200k

FIG 106 7A55 Bright Field x200k

FIG 107 7A56 Bright Field +15° Tilt x80k

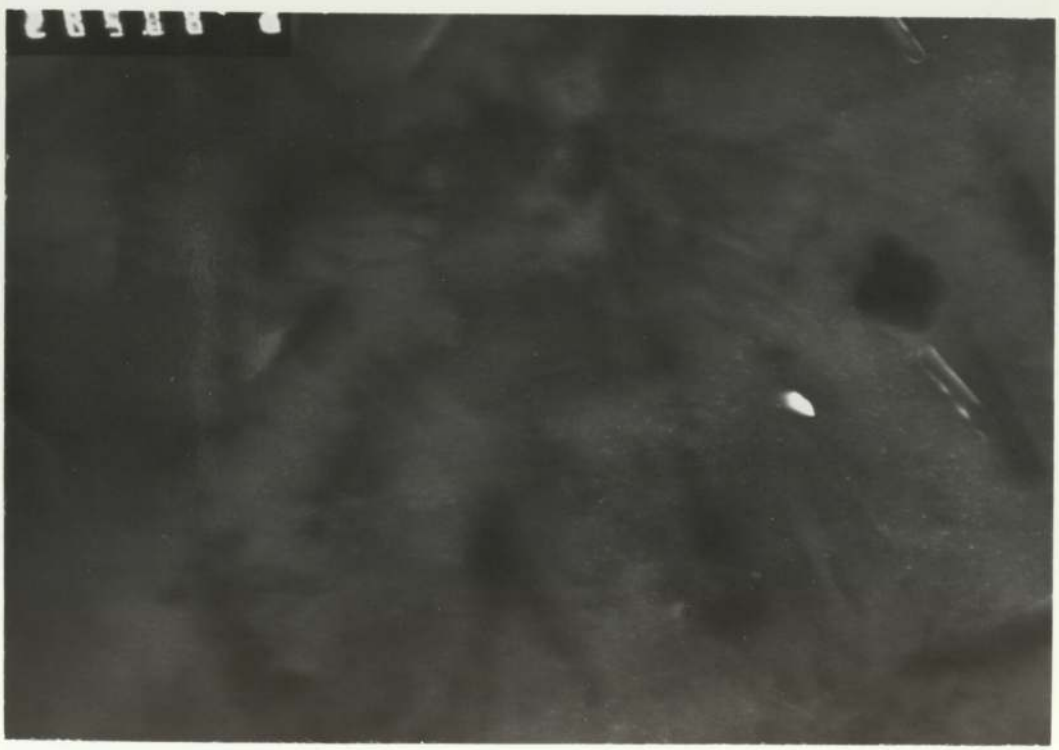

FIG 108 7A56 Centered Dark Field of Fig 107 x80k

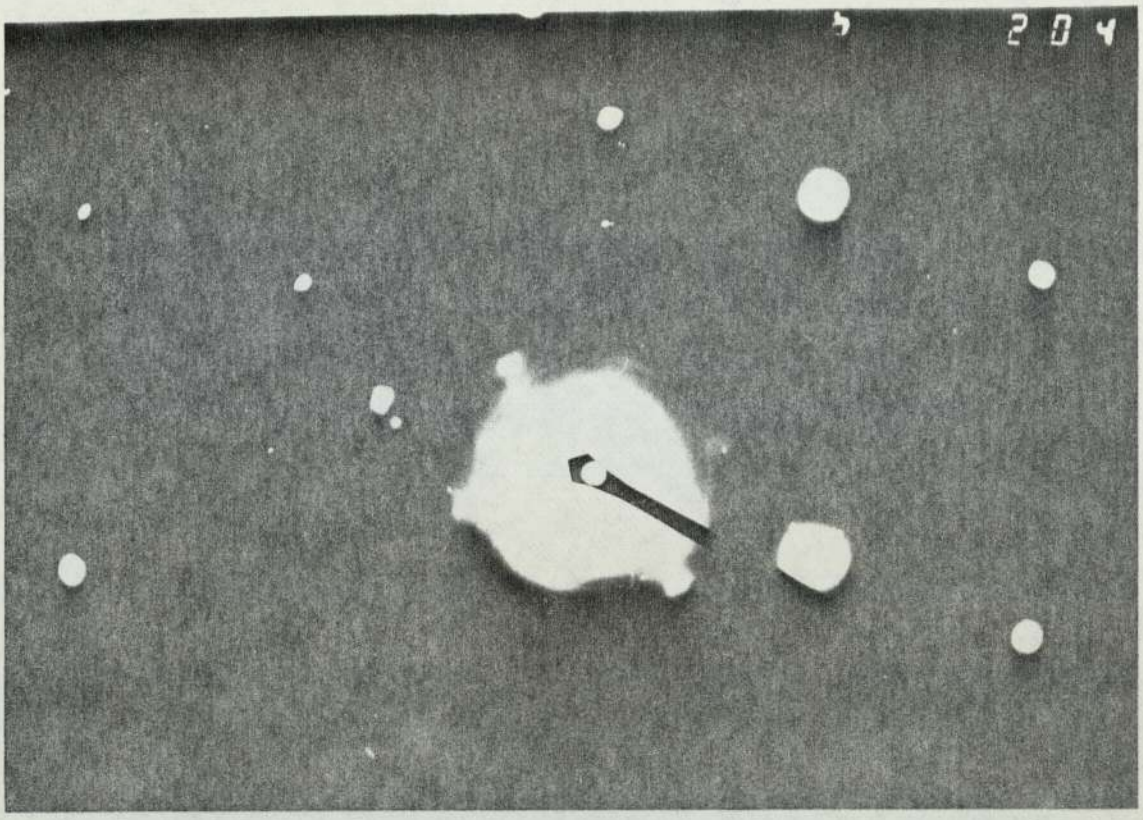

FIG 109 7A56 Selected Area Diffraction Pattern of Fig 107

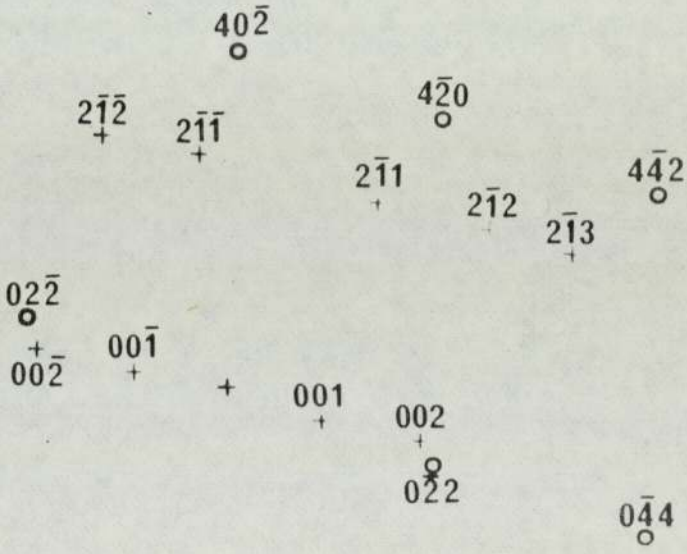

o matrix

+ ppt

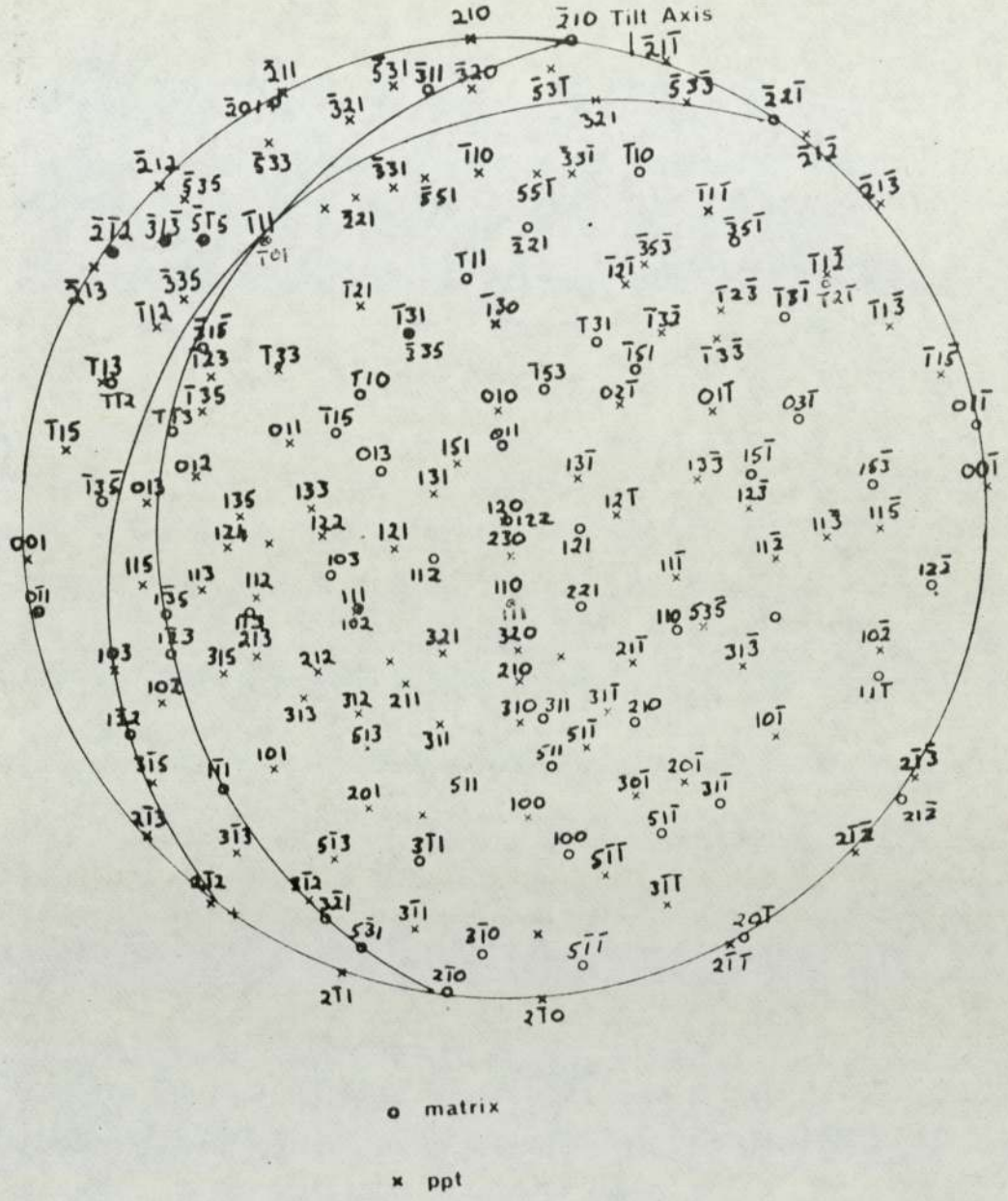

FIG 110 Stereographic Projection Showing Kurdjamov – Sachs Relationship

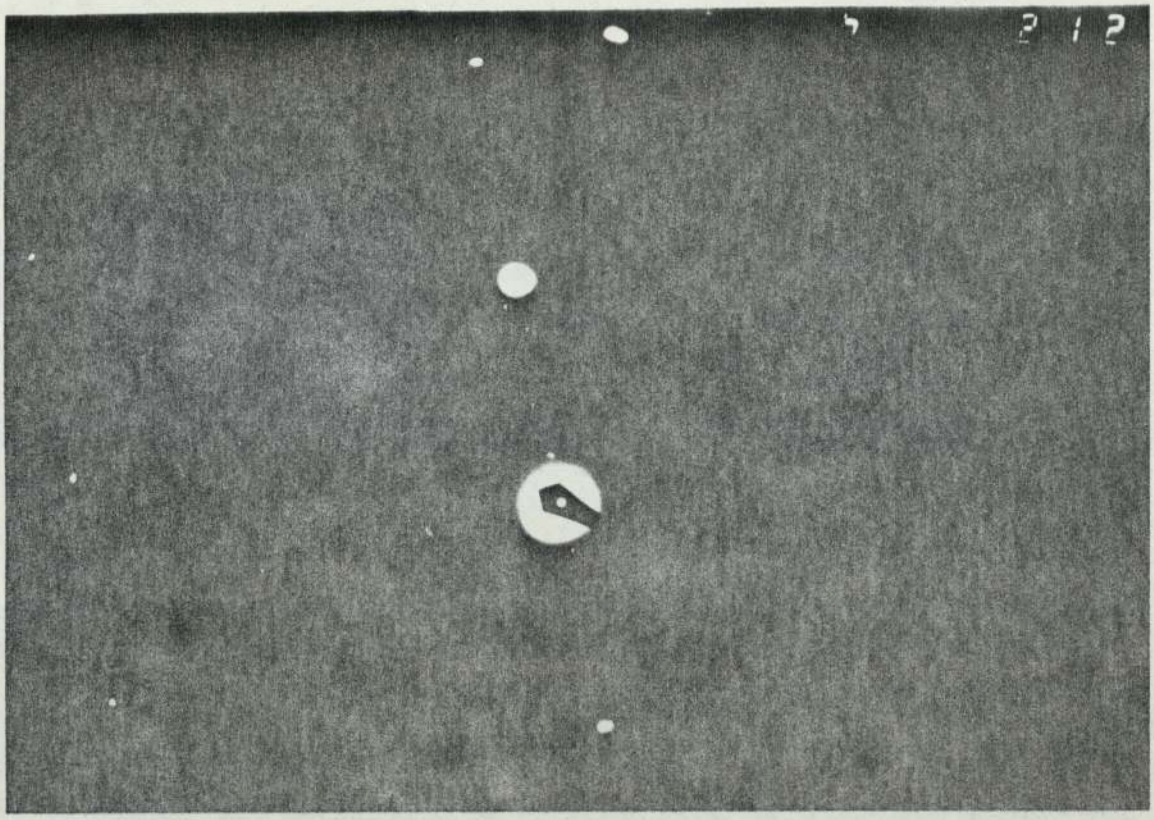

FIG 111 7A56 Selected Area Diffraction Pattern of Fig 107 + 17° Tilt

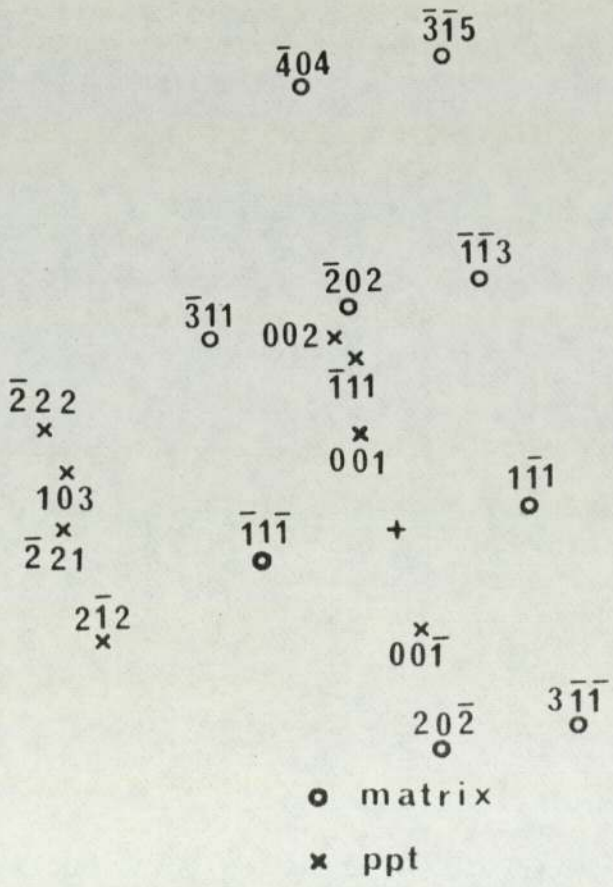

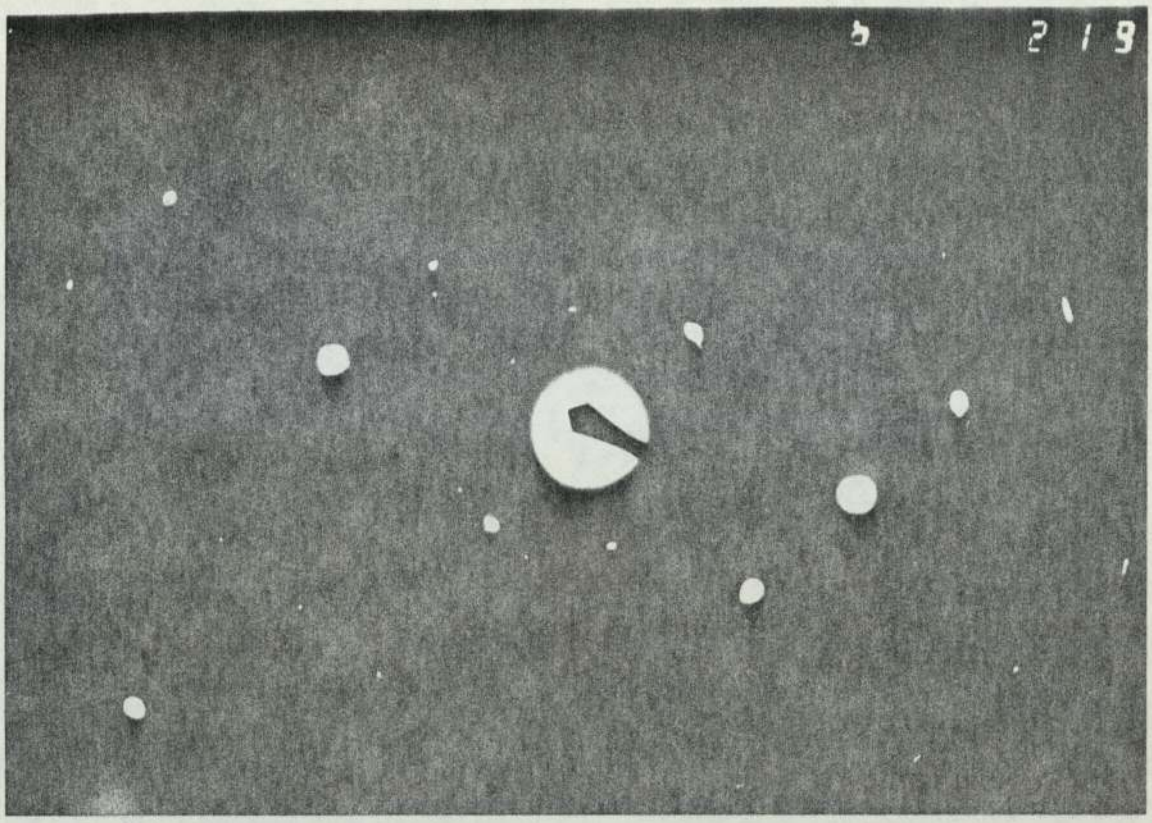

FIG 112 7A56 Selected Area Diffraction Pattern + 10° Tilt

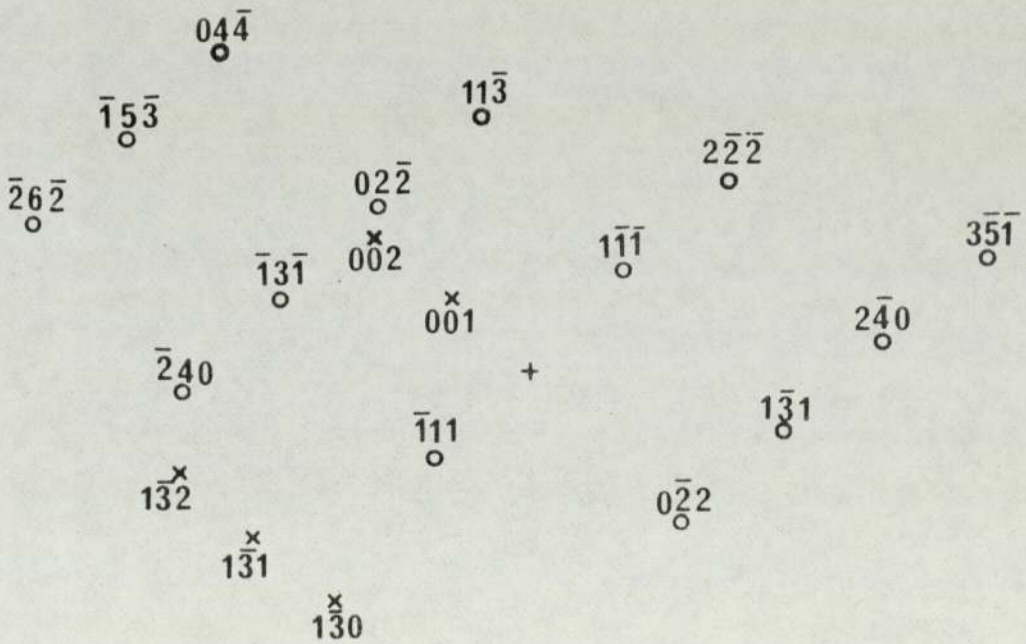

o matrix

× ppt

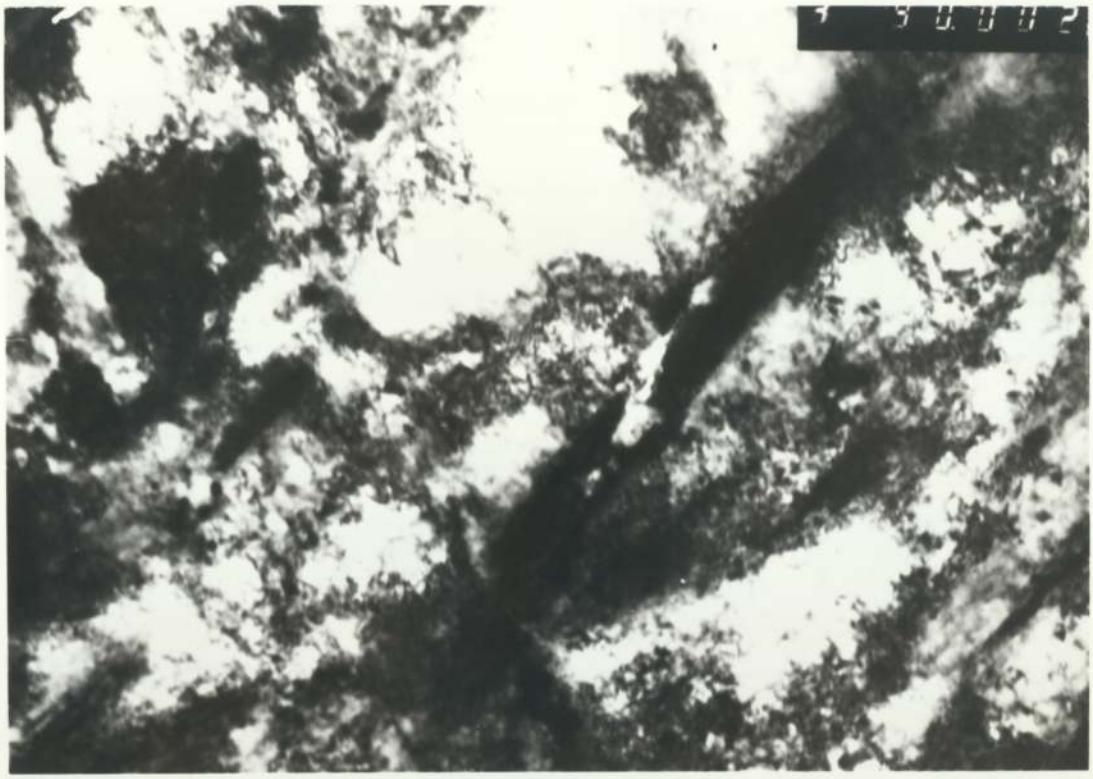

FIG 113 7C53 Bright Field x90k

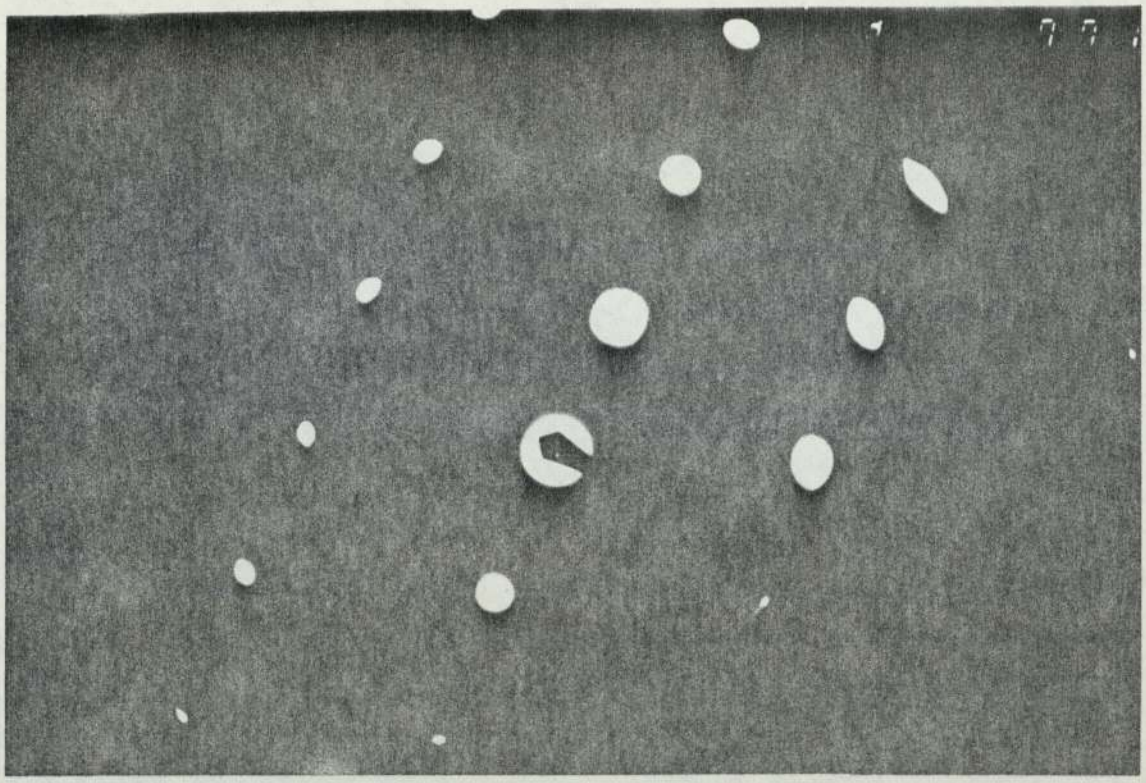

FIG 114 7C53 Selected Area Diffraction Pattern of Fig 113

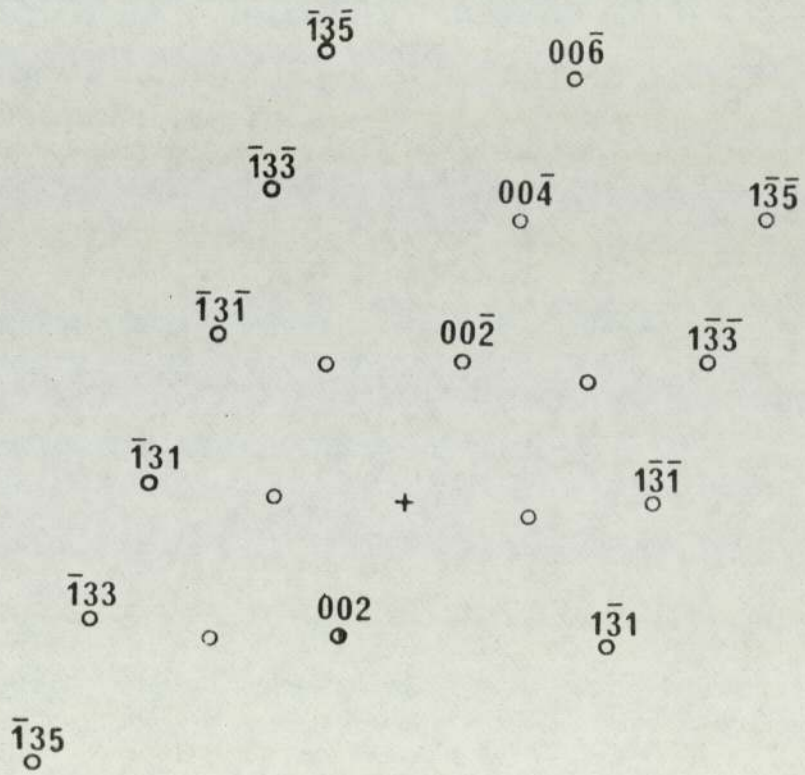

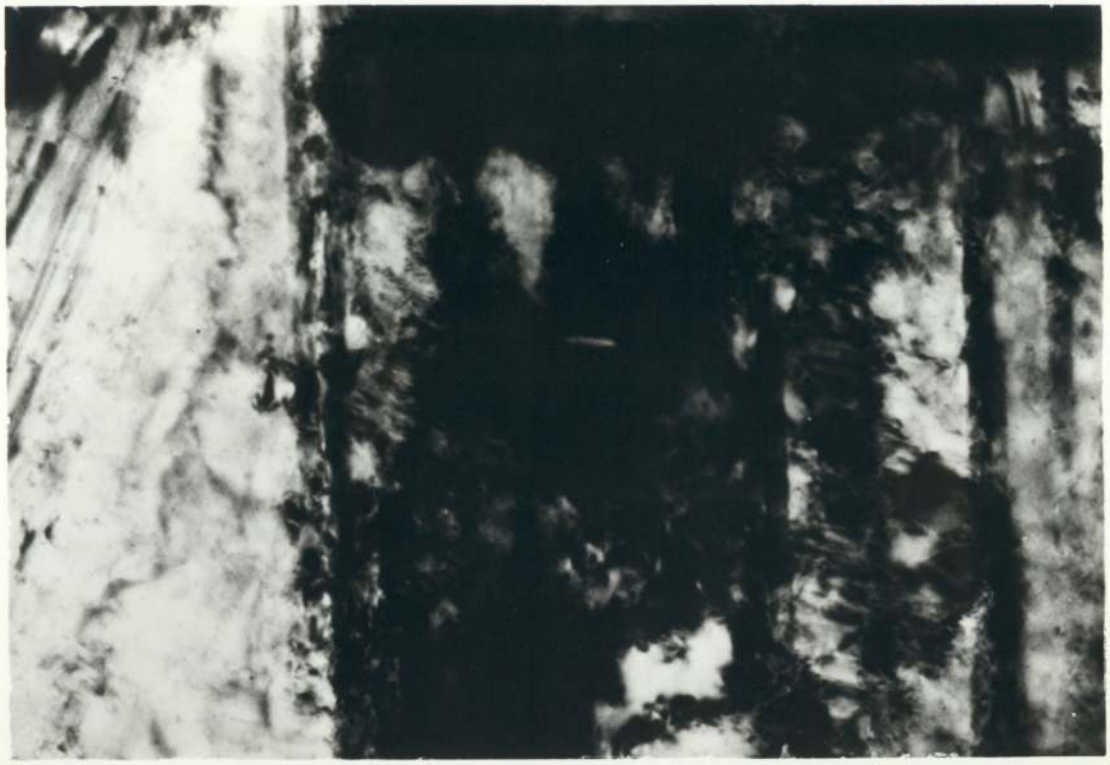

FIG 115 7C53 Bright Field x200k

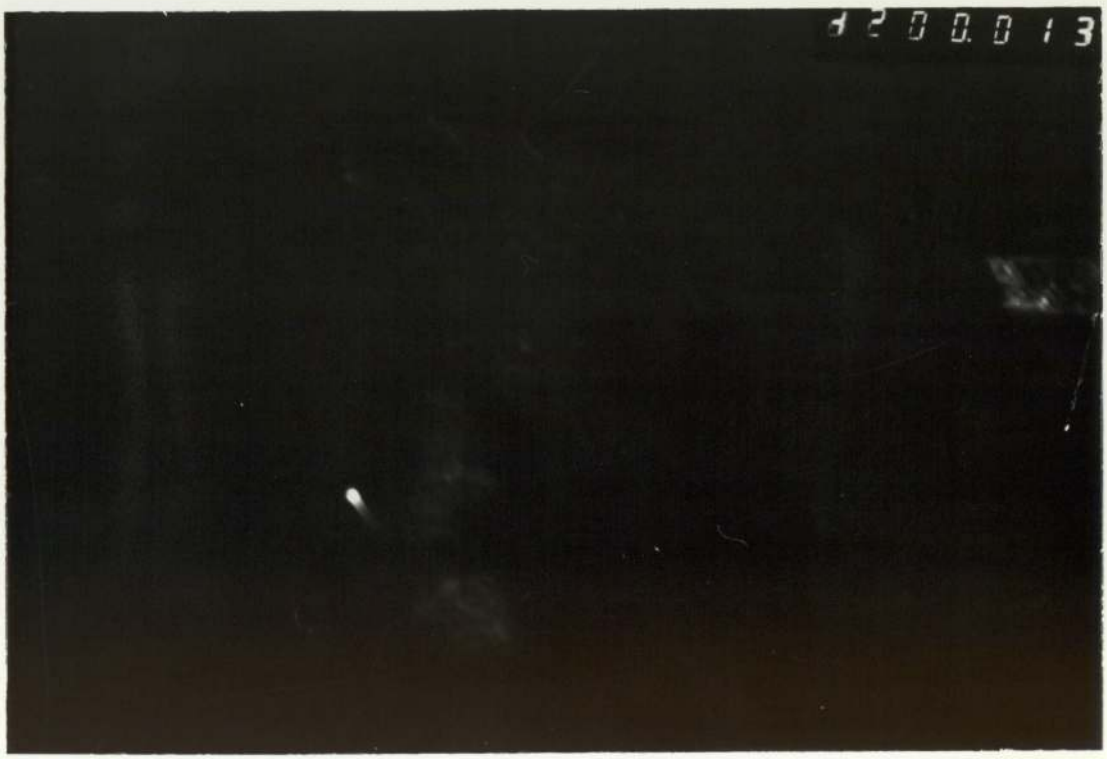

FIG 116 7C53 Centered Dark Field of Fig 115 x200k

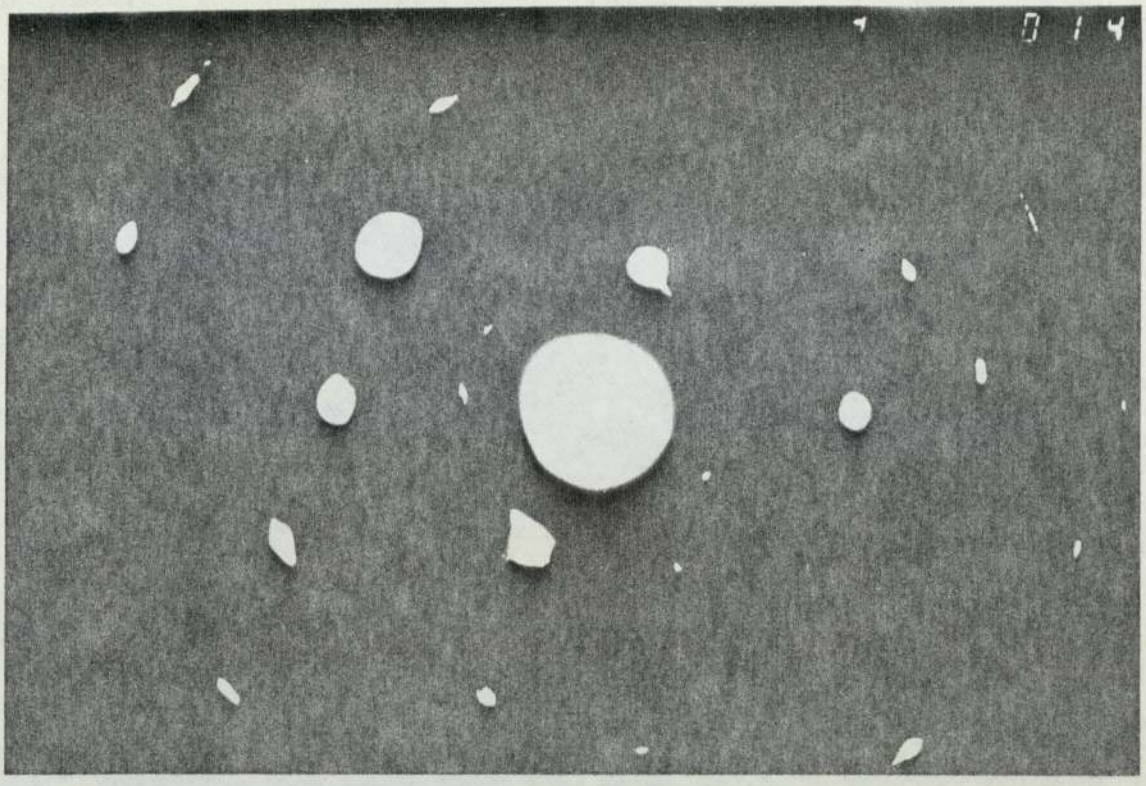

FIG 117 7C53 Selected Area Diffraction Pattern of Fig 115

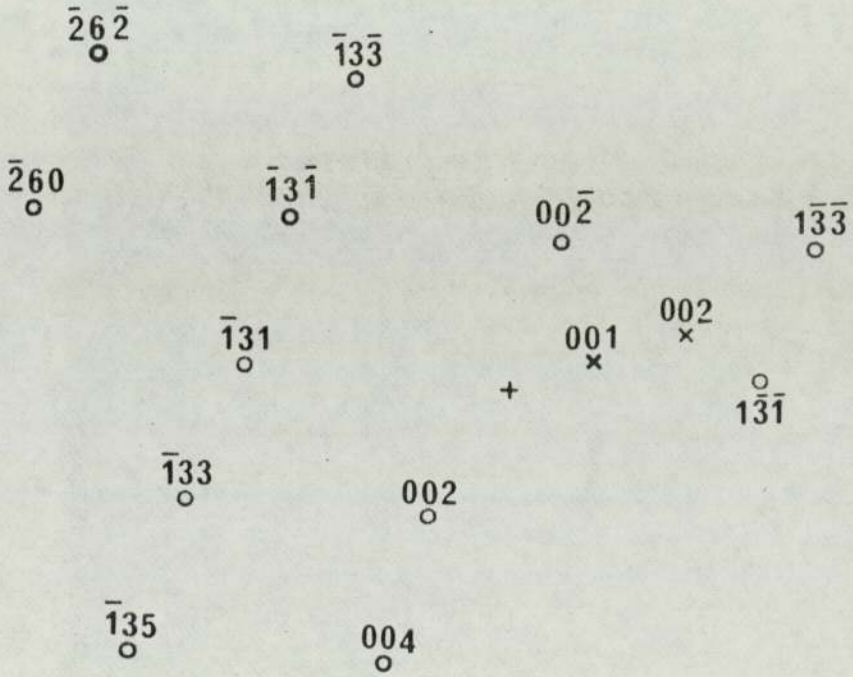

o matrix

× ppt

FIG 118 7C55 Bright Field x50k

FIG 119 7C55 Bright Field x50k

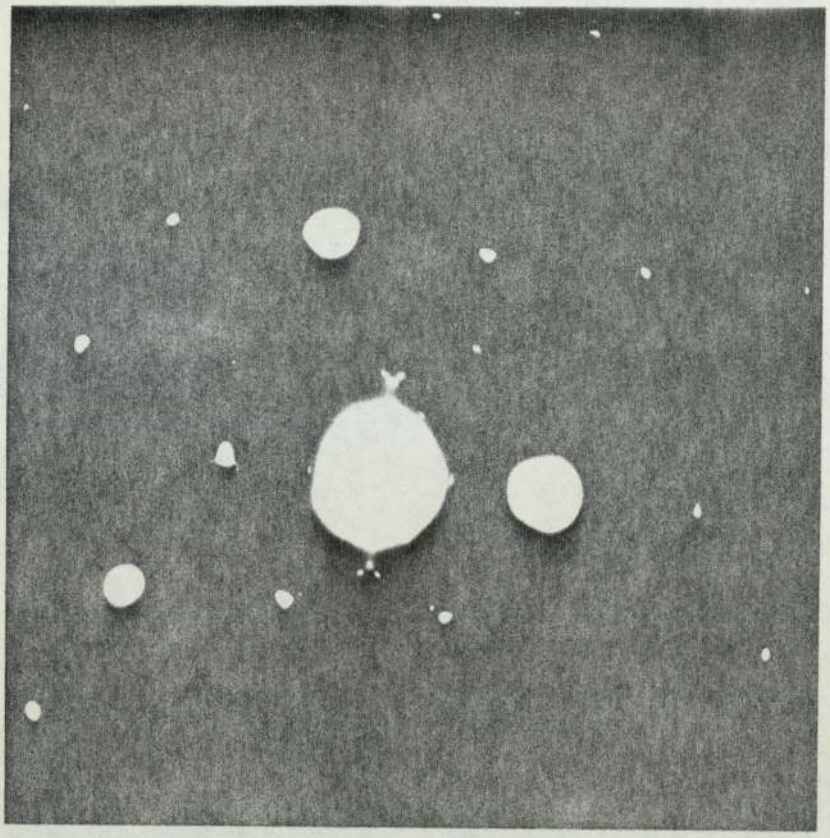

FIG 120 7C55 Selected Area Diffraction Pattern of Fig 119

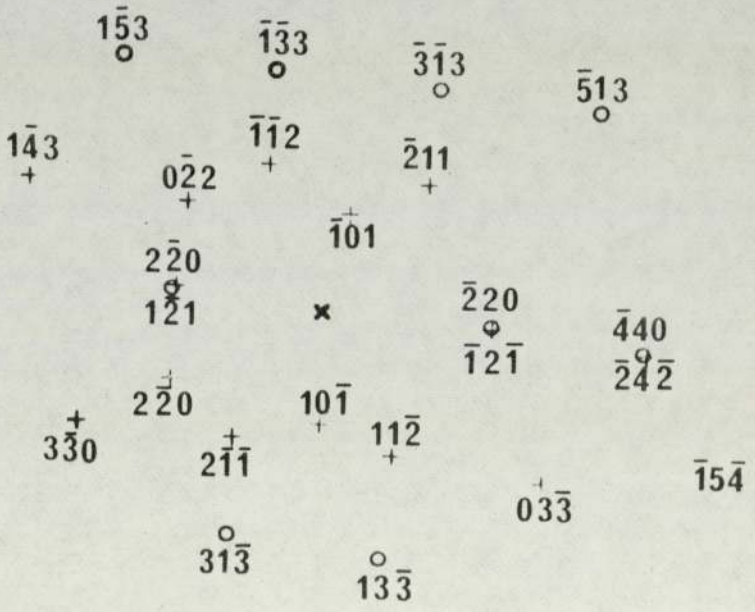

o Matrix

\+ Ppt

153

21 E vs. LOG I DIAGRAM OF 0B

HYDROCHLORIC ACID , pH 3·1

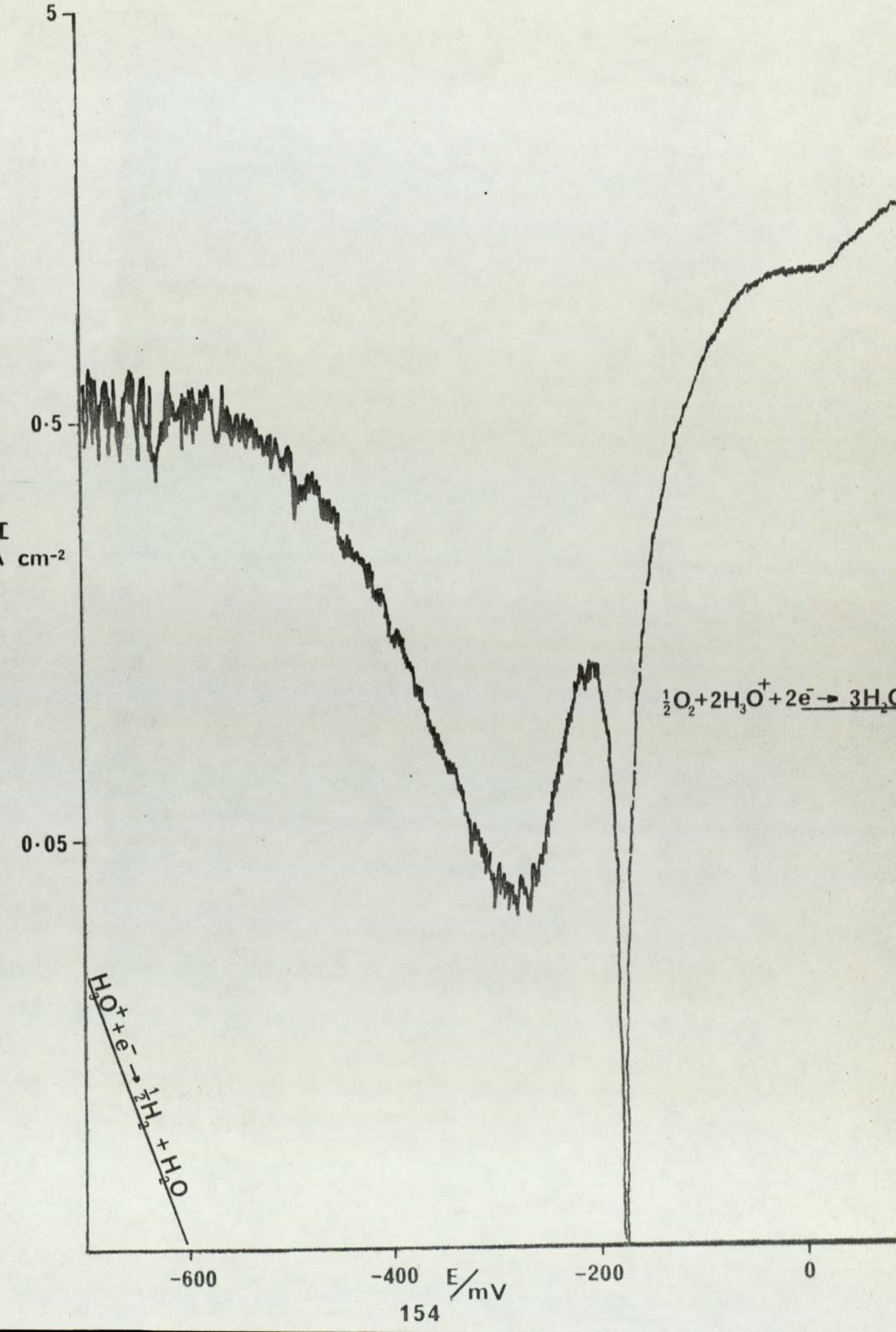

G 122

E vs. LOG I DIAGRAM OF 0B

SODIUM HYDROXIDE SOLUTION, pH 8·1

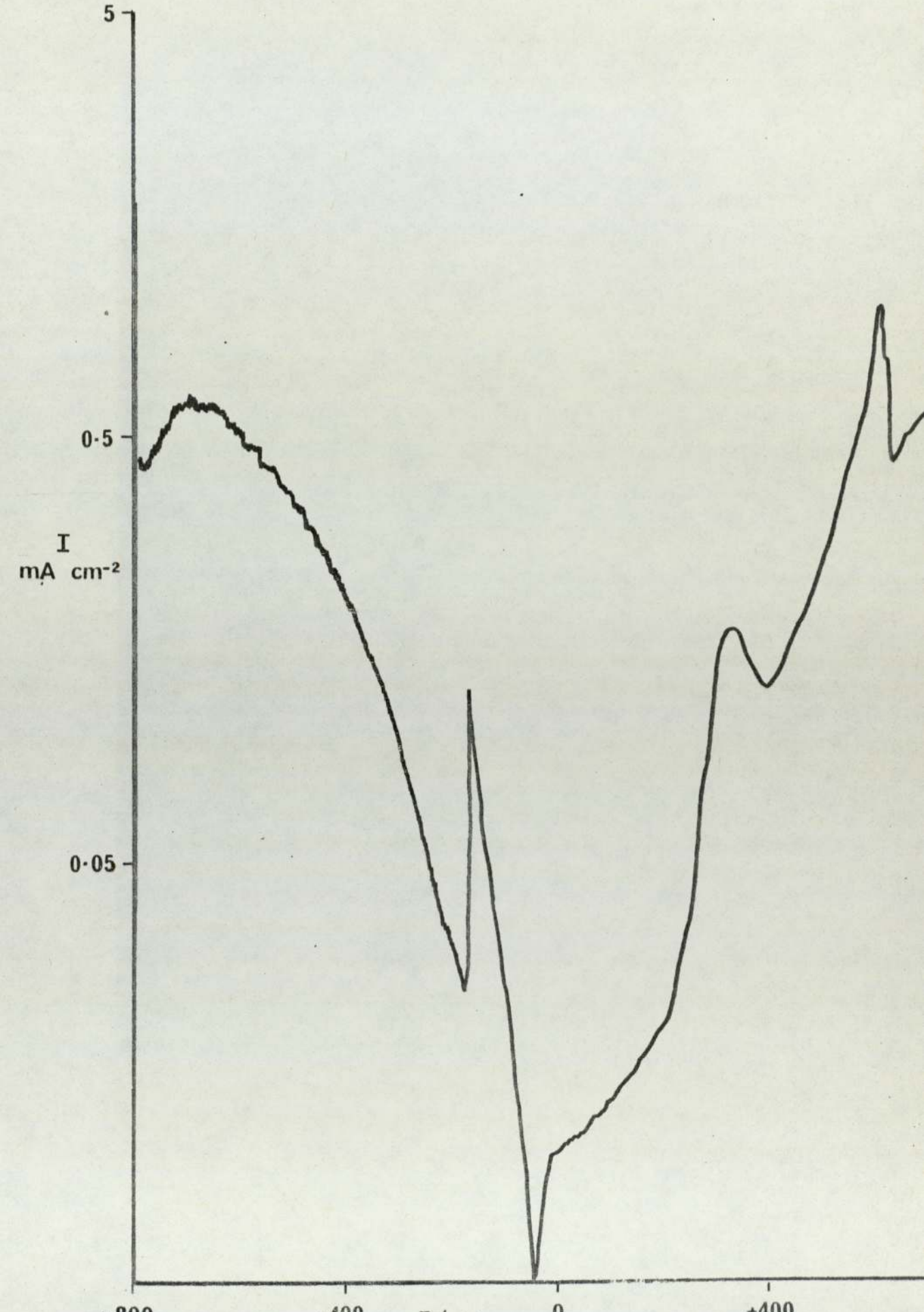

FIG 123 E vs. LOG I DIAGRAM OF OB SODIUM HYDROXIDE SOLUTION, pH 12·25

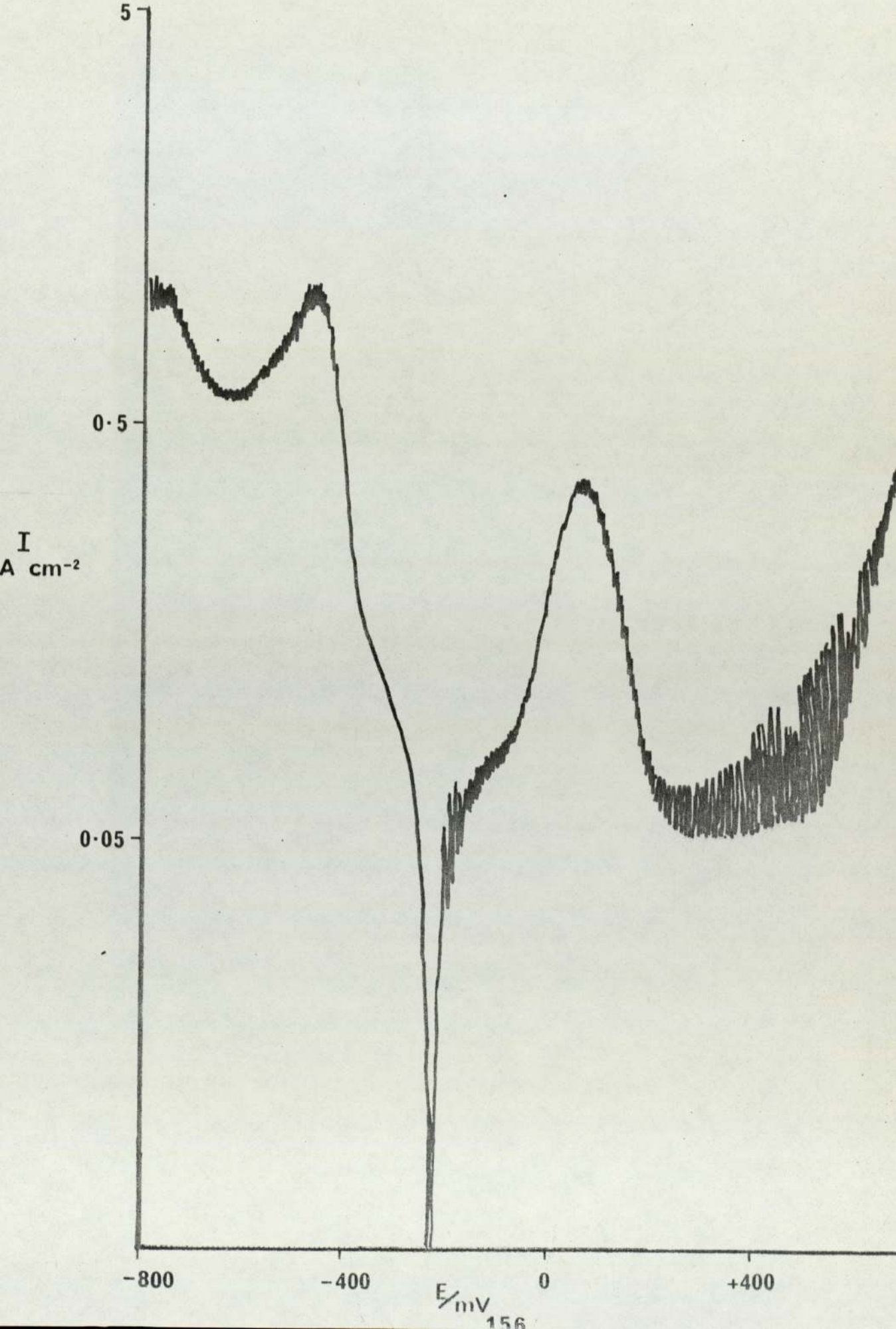

FIG 124 E vs. LOG I DIAGRAM OF OB

NaOH + 15ppm Cu^{+}

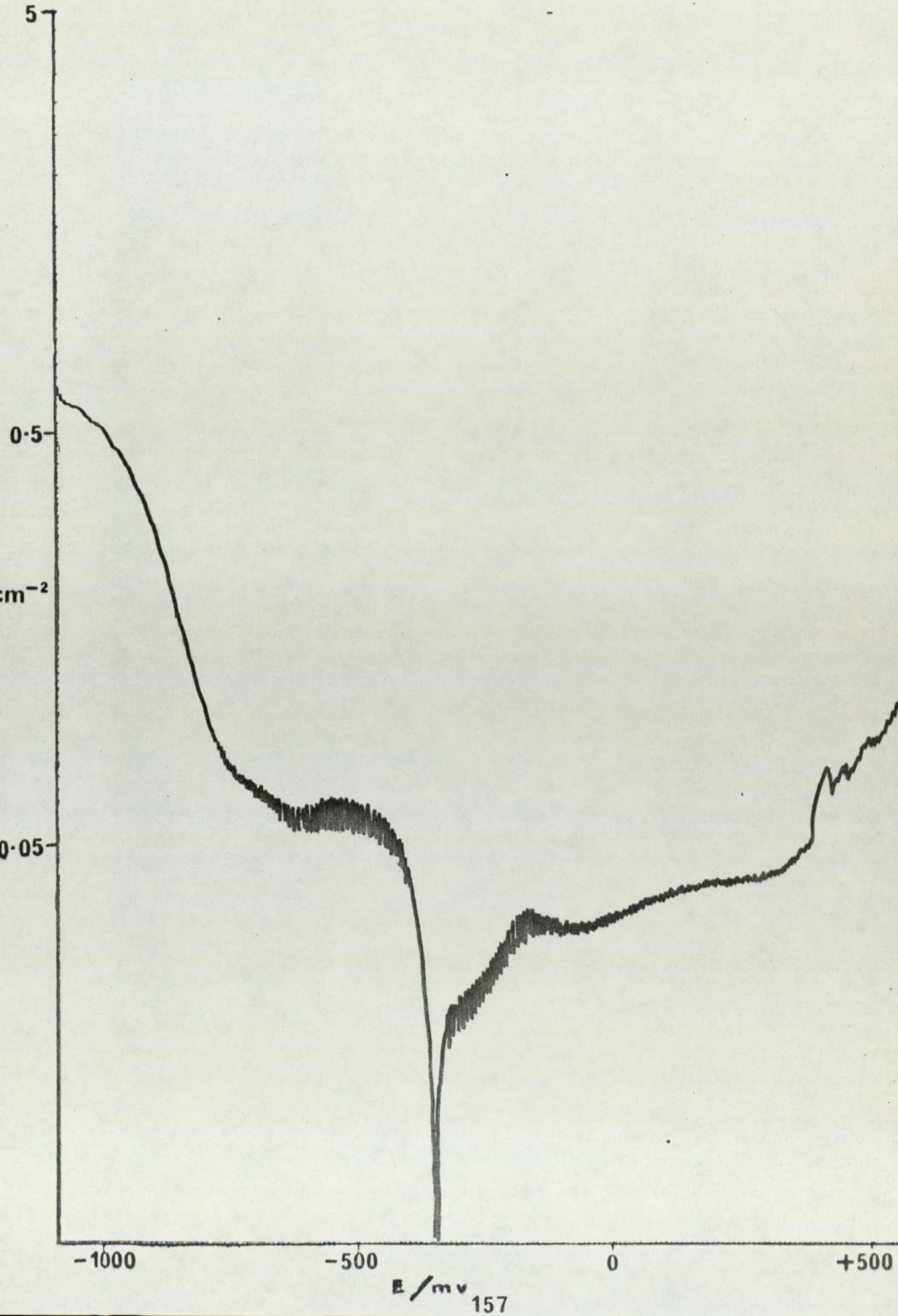

FIG 125 E vs. LOG I DIAGRAM OF OB

Na_2CO_3 pH 11·5

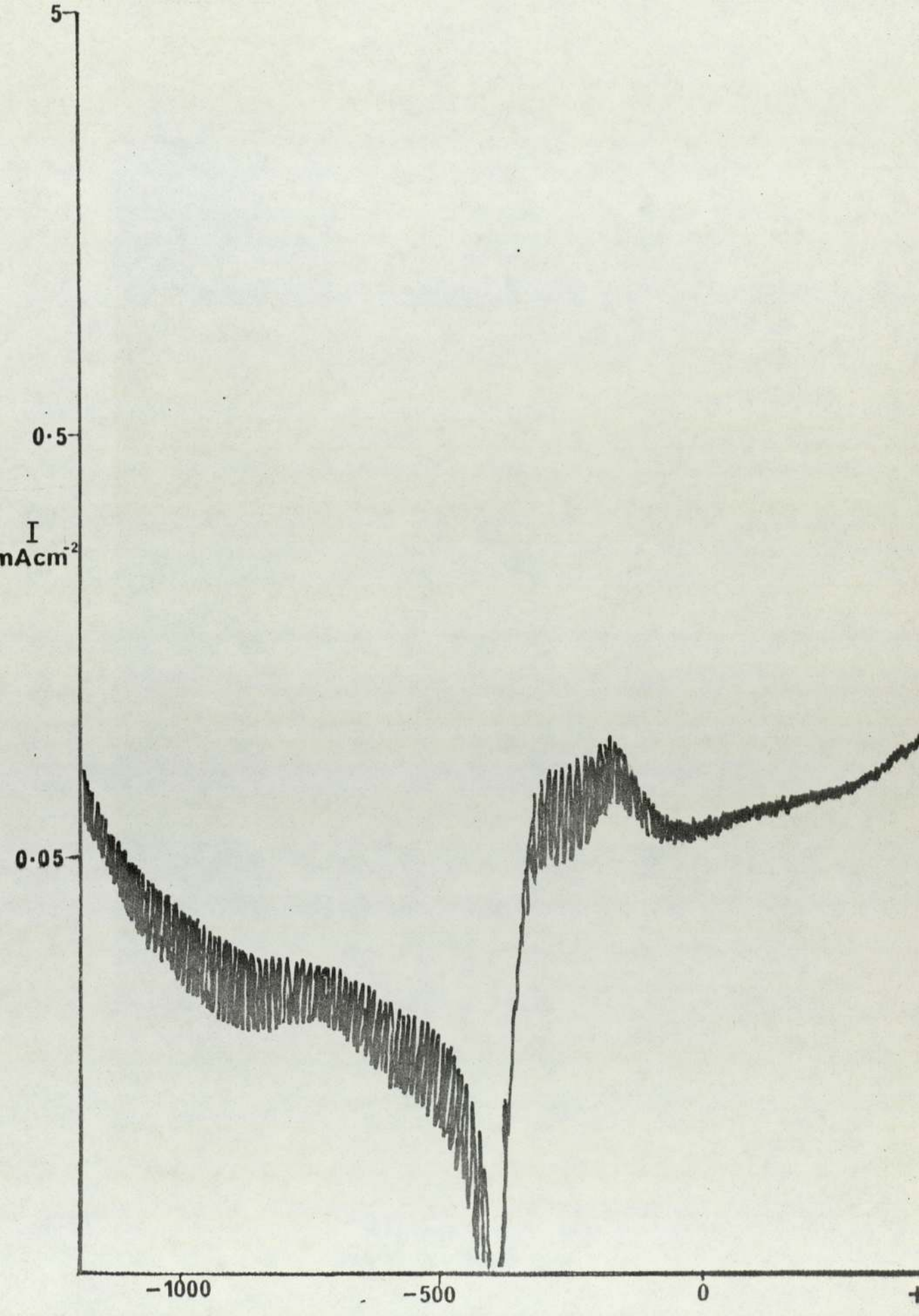

FIG 126 E vs. LOG I DIAGRAM OF OB

Na_2CO_3 + 15ppm Cu^+

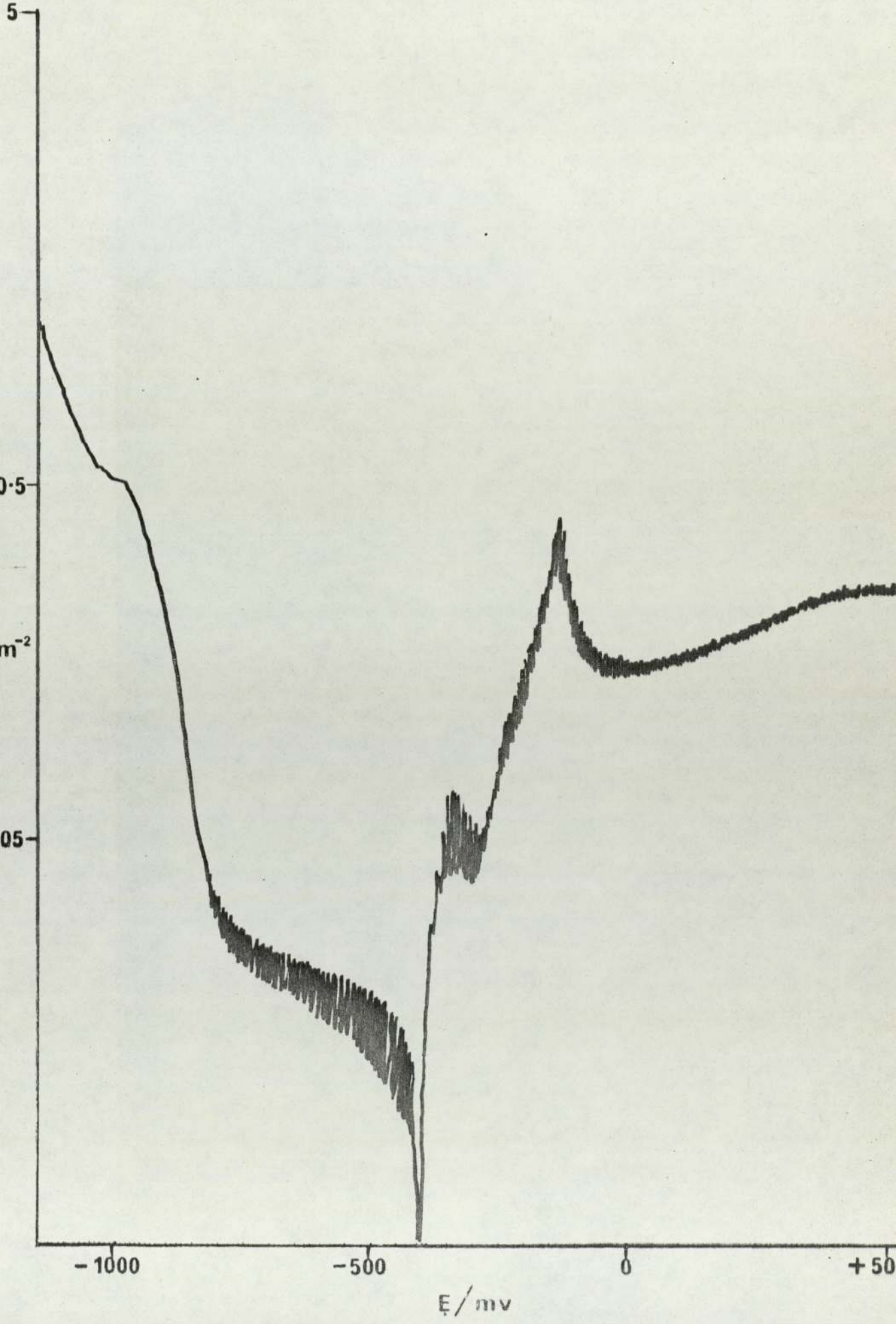

FIG 127 E vs. LOG I DIAGRAM OF 0B SEA WATER

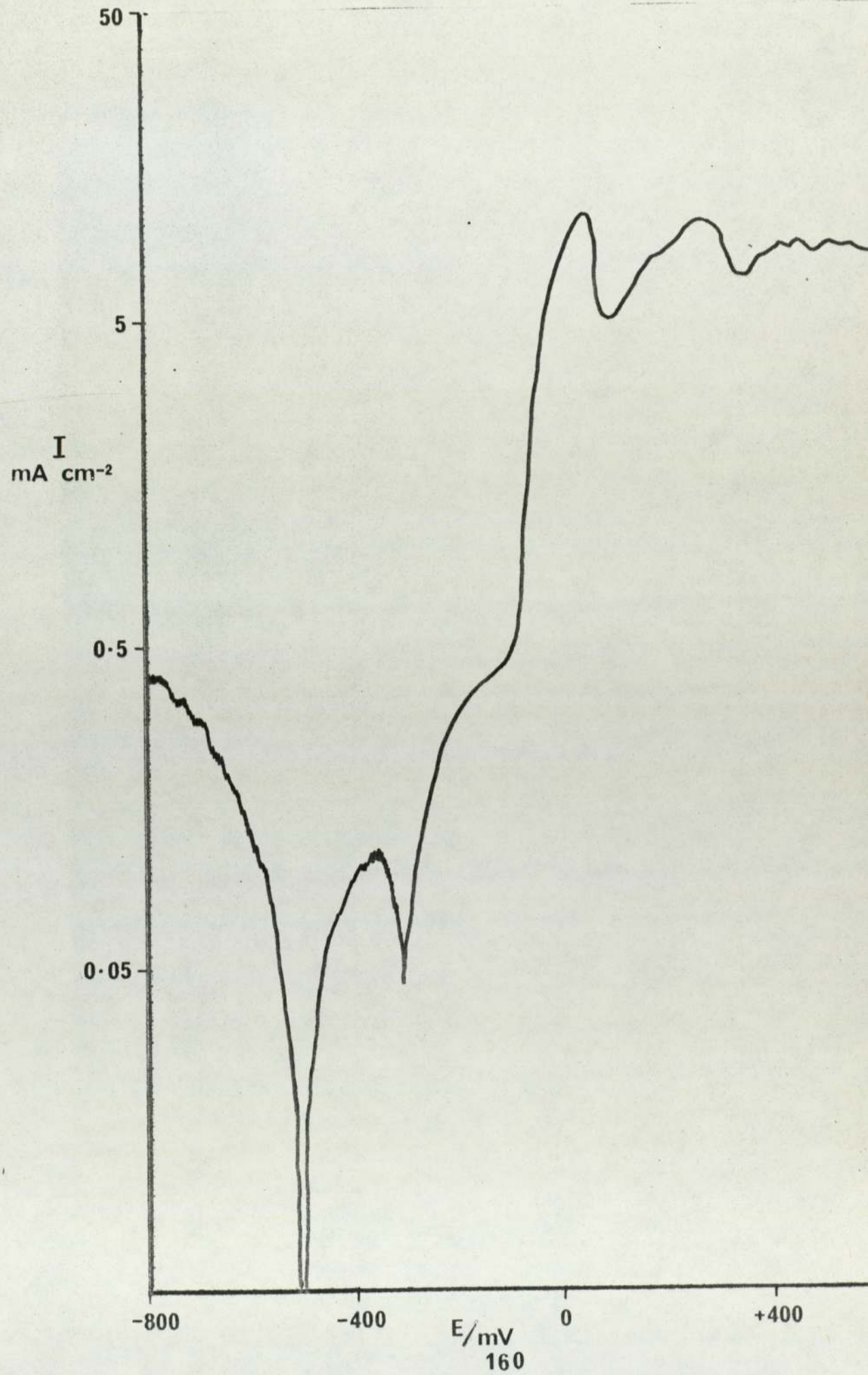

G 128 ANODIC E vs. LOG I PLOT FROM THE ENVIRONMENTA
EST POTENTIAL, OF 0B, SEA WATER

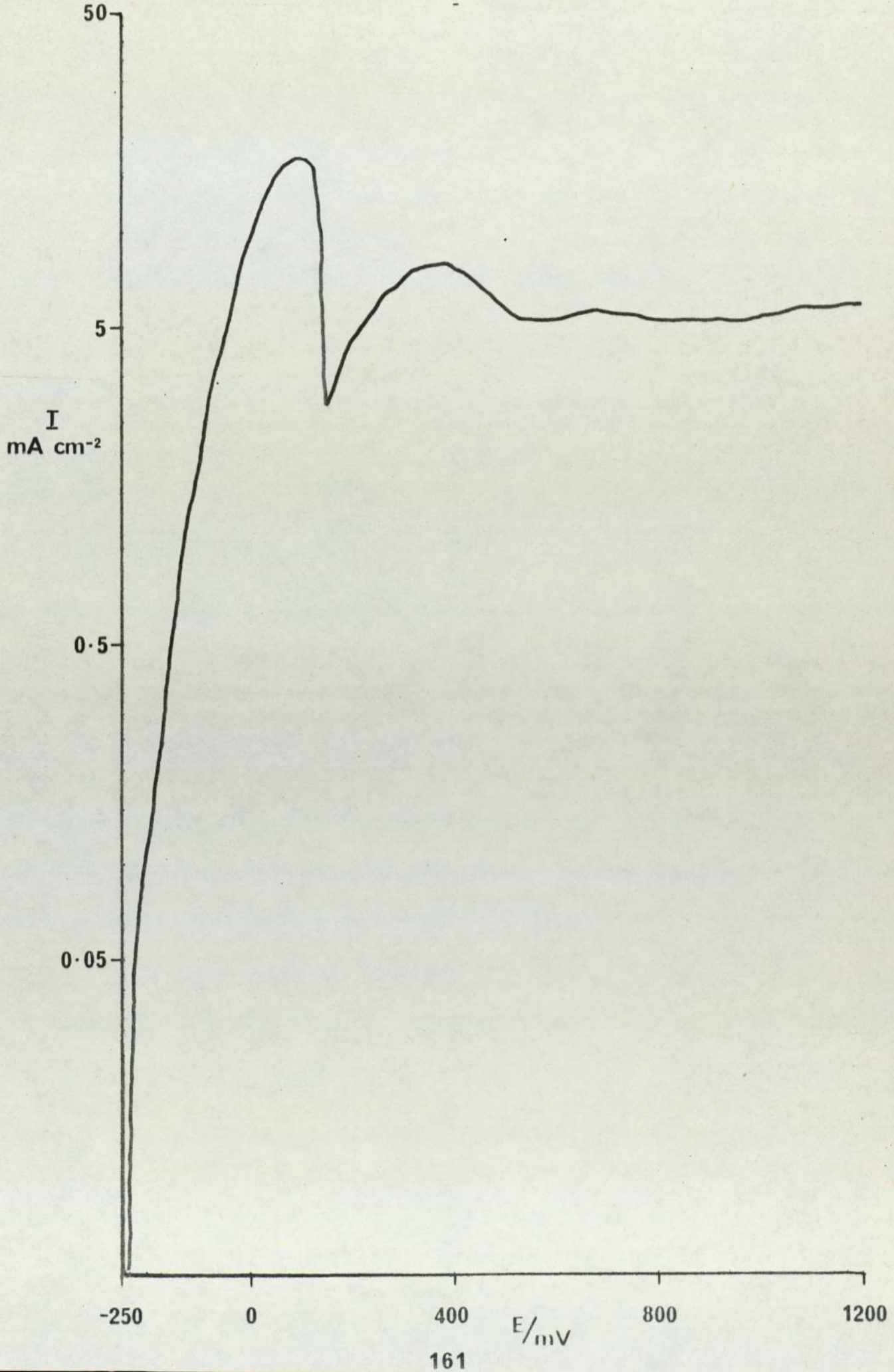

129 E vs. LOG I DIAGRAM OF (0A) IN SEA WATER

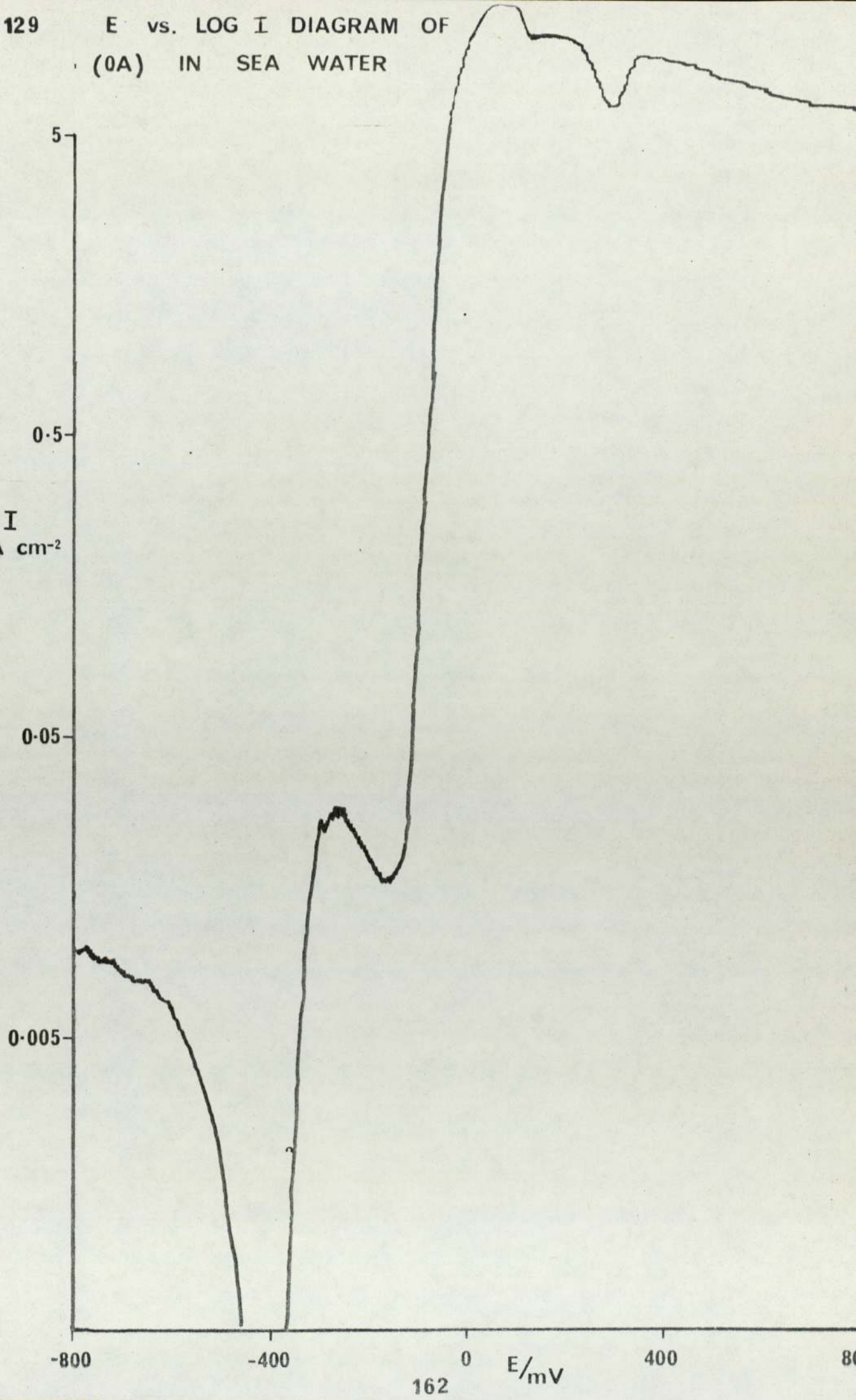

FIG 130 E vs. LOG I DIAGRAM OF 1B SEA WATER

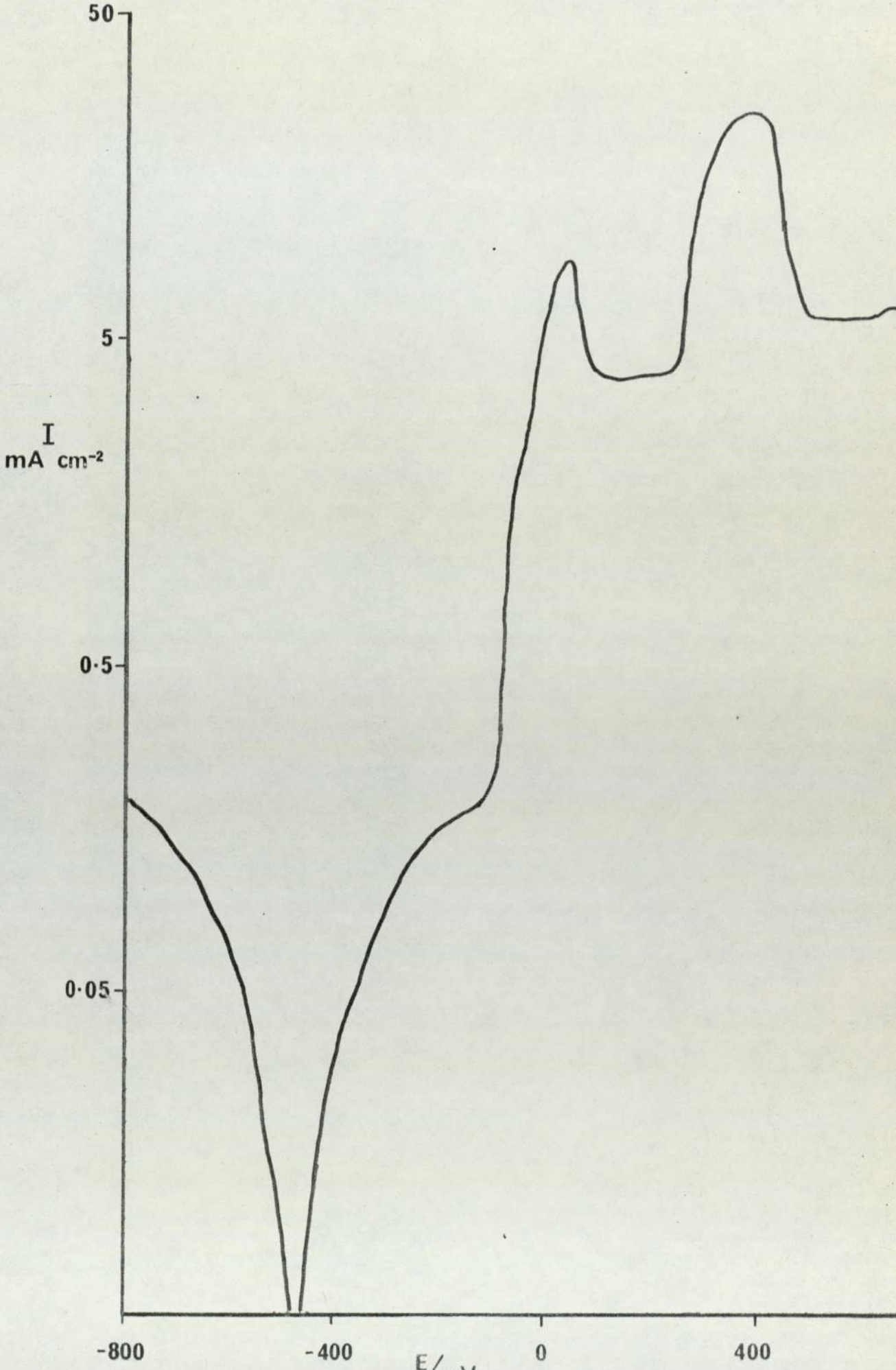

FIG 131 E vs. LOG I DIAGRAM OF 1A SEA WATER

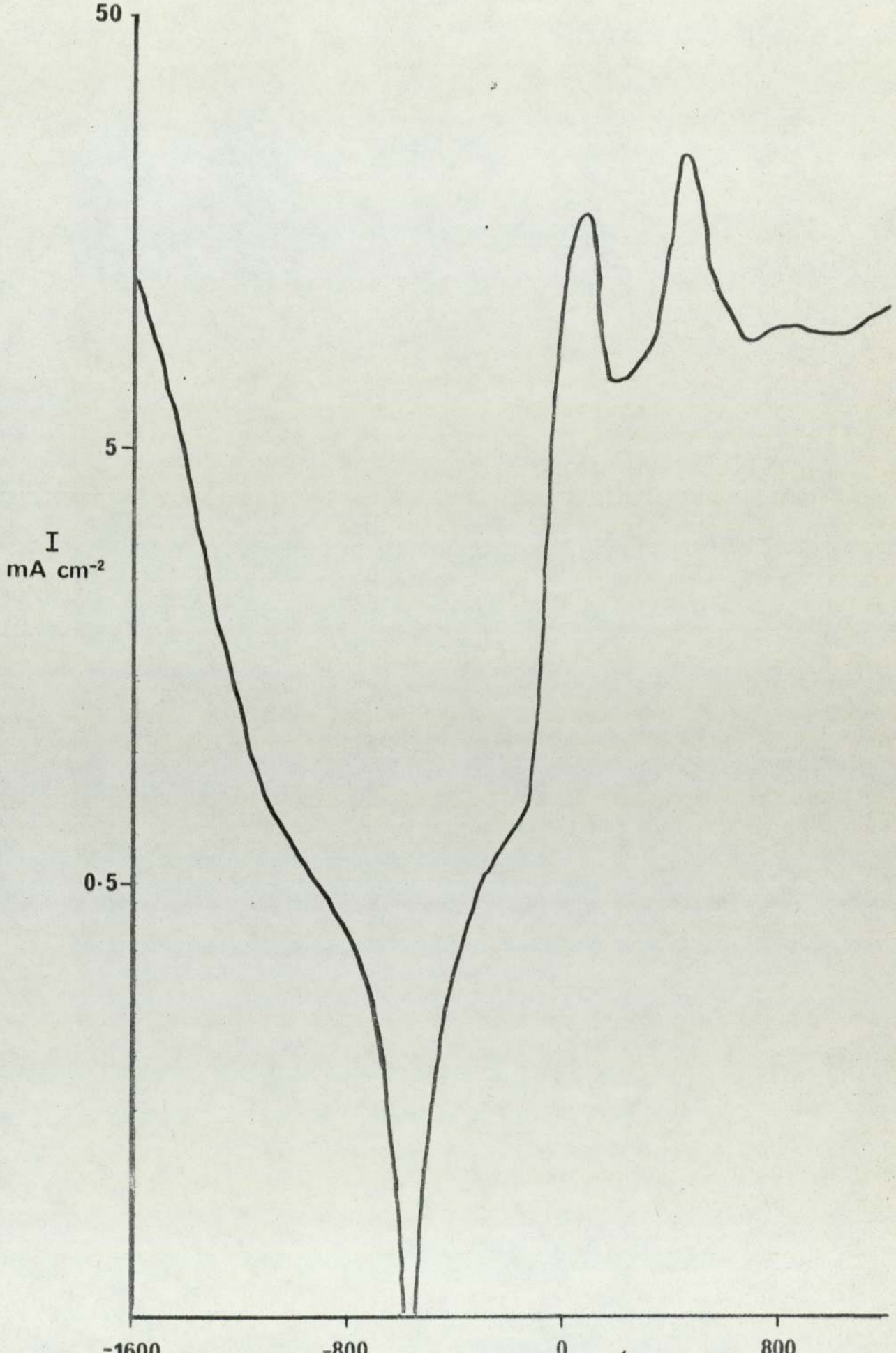

TABLE 2

Measured X-ray Diffraction Data from Corrosion Compounds

SEAWATER pH 8.5								SEAWATER pH 12.5			
-320mV		-100mV		+60mV		+340mV		0mV		+400mV	
I	d(Å)	I	d(Å)	I	d(Å)	I	d(Å)	I	d(Å)	I	d(Å)
w	4.33	w	5.47	m	5.50	w	5.54	m	0.94	5	5.47
w	3.43	vw	4.98	w	5.12	s	3.10	m	0.86	vw	4.70
w	3.35	m	3.27	vw	3.40	w	2.70	m	0.84	vw	3.30
w	3.24	s	2.83	vw	3.25	w	2.59			s	2.84
vw	3.05	m	2.27	vw	3.13	vw	2.43			s	2.68
s	2.84	s	2.00	s	2.79	w	2.26			s	2.24
w	2.37	w	1.82	m	2.26	vw	2.13			s	2.05
w	2.10	vw	1.71	vw	2.13	vw	2.03			w	1.95
s	2.00	w	1.63	m	2.00	s	1.91			m	1.78
w	1.82	vw	1.41	w	1.76	vw	1.83			m	1.68
vw	1.71	w	1.26	w	1.72	s	1.63			vw	1.62
m	1.63	vw	0.84	w	1.63	m	1.35			vw	1.49
w	1.55			w	1.41	m	1.24			w	1.35
m	1.41			w	1.38	m	1.11			m	1.26
w	1.38			w	1.26	m	1.04				
vw	1.29			w	1.15	w	0.96				
s	1.26			vw	1.00						
m	1.15			vw	0.94						
w	0.996			vw	0.89						
vw	0.953			vw	0.85						
m	0.942										
m	0.893										
vw	0.860										
w	0.851										

TABLE 3

Listed X-ray Diffraction Data

Ag(Cl,Br) PDF 14-255		NaCl PDF 5-628		$Cu_7Cl_4(OH)_{10}H_2O$ PDF 23-948		CuCl PDF 6-344		Cu_2O PDF 5-667		Cu(OH)Cl PDF 23-1063	
I	d(Å)	I	d(Å)	I	d(Å)	I	d(Å)	I	d(Å)	I	d(Å)
	3.24		3.26	100	5.49		3.12	9.0	3.02	70	5.56
	2.81		2.82	30	5.04		2.71	100	2.47	10	2.84
	1.99		1.99	50	2.84		1.92	37	2.14	10	2.78
	1.70		1.63	90	2.77		1.63	1.0	1.74	100	2.76
	1.62		1.41	55	2.75		1.35	27	1.51	30	2.52
	1.26		1.26	90	2.27		1.24	17	1.29	15	2.28
	1.15		1.15	20	1.83		1.11	4.0	1.23	25	2.24
	0.94		0.89	15	1.72		1.04	2.0	1.07	20	2.00
				10	1.39			4.0	0.98	10	1.93
							0.915	3.0	0.95	10	1.85
								3.0	0.87	15	1.77
								3.0	0.83	10	1.67
										20	1.61
										10	1.50
										10	1.39

TABLE 4

Constant Strain Rate Stress Corrosion Results

MATERIAL		TEST CONDITION	UTS (N/mm^2)	% Elong
OB	$\dot{\varepsilon}=1x10^{-7}/s$	Air	408	2.8
OB	$\dot{\varepsilon}=1x10^{-6}/s$	Air	413	4.5
OB	$\dot{\varepsilon}=1x10^{-3}/s$	Air	519	46.0
OB	$\dot{\varepsilon}=1x10^{-7}/s$	Sea Water Free Corrosion Potential	377	6.2
OB	$\dot{\varepsilon}=1x10^{-7}/s$	Sea Water -200mV	405	4.2
OB	$\dot{\varepsilon}=1x10^{-7}/s$	Sea Water -100mV	354	8.5
OB	$\dot{\varepsilon}=1x10^{-7}/s$	Sea Water + 10ppm Cystine Free Corrosion Potential	420	6.8
OB	$\dot{\varepsilon}=1x10^{-6}/s$	Sea Water Free Corrosion Potential	447	7.1
OB	$\dot{\varepsilon}=1x10^{-6}/s$	NaOH pH 12.3 Free Corrosion Potential	400	2.3
OB	$\dot{\varepsilon}=1x10^{-6}/s$	NaOH pH 12.3 + 500mV	424	5.4
OB	$\dot{\varepsilon}=1x10^{-6}/s$	NaOH pH 12.3 + 15ppm Cu^{+} Free Corrosion Potential	413	3.4
OB	$\dot{\varepsilon}=1x10^{-6}/s$	$Na_2CO_3+Cu^{+}$ pH 11.5 Free Corrosion Potential	408	3.4
OB56	$\dot{\varepsilon}=1x10^{-6}/s$	Sea Water Free Corrosion Potential	454	6.5
IA	$\dot{\varepsilon}=1x10^{-6}/s$	Sea Water Free Corrosion Potential	508	34
IA	$\dot{\varepsilon}=1x10^{-3}/s$	Air	505	62
IA54	$\dot{\varepsilon}=1x10^{-6}/s$	Sea Water Free Corrosion Potential	501	31.8
IA54	$\dot{\varepsilon}=1x10^{-3}/s$	Air	512	44
IA56	$\dot{\varepsilon}=1x10^{-6}/s$	Sea Water Free Corrosion Potential	531	23
IA56	$\dot{\varepsilon}=1x10^{-3}/s$	Air	555	40
IB	$\dot{\varepsilon}=1x10^{-3}/s$	Air	579	30.7
IB	$\dot{\varepsilon}=1x10^{-6}/s$	Air	570	11.3
IB	$\dot{\varepsilon}=1x10^{-6}/s$	Sea Water Free Corrosion Potential	567	13.6
IB	$\dot{\varepsilon}=1x10^{-6}/s$	Sea Water -200mV	574	16
IB	$\dot{\varepsilon}=1x10^{-6}/s$	NaOH pH 12.3 Free Corrosion Potential	569	12.8
IB54	$\dot{\varepsilon}=1x10^{-3}/s$	Air	601	34
IB54	$\dot{\varepsilon}=1x10^{-6}/s$	Sea Water Free Corrosion Potential	585	16.8
IB54	$\dot{\varepsilon}=1x10^{-6}/s$	NaOH pH 12.3 Free Corrosion Potential	578	19.1
IB56	$\dot{\varepsilon}=1x10^{-3}/s$	Air	620	36
IB56	$\dot{\varepsilon}=1x10^{-6}/s$	Sea Water Free Corrosion Potential	601	14.3
IB56	$\dot{\varepsilon}=1x10^{-6}/s$	NaOH pH 12.3 Free Corrosion Potential	589	14.3
IC	$\dot{\varepsilon}=1x10^{-3}/s$	Air	692	14
IC	$\dot{\varepsilon}=1x10^{-6}/s$	Sea Water Free Corrosion Potential	685	9.1
IC54	$\dot{\varepsilon}=1x10^{-3}/s$	Air	670	18
IC54	$\dot{\varepsilon}=1x10^{-6}/s$	Sea Water Free Corrosion Potential	678	9
IC56	$\dot{\varepsilon}=1x10^{-3}/s$	Air	583	39
IC56	$\dot{\varepsilon}=1x10^{-6}/s$	Sea Water Free Corrosion Potential	578	25.2

FIG 132 OB Air $\dot{\varepsilon}$ $1x10^{-3}/s$ x360

FIG 133 OB Air $\dot{\varepsilon}$ $1x10^{-3}/s$ x900

FIG 134 OB Air $\dot{\varepsilon}$ $1x10^{-6}$/s x650

FIG 135 OB Air $\dot{\varepsilon}$ $1x10^{-6}$/s x1000

FIG 136 OB Air $\dot{\varepsilon}^{\circ}$ $1x10^{-7}/s$ x800

FIG 137 OB Air $\dot{\varepsilon}^{\circ}$ $1x10^{-7}/s$ x900

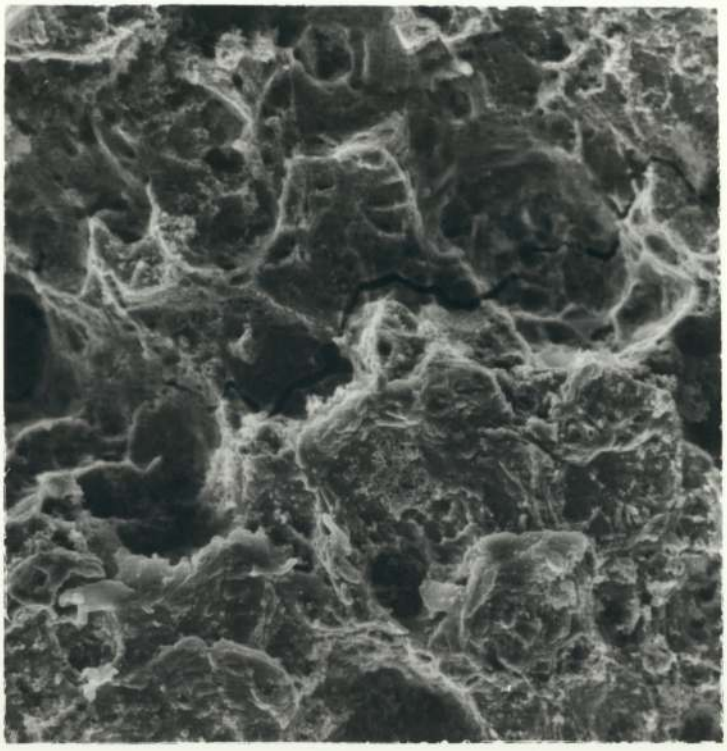

FIG 138 OB Sea Water Rest Potential $\dot{\varepsilon}$ $1x10^{-6}$/s x200

FIG 139 OB Sea Water Rest Potential $\dot{\varepsilon}$ $1x10^{-6}$/s x1000

FIG 140 OB Sea Water Rest Potential $\dot{\varepsilon}$ $1x10^{-7}/s$ x240

FIG 141 OB Sea Water Rest Potential $\dot{\varepsilon}$ $1x10^{-7}/s$ x800

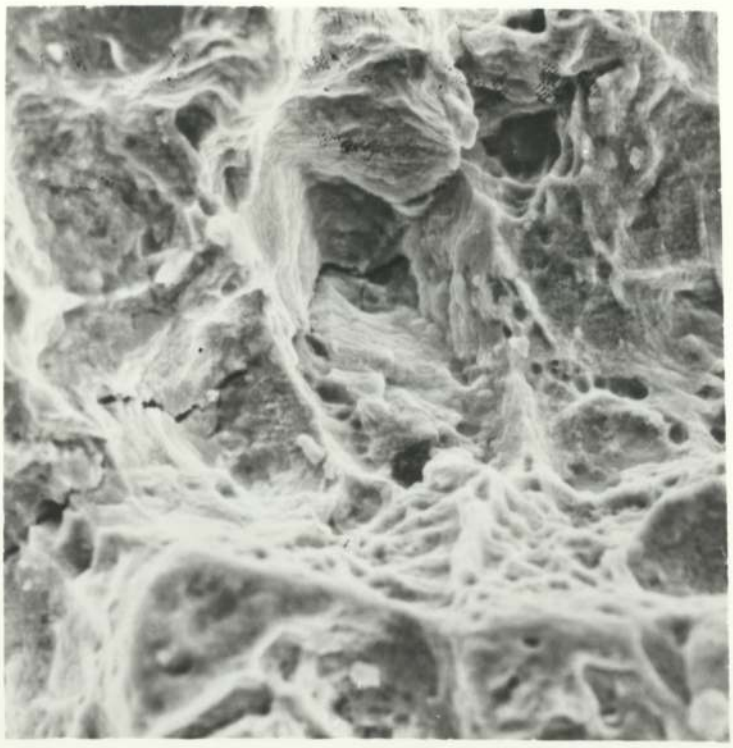

FIG 142 OB Sea Water −200 mV $\dot{\varepsilon}$ $1x10^{-7}/s$ x470

FIG 143 OB Sea Water −200 mV $\dot{\varepsilon}$ $1x10^{-7}/s$ x900

FIG 144 OB Sea Water −100 mV $\dot{\varepsilon}$ 1×10^{-7}/s x240

FIG 145 OB Sea Water −100 mV $\dot{\varepsilon}$ 1×10^{-7}/s x390

FIG 146 OB Sea Water + L Cystine Rest Potential $\dot{\varepsilon}^{o}$ $1x10^{-7}/s$ x650

FIG 147 OB Sea Water + L Cystine Rest Potential $\dot{\varepsilon}^{o}$ $1x10^{-7}/s$ x900

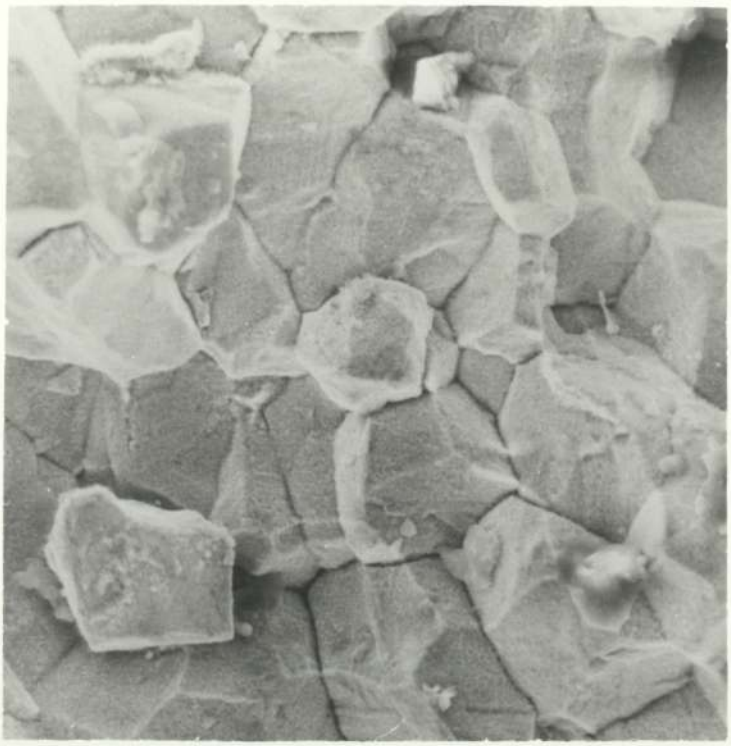

FIG 148 OB Na OH Rest Potential pH 12.3 $\dot{\varepsilon}$ $1x10^{-6}/s$ x300

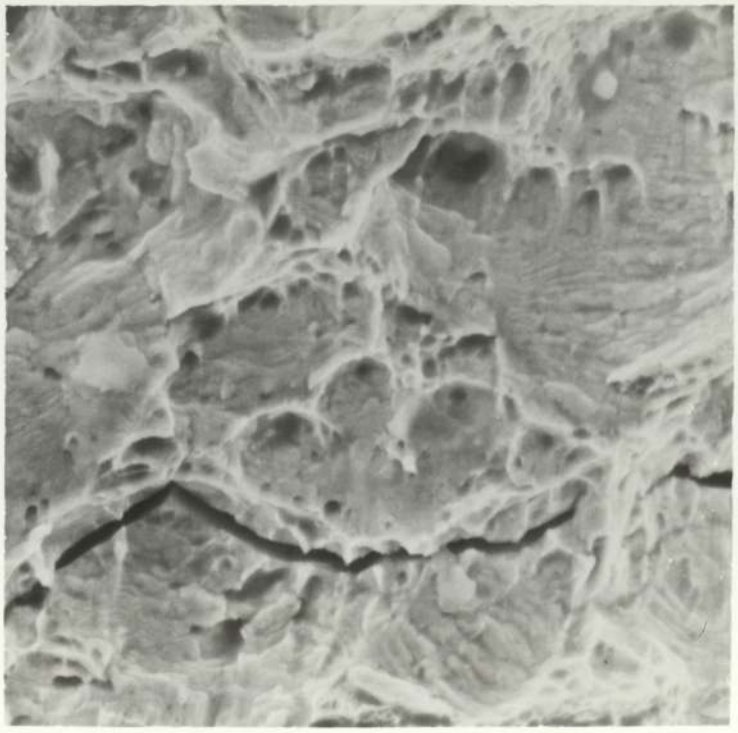

FIG 149 OB NaOH Rest Potential pH 12.3 $\dot{\varepsilon}$ $1x10^{-6}/s$ x750

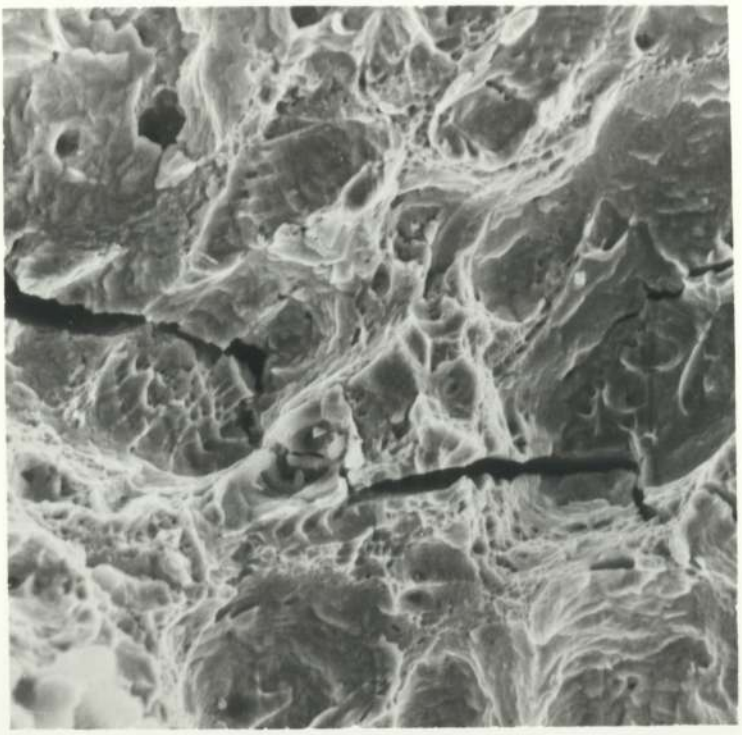

FIG 150 OB NaOH . +500 mV pH 12.3 $\dot{\varepsilon}^{c}$ $1x10^{-6}/s$ x550

FIG 151 OB NaOH +500 mV pH 12.3 $\dot{\varepsilon}^{o}$ $1x10^{-6}/s$ x1200

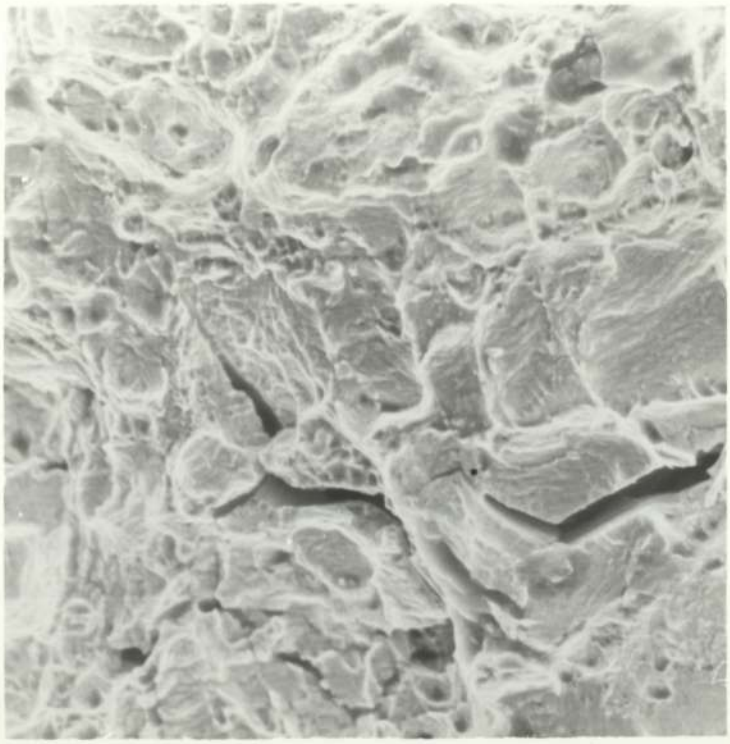

FIG 152 OB NaOH +Cu 15ppm pH 12.3 Rest Potential $\dot{\varepsilon}$ $1x10^{-6}$/s x330

FIG 153 OB NaOH + Cu 15ppm pH 12.3 Rest Potential $\dot{\varepsilon}$ $1x10^{-6}$/s x1000

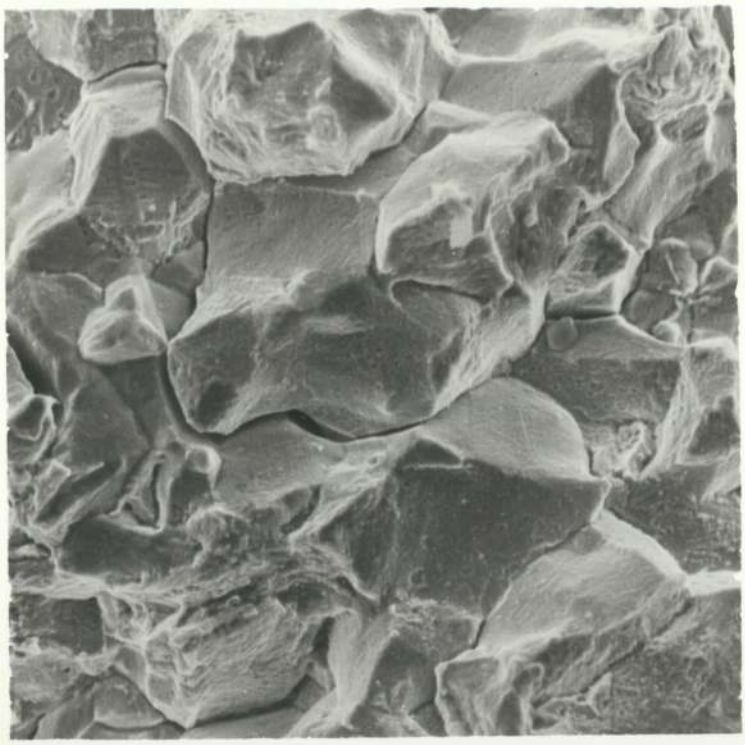

FIG 154 OB Na_2CO_3 + Cu 15ppm Rest Potential $\dot{\varepsilon}$ $1x10^{-6}$/s x300

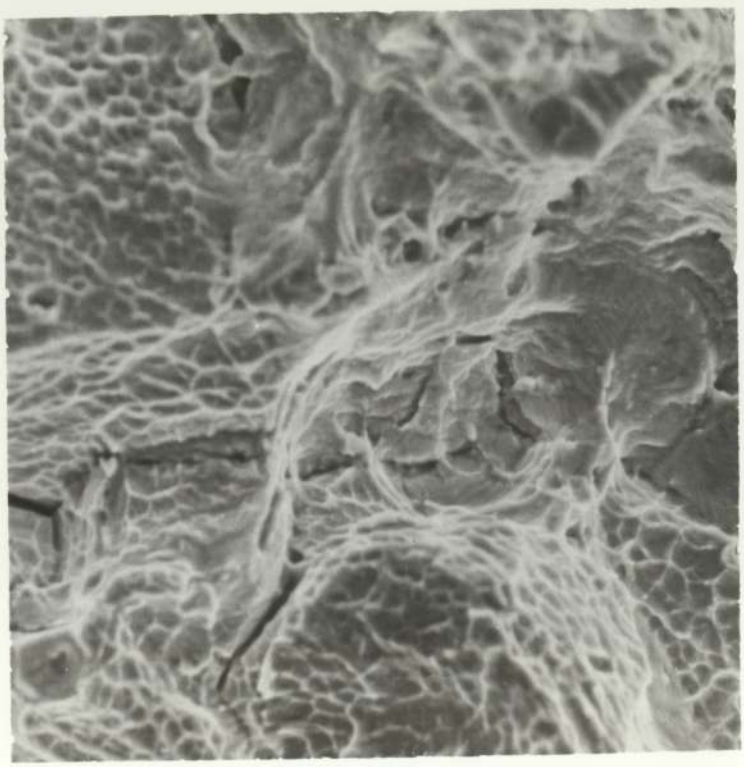

FIG 155 OB Na_2CO_3 + Cu 15ppm Rest Potential $\dot{\varepsilon}$ $1x10^{-6}$/s x600

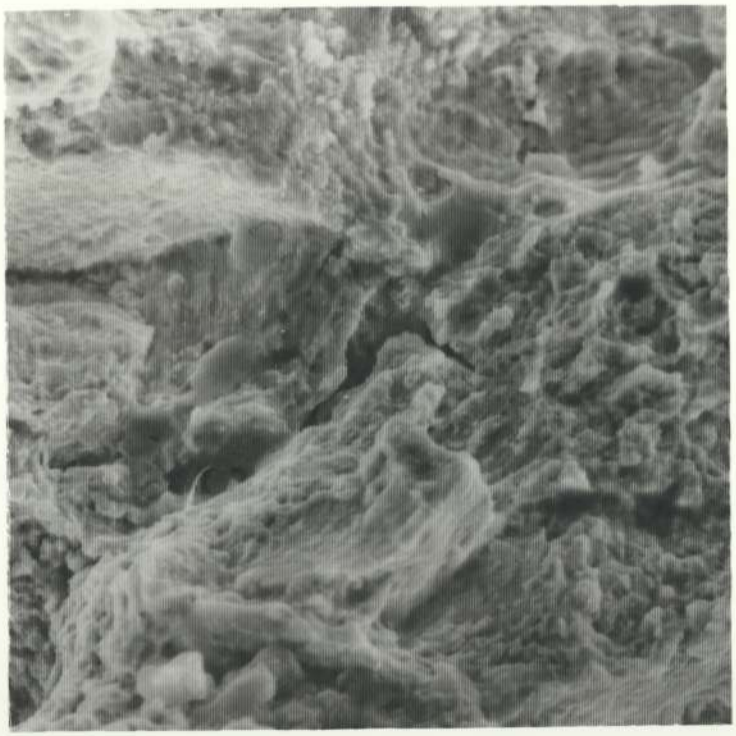

FIG 156 1B Sea Water Rest Potential $\dot{\varepsilon}$ $1x10^{-6}/s$ x550

FIG 157 1B Sea Water Rest Potential $\dot{\varepsilon}$ $1x10^{-6}/s$ x1000

FIG 158 1B Air $\dot{\varepsilon}$ $1x10^{-6}/s$ x750

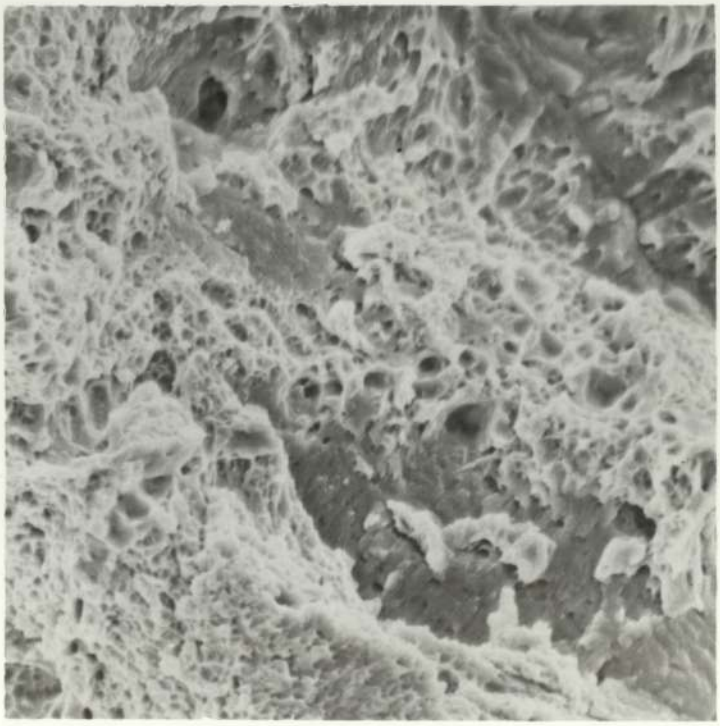

FIG 159 1B Air $\dot{\varepsilon}$ $1x10^{-6}/s$ x1000

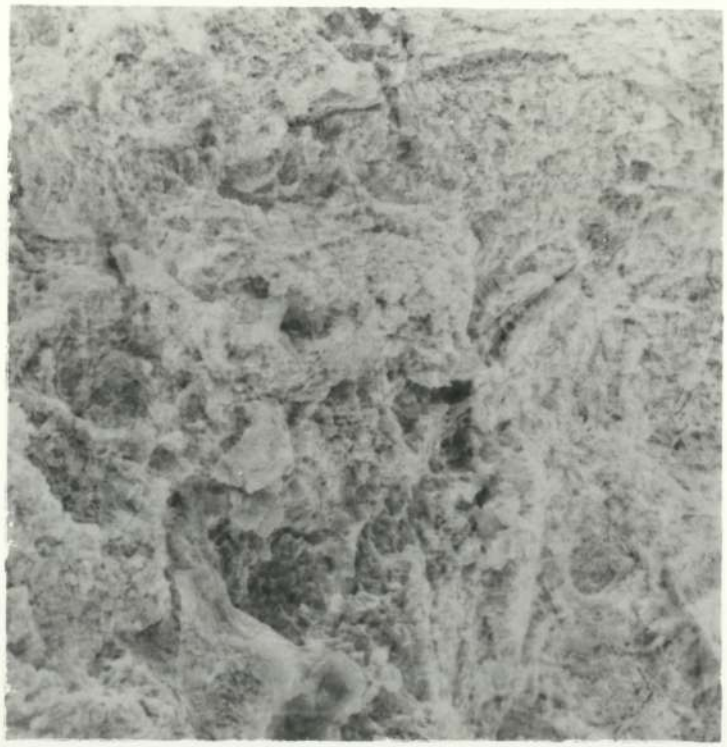

FIG 160 1B Sea Water −200mV $\dot{\varepsilon}$ $1x10^{-6}$/s x550

FIG 161 1B Sea Water −200mV $\dot{\varepsilon}$ $1x10^{-6}$/s x1300

FIG 162 1B54 Sea Water Rest Potential $\dot{\varepsilon}$ $1x10^{-6}$/s x1000

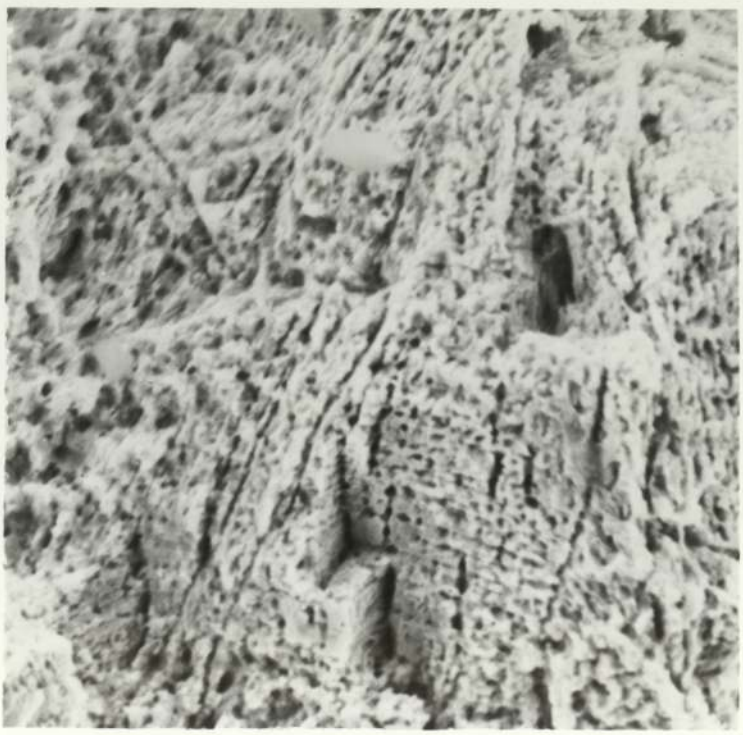

FIG 163 1B54 Sea Water Rest Potential $\dot{\varepsilon}$ $1x10^{-6}$/s x1200

FIG 164 1B56 Sea Water Rest Potential $\dot{\varepsilon}^{\circ}$ $1x10^{-6}/s$ x500

FIG 165 1B56 Sea Water Rest Potential $\dot{\varepsilon}^{\circ}$ $1x10^{-6}/s$ x1000

FIG 166 1A Sea Water Rest Potential $\dot{\varepsilon}^{o}$ $1x10^{-6}/s$ x800

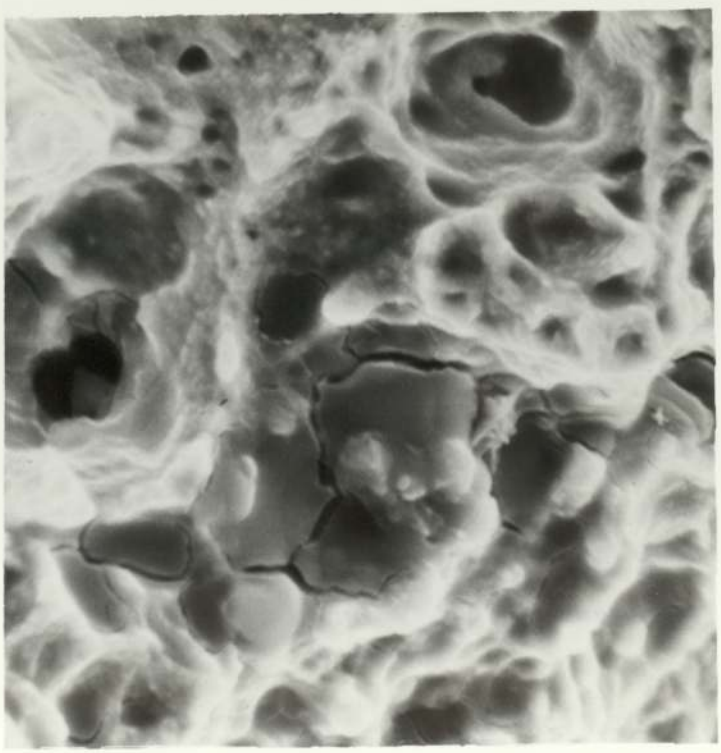

FIG 167 1A Sea Water Rest Potential $\dot{\varepsilon}^{o}$ $1x10^{-6}/s$ x1000

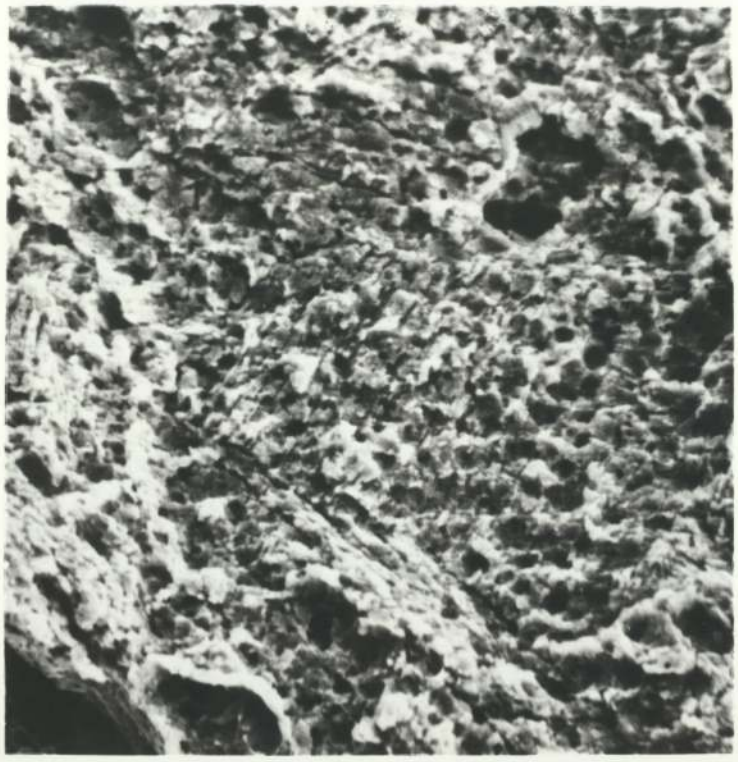

FIG 168 1A54 Sea Water Rest Potential $\dot{\varepsilon}$ $1x10^{-6}/s$ x1300

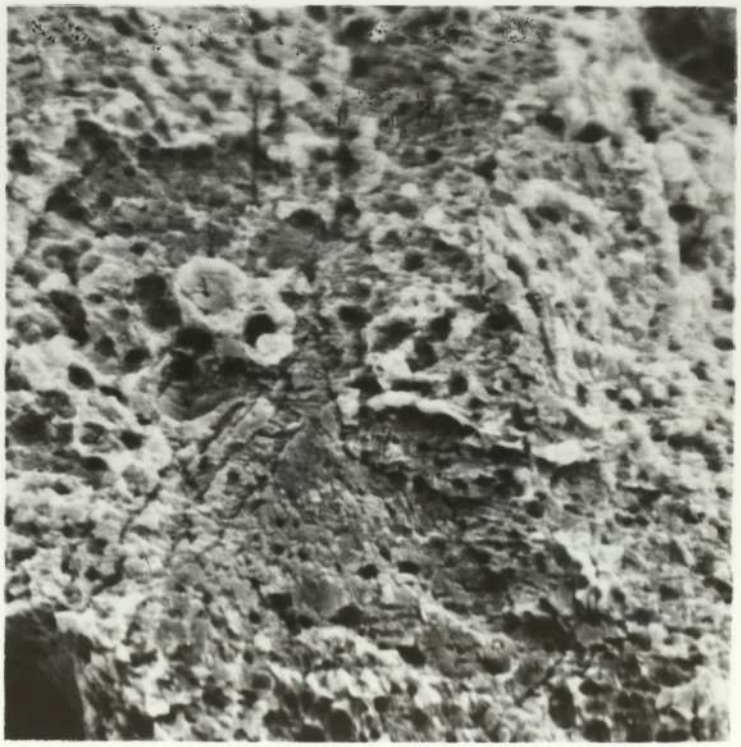

FIG 169 1A54 Sea Water Rest Potential $\dot{\varepsilon}$ $1x10^{-6}/s$ x1600

FIG 170 1A56 Sea Water Rest Potential $\dot{\varepsilon}$ $1x10^{-6}/s$ x1000

FIG 171 1A56 Sea Water Rest Potential $\dot{\varepsilon}$ $1x10^{-6}/s$ x1000

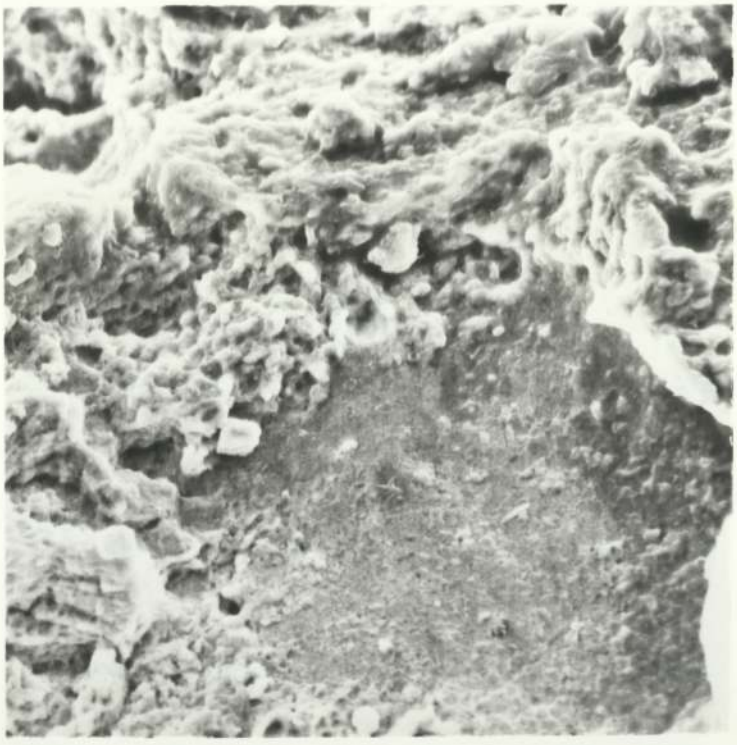

FIG 172 1C Sea Water Rest Potential $\dot{\varepsilon}$ $1x10^{-6}/s$ x600

FIG 173 1C Sea Water Rest Potential $\dot{\varepsilon}$ $1x10^{-6}/s$ x600

FIG 174 1C54 Sea Water Rest Potential $\dot{\varepsilon}$ $1x10^{-6}/s$ x360

FIG 175 1C54 Sea Water Rest Potential $\dot{\varepsilon}$ $1x10^{-6}/s$ x2000

FIG 176 1C56 Sea Water Rest Potential $\dot{\varepsilon}$ 1×10^{-6}/s x330

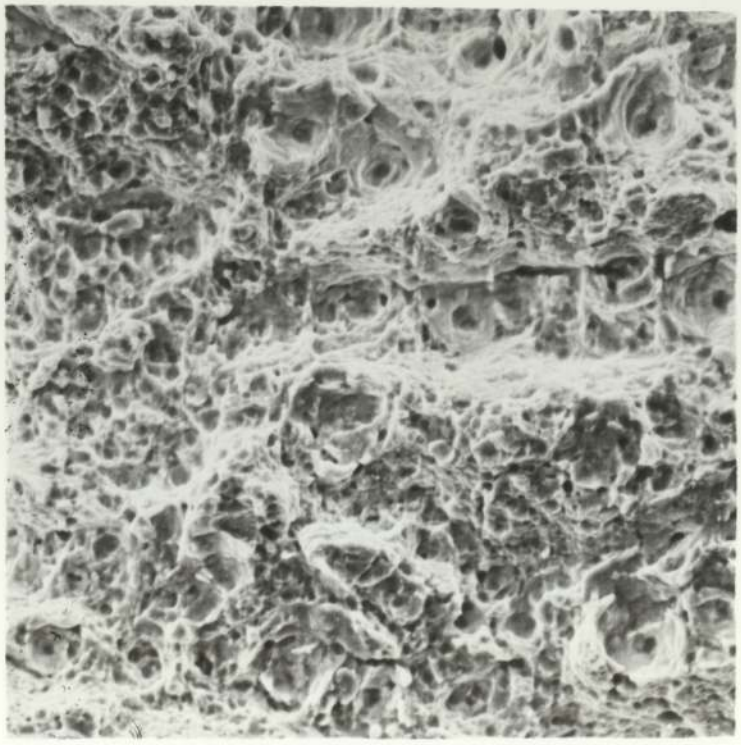

FIG 177 1C56 Sea Water Rest Potential $\dot{\varepsilon}$ 1×10^{-6}/s x600

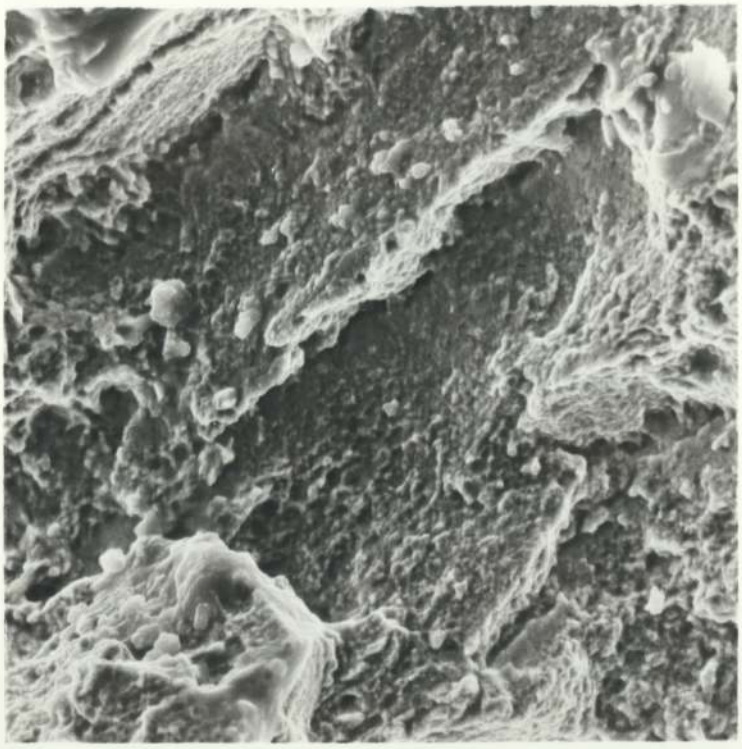

FIG 178 1B NaOH pH 12.3 Rest Potential $\dot{\varepsilon}$ $1x10^{-6}/s$ x500

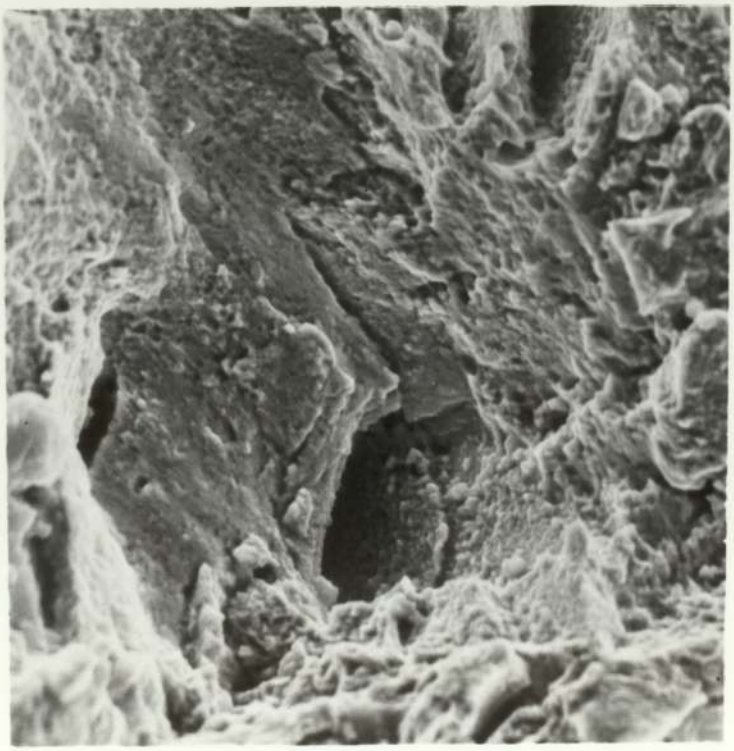

FIG 179 1B NaOH pH 12.3 Rest Potential $\dot{\varepsilon}$ $1x10^{-6}/s$ x550

FIG 180 1B54 NaOH pH 12.3 Rest Potential $\dot{\varepsilon}$ $1x10^{-6}/s$ x1000

FIG 181 1B56 NaOH pH 12.3 Rest Potential $\dot{\varepsilon}$ $1x10^{-6}/s$ x540

4. DISCUSSION

The metallographic examination of the as-received material has shown that all of the eleven alloy conditions being investigated essentially have a single phase microstructure. Reference to the binary copper-aluminium phase diagram (Fig 12) shows that for a 93/7 Cu/Al composition, a single phase alpha solid solution is thermodynamically stable up to the solidus temperature. Although the additions of cobalt and tin can form second phases with either copper or aluminium the level of the additions present in this investigation precludes the formation of a significant proportion of a second phase and therefore the alloys being investigated would be expected to be essentially single phase.

All of the alloys showed a twinned microstructure and since some twins were distinctly bent in the cold worked state it was concluded that they were annealing twins formed prior to deformation. Such a structure is indicative of a low stacking fault energy material which has been shown to result from substitutional solution of aluminium in a copper matrix.

A variation in grain size was observed in the as-received state of the alloys which did not relate to either the degree of cold work or the level of cobalt addition. This could indicate some variation in the production route of the alloys. Since the level of cold work within a compositional group was apparent from the density of slip lines present within the grains, this suggested that there had not been an interstage annealing treatment during the cold working operation, and that the variations in grain size had arisen from differences in the solution treatment operation.

Since it was possible to relate alloy composition to the slip line density, increased levels of cobalt giving an increased density of

slip lines, this indicated that the cobalt addition had affected the work hardening characteristics of the basic 93/7 Cu/Al alloy.

In all instances precipitates were observed in the as-received, solution treated and solution treated/cold drawn cobalt containing alloys. This suggests that either the alloy autohardens, which is not considered probable since work on similar alloy systems has indicated a lengthy incubation period prior to precipitation, or that the solution treatment has not been fully effective. Although the precipitation mechanism has been shown to require a lengthy incubation period, it has been reported that silicon, present as an impurity, may accelerate precipitation. Therefore precipitation may possibly occur during the hot working stages of fabrication until all the free silicon has been combined. This would account for the presence of the precipitation in the as-received solution treated condition, particularly if a separate solution treatment quench is not undertaken following the hot working operation. It is concluded that the solution treatment ($850^{o}C/W.Q$) employed by the manufacturers is a compromise which achieves a reasonable degree of solution of the precipitate phase without allowing excessive grain growth, which would occur if a higher temperature was used. The presence of a variable amount of precipitate could be a more probable cause of the variation in slip line density previously discussed, rather than substitutional effects conferred by the minor addition of cobalt.

The results of the tensile and hardness tests on the as-received material showed that the mechanical properties varied with cobalt content and level of cold work. The values of ultimate tensile strength, 0.2% proof stress and percentage elongation measured for the cobalt-free alloy in the solution treated and solution treated-cold drawn conditions are in broad agreement with those depicted in Fig 21. In general, strength values above these were obtained from the cobalt

containing alloys which indicated that this addition has contributed to the strength of the basic Cu/Al alloy. Since no significant yield point was observed in the stress-strain curve a strengthening mechanism involving locking of stationary dislocations is not considered as being operating. The cobalt addition has resulted in a shift in the stress-strain curve to higher values of stress which can be characteristic of a solid solution dislocation friction mechanism. However, in view of the low level of the addition, it is considered more probable that the increase in strength is caused by the precipitate identified in the microscopic examination. Furthermore the scatter observed between cobalt content and the mechanical property values can be related to an uncontrolled and therefore varying precipitate content between alloys, irrespective of their nominal cobalt contents.

Further evidence that precipitation was giving rise to an increase in strength was obtained by ageing the as-received material which showed that the mechanical properties of the cobalt containing alloys were dependent on ageing temperature, time at temperature and level of prior cold work. In general it was observed that a larger hardening response was obtained at the lower ageing temperature and for the higher level of prior cold work. It was also observed that the lengthy incubation period to strengthening was reduced by increasing the ageing temperature and level of cold work within the alloy. These responses are typical of precipitation hardening in general, and have been previously identified as occurring in a similar cobalt-containing aluminium bronze (80). There were also indications of multiple hardening peaks, which suggests that a multistage mechanism may be operating with the precipitation going through stages of being partially coherent or incoherent before the equilibrium phase is formed.

In comparison, the cold worked version of the cobalt free alloy softened on ageing, confirming the trend reported in Fig 22, whilst the properties of the solution treated material remained constant. This suggests that there is a tendency for either recovery or recrystallisation to occur on ageing the cobalt free alloy which is enhanced with increasing levels of cold work. Softening also occurs in the cold worked cobalt containing alloys but after a longer time at temperature presumably as a result of the cobalt addition. This indicates that mechanisms of strengthening and softening are competing during the ageing treatment and that the properties achieved for any ageing time-temperature combination are dependent on their relative contributions.

The absence of strengthening of the cobalt-free alloys suggests that the mechanism of anneal hardening is not playing an important role in the treatments undertaken. Furthermore the observed hardening of the unworked cobalt containing alloys also suggests that this mechanism is not operating in this system since one would expect increased hardening with increasing levels of cold work.

Precipitation hardening has been shown to alter the work hardening characteristics and is dependent on the relative stage in the hardening cycle. Initially if a coherent phase is formed the rate of work hardening will be low, similar to that of a pure metal, however, over-aged alloys containing incoherent phases will show an increased rate of work hardening. The greater the volume fraction of fine precipitate the greater is this effect. The work hardening exponent n gives a measure of the rate of work hardening, and although limited information was generated in this work the above trends have been detected in this alloy system. This also gives further support to a multistage precipitation process leading finally to overageing.

There are two main mechanisms which can cause softening of the cold worked state as a result of thermal treatment, namely recovery and recrystallisation. Although the mechanism of recovery can occur with both high and low stacking fault energy materials, the mechanism is normally associated with high stacking fault energy alloys. Very little dislocation rearrangement would be expected in a low stacking fault material such as the single phase aluminium bronze under investigation. In such materials therefore, recrystallisation would be expected to be the predominant mechanism for the removal of cold work. Grain boundary migration is an important factor in the ability for such alloy systems to undergo recrystallisation. The difference observed in the start of softening between alloys which contain cobalt and those which do not may therefore be considered as resulting from a retardation in the rate of grain boundary migration in the cobalt containing alloys. This could have resulted from precipitates pinning the grain boundaries. However, since, as reported in previous work, cobalt plays an important role in the precipitation, and softening was observed to occur at similar thermal treatments for the range of cobalt additions examined, solute attraction to grain boundaries should also be considered as a retarding mechanism. It should be noted that the cobalt containing alloys also contain a 0.2% tin addition when comparisons are made with the nominal 93/7 Cu/Al standard, particularly since this addition is made primarily to improve the intergranular stress corrosion resistance, and it has been reported that the improvement is due to selective segregation of the tin to the grain boundaries. However, the microscopic examination of the 12% cold worked, cobalt free alloy (OB) following ageing at 500^{o}C showed no evidence of grain boundary migration or of recrystallisation although softening was occurring. In fact the only visible microstructural change related to softening was a reduction in the internal strain lines. This suggests that recovery is taking place and can account for a significant degree of softening in this

alloy. In contrast recrystallisation was observed to coincide with softening in the cobalt containing alloy. However, it should be noted that recrystallisation was only observed in the 25% cold worked material and that recovery may be operating in the 12% cold worked condition and that the effects are marked by precipitation. Microscopic evidence of such precipitation was obtained on ageing. In the over-aged condition the precipitate size was too large for coherency. The precipitate was analysed by electron probe microanalysis (EPMA) as a cobalt-aluminium compound. This is in agreement with previous work on similar alloy systems.[84] Similar precipitates were also observed prior to the hardening peak and although the size prevented quantitative EPMA the analysis suggested a composition similar to the over-aged precipitate. However, this does not necessarily indicate that the precipitation takes place in one stage by the formation of an incoherent cobalt-aluminium intermetallic since the incoherent phase observed early on in the ageing treatment could have been the result of the incomplete solution treatment.

Transmission microscopy of the alloy containing 0.7% cobalt in the solution treated condition indicated the presence of a fine background precipitate and a large spheroidal phase. This further suggests that the solution treatment had been partially ineffective. Electron diffraction studies identified the large globular phase as being simple cubic with a lattice parameter of 3.08Å. It was noted that the observed lattice spacings of the precipitate were related to those of the compound CoAl (which has a cubic O_h^1-Pm3m symmetry) by a constant factor of 1.08X. Smaller globular precipitates having the same lattice parameter and crystal structure as the large ones were observed on ageing the alloy. These were found to be orientated with respect to the matrix by the Kurdjumov-Sachs relationship (111)m// (110)ppt, $[\bar{1}01]$ m// $[\bar{1}11]$ ppt for face centred and body centred cubic phases. Additional

orientations between precipitate and matrix were also identified, particularly from large precipitates. However, they did not conform to standard relationships and did not align close-packed planes in the matrix and precipitate. It is considered that these relationships have resulted from a precipitate growing in a matrix which has subsequently recrystallised. Such precipitates will have no fixed relationship with the matrix. Evidence supporting this hypothesis was obtained from the over-aged alloy 7C55 in which recrystallisation was confirmed by optical microscopy studies where rod-like precipitates were observed having a relationship with the matrix of $[34\bar{3}]$ m// $[\bar{1}11]$ ppt. (101)m// (211)ppt. This relationship differs from the Kurdjumov-Sachs relationship.

The presence of planar dislocation arrays in the solution treated condition indicates that the alloy system has a low stacking fault energy. From the evidence obtained it is postulated that initial strengthening takes place via a lowering of the stacking fault energy by segregation of cobalt atoms. This is characterised by the lack of recovery, the twinned nature of the material, the planar dislocation structure and a high rate of work hardening. Such a mechanism will be dependent on the degree of prior cold work through its effect on the stacking fault density. The observed relationship between the % cobalt addition and the amount of cold work necessary to achieve a given degree of strengthening is in accordance with this mechanism. It is observed that ageing gives rise to precipitation and it is suggested that in the initial stages the areas of stacking fault would be ideal sites for precipitation of cobalt. Cobalt exists as two allotropes, the alpha close packed hexagonal form predominates below 400^{o}C and the beta face centred cubic above that temperature. However, the transformation between the allotropes is sluggish and therefore it may be expected that for short ageing times the cobalt will be present in the alpha variant. Since the stacking sequence across stacking faults in a face

centred cubic matrix may be considered as equivalent to that of a region of hexagonal close packing, the cobalt would be expected to concentrate in these regions. The concentration at these locations is larger than average and as ageing proceeds it is reasonable to expect precipitation to start here. Further ageing may give a series of cobalt-aluminium precipitates prior to the formation of the identified CoAl compound. Although precipitation may give rise to a further increase in strength the concomitant removal of cobalt and aluminium from the stacking faults may offset this effect. The removal of cobalt and aluminium from solid solution could lead to an overall reduction in the work hardening rate by increasing the stacking fault energy and therefore lowering the density of dislocations. Since very small, coherent precipitates are ineffective barriers to dislocation movement, the work hardening exponent is not increased by the formation of the precipitate particles, i.e there is no compensation for the loss of aluminium and cobalt from the stacking fault. The increase in work hardening rate on prolonged ageing is, however, attributed to the precipitation mechanism since the density of dislocations is still decreasing. At such times commensurate with softening, incoherent precipitates are formed. The stress required to bow around these larger over-aged precipitates reduces as the particle size is increased. Prior to this the particles will be sheared and although this raises the yield point, it does not increase the work hardening rate. However, when bowing of dislocations around the particles occurs, the arrays of dislocation loops formed as plastic deformation proceeds will increase the work hardening rate.

The observed changes in dislocation networks, in particular the density of dislocations in planar arrays and the separation distance between partial dislocations are important factors in determining the resistance of the alloy to stress corrosion. This is also affected by

the observed development of precipitates and precipitate-free zones at grain boundaries and stacking faults. However, to fully characterise an alloys resistance to stress corrosion the electrochemical factors also need consideration.

The conditions of pH and applied potential identified from Pourbaix diagrams which correspond to a boundary between zones of corrosion and passivation may form a useful basis for predicting a sensitivity to stress corrosion cracking. However, these conditions relate to thermodynamically stable states, which may not necessarily exist during crack extension. In order to obtain a fuller understanding of the electrochemical reactions which may occur at the surface of a freshly formed crack, potentiostatic data have been determined for a range of environmental conditions. The resultant graphical plot of applied potential versus log current density is influenced by kinetic factors and the regions of instability existing adjacent to a boundary between corrosion and passivation may give a more accurate prediction of the conditions likely to produce susceptibility to stress corrosion cracking.

The form of the cathodic polarisation data was similar for all solutions examined and suggests that dependent on the applied potential, two distinct electrochemical mechanisms are controlling the corrosion rate. At large negative potentials a plateau in current density is observed. This indicates that a diffusion overpotential mechanism is controlling. At less negative potentials, activation overpotential plays a more significant role.

In order to ascertain which mechanism is controlling, the potential was calculated for a given current flow arising from the cathodic reductions of oxygen and hydrogen. In acid solutions the respective

reactions were assumed to be:

$$\tfrac{1}{2}\ O_2 + 2H_3O^+ + 2e^- \rightarrow 3H_2O$$

and

$$H_3O^+ + e^- \rightarrow \tfrac{1}{2}\ H_2 + H_2O$$

whilst in neutral and base solutions the reactions were taken as:

$$\tfrac{1}{2}\ O_2 + H_2O + 2e^- \rightarrow 2OH^-$$

and

$$H_2O + e^- \rightarrow \tfrac{1}{2}\ H_2 + OH^-$$

The equilibrium potential was calculated for the given pH from the Nernst equation

$$E = E^o + \frac{RT}{nF} \ln \frac{(ox)}{(red)}$$

as defined in section 1.2.2. The total potentials corresponding to a current density of 5×10^{-4} A/cm^2 and 5×10^{-5} A/cm^2 were calculated from the sum of this calculated value of E and the associated over potential. The value of the over potential for the respective values of i was calculated from the Tafel equation where:

$$\eta = \frac{RT}{BnF} \ln i_o - \frac{RT}{BnF} \ln i$$

The particular values of the exchange current density i_o [127] for the hydrogen and oxygen reactions were substituted into the Tafel equation for the various pH's of the solutions examined.

The results from the calculations plotted graphically in Fig 121 indicate that at low cathodic overpotentials the observed current for a given over potential is higher than that which can be attributed to hydrogen reduction. In contrast, higher values of current are predicted from the oxygen reduction reaction. However, as suggested previously, these values may not necessarily be achieved because diffusion control can lead to a limiting current density i_L. The value of i_L was calculated from the equation

$$i_L = \frac{DnFc}{\delta} \quad (128)$$

The value of D, the diffusion coefficient of O_2 in the solution was taken as 1×10^{-5} cm^2 S^{-1} and C the solute concentration of oxygen 1.3 mole m^{-3} (129). Substituting these values into the above equation with the appropriate values of F the Faraday constant, n the number of electrons involved and 0.05 cm for δ the diffusion layer thickness shows that diffusion control is indeed occurring, resulting in a limiting current density of 0.1 $mAcm^{-2}$. This is in reasonable agreement with the observed limiting value of 0.5 $mAcm^{-2}$.

The trough in current density on the cathodic side of the rest potential in hydrochloric acid and sodium hydroxide solutions at pH 3.1 and 8.1 respectively is considered to have resulted from potentiometric reduction of a surface metal oxide.

The anodic Tafel slope for the hydrochloric acid solution was determined using a least squares analysis to be 160 mV. A single electron reaction would give a slope of 120 mV and a double electron reaction a value of 60 mV. It is therefore most probable that at low anodic over potentials corrosion proceeds in two stages with the metal surface being raised initially to the I oxidation state and that the transfer coefficient B is not 0.5 as was assumed for the purpose of the calculation. A transition on increasing potential from immunity to a II oxidation state is predicted at a pH of 3.1 from the Cu-H_2O Pourbaix diagram (Fig 7).

In contrast, general corrosion was observed in seawater/pH 8.1 with increasing anodic over potentials leading to the formation of $Cu_7Cl_4(OH)_{10}H_2O$ and CuCl corrosion compounds. However, neither of these compounds adhered well to the metal surface and would not cause passivation. At potentials close to the corrosion potential there is a difference in the anodic polarisation behaviour between materials which had and had

not been previously cathodically polarised. This indicates that the corrosion behaviour of air filmed and freshly bared surfaces is different. Of particular interest is the more anodic corrosion potential of the cathodically cleaned surface and the minor passivation trough some 200 mV from the corrosion potential. X-ray diffraction analysis of the corrosion products formed in this region indicated that the deposit was either Ag(Cl,Br) or NaCl. Although there is 0.0002 ppm of silver in solution in seawater[130] and therefore it is conceivable that the film has formed as the product of an exchange reaction with copper, it is thought more feasible that the deposit was sodium chloride from evaporated seawater. The corrosion film is probably too thin and tenacious to remove from the metal surface.

Since there were no regions of unstable passivation identified in the seawater environment, a strain generated active path mechanism of stress corrosion is unlikely. However, it is more difficult to predict whether a pre-existing active-path mechanism is possible. Such a mechanism could occur if a grain boundary phase were present within the alloy.

In contrast, however, zones of unstable passivation were identified in solutions with pH 12.1 which relate to the formation of Cu_2O and Cu(OH)Cl films. In these environments a strain generated active-path mechanism could operate.

The results obtained from the polarisation studies suggest that all alloys examined behave in a similar bulk electrochemical manner, independent of composition and heat treatment. However, the addition of cobalt and the effect of cold work and ageing may give localised electrochemical variations, not resolvable by the experimental technique employed. These variations are related to associated metallurgical factors of precipitation and changes in the dislocation

networks and may cause a difference in sensitivity to stress corrosion cracking.

Constant strain rate tests undertaken in air on the cobalt-free alloy OB showed that there was a decrease in percentage elongation to failure associated with reducing strain rate. Commensurate with the decrease in ductility the fracture surface changed from one showing fine ductile dimples at the faster strain rate to one showing ductile dimples with areas of flat facets and secondary cracking at slower strain rates. Similar tests undertaken at the free corrosion potential (-250mV S.C.E) in seawater gave higher elongation values to failure. It may be postulated that since the alloy forms an oxide film in air, at sufficantly slow strain rates, some fracture mode, similar to the film rupture mode by a strain-generated active-path mechanism, is operating. At faster strain rates fracture occurs at a faster rate than oxidation of the crack front. However, although a corrosion film is formed on the fracture surface during testing in seawater, it may not be sufficiently adherent to result in passivation and therefore general corrosion may effectively blunt the tip of the advancing crack. Tests undertaken at a 50 mV anodic over potential with respect to the free corrosion potential in seawater gave an increase in susceptibility to stress corrosion cracking as measured by elongation to failure. Since no passive films are formed at this potential this increase in susceptibility to stress corrosion cracking must have resulted from selective corrosion. If a certain energy is necessary for corrosion to occur at a significant rate, and the material contains localised high energy regions, at low applied anodic potentials the high energy sites may corrode, but the low energy sites may remain immune. Although higher anodic over potentials gave significant intergranular corrosion of the fracture surface, this was accompanied by extensive general corrosion of the specimen and as such would not be expected to lead to

stress corrosion cracking. At these increased potentials the higher energy sites become more subject to attack and the low energy sites approach the point of significant corrosion. Further increase in potential then produces a reduction in the difference on attack between the high and low energy site attack, as both increase, and general corrosion ensues.

In addition to galvanic coupling giving an increase in the susceptibility to stress corrosion cracking, environmental changes may occur in seawater which also alter the sensitivity. For instance cystine may be released by bacterial decay of organic matter. This compound acts as a cathodic hydrogen depolariser and therefore corrosion can take place in the absence of oxygen. Further complications result with copper alloys, since if cystine is present in sufficient quantity in seawater, a protective copper-cystine derivative is found on the metal surface. Unfortunately this film will break down under applied stress, or fracture spontaneously if too thick, leading to selective attack. These conditions are ideal for promoting stress corrosion cracking. The results obtained from tests undertaken on the 93/7 Cu/Al alloy (OB) in seawater with an addition of 10 ppm of cystine indicated no increase in susceptibility as a result of the addition. However, it should be considered that there may be significant differences between naturally derived polluted waters and those manufactured in the laboratory.

In addition to the presence of cystine or sulphate-reducing bacteria in polluted water, environmental changes such as an increase in pH are also feasible, particularly in stagnant inboard situations. Tests undertaken at the free corrosion potential in NaOH solution (pH 12.3) showed a mixed mode of failure, giving a small area of intergranular cracking around the circumference of the specimen with the remainder being transgranular with evidence of cleavage. A black corrosion film, identified from polarisation studies as Cu_2O, was formed on the

specimen surface during testing under these conditions. This is similar to that produced by a strain-generated active-path mechanism postulated for brass in tarnishing solutions. However, in non-tarnishing solutions where a thick oxide coating is not formed, the dislocation structure determines the mode of cracking and in this instance transgranular cracking would be expected from materials having the planar dislocation arrays observed. It is therefore possible that initially the cracks formed in the OB alloy in sodium hydroxide are coated with a relatively thick oxide coating leading to intergranular failure. However, continuous tarnishing cannot occur during crack extension and therefore the influence of dislocation structure plays a predominant role under such conditions. At an anodic overpotential corresponding to the observed 'passivation' trough in the sodium hydroxide solution a lessening in the susceptibility to stress corrosion cracking, as measured by elongation to failure, was observed. In support, the fractographs showed evidence of ductile dimples although some cleavage and secondary cracking was still apparent. This change in susceptibility may be associated with the presence of a non-tarnishing Cu(OH)Cl film formed at this potential.

Although there was not a further reduction in % elongation, shown from the tests undertaken at the free corrosion potential in sodium hydroxide with an addition of 15 ppm of Cu^{+} ions, a higher level of inter-granular and secondary cracking was apparent and there was no evidence of intergranular failure. It may therefore be suggested that as corrosion proceeds, thereby increasing the Cu^{+} concentration of the solution, there is a greater tendency for a dislocation-determining mode of failure.

An indication that the mode of failure was dependent on pH of the solution as opposed to the specific ions giving rise to the pH was obtained from the tests undertaken in saturated sodium carbonate. This

suggests that the corrosion product is the same at these pH levels and gives rise to a strain-generated active-path mechanism.

Tests undertaken in seawater at the free corrosion potential on the cold worked cobalt-containing alloy (IB) showed a higher elongation to failure than the comparable results from the cobalt free alloy. However, this does not necessarily indicate a lessening in sensitivity to stress corrosion cracking since the alloy which contains cobalt has a lower strain rate sensitivity as demonstrated by tests undertaken in air. Ductile dimples were predominant on the fracture surface at all strain rates for both the cobalt-free and cobalt-containing alloys tested in air. Such a fracture mechanism results from micro-void coalescence, the voids being predominantly nucleated by shear of inclusions or second phase particles. The elongation to failure in this situation is related to the spacing of the dimples and thereby the interparticle spacing. Lower values of elongation would therefore be expected from the precipitation-hardened cobalt-containing alloy. However, hydrostatic stress is necessary for the voids to grow and finally coalesce. Such a stress system is normally generated by necking and will depend on the degree of homogeneity of the material. The cobalt-containing alloy will necessarily be less homogeneous because of the segregation of precipitates and will show a greater tendency for necking. Although the specimens used in this work contained a pre-machined 127 μm radius notch, the notch may not be sufficiently deep to obviate the need for necking. If this is assumed, then it may be postulated that as the strain rate is decreased there will be a greater probability of the formation of localised differences in metallurgical structure necessary for the development of plastic instability at an earlier stage. The cobalt-containing alloy will show a lower strain rate sensitivity because it is less homogenous.

Although ductile dimples were also present on the IB test specimen that had been anodically polarised in seawater, selective corrosion was also apparent and at a more significant level than for the cobalt-free alloy. This is in agreement with the proposal that the cobalt addition decreases the stacking fault energy.

Ageing the alloy to pre-peak conditions further enhances the selective corrosion of the fracture surface of specimens tested at the free corrosion potential in seawater and suggests an enhanced susceptibility to stress corrosion cracking. However there is an increase in elongation from the aged condition in comparison to the solution treated cold worked condition. This does not necessarily indicate a lessening of stress corrosion susceptibility since the UTS is also higher and there is a reduction in the work hardening rate. Both of these factors would lead to an intrinsic increase in elongation to failure. Electron microscopy and mechanical property studies have shown that precipitation occurs during ageing which decreases the stacking fault energy. It is therefore proposed that the preferential attack of stacking faults is maintained and intensified following ageing, although the stacking fault energy is increasing due to precipitation at those sites. Similar tests on the IB material that had been aged to peak hardness showed a further increase in susceptibility to stress corrosion cracking identified by the reduction in the elongation to failure and the presence of a cleavage fracture mode. Tests in sea-water on the solution treated and aged versions of the cobalt alloy IA showed similar trends to the solution treated cold drawn IB material. It was noted, however, that the fractographical features from the corresponding ageing treatments were not as marked as those from the IB alloy. In comparison the tests in seawater on the IC alloy showed that prolonged ageing of this material increased the elongation to failure and restored the fracture surface to one showing ductile

dimples as opposed to cleavage. These findings parallel the observed ageing responses of the alloys. The solution treated cold drawn material ages more rapidly than the solution treated material, the effect being greater the higher the level of cold work. It is concluded that the sensitivity to stress corrosion cracking in seawater increases as the alloy ages, reaching a maximum at peak hardness, and then decreases following over-ageing. The sensitivity to stress corrosion cracking in this environment is attributed to a pre-existing active-path mechanism resulting from precipitation at stacking faults. In the over-aged condition where the sensitivity to stress corrosion is removed, recrystallisation has occurred and therefore the precipitate may no longer be located at stacking faults.

Tests undertaken on the IB alloy in NaOH (pH 12.3) at the free corrosion potential showed flat fracture surfaces characteristic of cleavage. Comparative tests undertaken on the aged version of this alloy also showed features typical of cleavage. Since ageing the alloy containing cobalt does not significantly affect the stress corrosion resistance in sodium hydroxide solution this supports the assumption that failure in this environment occurs by a strain generated active path. The incidence of cleavage was less predominant in the IB alloy than in the cobalt-free OB alloy which emphasises the reduction in sensitivity to stress corrosion cracking obtained by the addition of cobalt. This could result from a change in the filming characteristics of the basic 93/7 Cu/Al alloy due to the presence of cobalt and tin in the layer.

The evidence obtained from the constant strain rate tests has shown that the 93/7 Cu/Al alloy system is not immune to stress corrosion cracking. However, although a sensitivity to stress corrosion cracking has been identified, the ultimate tensile stresses associated with the stress corrosion tests are similar to those recorded from tensile tests undertaken in air. This indicates that the threshold stress, or

as has been suggested, the resultant strain rate, required to promote stress corrosion cracking is high. These findings do not automatically preclude the use of this alloy for bolts where the applied loading may be designed to be below this critical stress level. Recent work has indicated that similar conclusions apply to the complex nickel aluminium bronze alloy CA 104. This alloy is generally considered immune to stress corrosion cracking in a seawater environment. Although instances of such failures have been reported (Fig 19, 20), the particular conditions pertaining to the failure were not identified. However, more recent studies of failed studs has attributed the failure to stress corrosion resulting from torque loadings approaching the ultimate tensile stress. In contrast seawater immersion trials on bolts loaded to lower values (90% proof stress) have not shown any evidence of cracking following an 18 month testing period.

The selection of a bolting material based on the aluminium bronze alloy system by the criterion of stress corrosion resistance is therefore not clear cut. Trials in seawater on bolts manufactured from the contender aluminium bronze alloys are presently being undertaken. From this work it is hoped to classify the resistance of these alloys to stress corrosion cracking by obtaining maximum torque loadings which may safely be applied. It must be borne in mind that this test will not determine the influence of specific environmental factors or of the presence of an overpotential, however, it will demonstrate a fitness for purpose in clean flowing seawater.

Other factors which determine the selection of materials for bolts are adequate proof stress ($\simeq$ 400 N/mm^2) and ductility ($\simeq$ 15%). This work has demonstrated that a wide range of properties may be developed in the 93/7 Cu/Al-cobalt containing alloy system, depending on the percentage cobalt, degree of prior cold work, and the ageing time and temperature. Commensurate with the 0.2% proof stress requirement of

400 N/mm^2 the cobalt-containing alloy will have an elongation to failure of 40%, whereas although similar strength levels are achieved in the complex nickel-aluminium bronze alloy CA104, the elongation value is approximately halved. This lack of ductility in the CA104 alloy has meant that air cooling from 800°C is necessary to pass a quality assurance wedge test. The increased elongation associated with cobalt alloy should be beneficial in this respect.

In addition to these mechanical property requirements, material properties governing fabrication are also important. The CA104 alloy has an alpha-beta microstructure at elevated temperatures and is therefore ideally suited to bolt production by a hot heading route. The multiphase microstructure at room temperature limits the amount of cold reduction and therefore cold heading is not undertaken. However, since the cobalt-containing alloy is single phase at room temperature, cold heading in this material may be feasible. To ascertain the manufacturing routes possible with the cobalt-containing alloy, bolts have been manufactured commercially by the routes given below.

1. As solution treated bar stock - hot headed.
2. Solution treated plus 15% cold drawn - hot headed bar stock.
3. As solution treated bar stock - cold headed to give 13% cold work in neck of bolt.

Further work is in hand to evaluate these bolts and to establish a recommended ageing treatment. However, preliminary studies have shown that either manufacturing routes may be used, although it is realised that a size restriction may apply to the cold heading route related to press capacity.

5. CONCLUSIONS

1. A wide range of mechanical properties may be achieved by the 93/7 Cu/Al + cobalt alloy system depending on level of cobalt addition, degree of prior cold work and a combination of ageing time and temperature.

2. The mechanical properties measured in this investigation are not necessarily typical for the alloy system since it is concluded that the manufacturer's solution treatment has not been fully effective. However, it is shown that the requirement of a 400 N/mm^2 0.2% proof stress may be achieved with an elongation of approximately 40%.

3. Strengthening of the alloy system initially results from a lowering of the stacking fault energy probably by segregation of cobalt atoms. Ageing the alloy gives rise to multistage precipitation sequence. The final precipitate is a compound having a lattice parameter of 3.08Å and a cubic O_h^1 - Pm3m symmetry. This is considered to be a form of CoAl, with a slightly larger structure cell. The phase is orientated with respect to the matrix by the Kurdjumov-Sachs relationship $(111)m // (110)ppt, [\bar{1}01]\ m // [\bar{1}11]$ ppt.

4. The alloy system shows a sensitivity to stress corrosion cracking as identified by a constant strain rate test, although the failure stresses were similar to those from tests undertaken in air. Two modes of stress corrosion cracking were identified 1) in high pH solutions (≃ 12.3) by a strain generated active path 2) in seawater (pH 8.3) by a pre-existing active path. Sensitivity to cracking in seawater, commensurate with a pre-existing active path, is dependent on the metallurgical condition; ageing the alloy to peak hardness increases the

sensitivity to stress corrosion cracking.

5. The observed sensitivity to stress corrosion cracking does not necessarily preclude the use of this material for bolting applications if it can be demonstrated that a threshold stress for cracking operates and that this value is in excess of the torque loading necessary for bolt tightening.

6. Preliminary work has indicated that bolts can be manufactured from the alloy both by cold or hot heading routes.

6. FURTHER WORK

The present work has demonstrated the mechanical properties and stress corrosion resistance achieved from this alloy system, and has proposed a probable strengthening mechanism. However, before the alloy can be recommended for use as a bolting material in a seawater environment further work is necessary.

It is proposed that the bolts manufactured by the hot and cold heading routes be examined, and the effect of ageing treatment on the mechanical properties of the bolts be determined.

It is further proposed to undertake immersion trials in seawater on bolts tightened to various torque values and to compare their resistance to stress corrosion cracking with competitive bolting alloys.

REFERENCES

1. Y-ARD Report Y409/1, Y-ARD Ltd, Charing Cross Tower, Glasgow, 1971.

2. Navy Boards Report 31/8/1763 reprinted Marine Fouling and its Prevention U.S.N.I Maryland, 1952.

3. L Shrier. Corrosion 1:45. Newness-Butterworth 1976.

4. G. Bengaugh, R. May, J.Inst Metals 32, 81, 1924.

5. V. F. Lucey Brit. Corr. J. 1, 9, 1965.

6. R. Jones. Internal Report TM M4/74, AMTE(DL) Portsmouth, 1974.

7. Metals Handbook, 8th Edition, 1, 1028, ASM, 1961.

8. G. Bailey J. Inst Metals, 79, 243, 1951.

9. K. D. Efird. Corrosion 33, 347, 1977.

10. S. Gavin. Ph.D Thesis Cranfield Inst. Tech. 1978.

11. I. F. Pruzhinin, Russian Metall, 6, 138, 1975.

12. V. Rozenberg, Fundamentals of the Heat Resistance of Metals, Metallurgiya, 1973.

13. I. Kornilov, Physico-Chemical Fundamentals of the Heat Resistance of Alloys IZD-VO AN SSSR, 1961.

14. H. Orkawa et al Scripta Met, 5, 909, 1971.

15. H. Suzuki, Dislocations and Mech. Props of Crystals. J. Wiley & Sons, 1957.

16. A. Cottrell. Relation of Properties to Microstructure ASM Cleveland, 1954.

17. G. Schoeck, A. Seeger, Act Met, 7, 467, 1959.

18. A. Cottrell et al. Phil Mag. 44, 1064, 1953.

19. N. Mott, F. Nabarro, Strength of Solids Conf. Bristol 1948.

20. R. Fleisher. Acta Met 9, 996, 1961 and 11, 203, 1963.

21. J. Fisher. Acta Met 2, 9, 1954.

22. H. Sebastian Z. Metallkde 52, 825, 1961.

23. D. R. Hashiguti. J. Japan Inst. Met. 19, 103, 1955.

24. R. R Hart et al. Chin. Metall Trans 1, 3163, 1970.

25. O. Izumi, Sci Rep. Ritu A18, 9, 1966.

26. O. Izumi et al. Sci. Rep. Ritu. A11, 201, 1969.

27. J. M. Popplewell et al. Metal Trans 2, 3411, 1971.

28. V. Iveronova et al. Phys Met Metallogr 24, 190, 1967.

29. K. Nakajima et al. Trans ASM 58, 14, 1965.

30. M. Warlimont. Proceedings 3rd International Conf. on Strength of Metals and Alloys, 1, 554, London, 1973.

31. A. H. Cottrell. Dislocations and Plastic Flow in Crystals, Clarendon Press 1953.

32. O. Izumi, Sci. Rep RITU A18, 9, 1966.

33. S. Meura, T. Tajima, Metal Science April, 183, 1978.

34. N. Nott, F. Nabarro, Proc Physics Soc. 52, 86, 1940.

35. E. Orowan, Symposium on Internal Stresses in Metals, London 1948.

36. M. Ashby. Z. Metallk, 55, 5, 1964.

37. G. Ansell. Oxide Dispersion Strengthening AIME. Gordon and Beach, New York, 1968.

38. A. Kelly, B. Nickolson. Progress in Materials Science, 10, 3, 1963.

39. J. Fisher, E. Hart, R. Pry. Acta Met, 1, 336, 1953.

40. R. Ballough, R. Newman, Proc Royal Soc. A249, 427, 1959.

41. J. West. Metal Science Journal 7, 169, 1973.

42. C. Tyzach. Brit Corr Journal 6, 5, 1971.

43. R. Parkins, B. Corr. J. 7, 15, 1972.

44. E. Dix. Trans Amer. Inst. Min. Met. Engres., 137, 11, 1940.

45. S. Parr et al. Univ. III Bull. 177, 1928.

46. J. Green et al. J. Electrochem Soc. 117, 433, 1970.

47. P. Swann. Corrosion 19, 102t, 1963.

48. D. Vermihye. Stress Corrosion Cracking and Hydrogen Embrittlement of Iron Base Alloys, NACE, 1975.

49. H. Uhlig. Fundamental Aspects of Stress Corrosion Cracking, NACE, 1969.

50. B. Brown et al. Inter Report Naval. Research Lab Washington DC, 1968.

51. L. Shrier. Corrosion 1, 8:1. Newness-Butterworth, 1976.

52. H. Kaesche, Die. Korrosion der Metalk, Springer Verlag, Berlin, Heidelberg. New York, 1966.

53. U. Frank, Z. Naturforschy 4a, 378, 1949.

54. Atlas of Electrochemical Equilibria in Aqueous Solutions. M. Pourbaix, Pergamon Press. 1966.

55. G. Bianchi, P. Lough. Corrosion Science, 13, 853. 1973.

56. L. Shreir, Corrosion 9:69, Newness-Butterworth, 1976.

57. C. Wagner et al. Z. Electrochem, 44, 391, 1938.

58. M. Prazak, V Prakak. Hutniche. Listy, 11, 91, 1956.

59. J. Green, E. Haney. Corrosion, 23, 5, 1967.

60. F. C. Althof. Z. Metallkunde, 36, 177, 1944.

61. L. Graf., M. Lacour, Z f Metallkunde, 51, 1960, 152.

62. T. Hoar, J. Scully, J. Electrochem, Soc, 111, 348, 1944.

63. E. Pugh. A. Westwood. Phil. Mag., 13, 167, 1966.

64. E. Pugh et al. Trans ASM, 61, 468, 1968.

65. A. Forty, P. Humble. Phil. Mag., 8, 247, 1963.

66. A. Mc. Evity., A Bond. J. Electrochem Soc, 112, 131, 1965.

67. E. Pugh. The Theory of Stress Corrosion Cracking in Alloys NATO, Brussels, 1971.

68. S. Birley, D. Tromans. Corrosion, 27, 297, 1971.

69. H. Leidheiser, R. Kissinger. Corrosion, 28, 218, 1975.

70. R. Procter, G. Stevens. Corrosion Science, 15, 349, 1975.

71. A. Blackwood, N. Stoloff. Trans ASM, 62, 677, 1969.

72. A. J. Forty, Phys. Met of Stress Corr. Fracture, p.99 Interscience 1959.

73. P. R. Swann, J. Nutting, J.I.M. 50, 113, 1961.

74. P. R. Swann, Ph. D Dissertation, reported in J.I.M 50, 113, 1961.

75. R. Stricklel. S. Barnarff. J. Electro Chem. Soc. 109, 343, 1962.

76. P. Swann, J. Nutting, J.I.M 88, 478, 1960.

77. T. J. Koppeneal, M. Fine, Trans AIME 221, 1178, 1961.

78. L. Willey, Aluminium Vol 1, ASM, 1967.

79. A. Yutaka, Nippon. Kinzoku. Gakkai - Si, 5, 136, 1941.

80. J. Dennison. Corr. 16, 127, 1960.

81. Mesuda, J. Jap. Met. Soc. 16, 359, 1952.

82. K. Suzuki, Nippon, Kinzoku. Gakkai - Si, 29, 5, 1965.

83. K. Suzuki, Nippon, Kinzoku. Gakkai - Si, 29, 6, 1965.

84. V. Payak, Fiz. Metal Metalloved, 37, 1032, 1974.

85. W. Pearson. Handbook of Lattice Spacings and Structures of Metals. Pergamon, Vol 2, 1967.

86. F. Wilson. Trans AIME, 175, 262, 1948.

87. D. West., J. Inst. Met, 85, 97, 1956.

88. W. Alexander. J. Inst. Met. 63, 163, 1938.

89. M. Cook et al. J. Inst. Met. 80, 419, 1951.

90. W. Crofts et al. British Foundryman, 57, 89, 1964.

91. P. Machen & A. Smith. The Aluminium Bronzes CDA Publication No 31. 1966.

92. P. Bresina. Unpublished doctorite thesis referenced Fonderie, 28, 123, 1973.

93. P. Weill-Couly & D. Arnead. Fonderie, 28, 123, 1973.

94. E. A. Culpan & G. Rose, Internal Report WLTM No 111/77, AUWE Portland, 1977.

95. W. Pearson. Handbook of Lattice Spacings. Pergamon, Vol 2, 1967.

96. J. Regidor et al. Rev. Metal. Cenim. 10, 165, 1974.

97. J. Booth Private Communication ref WLTM No 111/77.

98. J. Klement, Corr. 10, 127, 1960.

99. B. Upton, Corr. 19, 204, 1963.

100. J. Rowlands. Corr Science, 2, 89, 1962.

101. F. Aldridge. Private Communication.

102. A. Yutaklea, Nippon, Kinzoku, Gakkai - Si, 5, 136, 1951.

103. B. Upton. Internal Report GNZ, AMTE(DL) Portsmouth, 1962.

104. J. Rowlands, T. Brown, Proceeding 4rd International Corr. Conf. RNTIBES, 1976.

105. R. Jones. Unpublished work.

106. R. Jones. Internal Report M69/75, AMTE(DL) Portsmouth, 1975.

107. G. Newcombe, C. Dimbylow, R. Jones. Welding of Castings Conference Bradford, 1976.

108. Min of Supply S & T Memo 16/49, 1948.

109. H. Johnson. Corr 22, 6, 1966.

110. R. L. Jones. Unpublished work.

111. R. Parkins, Internal Report AT/2043/049 AML/M 1978, AMTE(HH) Poole, 1978.

112. P. Macken, A. Smith. The Aluminium Bronzes. CDA Publication, 1966.

113. R. L. Jones. Internal Report TM No M91/76., AMTE(DL) Portsmouth, 1976.

114. A. Glough. University of Manchester 3rd year project report, 1976.

115. J. Waring. The Metallurgist & Materials Technologist, 5, 8, 1973.

116. DG Ships Specification 348. DGS, Foxhill, Bath.

117. P. Stanley, Internal Report TM No M3/76. AMTE(DL) Portsmouth, 1976.

118. P. Stanley, Internal Report TM No M87/72. AMTE(DL) Portsmouth, 1972.

119. C. Dimbylow, Internal Report TM No M101/74. AMTE(DL) Portsmouth, 1974.

120. R. Parkins et al, B. Corr. J., 7, 15, 1972.

121. M. Henthorne, R. Parkins. Corr. Sci., 6, 357, 1966.

122. M. Humphries, R. Parkins, Corr. Sci., 7, 747, 1967.

123. J. Breattle, S. Orman, Internal Report No 022/73. AWRE Aldermaston, 1973.

124. H. Heinzel et al. Z. Metallkunde, 61, 511, 1970.

125. Sverdrop, Johnson, Fleming. The Oceans Chap IV., Prentice-Hall, 1942.

126. Link Systems Z.A.F. Correction Programme. Link Ltd, High Wycombe, 1976.

127. Parsons. Handbook of Electrochemical Constants. Butterworth 1959.

128. L. Shier. Corrosion 9.40, Newnes-Butterworths 1976.

129. D. Barker, Portsmouth Polytechnic Private Communication.

130. Handbook of Chemistry and Physics. F.190. 55th Ed. GRC Press, 1975.